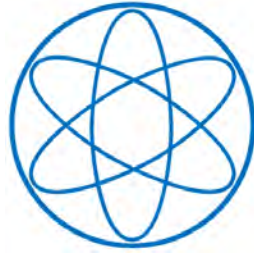


PHYSIK - DEPARTMENT



The new 2D-ACAR spectrometer
for spin-resolved measurements of
the electronic structure in correlated
systems

DISSERTATION
VON

HUBERT ANDREAS CEEH



TECHNISCHE UNIVERSITÄT MÜNCHEN

TECHNISCHE UNIVERSITÄT MÜNCHEN

Physik-Department

Lehrstuhl E21 für Experimentalphysik

**The new 2D-ACAR spectrometer for
spin-resolved measurements of the
electronic structure in correlated systems**

Hubert Andreas Ceeh

Vollständiger Abdruck der von der Fakultät für Physik der Technischen Universität München zur Erlangung des akademischen Grades eines

Doktors der Naturwissenschaften (Dr. rer. nat.)

genehmigten Dissertation.

Vorsitzender: Univ.-Prof. Dr. Wilhelm Zwerger

Prüfer der Dissertation:

1. Priv.-Doz. Dr. Christoph Hugenschmidt
2. Univ.-Prof. Jonathan Finley. Ph.D.
3. Univ.-Prof. Dr. Friedrich Reinert
Julius-Maximilians-Universität Würzburg
(nur schriftliche Bewertung)

Die Dissertation wurde am 13.8.2015 bei der Technischen Universität München eingereicht und durch die Fakultät für Physik am 30.11.2015 angenommen.

To my beloved wife, Doris

Abstract

Virtually all material properties of a solid are determined by its electronic structure. This in turn results from the fundamental interaction principles of electrons with each other and with the ions in the crystal. Due to the fermionic nature of the electrons every state can include two electrons and all states up to a maximum energy, the so-called Fermi energy are occupied. In reciprocal space this results in a surface of constant energy, the Fermi surface, which separates the occupied and unoccupied electronic states. The topology of the Fermi surface therefore defines the electronic structure in metals and consequently the properties of the solid.

The topology of the Fermi surface can be obtained from theoretical considerations by band structure calculations and provides, compared to experimentally obtained spectroscopic variables such as electrotransport or reflectivity, a very pure characteristic of metals. Therefore, measurements of the Fermi surface provide an ideal benchmark for theoretical calculations.

Among the experimental methods for determining the Fermi surface the most widely known are based on quantum oscillations. Here the oscillations of transport properties either based on the de-Haas-van Alphen effect or on the Shubnikov de-Haas effect are measured in an external magnetic field at low temperatures. Another popular method to determine the Fermi surface experimentally is angle-resolved photo emission spectroscopy (ARPES). In ARPES the density of states is directly determined as a function of energy and momentum. This method is particularly well suited for two-dimensional electronic systems.

In this work the main focus is on a powerful technique for determining the Fermi surface and the electronic structure in general: the measurement of the two-dimensional angular correlation of electron positron annihilation radiation (2D-ACAR). A 2D-ACAR spectrum represents a measurement of a projection along one momentum component of the electron momentum density. In contrast to the above mentioned methods, the advantage of 2D-ACAR lies in the fact that one obtains real bulk information unlike ARPES and in contrast to quantum oscillations the electronic structure can be studied over a wide temperature range.

In this work, a new 2D-ACAR spectrometer was set up and successfully put into operation. With this spectrometer measurements were carried out on systems with strongly correlated electrons. Firstly, the electronic structure of chromium was determined in the paramagnetic and the anti-ferromagnetic state. The observed differences can be linked to a specific sheet of the Fermi surface of chromium. An investigation of anti-ferromagnetic chromium with only a single magnetic domain results in no significant deviation of space symmetry of the electronic structure. Furthermore, spin-resolved measurements have been performed on ferromagnetic nickel and compared with theoretical calculations dependent on the local electron-electron repulsion, the so-called Hubbard U . For this purpose the magnetic quenching of ortho-positronium in single-crystalline quartz was used to determine the degree of polarization of the positrons to 31 % in a separate experiment. A comparison of the theoretical calculations with the experimental data obtained on nickel shows that a value of $U = (2.0 \pm 0.1)$ eV describes the data best. This way, it could be shown that by spin resolved positron annihilation spectroscopy a free parameter of the theoretical model can be determined unambiguously with high accuracy.

Zusammenfassung

Praktisch alle wesentlichen Eigenschaften eines Festkörpers werden durch seine elektronische Struktur bestimmt. Diese ergibt sich wiederum aus den fundamentalen Wechselwirkungsprinzipien der Elektronen zum einen untereinander und zum anderen mit den Kristallionen. Aufgrund der fermionischen Natur der Elektronen finden sich in jedem besetzten Zustand zwei Elektronen und alle Zustände bis zu einer bestimmten Maximalenergie, der sogenannten Fermienergie sind besetzt. Daraus ergibt sich im reziproken Raum eine Fläche konstanter Energie, die Fermi-Fläche, die besetzte und unbesetzte Zustände voneinander trennt. Die Topologie der Fermi-Fläche definiert daher die elektronische Struktur und damit einhergehend die Eigenschaften des Festkörpers.

Die Topologie der Fermi-Fläche kann aus theoretischen Überlegungen durch Bandstrukturberechnungen bestimmt werden, und stellt im Vergleich zu experimentell bestimmten spektroskopischen Größen wie Elektrotransport oder Reflexionsvermögen ein fundamentales Charakteristikum von Metallen dar. Daher bieten Messungen der Fermifläche eine ideale Referenz für theoretische Rechnungen.

Zu den Methoden zur Bestimmung der Fermifläche zählen Quantenoszillationsmessungen, hierbei werden über den de-Haas-van-Alphen Effekt oder über den Shubnikov-de-Haas Effekt die Oszillationen von Transportgrößen im externen Magnetfeld bei niedrigen Temperaturen gemessen. Eine weitere verbreitete Methode um die Fermi-Fläche experimentell zu bestimmen ist die winkelaufgelöste Photoelektronenemissionsspektroskopie (ARPES). Bei ARPES wird die Zustandsdichte direkt als Funktion der Energie und des Impulses bestimmt. Dieses Verfahren eignet sich besonders für zweidimensionale elektronische Systeme.

In dieser Arbeit liegt das Hauptaugenmerk auf einer anderen leistungsfähigen Methode zur Bestimmung der Fermi-Fläche und der elektronische Struktur im Allgemeinen: die Messung der Winkelkorrelation der Elektron-Positron-Annihilationsstrahlung (2D-ACAR). Ein 2D-ACAR Spektrum stellt die Messung einer Projektion der Elektronenimpulsdichte entlang einer Impulskomponente dar. Im Gegensatz zu den oben genannten Methoden liegt der Vorteil dieses Verfahrens in der Tatsache, dass man im Gegensatz zu ARPES echte Volumeninformation erhält und dass man im Vergleich zu Quantenoszillationsmessungen die elektronische Struktur über einen weiten Temperaturbereich untersuchen kann.

In dieser Arbeit wurde eine neues 2D-ACAR Spektrometer aufgebaut und erfolgreich in Betrieb genommen. Mit diesem Spektrometer wurden Messungen an Systemen mit stark korrelierten Elektronen durchgeführt. Zunächst wurde die elektronische Struktur von Chrom in der paramagnetischen und antiferromagnetischen Phase bestimmt. Die beobachteten Unterschiede konnten mit einem speziellen Teil der Fermi-Fläche von Chrom zurückgeführt werden. Eine Untersuchung der anti-ferromagnetischen Phase von Chrom mit nur einer einzigen magnetischen Domäne ergab keine signifikante Abweichung der beobachteten Symmetrie von der paramagnetischen Phase. Weiterhin wurden Spin aufgelöste Messungen in ferromagnetischem Nickel durchgeführt und mit theoretischen Rechnungen verglichen, die in Abhängigkeit von der lokalen Elektron-Elektron-Wechselwirkungsstärke, dem sogenannten Hubbard U berechnet wurden. Dazu wurde in einem gesonderten Experiment zur Messung der magnetfeldinduzierten Mischung der Positroniumzustände in einkristallinem Quarz der Polarisationsgrad der Positronen zu 31 % bestimmt. Ein Vergleich der theoretischen Rechnungen mit dem Experiment ergibt, dass ein Wert für $U = (2.0 \pm 0.1) \text{ eV}$ die Daten am besten beschreibt. Hierdurch konnte gezeigt werden, dass mittels spinaufgelöser Positronenannihilationsspektroskopie ein freier Parameter des theoretischen Modells mit hoher Genauigkeit und in Übereinstimmung mit anderen Methoden bestimmt werden kann.

Contents

Abstract	i
Contents	iv
1 Introduction	1
2 2D-ACAR spectroscopy	5
2.1 The positron as a probe particle	5
2.1.1 Positron sources	6
2.1.2 Positron implantation and thermalisation	7
2.2 Fundamental aspects of 2D-ACAR spectroscopy	9
2.2.1 Electron momentum density	13
2.2.2 Positron wave function effects and electron-positron correlations	15
2.3 2D-ACAR in literature - an overview	20
2.3.1 Transition metals	20
2.3.2 Intermetallic compounds and alloys	26
2.3.3 Rare earth metals and compounds	29
2.3.4 Oxides and exotic materials	31
3 Experimental setup	33
3.1 Layout of the new 2D-ACAR spectrometer	33
3.1.1 Overview	33
3.1.2 Detector system	33
3.1.3 Data acquisition	41
3.1.4 Data treatment	43
3.1.5 Sample environment	45
3.1.6 Design of the source-sample chamber	46
3.1.7 Magnetic field configuration	48
3.2 Performance	52
3.2.1 Positron transport efficiency	53
3.2.2 Determination of the positron spot size	54
3.2.3 Determination of the angular resolution	55
4 Determination of the positron polarisation	61
4.1 Positronium	61
4.1.1 Properties	61
4.1.2 Decay modes	62
4.2 Positronium in matter	63
4.3 Positronium in an external magnetic field	66
4.4 Magnetic quenching of ortho-Positronium	68
4.5 Experimental determination of the positron polarisation	70
4.5.1 Experimental procedure	70

4.5.2	Results and discussion	72
5	The electronic structure of chromium studied by temperature-dependent 2D-ACAR	75
5.1	Study of the magnetic phase transition of multi- q chromium	77
5.1.1	Temperature-dependent measurements	77
5.1.2	Results from the LCW analysis and comparison to theory	78
5.1.3	Comparison with Mo and W	80
5.1.4	Discussion	81
5.2	Investigation of the symmetry breaking in single- q chromium	82
5.2.1	Experimental procedure	82
5.2.2	Results	83
5.2.3	Conclusion	87
6	Spin-polarized 2D-ACAR measurements on Nickel	91
6.1	Introduction to spin-polarized 2D-ACAR	92
6.2	Fundamentals of the theoretical calculations	95
6.3	Experimental results	96
6.4	Comparison between theory and experiment	97
6.5	Spin decomposition of 2D-ACAR spectra	99
6.6	Discussion	101
6.6.1	Positron probe effects in Ni	101
6.6.2	Can polarised positrons be used as a workaround to the enhancement problem?	102
6.7	Conclusion	104
7	Defect studies	105
7.1	Time dependent radiation damage in SiO ₂	105
7.2	Defects in Heusler compounds studied with DBAR and 2D-ACAR	108
7.2.1	Fe ₂ TiSn	109
7.2.2	Ni ₂ MnGa	115
8	Summary and Outlook	119
	Appendix	
A	Determination of the source activity	121
B	A GEM-based gamma camera prototype for 2D-ACAR	129
C	Study of position-sensitive PMTs as gamma cameras for 2D-ACAR	133
D	Integration of the 2D-ACAR spectrometer at NEPOMUC	137
E	Experimental Parameters	141
F	Technical drawings	143
	Abbreviations	153
	List of Publications	155
	Bibliography	157
	Acknowledgements	177

1

Chapter 1.

Introduction

Almost all properties of materials are defined by their electronic structure. For a metal, the most important characteristic is the boundary between occupied and unoccupied states in reciprocal space, which is called the Fermi surface (FS). In fact, a wide range of phenomena can be explained in terms of the FS topology.

The traditional experimental methods for studying the Fermi surface rely on quantum-oscillations, such as the de-Haas van Alphen effect, which record the response of the sample magnetisation to high external magnetic fields. However, quantum oscillatory methods usually require, besides high magnetic fields, low measurement temperatures and highly ordered systems.

The method of Angle Resolved Photo-Emission Spectroscopy (ARPES), is only sensitive to surfaces, i.e. to the topmost few atomic layers and the photon matter interaction usually the proper analysis of the system [DHS03]. Both methods, quantum-oscillations and ARPES, therefore cannot serve as a general-purpose tool at finite temperatures for studying the bulk electronic structure and effects such as bulk phase transitions.

Angular Correlation of Annihilation Radiation (ACAR) from positron-electron annihilation in matter is free from limitations such as low temperatures and high magnetic fields. Therefore, ACAR enables temperature dependent studies of the electronic structure.

ACAR works as follows: in ACAR experiments the deviation from the anti-parallel propagation directions of the two annihilation quanta is measured in coincidence. Using spatially resolved detectors, two dimensional projections of the electron momentum density can be measured, which are used to reconstruct the three dimensional electron momentum density of the sample. Numerous examples for 2D-ACAR investigations of the electronic structure are found in the literature. For example, the relation of magnetic ordering to features of the Fermi surface has been studied in rare earths and their compounds [DFA⁺97, FDA⁺99, CDM⁺04]. Also, the so-called Fermi surface nesting which results from anisotropies in the Fermi surface, can cause the formation of a spin- or charge-density ground state and has been observed by 2D-ACAR [BFKSC02, HDM⁺04, LDM⁺05]. Moreover, using a ²²Na positron source allows for the spin resolved determination of the electronic structure, i.e. the Fermi surface. Respective investigations were undertaken in ferromagnetic [GMWP91] and half-metallic [HMRB90] materials. In addition, 2D-ACAR has been applied to gain insight to many other phenomena linked to Fermi surface nesting, such as the ferromagnetic shape-memory effect [HWL⁺12] and superconductivity [HKR⁺91, DAW⁺99, HSTT88]. Furthermore, positrons are uniquely well suited to probe the Fermi surface [NCT⁺01, LHAD10] and compositional or structural changes [EVS⁺06] of nano

scale precipitates. This short list makes no claim to completeness, however, it shall give a rough overview of the physical problems that can be addressed with 2D-ACAR.

Within the scope of this thesis a conventional 2D-ACAR spectrometer using a ^{22}Na positron source was designed, constructed and set into operation. The spectrometer consists of two main components: the source and sample stage and the detector system. The source-sample stage features a normal-conducting electro-magnet with a newly developed pole-piece geometry. The magnetic field geometry ensures a small positron beam spot on the sample, which is crucial to achieve good resolution, in combination with a high transport efficiency in order to guarantee a sufficient count rate. The sample-stage features two interchangeable sample holders for heating and cooling the sample. This allows for a variation of the sample temperature between 10 K and 650 K in order to perform temperature dependent measurements and to reduce the effects of temperature smearing of the positron momentum at low temperatures. The detector system consists of two spatial resolving Anger-type γ -cameras. The spectrometer was set up at the experimental Hall of the Maier-Leibnitz accelerator Laboratory in Garching with a detector-detector distance of 16.5 m and the source-sample chamber positioned symmetrically between the detectors. A performance test of the spectrometer showed that it fulfilled the design goals and a resolution of $1.5 \text{ mrad} \times 1.6 \text{ mrad}$ could be achieved.

Once the spectrometer was in routine operation first measurements of the electronic structure were carried out. First, an extensive study of the paramagnetic/anti-ferromagnetic phase transition in chromium was performed. Since the Néel-temperature of chromium is 311 K the paramagnetic phase cannot be studied by quantum-oscillation techniques. Drastic changes in the electronic structure could be observed between the paramagnetic and the longitudinal anti-ferromagnetic state (AF1). As these changes are commonly attributed to Fermi surface nesting. A further investigation was performed on an anti-ferromagnetic chromium sample with only a single magnetic domain. In this study anisotropies in the electronic structure with respect to the orientation of the q -vector were investigated in both the longitudinal phase (AF1) and in the transversal phase (AF2). However, no significant anisotropies have been found. To round off the chromium study, first principle calculation were performed for the paramagnetic state and compared to the experiment. As the agreement was unsatisfactory, additional calculations and experiments on the iso-electronic partners of chromium, namely molybdenum and tungsten were performed. In the case of molybdenum and tungsten it was found that the agreement between theory and experiment is much better than for chromium. This leads to the conclusion that a fundamental aspect of the positron annihilation, i.e. the electron-positron interaction in chromium is not well understood, in agreement with the theoretical and experimental studies in literature.

The second major investigation which was carried out was the spin dependent analysis of the electronic structure of nickel. For this purpose it was necessary to determine the degree of polarisation of the positrons hitting the sample. This was achieved by measuring the magnetic quenching of ortho-positronium in a single-crystalline quartz sample. Once the polarisation of the beam was determined magnetic ACAR measurements were performed on nickel. The aim of this study was to gain insight into electron-electron-correlation effects in nickel by comparing the measured magnetic 2D-ACAR spectra with first principles calculations. These calculations were carried out in the dynamic mean field theory framework by collaboration partners from Universität Augsburg. The application of magnetic ACAR allowed to investigate the "enhancement problem" that one has to face when comparing theoretical to experimental

data. The so-called enhancement describes the electron-positron correlation that is generally not included in electronic structure calculations and has to be treated separately. The strength of the electron-electron correlation was varied in the theoretical calculations and the resulting spectra were compared with the experimental data including a detailed analysis of the enhancement effects. This way, it was possible to pinpoint a value of $U = 2.0$ eV for the local electron-electron repulsion, the so-called Hubbard U , which is in general a free parameter of any DMFT calculation.

The course of this thesis will be the following: First the reader will be introduced to the fundamental principles of positron annihilation spectroscopy. In particular the 2D-ACAR technique is presented with a special focus laid on the enhancement problem, followed by a brief review of the most famous 2D-ACAR experiments reported in literature. Then the experimental setup of the 2D-ACAR spectrometer is discussed together with the performance measurements. The main part of this work focusses on the study of the magnetic phases of chromium, the determination of the positron beam polarisation and finally the study of electron-electron and electron-positron correlations in nickel. The future prospects of 2D-ACAR are briefly summarized and discussed.

2 Chapter 2.

2D-ACAR spectroscopy

Already in the 1940s it was discovered that the observables of a positron annihilation experiment, namely the positron lifetime and the energy- and angular distribution of the annihilation quanta, depend on the material in which the positron annihilates and are independent on the used positron source. Once the basic principles of positron annihilation in solids were established it was only a matter of time before first investigations of material properties using positrons were performed. It was found that due to the fact that the positron assumes the ground state in a material it is especially sensitive to defects in the crystal lattice. This is due to the fact that the repulsive potential of the atomic nucleus is missing in a defect. Therefore, the positron annihilation techniques have taken a leading role when it comes to defect spectroscopy. The most prominent technique for defect studies is the positron annihilation lifetime spectroscopy (PALS) followed by the Doppler-Broadening of Annihilation Radiation (DBAR) technique.

Besides the study of defects the positron can also be used to investigate defect-free single crystals, in particular the electronic structure, which is the main focus of this work. In this chapter we will develop the fundamental properties of the positron as a probe particle in solid state physics: how positrons are produced and how they interact with matter. Subsequently the positron annihilation is discussed (see section 2.2) since in this process the information on the material, i.e. the momentum of the electron, is coded into the properties of the annihilation radiation and carried out of the sample material. Of course, this discussion is centred around the 2D-ACAR technique but not limited to it. Finally, a brief review of the most prominent 2D-ACAR experiments found in literature is given (see section 2.3) in order to familiarise the reader with potential of 2D-ACAR.

2.1. The positron as a probe particle

The positron is the anti-particle to the electron: both particles have the same mass, however opposite charge and magnetic moment since both particle states can be converted into each other by a time-reversal or CP-transformation.

Due to a matter anti-matter asymmetry in the early universe electrons are abundantly found while positrons are relatively rare. Therefore, if one wants to use positrons for the investigation of condensed matter one has to rely on artificial positron sources such as radioactive β^+ -emitters like ^{22}Na or more elaborate sources that use high energy γ -radiation from linear accelerators or nuclear reactors for pair production. In the following sections the two sources that are relevant

to this thesis are discussed, as they are used in the present setup (see section 3.1.6) and planned to be used in a future upgrade once the new experimental hall east at the MLZ (Maier Leibnitz Zentrum) becomes available (see section D). In particular these are on the one hand radioactive ^{22}Na sources and on the other hand the reactor based NEPOMUC facility.

2.1.1. Positron sources

For laboratory scale experiments typically radioactive sources are used. The most prominent nuclide in this case is ^{22}Na , which is favourable due to its half life of 2.6 years, its high β^+ branching ratio of 90.5% and the fact that a prompt γ -quantum of 1275 keV is emitted right after the creation of the positron. The latter fact is exploited in positron annihilation lifetime studies where the prompt γ -quantum is used as a start signal. Furthermore, positrons can be created via the pair production process at large-scale facilities. Here high energy γ radiation is converted into pairs of positron and electrons. In this case reactors or particle accelerators are used to produce high energy γ radiation. In the following the radioactive positron source used in the 2D-ACAR setup is discussed as well as the reactor based positron source NEPOMUC which will serve as an example for a large-scale positron source. Also NEPOMUC will be used in the future extension for the 2D-ACAR experiments.

The ^{22}Na β^+ -positron source

In order to be used in laboratory experiments a positron source has to fulfil certain requirements. The radioactive nuclide has to be sealed in a capsule to prevent contamination of the setup. At the same time the positrons have to be able to exit the capsule to be used in an experiment. A schematic drawing of the source capsule is shown in figure 2.1. The radioactive nuclide is deposited on a small tantalum cylinder. Due to the high Z of the tantalum positrons are efficiently reflected which increases the positron flux through the $4\ \mu\text{m}$ titanium window that covers the radioactive nuclide. The nuclide itself is produced by iThemba Labs in South Africa at a cyclotron by irradiation of a magnesium target with 66 MeV protons. The target is then dissolved in potassium hydroxide and the sodium is separated by a precipitation process in the form of sodium carbonate. The concentrated sodium carbonate solution is then dripped onto the tantalum support and dried under a heat lamp. This process is repeated until the desired activity of up to 50 mCu is reached. The daughter nuclide of ^{22}Na is the noble gas ^{22}Ne which cannot be chemically bound. Therefore, a bore in the base of the source capsule is necessary to accommodate the neon so that the increasing pressure does not rupture the titanium window.

The positron source NEPOMUC

The NEPOMUC facility operates as follows: thermal neutrons are captured in a cadmium cap that is arranged around a platinum pair-production target. The nuclide ^{113}Cd with a neutron capture cross-section of 20600 barn is almost exclusively responsible for the neutron absorption and has been enriched from its natural abundance of 11.6% to about 80%. After the neutron capture the ^{113}Cd nucleus is in a highly excited state and relaxes via the emission of a cascade of high energy γ -quanta into the ground state. On average 2.3 of the high energy γ -quanta have an energy of more than 1.5 MeV [HKR⁺04] and can therefore participate in the pair production process. The pair-production mainly occurs in the platinum structures due to high Z of platinum. The platinum serves for a two purposes: on the one hand it serves as pair

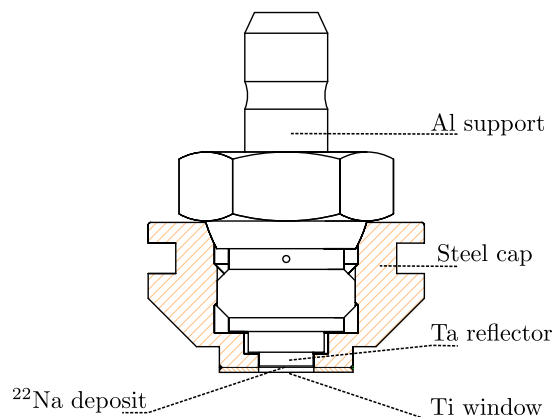


Figure 2.1.: Schematic drawing of the source capsule used in the 2D-ACAR spectrometer [Reh14]. The capsule is designed for the use in ultra high vacuum. It is non-magnetic and can withstand cryogenic as well as elevated temperatures up to 200 °C.

production target and on the other hand it also acts as moderator for the produced positrons. Due to the fact that platinum exhibits a negative work function for positrons the produced positron are emitted from the platinum structure. By use of an electrical lens system a beam is formed and coupled into a longitudinal magnetic guidance field with a strength of about 7 mT. The sketch of the heart of NEPOMUC is shown in figure 2.2.

The energy of the moderated positrons is determined by the electric potential of the platinum structure at typically 1000 V. First, NEPOMUC achieved an intensity of up to $9 \cdot 10^8$ [HLM⁺08] moderated positrons per second and became therefore the most powerful positron source worldwide. At present the NEPOMUC upgrade amounts to $> 10^9$ positrons per second [HCG⁺14]. NEPOMUC also features to the option to use a second moderator, the so called remoderator, which is a second moderation stage inside the experimental hall closer to the experiments [PKE⁺08]. The main purpose of the remoderator is to increase the beam brilliance. The remoderation process has an efficiency of $\approx 5\%$, however, the brilliance of the remoderated beam is increased by a factor of up to 40 with respect to to the primary beam. The energy of the remoderated beam can be tuned between 20 – 200 eV.

A mono-energetic positron beam would enable depth-dependent 2D-ACAR measurements. This adds a whole new quality to the measurement as the evolution of the electronic structure from the surface to the bulk can be observed. Moreover, the use of a positron beam greatly reduces the background in the detectors as there are no secondary γ 's from the source.

Since from the beginning of the present work it was planned to install the 2D-ACAR spectrometer in the east experimental hall (after successful commissioning of the hall) at the NEPOMUC beam. For this reason, a design study on the integration of a 2D-ACAR spectrometer at the NEPOMUC positron beam can be found in the appendix of this thesis (see section D).

2.1.2. Positron implantation and thermalisation

When positrons impinge on a material they can be reflected with a certain probability depending on the positron energy and the Z of the material. In the low energy region below 30 keV this probability is almost independent of the positron energy however strongly dependent on the Z

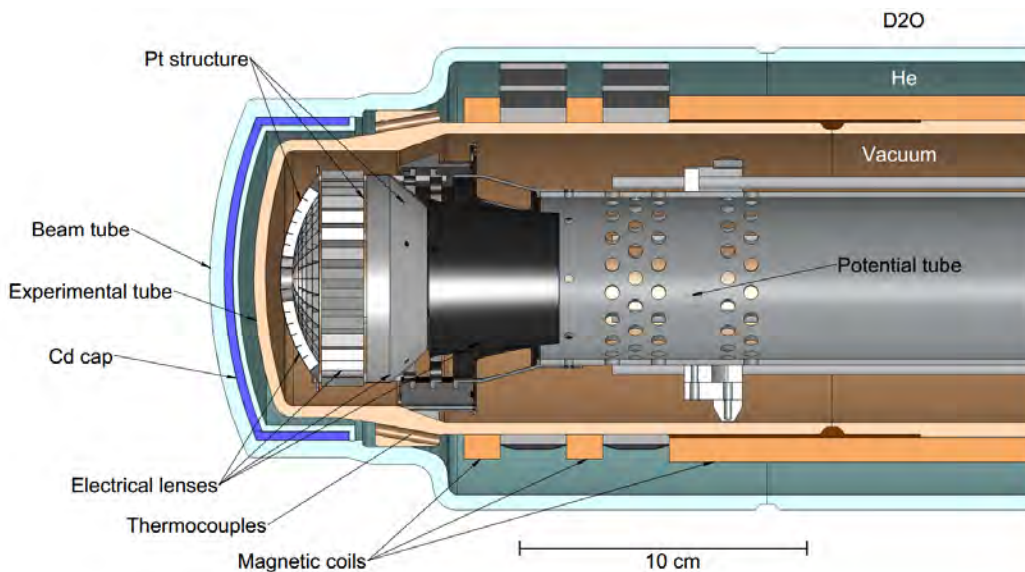


Figure 2.2.: Schematics of the in-pile element of NEPOMUC [HCG⁺13].

of the target and can reach values of up to 40 % [MPMH92]. Once a positron enters a solid it rapidly loses its energy. In the energy range above 10 keV elastic scattering on electrons plays the dominant role (ionisation). As long as the binding energy of the electron is small compared to the energy transfer the electron can be considered as a free particle and only very little energy is transferred to the rest ion. The time dt it takes the positron to bridge the energy dE can be calculated using the Bethe-Bloch-formula for positrons in the low energy limit ($\beta < 1$)

$$-\frac{dE}{dx} = \frac{2\pi NZ}{m_e v^2} \left(\frac{e^2}{4\pi\epsilon_0} \right)^2 \left[\underbrace{\ln \left(\frac{\gamma + 1}{2} \frac{E^2}{I^2} \right)}_{\text{Ionisation}} + \underbrace{f(\gamma)}_{\text{Scattering}} \right] \quad (2.1)$$

with the transform

$$\frac{dt}{dE} = \frac{\frac{dt}{dx}}{\frac{dE}{dx}} = \frac{1}{v \frac{dE}{dx}} \quad (2.2)$$

and

$$v(E) = c \sqrt{1 - \left(\frac{m_e c^2}{E} \right)^2} \quad (2.3)$$

to obtain

$$-\frac{dt}{dE} = \frac{8\pi\epsilon_0^2 m_e}{e^4 N Z} \cdot \frac{c \sqrt{1 - \left(\frac{m_e c^2}{E} \right)^2}}{\ln \left(\frac{\gamma + 1}{2} \frac{E^2}{I^2} \right) + f(\gamma)} \quad (2.4)$$

the time dependent energy loss, with the positron energy E , m_e the electron mass, N the atomic density, Z the proton number of the nucleus, I the mean excitation energy of the atoms ($I \approx Z \cdot 13.6 \text{ eV}$), the Lorentz factor γ and the scattering term $f(\gamma) = 2 \ln 2 - \frac{\beta^2}{12} \left(23 + \frac{14}{\gamma+1} + \frac{10}{(\gamma+1)^2} + \frac{4}{(\gamma+1)^3} \right)$ using and the Bhabba (e^-e^+)-scattering cross section [Koh61].

By integrating equation 2.4 for an energy of 210 keV (the mean positron energy of ^{22}Na) one finds that the positron takes less than 0.25 ps in a light material such as water and less than 0.08 ps in a heavy material like iron to reach an energy lower than 10 keV. In the intermediate energy region between 1 keV and 100 eV inelastic scattering of positrons with single atoms is the dominant energy-loss mechanism. When the positron hits an atom it can leave the atom in an excited state losing energy in the process. At even lower energies below 50 eV collective excitations of the electronic system in the form of plasmon and phonon excitation become dominant. Finally, the positron reaches thermal equilibrium with the material within a few picoseconds.

2.2. Fundamental aspects of 2D-ACAR spectroscopy

Now we will focus on the observables of positron annihilation spectroscopy. Once the positron is fully thermalized it will eventually annihilate with an electron. The annihilation rate Γ (the inverse of the lifetime) is thereby determined by the electron density n_e via

$$\Gamma = \sigma v n_e \approx r_0^2 c n_e \quad (2.5)$$

with electron-positron annihilation cross section σ and the relative velocity between electron and positron v . In the low energy limit for $v \ll c$ the product σv becomes constant and is given by the product of the square of the classical electron radius r_0 and the speed of light [Dir30]. So the positron lifetime can be used as a measure for the mean electron density. The PALS technique associated with this observable is used to perform studies of open volume defects in solids. In a defect, for example a vacancy, the electron density is lower than in the bulk of the crystal due to the missing attractive potential of the nucleus. Hence, the lifetime in such a defect is higher compared to the bulk. Therefore, by measuring the positron lifetime the concentration and type of defects can be studied.

PALS is a well established technique in material science and widely used, for example for the determination of the vacancy formation enthalpy [Sch87].

In this thesis, however, we will deal with another quantity that is also accessible via positron annihilation namely the electron momentum density. As it was stated before at the moment of annihilation the positron is fully thermalized and therefore assumes its ground state in the combined potential of the crystal ions and the electrons. The electrons on the other side occupy all states up to the Fermi level, which represents the energetically highest occupied state. So the total momentum of an annihilating electron-positron pair is in general non-zero and almost exclusively defined by the electron momentum. The momentum of the pair has to be conserved in the annihilation radiation. Due to the conservation of energy and momentum the number of annihilation quanta has to be two or higher. However, the two- γ -annihilation is the most probable due to the fact that each additional photon vertex gives an additional factor of $\alpha \approx 1/137$ to the annihilation rate. The second order three- γ -annihilation is therefore suppressed by $1/371$ with an additional reduction of a factor $9/\pi$ from quantum field theory. For this reason, from now on only the two- γ -annihilation is considered. In the center of mass frame both annihilation γ -quanta in general have the same energy and are emitted collinear in opposite direction. In the laboratory frame the quanta have different energies and the observed emission direction deviates from collinearity. This can be understood in terms of a Lorentz

transformation (without loss of generality it is assumed that the electron-positron pair moves along the x -axis):

$$\begin{pmatrix} E \\ p_{\parallel} \\ p_{\perp} \end{pmatrix} = \begin{pmatrix} \gamma & \beta\gamma & 0 \\ \gamma\beta & \gamma & 0 \\ 0 & 0 & 1 \end{pmatrix} \begin{pmatrix} E^{\text{CM}} \\ p_{\parallel}^{\text{CM}} \\ p_{\perp}^{\text{CM}} \end{pmatrix} \quad (2.6)$$

with the velocity β of the center of mass frame and $\gamma = (1 - \beta^2)^{-\frac{1}{2}}$. In the center of mass frame both annihilation quanta have an energy of

$$E^{\text{CM}} = \frac{1}{2}Mc^2 \quad (2.7)$$

with the mass of the electron positron pair $M = 2m_0$. Since the photons have zero rest mass the momentum is simply given by

$$p^{\text{CM}}c = E^{\text{CM}} \quad (2.8)$$

Since the two- γ -annihilation occurs from a singlet state the emission direction of the annihilation quanta is isotropic. The angle between the first photon and the x -axis is denoted as Θ (as indicated in figure 2.3). Then the emission angle of the second photon relative to the direction of motion is given by $\pi - \Theta$. With this the energies of the photons in the laboratory frame are given by:

$$E_1 = \gamma \frac{Mc^2}{2} + \gamma\beta p_{\parallel}^{\text{CM}} = \gamma \frac{Mc^2}{2} + \gamma\beta \frac{Mc^2}{2} \cos \Theta = \gamma \frac{Mc^2}{2} (1 + \beta \cos \Theta) \quad (2.9)$$

$$E_2 = \gamma \frac{Mc^2}{2} + \gamma\beta p_{\parallel}^{\text{CM}} = \gamma \frac{Mc^2}{2} - \gamma\beta \frac{Mc^2}{2} \cos \Theta = \gamma \frac{Mc^2}{2} (1 - \beta \cos \Theta). \quad (2.10)$$

In the low energy limit γ is nearly unity and with $\gamma\beta \approx \frac{p}{Mc^2}$ it follows:

$$E_1 = E + \Delta E = m_0c^2 + \frac{pc \cos \Theta}{2} \quad (2.11)$$

$$E_2 = E - \Delta E = m_0c^2 - \frac{pc \cos \Theta}{2}. \quad (2.12)$$

So one photon is blue shifted while the other is red shifted. The energy shift ΔE is given by the longitudinal component $p \cos \Theta$ of the momentum of the electron positron pair relative to the direction of emission. In order to determine the opening angle α (see figure 2.3) the scalar product of the energy-momentum four-vectors of the two annihilation quanta is calculated. In the laboratory one finds

$$\mathbf{p}_1 \mathbf{p}_2 = E_1 E_2 - p_1 p_2 c^2 \cos \alpha = E_1 E_2 (1 - \cos \alpha) \quad (2.13)$$

and for the center of mass system:

$$\mathbf{p}_1 \mathbf{p}_2 = E_1^{\text{CM}} E_2^{\text{CM}} - p_1^{\text{CM}} p_2^{\text{CM}} c^2 = 2 \left(\frac{M}{2} \right)^2. \quad (2.14)$$

Since the scalar product of two four-vectors in Lorentzinvariant it is found that:

$$E_1 E_2 (1 - \cos \alpha) = 2 \left(\frac{M}{2} \right)^2 \quad (2.15)$$

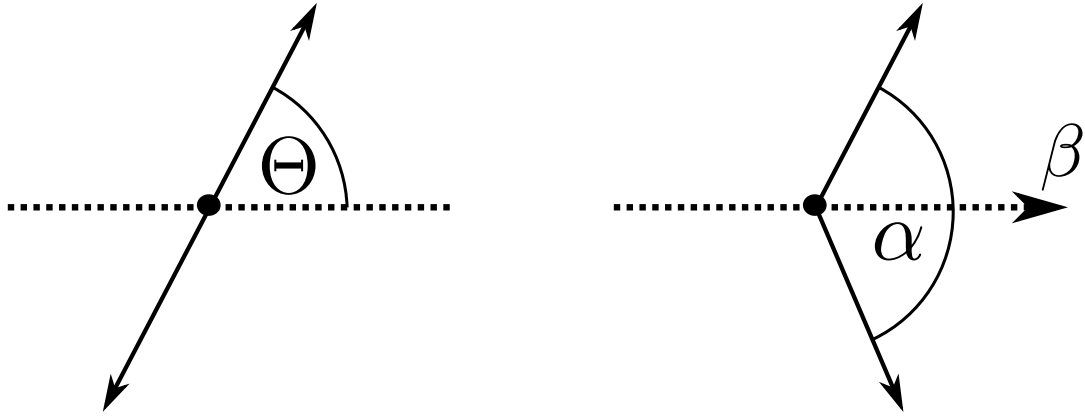


Figure 2.3.: *Left:* Annihilation in the center of mass system. The annihilation quanta are emitted collinear in opposite direction with an angle Θ relative to direction of motion (indicated by the dotted line). *Right:* Annihilation in the laboratory frame. The angle α between the annihilation quanta deviates from 180° .

which leads to

$$1 - \cos \alpha = \frac{M^2}{E_1 E_2}. \quad (2.16)$$

The deviation of α from 180° is expected to be small, therefore α is expressed as $180^\circ - \Delta\theta$. Then using the small angle approximation results in

$$\Delta\theta^2 = 4 - \frac{M^2}{E_1 E_2}. \quad (2.17)$$

Using the results from equations 2.11 and 2.12 and the identities $\beta^2 \gamma^2 = \frac{p^2}{M^2 c^2}$ and $\gamma^2 = 1 + \frac{p^2}{M^2 c^2}$ one finds:

$$\Delta\theta^2 = \frac{4p^2 \sin^2 \Theta}{M^2 c^2 + \underbrace{p^2 \sin^2 \Theta}_{\ll M^2 c^2}}. \quad (2.18)$$

In the low energy limit the second term in the denominator can be omitted and with $M = 2m_0$ the final result is obtained:

$$\Delta\theta = \frac{p \sin \Theta}{m_0 c}. \quad (2.19)$$

Consequently the transversal projection of the momentum of the annihilating pair onto the direction of emission of the annihilation quanta $p \sin \Theta$ leads to a deviation from collinearity. For example, annihilation with an electron with the kinetic energy of 1 eV results in an angular deviation of maximal $\Delta\theta = 2.0$ mrad.

To summarize, above considerations show that due to the conservation of energy and momentum the longitudinal component of the electron momentum relative to the direction of emission leads to shift in energy due to the Doppler effect and the transversal components leads to a deviation from collinearity. This is illustrated in figure 2.4. So by measuring the energy shift and the angular deviation the momentum of the electron can be determined experimentally. The experimental technique associated with measuring the Doppler shift is the so called Doppler

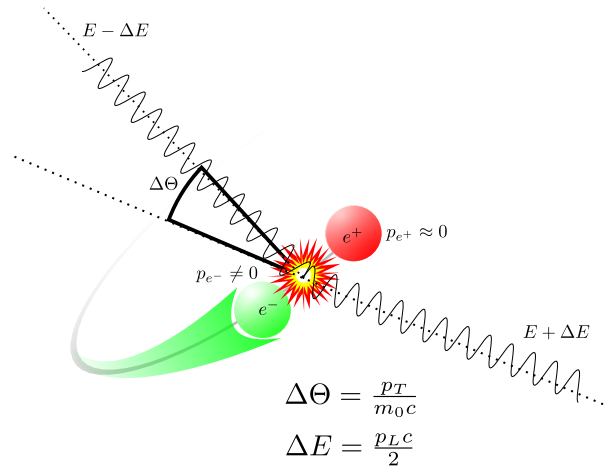


Figure 2.4.: Illustration of the 2D-ACAR principle. The momentum of the positron is small compared to the electron momentum, therefore, the total momentum is dominated by the electron momentum. The conservation of momentum leads to a Doppler shift ΔE and a deviation from collinearity $\Delta\Theta$ of the annihilation quanta in the lab frame. This angular deviation is given by the transverse momentum component of the total momentum with respect to the emission direction of the two annihilation quanta.

Broadening of Annihilation Radiation Spectroscopy. For this technique detectors with high energy resolution, typically high-purity germanium, detectors are used. For details on this technique please refer to the works of Stadlbauer and Pikart [Sta08, Pik12].

The 2D-ACAR (Two Dimensional Angular Correlation of Annihilation Radiation) technique, which is the main part of this thesis, deals with the measurements of the angular deviation of the annihilation quanta which gives information on the transversal components of the electron momentum. The principle setup of a 2D-ACAR experiment is shown in figure 2.5. Two spatially resolving detectors are used to determine the angular deviation. The detectors are positioned with their line of sight along the z -axis at distance l_1 and l_2 on opposite sides of the sample. The positions $(x_1|y_1)$ and $(x_2|y_2)$ of the annihilation photons hitting the detectors are measured in coincidence allowing the determination of the angular deviation relative to the x - and y -axis:

$$\theta_x = \arctan \frac{x_1}{l_1} - \arctan \frac{x_2}{l_2} \approx \frac{x_1 l_2 - x_2 l_1}{l_1 l_2} \quad (2.20)$$

$$\theta_y = \arctan \frac{y_1}{l_1} + \arctan \frac{y_2}{l_2} \approx \frac{y_1 l_2 + y_2 l_1}{l_1 l_2} \quad (2.21)$$

The negative sign in the second term of 2.20 is due to the fact that the detectors face each other and that therefore the image of one detector has to be flipped vertically. These two angles can now be directly converted to the momentum components p_x and p_y of the annihilating pair via equation 2.19:

$$p_x = \theta_x \cdot m_0 c \quad (2.22)$$

$$p_y = \theta_y \cdot m_0 c. \quad (2.23)$$

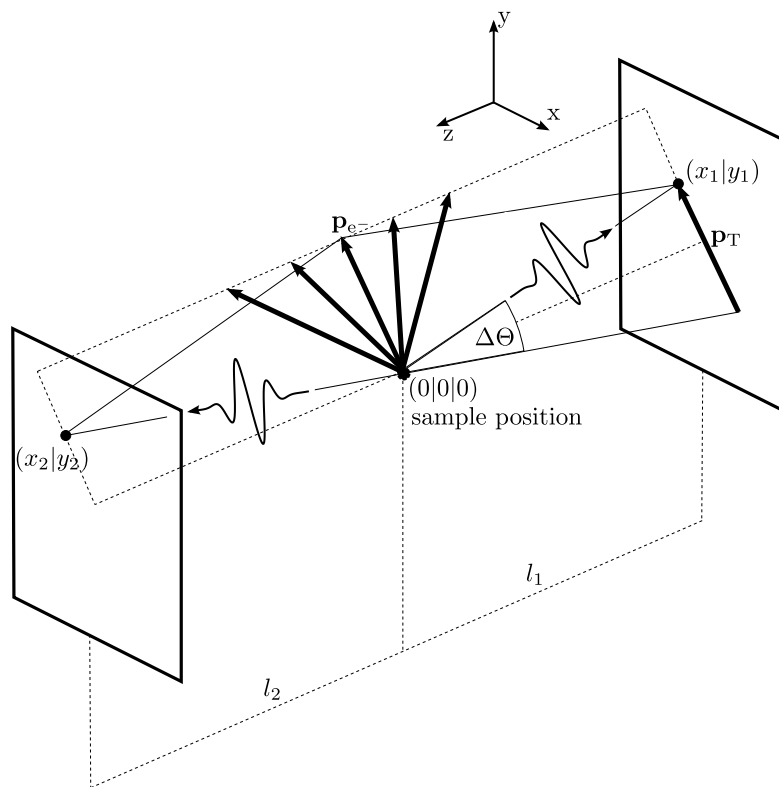


Figure 2.5.: Schematic representation of a 2D-ACAR experiment. Two spatially resolving detectors are placed around the sample on a common line of sight. The positions of both annihilation quanta hitting the detectors are registered in coincidence which allow the determination of the transversal component of the electron momentum. Since scintillation detectors are used the longitudinal component of the electron momentum is lost and the resulting 2D-ACAR spectrum represent a one-dimensional integral over the electron momenta.

As indicated in figure 2.5 the information on the longitudinal component cannot be determined. Therefore the resulting 2D-ACAR spectrum $N(p_x, p_y)$ represents a projection of the electron momenta and is represented by a one-dimensional integral along the z -direction:

$$N(p_x, p_y) = \int \rho^{2\gamma}(\mathbf{p}) dp_z \otimes R(p_x, p_y) \quad (2.24)$$

with the electron positron momentum distribution $\rho^{2\gamma}$ also called two-photon momentum distribution (TPMD). The finite resolution of the detectors is considered by a convolution with the resolution function R .

2.2.1. Electron momentum density

The measured projection of the TPMD is basically a two-particle quantity containing the electron and the positron. Before the influence of the positron is discussed the underlying quantity, the electron momentum distribution (EMD) is considered. The EMD describes the electron density in momentum space and is given by the Fourier-transform of the real space

density

$$N(\mathbf{p}) = \left| \sum_j \int \exp^{-i\mathbf{p}\mathbf{r}} \Psi_j^{e^-}(\mathbf{r}) \right|^2 \quad (2.25)$$

$$n_i = \frac{1}{e^{\frac{\epsilon_i - E_F}{k_B T}} + 1} \quad (2.26)$$

with ϵ_i the energy of the i -th state, the Boltzmann constant k_B , the Fermi energy E_F and the temperature T . At zero Kelvin only states up to the Fermi energy are occupied. The momentum associated with the highest filled state the so-called Fermi momentum is given by:

$$k_F = \frac{\sqrt{2m_0 E_F}}{\hbar}. \quad (2.27)$$

Consequently the electron momentum distribution $N(p)$ is constant up to the Fermi momentum where a sharp break appears. This boundary between occupied and unoccupied states in reciprocal space is called *Fermi surface*. For the ideal electron gas the Fermi surface is a sphere of radius k_F . In the periodic potential of a crystal the simple approximation of a free electron gas does not hold. In this case the tight binding method, i.e. a super-position of atomic wave functions, can be used to illustrate the electron momentum distribution in a solid. A derivation of this method can be found in standard solid-state physics text books. In the tight binding approach the super-position of the atomic wave functions ψ is given by

$$\Psi_{\mathbf{k}} = \frac{1}{\sqrt{N}} \sum_j \exp^{i\mathbf{k}\mathbf{r}} \Psi(\mathbf{r} - \mathbf{r}_j) \quad (2.28)$$

with r_j the positions of the neighbour atoms and the wave vector \mathbf{k} . The energy values of electrons with the wave vector \mathbf{k} are then given by the diagonal element of the Hamilton operator

$$E_{\mathbf{k}} = \langle \mathbf{k} | H | \mathbf{k} \rangle \quad (2.29)$$

$$= \frac{1}{N} \sum_{j,m} \exp^{i\mathbf{k}(\mathbf{r}_j - \mathbf{r}_m)} \langle \Psi(\mathbf{r} - \mathbf{r}_j) | H | \Psi(\mathbf{r} - \mathbf{r}_m) \rangle \quad (2.30)$$

$$= \sum_m \exp^{i\mathbf{k}\mathbf{a}_m} \int dV \Psi^*(\mathbf{r} - \mathbf{a}_m) H \Psi(r) \quad (2.31)$$

using the summation over all lattice vectors \mathbf{a}_m . If one considers only nearest neighbour interaction the energy is given by an on-site term α and the neighbour exchange energy γ to:

$$\alpha = - \int dV \Psi^*(\mathbf{r}) H \Psi(r) \quad (2.32)$$

$$\gamma = - \int dV \Psi^*(\mathbf{r} - \mathbf{a}_m) H \Psi(r). \quad (2.33)$$

The tight-binding method is not limited to the nearest neighbour interaction. However, even if only the Fourier-coefficients of the nearest neighbour interaction are considered this allows for a descriptive modelling of the Fermi surface in a crystal lattice. The iso-surfaces of constant energy like the Fermi surface are only determined by the exponential term in equation 2.31 since the parameters α and γ are constant. To illustrate this without loss of generality a fcc

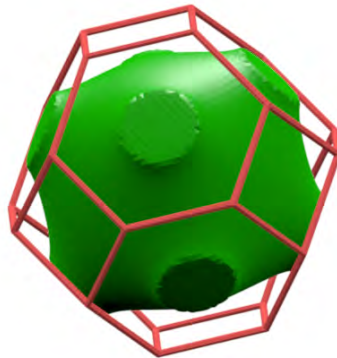


Figure 2.6.: Surface of constant energy obtained by tight binding for a generic FCC metal. The chosen energy parameter is $E' = 0.65$.

lattice is considered. In the fcc lattice the 12 nearest neighbours have the positions

$$\mathbf{a}_1 = \begin{pmatrix} \pm \frac{a}{2} \\ \pm \frac{a}{2} \\ 0 \end{pmatrix} \quad \mathbf{a}_2 = \begin{pmatrix} \pm \frac{a}{2} \\ 0 \\ \pm \frac{a}{2} \end{pmatrix} \quad \mathbf{a}_3 = \begin{pmatrix} 0 \\ \pm \frac{a}{2} \\ \pm \frac{a}{2} \end{pmatrix} \quad (2.34)$$

and hence the dispersion relation 2.31 reads for the FCC lattice

$$E_{\mathbf{k}} = -\alpha - 4\gamma \cos\left(\frac{k_y a}{2}\right) \cos\left(\frac{k_z a}{2}\right) - 4\gamma \cos\left(\frac{k_x a}{2}\right) \cos\left(\frac{k_y a}{2}\right) \quad (2.35)$$

$$- 4\gamma \cos\left(\frac{k_x a}{2}\right) \cos\left(\frac{k_z a}{2}\right). \quad (2.36)$$

The surfaces of constant energy can then be found in terms of a dimensionless parameter $E' = -\frac{E_{\mathbf{k}} - \alpha}{\gamma}$ for a generic fcc metal. The only iso-surface that has physical relevance is the Fermi surface, the iso-surface of the highest occupied state in \mathbf{k} -space. An illustration of an generic fcc Fermi surface with an energy parameter of $E' = 0.65$ is shown in figure 2.6. In the tight binding approximation it is only given by nearest neighbour interaction, which is insufficient to describe more complex system especially if one considers electron-electron interactions that, of course, is of great importance for correlated materials. However, the tight binding approximation gives an impression of the electron momentum density in a crystal lattice.

2.2.2. Positron wave function effects and electron-positron correlations

For the interpretation of 2D-ACAR measurements the influence of the positron has also to be considered. The positron is positively charged and therefore interacts with the negatively charged electrons as well as the positively charged nuclei. So a 2D-ACAR spectrum is the measurement of the many-particle quantity Ψ_i^{ep} containing the interactions of all electrons and the positron:

$$N(p_x, p_y) = \int \sum_i^{\text{occ.}} \left| \int e^{-i\mathbf{p}\mathbf{r}} \Psi_i^{ep}(\mathbf{r}, \mathbf{r}) d\mathbf{r} \right|^2 dp_z \quad (2.37)$$

This equation is usually treated by approximating the solution of the true many-particle problem as a product of the electronic and the positron wave functions and an additional electron-positron correlation function γ which is called enhancement factor:

$$N(p_x, p_y) = \int \sum_i^{\text{occ.}} \left| \int e^{-i\mathbf{p}\mathbf{r}} \Psi_+(\mathbf{r}) \Psi_i(\mathbf{r}) \sqrt{\gamma(\mathbf{r})} d^3\mathbf{r} \right|^2 dp_z \quad (2.38)$$

This way the probe effects introduced by the positron can be separated into positron wave function effects and electron-positron correlation effects. The effect of the positron wave function can be understood as follows: Due to the repulsive potential of the nuclei the positron is more likely to be found at interstitial positions (where the repulsive force from the nuclei is lower). This leads to a non-uniform sampling of the electronic states by the positron. Typically highly localized states like s or p -states have a lower overlap with the positron wave function and contribute therefore less to the 2D-ACAR spectrum as they participate less in the annihilation process. A detailed calculation of the annihilation probabilities with different orbitals was performed by Jensen et al. [JW90]. Their results show that for example for $3d$ electron systems the annihilation probability for s and p orbitals is about three orders of magnitude lower than for annihilation with the valence band. This means that the electrons contribute with different weights to the 2D-ACAR spectrum and that the valence electrons, i.e. the electrons located at the Fermi surface have by far the highest weight. For this reason 2D-ACAR is particularly well suited for the investigation of the FS. However, it also has to be considered that the weighting of electrons in the valence band can also differ due to a different symmetry of the electron and positron wave function. This is e.g. the case in ferromagnetic nickel [SM74] where it was found that the contribution of two different valence electron bands is reduced in positron annihilation due to the symmetry of the wave function. Therefore, the identification of two Fermi surface sheets is complicated as the associated Fermi surface breaks are obscured.

Besides the wave function effects also the electron-positron correlation known as *enhancement* has to be considered. When a positron is immersed in an electron gas it will attract the electrons by polarizing the electronic medium. The positron density is thereby assumed to be low and will therefore not influence the electronic states. However, the probability of finding an electron near the positron is increased due to the mutual attractive interaction. Hence, the positive charge of the positron is shielded by the attracted electrons. Typically, the more mobile electrons located close to the Fermi surface will participate dominantly in this shielding process. This effect attracted great interest after it was found that the description of the non-interacting system the so-called independent particle model (IPM) with $\gamma = 1$ that does not include the short range screening is insufficient to describe the experimental data. Kahana was the first to address this problem on the basis of a non-interacting electron gas [Kah63]. As a result the famous Kahana-type momentum dependent enhancement was derived:

$$\gamma = \gamma(p) = a + b \left(\frac{p}{p_F} \right)^2 + c \left(\frac{p}{p_F} \right)^4 \quad (2.39)$$

with the Fermi momentum p_F and the parameters a , b and c which depend on the electron density. The density is usually given in terms of the Wigner-Seitz radius $r_s = \left(\frac{3}{4\pi n_{e^-}} \right)^{\frac{1}{3}}$ with the electron density n_{e^-} , i.e. the radius of a sphere that contains one electron. One problem of this approach was that it did not include momenta above p_F as the model only considers a non-interaction

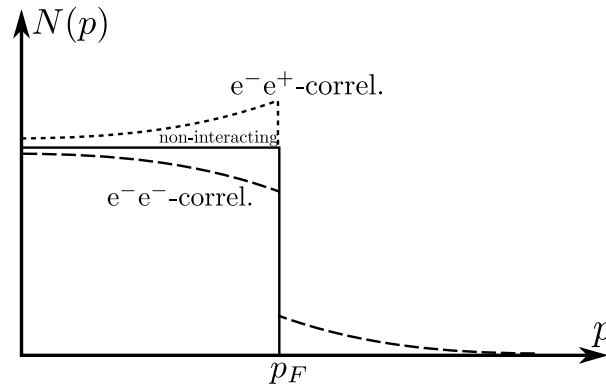


Figure 2.7.: Illustration of the effect of a Kahana-like momentum dependent enhancement on the observed momentum density $N(p)$. Electron-electron correlations lead to a tail of momenta above the Fermi momentum p_F . The electron-positron correlations lead to an increase in $N(p)$ near the Fermi momentum whereas the high momentum components are suppressed. According to the model of Carbotte and Kahana [CK65] an annihilating electron positron pair, observed from outside, may be regarded as a neutral quantity, therefore no high momentum tail beyond the Fermi momentum should be observed.

electron gas. This was later resolved by Carbotte et al. [CK65] who extended the Kahana scheme to an interacting electron gas (jellium). The authors found that the electron-electron and the electron-positron self-energy terms cancel out for $p > p_F$ which leads to a suppression of the high momentum tail introduced by the electron-electron interactions in the calculated spectra. However, the main effect of the enhancement effect remained the same: positrons close to the Fermi surface participate more in the annihilation process (see figure 2.7) while at the same time the high momentum components above p_F are suppressed. A refinement of the Kahana formalism was performed by Rubaszek and Stachowiak [RS88] who developed a fully self-consistent solution that avoids the divergence present in the low-density limit of the Kahana formalism. For the sake of completeness a different approach by Arponen and Pajane [AP79] has to be mentioned. By contrast to most other approaches, their treatment does not rely on the Kahana formalisms. The authors used an algebraic bosonic treatment of the electron gas as a system of interacting collective excitations. By contrast to the Kahana-like enhancement also high momentum components above p_F are found in the calculated ACAR spectra.

It was soon found that the jellium model is insufficient to describe real metals due to the periodic potential of the crystal which results in case of the transition metals in a strongly inhomogeneous electron gas. These lattice effects have first been discussed by Fujiwara et al. [FHO72] and have been intensively investigated by Sormann (see [Sor96] and references therein). The authors found that due to the inhomogeneity of the electronic system the Kahana-like momentum dependence of the enhancement can be completely hidden. This is due to the fact that in the free electron gas or in the jellium the electron can always be scattered into a free state. However, if the range of the electron-positron correlation comes in the range of the atomic distances the Bloch nature of the electronic states has to be considered, which reduces the number of available final states for the electron. Hence, for a model that does not incorporate the lattice effects it is generally not expected to deliver reliable results for $3d$ -electron systems. In order to overcome this shortcomings an empirical model for the enhancement parametrized

in energy not momentum was proposed by Mijnarends and Singru [MS79]:

$$\gamma = \gamma(E) = a + b \left(\frac{E - E_{\min}}{E_F - E_{\min}} \right) + c \left(\frac{E - E_{\min}}{E_F - E_{\min}} \right)^2 \quad (2.40)$$

with the parameter a, b and c dependent on the density parameter r_s and E_{\min} the minimal energy of the band (at $\mathbf{k} = 0$). For parabolic bands like s -orbitals the energy dependent enhancement yields the same results as the momentum dependent enhancement. However, for hybridised sd -bands like in copper this model could significantly improve the description of the according ACAR spectra, although it is purely phenomenological. This phenomenology treatment was extended by several authors [MASAKM88, SKS92, KKN⁺91] to a state dependent parametrisation

$$\gamma = \gamma(E) = a_l + b_l \left(\frac{E - E_{\min}}{E_F - E_{\min}} \right) + c_l \left(\frac{E - E_{\min}}{E_F - E_{\min}} \right)^2 + d_l \left(\frac{E - E_{\min}}{E_F - E_{\min}} \right)^3 \quad (2.41)$$

for the angular momentum state l , the energy E_{\min} at $\mathbf{k} = 0$ and the state dependent parameters a_l, b_l, c_l, d_l . These parameter are usually obtained by least-squares fitting to the experimental data [MASAKM88].

An alternative description of the enhancement was developed by moving from a momentum space description to real space description. The enhancement was parametrized in terms of the unperturbed local electron density $n_{e^-}(r)$ at the position of the positron r . This approach was first presented by Boronski and Nieminen [BN86], who interpolated the results from Fermi liquid theory [Lan87]. A further important treatment of the enhancement within the local density approximation was performed by Jarlborg and Singh [JS87]. The authors solved the two-particle Schrödinger equation within a spherical correlation cell. Both approaches have in common that the enhancement γ is now treated as a function of a local quantity of the electron gas, the electron density $n_{e^-}(r)$. The most famous parametrisation of γ is given by Boronski and Nieminen who found for the limit of a vanishing positron density $n_{e^+} \approx 0$ and for electron densities in the typical range of transition metals $r_s \approx 2$:

$$\gamma = 1 + 1.23r_s + 0.8295r_s^{3/2} - 1.26r_s^2 + 0.3286r_s^{5/2} + \frac{1}{6}r_s^3 \quad (2.42)$$

with the density parameter r_s dependent on the local electron density $r_s(r) = \left(\frac{3}{4\pi n_{e^-}(r)} \right)^{1/3}$. The local density treatment has had great success in the description of both the electron positron annihilation rate in PALS as well as the electron-positron momentum density. However, it was found that the Boronski-Nieminen parametrisation gives unsatisfactory results for low electron densities [MB02]. Also on the basis of the LDA but with a different correlation functional based on a state dependent parametrisation on the local kinetic energy $\Xi_{i,\mathbf{r}}$ and density of the electron an energy dependent enhancement $\gamma = \gamma(n_{e^-}, \Xi_{i,\mathbf{r}})$ was proposed by Daniuk et al. [Dan89], often referred to as LDA(E). This puts the phenomenological enhancement of Mijarends on physical grounds and also considers the effect of the crystal potential.

Using the methodology of Arponen and Pajane [AP79] another parametrisation of the enhancement was found within the LDA by Babiellini [BPTN95, BPK⁺96] and further improved by using the generalized gradient approximation. According to the authors the LDA enhancement

reads:

$$\gamma_{\text{LDA}} = 1 + 1.23r_s - 0.0742r_s^2 + \frac{1}{6}r_s^3. \quad (2.43)$$

Taking the inhomogeneity of the electron gas into account by using the GGA in the form of

$$\gamma_{\text{GGA}} = 1 + (\gamma_{\text{LDA}} - 1) \exp^{-\alpha\epsilon} \quad (2.44)$$

with a free parameter α and the GGA corrections ϵ the enhancement is now dependent on the local electron density and the gradient of the electron density. The authors also found that a value of $\alpha = 0.22$ yields best agreement with the experiment. It was found that the GGA gives slightly better agreement with the experiment and that compared to the LDA, the GGA leads to a suppression of the electron-positron correlation effects and also reduces the partial annihilation rates for the core states [BHP⁺97]. The GGA scheme was further extended to study the enhancement of individual electronic states [BHP⁺97]. For the state dependent description the enhancement factor to be used in equation 2.38 is treated without momentum or position dependence as $\gamma_i = \lambda_i/\lambda_{\text{IPM}}$ the ratio of the partial annihilation rate of the state to the annihilation rate obtained in the independent particle model (IPM). The partial annihilation rate is given by

$$\lambda_i = \pi r_e^2 c \int d\mathbf{r} \gamma(n_{e^-}) n_{i,e^-} n_{e^+} \quad (2.45)$$

with the classical electron radius r_e , the speed of light c , the positron density n_{e^+} , the electron density of the state i $n_{i,e^-} = |\Psi_i(\mathbf{r})|^2$ and the enhancement factor γ given in LDA or LDA-GGA as function of the local electron density. To obtain λ_{IPM} the enhancement is set to one $\gamma = 1$. Makonnen et al. [MHP06] performed an intensive comparison between the state dependent and the position dependent enhancement as well as between the LDA enhancement and the LDA-GGA enhancement by comparison of the predictions with experimental Doppler spectra. They found that the state dependent enhancement yields better agreement with the experiment especially for the high momentum area than the position dependent enhancement. Also, no major differences between the LDA (using the Boronski Nieminen parametrisation) and the LDA-GGA were found. However, the authors conclude that the LDA is preferable because it relies on a two-component DFT and requires no additional semi-empiric parameters. A piratical application of the state dependent enhancement was done by Laverock et al. [LHAD10]. The authors studied the effect of the state dependent enhancement in several transition metals (Cr, V, Al and Ag). By use of linearised muffin tin orbitals (LMTO) calculations the authors applied enhancement factors associated to the different orbitals (s,p,d,f). This way an implicit \mathbf{k} -dependence of the enhancement is incorporated as the bands can change their character due to hybridisation. By comparing the effect of different enhancement models (IMP, Jarlborg-Singh and a simplified GGA description (according to reference [BPTN95]) to experimental data it is found that the data is always described best by the state dependent enhancement based only on the character of the orbital. In the GGA description the authors determined the partial annihilation rates also according to the character (s,p,d,f) of the states neglecting a possible \mathbf{k} -dependence of the electron density in the orbitals due to hybridisation. However, no comparison the LDA scheme of Boronski and Nieminen is made. It may be speculated that it should give similar results to the Jarlborg-Singh prescription, at least for Ag, Cr and V due to the weak lattice effects in these systems.

In the discussion of the state dependent enhancement [BPTN95, BHP⁺97, MHP06, LHAD10]

the appearance of the famous high momentum tails due to electron-electron correlation receives only marginal attention. However, since the treatment of the electron-positron correlation is performed on the basis of the approach by Arponen and Pajane [AP79] the effect should also be present in the state dependent enhancement as well [BPTN95]. Beyond the state dependent enhancement several authors, most notably Sorman and Kontrym-Sznajd [Sor96, SKS06, KSSB12, KSS14b], investigated the the influence of lattice effects on the electron-positron momentum density by using a so-called Bloch-modified ladder approximation in the calculation within the LDA. This means that free electron states in the ladder approximation used by Carbotte and Kahana [CK65] are replaced by Bloch states accounting for the periodicity of the crystal. This is necessary in order to explain the high momentum components due to electron-electron correlations that were experimentally found in 2D-ACAR and are in accordance also in terms of strength to those found in a Compton scattering experiment which is naturally free of electron-positron correlation effects [KSSCP⁺02]. In summary:

- Kahana-like momentum dependence leads to increased enhancement at the Fermi surface, but suppresses higher momenta.
- State-independent LDA treatment of the enhancement works well for positron lifetime but differs only little from the IPM when it comes to electron-positron momentum densities.
- State dependent enhancement in the LDA(E) of Daniuk or the GGA by Babiellini predict the electron momentum densities better.
- As far as no solution of the two-particle problem is obtained the BML theory is the most accurate treatment of the enhancement in the Kahana formalism.

2.3. 2D-ACAR in literature - an overview

In this section the focus is put on the experimental aspects of 2D-ACAR spectroscopy, in particular what properties of the electronic structure of solids can and have been determined in 2D-ACAR experiments. Different phenomena arising from the electronic structure have been studied with 2D-ACAR, for example superconductivity, magnetism, the effects of alloying on the Fermi surface, Fermi surface nesting, etc. This overview compiled in this section makes no claim of completeness but is rather meant to familiarize the reader with possibilities of 2D-ACAR spectroscopy.

2.3.1. Transition metals

The class of transition metals attracts much interest due to the itinerant character of the valence d -bands which leads to strong electron-electron correlation effects in the electronic structure. The theoretical aspects of the positron probe effects in highly correlated materials are discussed in depth in section 2.2.2. Numerous 2D-ACAR investigations in these systems have been performed and published in literature. Some of the most prominent investigation and results are presented in the following.

Chromium

Chromium is a very interesting system due its spin-density wave ground state at room temperature. The Néel-temperature of chromium is 311 K. Therefore, the paramagnetic state cannot be investigated by means of quantum oscillations since the required long scattering length can only be achieved at cryogenic temperatures. Hence, this system is predestinated to be investigated with 2D-ACAR since elevated temperatures may lower the resolution in an ACAR experiment but do not obscure the signal from the electronic structure. An early in-depth study of chromium was performed by Shiotani et al. [SOS⁺77] using 1D-ACAR. The authors found that the low momentum region which is dominated by the valence bands as well as the high momentum region which originated from annihilation with core electrons are under-represented when comparing the experimental results to their calculations. This effect was ascribed to electron-positron correlation effects and was a first proof of the complicated behaviour of the positron in chromium. Stimulated by these findings Singh and Singru [SS83] calculated 2D-ACAR spectra for paramagnetic chromium. However, besides the treatment of wave function effects the electron-positron correlation were not included. The calculated spectra of Singh and Singru show that valuable information on the Fermi surface of chromium can be obtained with 2D-ACAR, i.e electrons from the band associated with the H-hole-octahedra strongly participate in the annihilation process. In the following Singh et al. [SMW88] performed 2D-ACAR measurements in the anti-ferromagnetic as well as in the paramagnetic state. To reach the paramagnetic state a sample of pure chromium was heated above the Néel-temperature and a sample of Cr_{0.95}V_{0.05} was used for comparison as well. Cr_{0.95}V_{0.05} is paramagnetic even at low temperatures. In order to interpret their results the authors used the at that time newly developed Lock-Crisp-West [LCW73] back folding routine as the calculations were still performed in the independent particle model. The authors found that when going from the paramagnetic to anti-ferromagnetic state an electron-pocket located at the X-points of the Brilluin zone disappears. This is attributed to the appearance of a gap at the zone boundary due to the magnetic interactions as can be seen in the dispersion relation shown in figure 2.8.

A full three-dimensional measurement of paramagnetic chromium was performed by Kubota et al. [KKN⁺91] by measuring multiple projections in 5° steps. In order to obtain the three-dimensional density an analytical method based on the direct Fourier reconstruction technique was applied. For further analysis the obtained **p**-space density was folded back into **k**-space using the LCW-method and the results were compared to calculations for the occupation number. A satisfactory agreement to the calculated shape of the Fermi surface was found. The authors were able to identify the Γ -centred electron sheet and the *H*-centred hole pocket. Furthermore, the authors conclude that the *N*-hole pockets are too small to be resolved due the limited resolution (as shown in figure 2.9).

By use of an advanced data evaluation technique based on maximum entropy filtering Dugdale [DFH⁺98] and Fretwell [FDH⁺98] were able to identify the *N*-hole pockets in LCW-folded 2D-ACAR projections of paramagnetic chromium without the need for a three-dimensional reconstruction. The maximum entropy filtering, a method readily used in image processing, allowed the authors to correct the experimental spectra for the limited resolution of the spectrometer. The key feature of this method is thereby that the information content in the corrected spectra remains unchanged compared to the initial spectra so that no artefacts are introduced. In the maximum entropy filtered data the breaks associated with a band crossing the Fermi energy appear steeper and can be identified more reliably. This way, the authors were

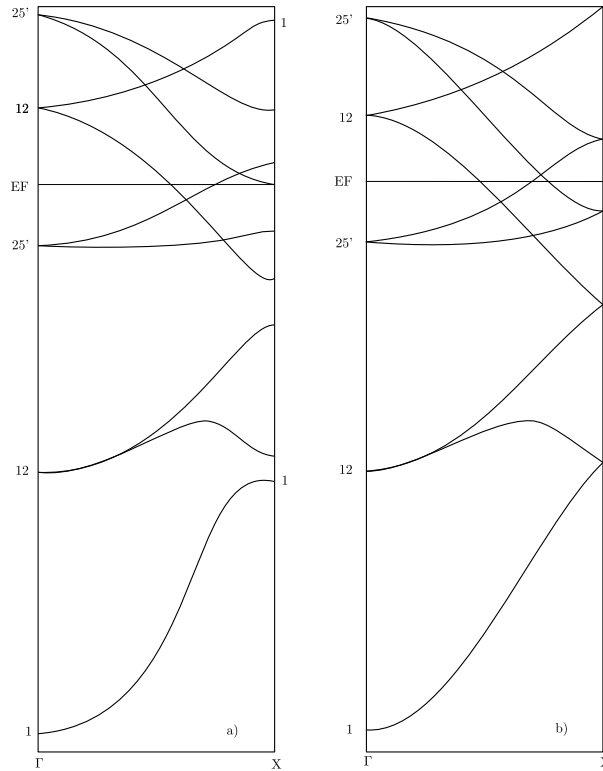


Figure 2.8.: Band structure calculation for paramagnetic (*left*) and anti-ferromagnetic (*right*) chromium adapted from reference [SMW88]. A gap at the zone boundary present in the anti-ferromagnetic state disappears in the paramagnetic lattice. Both band structure calculations are shown in the simple cubic lattice of the anti-ferromagnetic state.

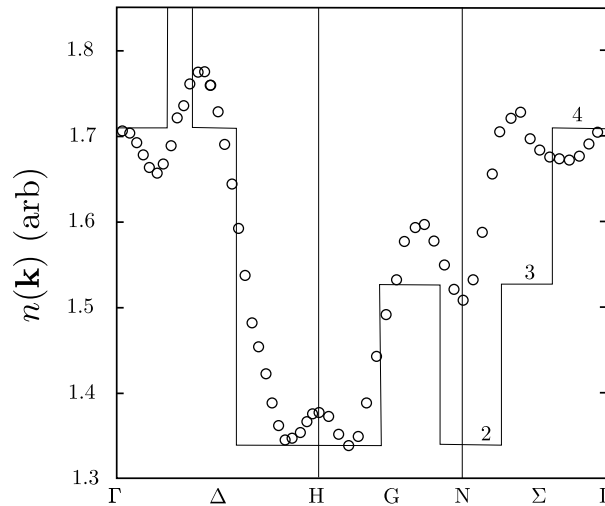


Figure 2.9.: $N(\mathbf{k})$ of paramagnetic chromium (data taken from reference [KKN⁺91]). The experimental data (circles) is compared to the calculated occupation number (solid line). The data was obtained by three-dimension reconstruction of multiple 2D-ACAR measurements. The predicted N -hole-pocket is too small to be resolved in the experiment.

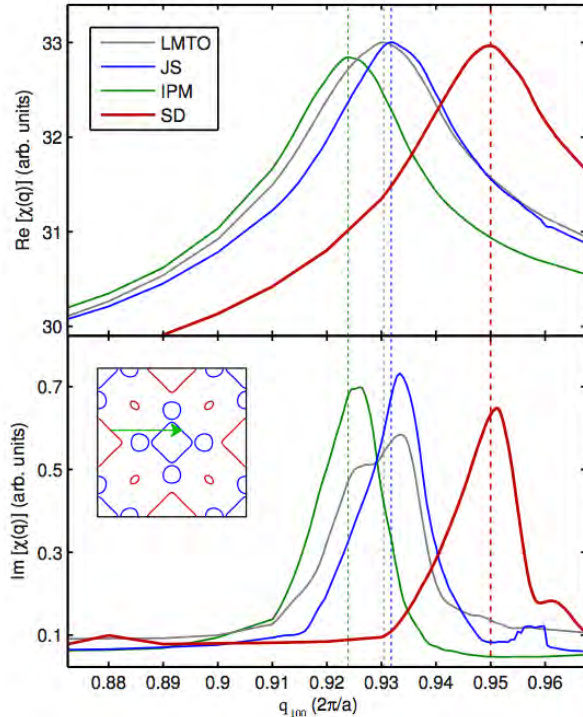


Figure 2.10.: With a state dependent enhancement model the nesting vector of the chromium Fermi surface can be determined by a rigid-band shift. The real (top) and imaginary (bottom) parts of the static susceptibility of paramagnetic chromium, calculated for the raw LMTO band calculations as well as the results of the rigid-band fit to the data within the IPM and using the Jarlborg-Singh enhancement or the state dependent models for the enhancement. The dashed vertical line represents the peak in the real part of the susceptibility. The inset shows a slice of the Fermi surface through the [100] plane, with the arrow depicting the nesting that gives rise to the peak in the imaginary susceptibility between the N -hole octahedron (red) and electron jack (blue). Reprinted from [LHAD10] with permission.

able to give precise estimates on the projected radius of the N -hole ellipsoid.

An alternative approach to calliper the Fermi surface of chromium was undertaken by Biasini [Bia00]. Here a parametrisation of the Fermi surface in terms of polyhedra was applied. The N -hole pockets are described as ellipsoids with the dimensions of semi axes as free parameters, the Γ -centred electron surface, the so-called electron-jack, was described as combination of a distorted octahedron with spheres located at its corners and the H -hole surface was parametrised by a single distorted octahedron. The free parameters, i.e. the geometric dimensions of the polyhedra, of this simplified geometrical model are then fitted to the data and the dimensions of the Fermi surface are obtained from the model. The results for the dimension of the N -hole ellipsoid obtained by the geometrical model are found to be in agreement with the results obtained by Fretwell et al. [FDH⁺98].

Much information on the Fermi surface of chromium could be gained by the geometrical model [Bia00] or from filtered spectra, however discrepancies between the measured data and the LDA predictions made a detailed evaluation of the chromium Fermi surface virtually impossible. This could be resolved by the approach of Laverock et al. [LHAD10]. The authors compared theoretically calculated spectra with the experimental data using the rigid band shift technique. As the name implies in this technique the shape of the bands is conserved but the position relative to the Fermi level is shifted. This results in small changes in the shape of the Fermi surface depending on the slope of bands crossing the Fermi level. Also several different models

for electron-positron correlations have been included and compared by the authors, e.g. the Jarlborg-Singh enhancement and a state dependent enhancement model. It was found that the state dependent enhancement, where each band is associated with an individual constant enhancement factor describes the data best. Further quantitative results could be achieved by rigidly shifting the bands in energy in order to improve the description of the data, with a least-squares fitting procedure. From the improved theoretical band structure the susceptibility was calculated (see figure 2.10) which can serve as measure for the number of coupling of electrons from different \mathbf{k} -states. Therefore, the position of the peak in the susceptibility corresponds to the length of the nesting vector. The length of the nesting vector \mathbf{q} was found to be $|\mathbf{q}| = 0.950(2)\frac{2\pi}{a}$ which is in good agreement to the results from neutron scattering experiments [Faw88]. However, since the origin of these effects remains an open question Cr was experimentally measured within the present work (see chapter 5).

Nickel

Ferromagnetic nickel is a very interesting system due to its almost completely filled $3d$ band which results in an almost balanced density of states in both spin channels. Compared to other pure ferromagnetic systems like iron and cobalt, nickel shows a relative small magnetic moment of $0.46 \mu_B$ per formula unit.

Nickel was and still is the subject of many 2D-ACAR studies including spin polarized 2D-ACAR measurements. A study on the strength of the magnetic exchange coupling was performed by Genould et al. [GMWP91] with spin polarized 2D-ACAR. The evolution of the magnetic ACAR signal, i.e. the difference of two-ACAR spectra taken with the magnetisation of the sample orientated parallel and anti-parallel to the positron emission direction, was investigated for different temperatures below and above the Curie temperature T_C . The authors found that the magnetic ACAR signal is independent of temperature below T_C . By comparison with theoretical calculation it was found that the magnetic exchange coupling may however decrease by $\approx 28\%$ from the value at 4.2K when approaching the T_C . Above T_C the magnetic ACAR signal diminishes but is still observable due to magnetic fluctuations. The observation of the magnetic ACAR signal by Genould in ferromagnetic nickel hence motivated the study on electron-electron correlations presented in this thesis.

Hamid et al. [HU04] performed a three-dimensional reconstruction of several projection taken for different orientations of the magnetisation. The authors claim to have identified five different Fermi surface sheets by use a maximum gradient filtering of the LCW folded data and compare their results to theoretical calculation, which are found to be in agreement. Although the authors state that the Fermi surface breaks were identified by the maximum gradient the complete opposite seems to be case. The results should also be treated with caution as it is known from theoretical calculations [SM74] that due to positron wave function effects present in nickel several Fermi surface sheets are difficult to observe with 2D-ACAR.

Cobalt

An experimental in-depth study of ferromagnetic cobalt was performed by Kondo et al. [KKN⁺92] by means of spin-polarized 2D-ACAR. Seven projections were measured with the magnetic field parallel and anti-parallel to the emission direction of the positrons. However, since the authors did not have information on the positron polarisation they were unable to separate

the contributions from the minority and majority channels. The difference in the magnetic ACAR spectra was observed to be about 3% of the maximum value for the spin-averaged case. For each field direction the three-dimensional density was reconstructed using an analytical method based on the direct Fourier transform technique. Directional anisotropies were observed for the magnetic signal which were most striking in the plane perpendicular to the c -axis and almost not observable in the parallel planes. This led the authors to the conclusion that the magnetic electrons in cobalt behave in a two-dimensional manner, which means that the magnetic coupling is strongest in the basal plane perpendicular to the c -axis and weak out-of-plane.

Copper

Due to the relatively simple topology of the Fermi surface of copper, that can even be approximated by the tight-binding approach (see section 2.2.1), this system is often used as benchmark for three-dimensional reconstruction techniques (see for example [WCH⁺14, KKN⁺93, LWC15]). A detailed discussion of the different reconstruction techniques is beyond the scope of this thesis therefore refer to Weber [WCH⁺14] and references therein.

A study of copper different to those above was presented by Nagai et al. [NCT⁺01] who studied copper forming a bcc structure inside an iron matrix. Copper precipitates inside a single crystalline iron matrix are found to crystallize in the bcc structure coherent to the iron host lattice. The copper precipitates have a higher positron affinity than the Fe matrix and therefore the positrons are more likely to annihilate inside the precipitates than in the iron matrix. By subtracting the contribution of bulk iron the 2D-ACAR signal from the copper precipitates was recovered and compared with theoretical calculations. In contrast to the eight necks of the FS of fcc copper the Fermi surface of bcc copper has 12 necks. This study was the first direct observation of the FS of bcc copper.

Molybdenum

According to Lomer [Lom62] all chromium group metals are expected to have similar Fermi surface topologies. Therefore, molybdenum is readily used for comparison with chromium as its non-magnetic counterpart. Hence, basically all 2D-ACAR investigations dealing with chromium also consider molybdenum for comparison [Bia00, FDH⁺98, DFH⁺98]. In general it is found that the theoretically predicted 2D-ACAR spectra describe molybdenum better than chromium what most authors ascribe to the different nature of electron-positron correlation in those two metals. However, Biasini [Bia00] points out that when comparing quantitative measures of the Fermi surface also in the case of molybdenum discrepancies between theory and experiment are found.

Yttrium

Dugdale et al. [DFA⁺97] obtained the Fermi surface of yttrium (see figure 2.11) by subsequent maximum entropy filtering and three-dimensional reconstruction of multiple 2D-ACAR spectra using Cormack's method. By identifying the zero-crossing contour on the $KMLH$ Brillouin zone face in the difference between the reconstruction of the raw data and the maximum entropy filtered data the authors were able to determine the so-called "webbing" structure in the Fermi surface of yttrium. This method is similar to edge-detection methods used for image



Figure 2.11.: Reconstructed Fermi surface of yttrium reprinted from reference [DFA⁺97] with permission. The three-dimensional density was reconstructed from five projections.

processing (for details see reference [DAF⁺94]). In the analysis of this "webbing" feature possible nesting vectors were identified. The magnitude of these nesting vectors was found to be in good agreement with quantum oscillation measurements. A following analysis of the same data by Kontym-Sznajd [GKS01] performed in \mathbf{p} -space revealed two hole-like Fermi surface sheets. These two sheets were found to almost coincide in \mathbf{k} -space and could therefore not be separated in the analysis of the LCW-folded \mathbf{k} -space densities of Dugdale et al. [DFA⁺97].

Also based on the data of Dugdale et al. [DFA⁺97] and combined with Compton scattering data as well as theoretical calculation the work of Kontym-Sznajd et al. [KSSCP⁺02] resembles one of the most important works from the last decade. In this work it was unambiguously shown that electron-electron correlation effects are observable with 2D-ACAR. This fact has long been disputed since in the Kahana formalism the high momentum tails that are associated with electron-electron correlations are strongly suppressed. The authors used a full three dimensional reconstructions of the 2D-ACAR and the Compton scattering data in \mathbf{p} -space to compare the effects of electron-electron correlations. It was found that the shape and the magnitude of the high momentum tails is the same for both experimental techniques which is a direct disprove of the presence of a Kahana-like enhancement.

2.3.2. Intermetallic compounds and alloys

Intermetallic compounds exhibit many different physical properties, like for example magnetism in the class of Heusler alloys, shape memory effect or half-metallicity, that are not inherent to their constituents. Therefore these materials are of high interest as constantly new functional material are sought for technology application [OK02]. One example that has already found its way to technical application, for example in medicine, are NiTi alloys which are used for their super-elasticity and shape memory effect. Most of the properties of these materials are related to their electronic structure and the shape of the Fermi surface. Hence, numerous investigations applying 2D-ACAR to these systems have been undertaken. The most prominent works are presented in this section starting with two examples of Heusler type materials.

NiMnSb

The intermetallic compound NiMnSb is part of a subgroup of Heusler materials. Heusler alloys form a crystal lattice of $L2_1$ -type which resemble four face centred sub-lattices. In the group of half-Heuslers one sub-lattice remains unoccupied, resulting in a lattice of $C1_b$ -type. Theoretical calculation of the electronic structure of NiMnSb reveal that this material is expected to be

a half-metal which means that only the bands of one spin population cross the Fermi level [CKGL03]. By use of spin polarized 2D-ACAR Hanssen et al. [HM86, HMRB90] studied the half-metallic character of NiMnSb. Like the spin polarized ACAR measurements on nickel by Genould the work by Hanssen is also based on alternating the sample magnetisation relative to the positron spin. However, the authors determined the net polarisation of their positron source which allowed them to extract the individual contributions from the spin-majority and the spin minority channels. By comparison with LDA calculation for the individual spin channels the authors concluded that a Fermi surface could be found only for the majority spin channel. The authors assumed in their calculations a fully filled minority band with nine electrons and allowed the occupation to slightly change by moving the bands in energy. The best agreement between theory and experiment was reached for an occupation of the minority band of $8.995_{-0.012}^{+0.020}$ electron per formula unit which resembles the half-metallic state. Up to date this has been the only study of a half-metal with spin polarized 2D-ACAR although the results impressively demonstrate the capabilities of spin polarized 2D-ACAR.

Ni₂MnGa

Haynes et al. [HWL⁺12] determined the Fermi surface of the ferromagnetic shape-memory alloy of Ni₂MnGa by means of 2D-ACAR. Ni₂MnGa undergoes a martensitic phase transition in the ferromagnetic phase and is therefore interesting for the application as magnetostrictive actuator [OK02]. Haynes determined the Fermi surface following the traditional recipe of the Bristol group [DFA⁺97, LHAD10] by reconstruction of the three-dimensional density according to the implementation of Cormacks method for positron data (see [KS08a] and references therein) from six maximum entropy filtered 2D-ACAR projections then applying the LCW back folding into **k**-space followed by the identification of the discontinuities which are associated with the Fermi surface breaks. Two Fermi surface sheets could be identified, one of which was found to exhibit strong nesting features that may stabilize the martensitic phase. The interpretation of the experimental data is supported by LMTO-calculations of the TPMD using a state-dependent enhancement model.

Ni₃Al

The weak ferromagnet Ni₃Al crystallizes in the L1₂ structure similar to the Heusler alloys but with a simple cubic unit cell and is known to exhibit a behaviour consistent with proximity to the quantum critical point [SBNL03]. Hamid et al. [HUM⁺11] performed a 2D-ACAR investigation of the electronic structure of Ni₃Al in the ferromagnetic as well as in the paramagnetic state. For both states a full three-dimensional reconstruction was performed using the Bristol recipe (see above) and compared to theoretical LMTO calculations and FLAPW calculations. The measurements of the paramagnetic state were performed by the Bristol group and the measurements of the ferromagnetic state were carried out in Japan at the university of Tskuba. Therefore, two different philosophies of 2D-ACAR spectroscopy are combined in this work. One is taking more projections with less statistics the other recording less projections with better statistics. For both states two Fermi surface sheets could be obtained, while for the ferromagnetic state the resolution of the Tskuba spectrometer was insufficient to resolve the majority and minority Fermi surface sheet separately. The theoretical data was further subjected to the rigid-band shift procedure [LHAD10] in order to describe the experiment better. However, a third Fermi

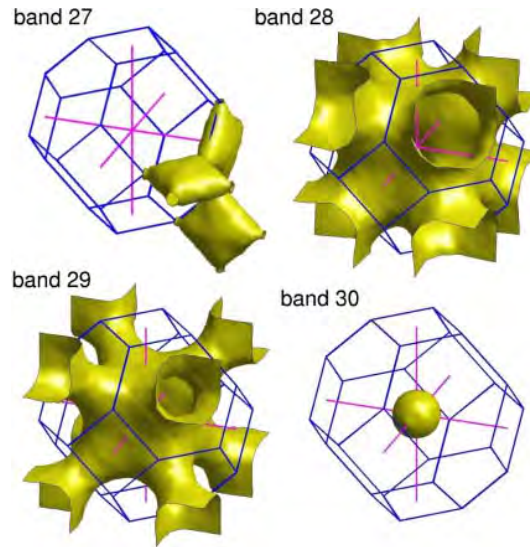


Figure 2.12.: Reconstructed Fermi surface of ZrZn_2 reprinted from reference [MDW⁺04] with permission. The three-dimensional density was reconstructed from six projections. Prior to the reconstruction the experimental resolution was deconvolved from the spectra by maximum entropy filtering.

surface sheet could not be observed and the authors conclude that it might be indeed absent which is not predicted by the LMTO calculations.

ZrZn_2

The heavy fermion system ZrZn_2 is famous for the coexistence of superconductivity and ferromagnetism [PUH⁺01]. Major et al. [MDW⁺04] performed 2D-ACAR measurements in the paramagnetic state of ZrZn_2 and were able to obtain four Fermi surface sheets (see figure 2.12) by the now well known Bristol recipe. One of these sheets (band 29) is associated with the heavy fermion behaviour of ZrZn_2 and could be resolved with 2D-ACAR while it is not observed in quantum oscillation measurements. Also, on this Fermi surface sheet possible nesting sections could be identified that might give rise to nesting driven spin fluctuations.

$\text{Cu}_{1-x}\text{Pd}_x$

The work of Wilkinson et al. [WHM⁺01] on the Fermi surface nesting of disordered $\text{Cu}_{1-x}\text{Pd}_x$ alloys serves as an excellent example for the capability of 2D-ACAR to resolve the Fermi surface in disordered systems. The authors investigated the theoretically predicted flattening of the Fermi surface perpendicular to the [110] direction. The Fermi surface was obtained by treating the data according to the Bristol recipe of maximum entropy filtering, three-dimensional reconstruction according to Cormacks method, LCW back folding into \mathbf{k} -space and followed by the identification of the Fermi surface breaks by the discontinuities of the \mathbf{k} -space density. The authors found the predicted flattening of the Fermi surface with increasing Pd content and were also able to determine the relative size of the nesting sections of the Fermi surface.

2.3.3. Rare earth metals and compounds

The elements in the class of rare earth metals are known to have interesting electronic structures. The f -electrons are strongly localized and are therefore screened by the outer s and p orbitals from forming electron bands. Therefore, also the magnetic moments are localized in the case of magnetic rare earth metals and give rise to interesting magnetic ordering phenomena like helical-ordering for example in the case of Er, Dy, Tb or Ho via the indirect Ruderman-Kittel-Kasuya-Yosida interaction.

Gadolinium

In their study on the reconstruction of the Fermi surface of gadolinium Pylak et al. [PKSD11] compared the performance of two different reconstruction methods: Cormacks methods according to the implementation of Kontrym-Sznajd [KS08a] and a least-squares method using a regularisation functional based on maximum entropy. The authors reconstruct the electron momentum density of gadolinium from 16 resolution corrected 2D-ACAR spectra measured perpendicular to the c -axis with a spacing of 2° obtained with the Bristol spectrometer. It is found that the maximum entropy method produces smoother results and by construction avoids negative values for the density which can occur for higher momenta when Cormacks method is used. But in general the two methods yield similar results.

Holmium

A spin dependent investigation of the electronic structure of Holmium was undertaken by Hamid et al. [HU04]. Using a discrete Fourier transform method for the reconstruction of the three-dimensional density the authors were able to identify several Fermi surface sheets.

CeIn₃

The work on CeIn₃ resembles another 2D-ACAR study on a rare earth compound performed by the Bologna group around Biasini et al. [BFC03]. The Bologna method of obtaining the Fermi surface differs only in details from the method of the Bristol group. The Gerhard de-Citter algorithm [GMSW98] is used to correct the experimental data for the finite resolution of the spectrometer. This method is closely related to the maximum entropy filtering employed by the Bristol group. From the corrected spectra the three-dimensional electron-positron momentum density is reconstructed either by using Cormacks method or the filtered back-projection technique. Then the three-dimensional LCW-transformation is used to fold the \mathbf{p} -space density back into \mathbf{k} -space where the Fermi surface breaks are identified by the discontinuities in the resulting distribution. The author applied this prescription to five 2D-ACAR projections of CeIn₃ and were able to intensify two hole-like and one electron-like Fermi surface sheet of CeIn₃. The obtained experimental results are then compared to two different theoretical predictions of the Fermi surface for itinerant or localized f -electrons. It was found that the so-called f -core model with localized f -electrons describes the data best. Therefore, within this study the authors were able to ascertain the localized behaviour of the f -electrons which has been disputed in literature.

TmGa₃

Biasini et al. [BKSM⁺01] have undertaken a Fermi surface study on the rare earth compound TmGa₃ which shows anti-ferromagnetic ordering which is related to the topology of the Fermi surface. It also shows a complex low temperature phase diagram (see for example reference [PCG⁺99]) with different magnetically ordered states. Like Ni₃Al this system crystallizes in the cubic L1₂ structure. The authors used a Gerhard de-Citter algorithm [GMSW98] to correct the raw spectra for the experimental resolution and used then two different methods for the three-dimension reconstruction: Cormacks method and a filtered-back-projection. The authors state that both reconstruction methods deliver comparable results. Different Fermi surface sections capable of nesting could be identified and the values for the spanning vector obtained from both reconstruction method agree within the error limits. The length of the spanning vector is found to be compatible with commensurate anti-ferromagnetic ordering. The authors proceed by obtaining the specific heat parameter of the electronic system by determining the number of states at the Fermi surface. This way the specific heat parameter associated with the hole-like and electron-like Fermi surface sheets could be estimated. However, since no re-normalisation of the electron band mass can be obtained from 2D-ACAR data the values are only in fair agreement with the theoretical predictions.

UGe₂

Like the transition metal compound ZrZn₂ the rare earth compound UGe₂ shows a coexistence of ferromagnetism and superconductivity [SAA⁺00]. Biasini et al. [BT03] performed a 2D-ACAR investigation in the paramagnetic phase of UGe₂. 2D-ACAR is the method of choice to investigate this system since in the high fields used in quantum oscillation measurements the Fermi surface is perturbed due to the Zeeman splitting or even magnetic breakdown. The 2D-ACAR spectra were corrected for the resolution of the spectrometer using the Gerhard de-Citter algorithm [GMSW98] and analysed in terms of the radial anisotropy and LCW-folded two-dimensional projections. The obtained **k**-space projections are compared with LDA calculations using the so-called *f*-band model. It is found that the discrepancies between theory and experiment can neither be attributed to positron probe effects nor to the consequence of an oversimplified band-structure calculation. By comparison with results from dHvA measurements the authors conclude that the *f*-electrons do not contribute to the superconductivity of UGe₂.

GdTe₃

A study on rare earth compounds performed by the Bristol group was published by Laverorck et al. [LDM⁺05]. The authors studied the class of rare earth tellurides by the example of GdTe₃. Due to the high anisotropy in these system they are often considered as low-dimensional metals and show a charge density wave ground state. The authors analysed the 2D-ACAR data by comparison between the experimental LCW-folded data and LCW-folded projections of the electron density from band structure calculations. This is sufficient to determine the Fermi surface since it has a strong two-dimensional character. The Fermi surface was obtained using the zero-crossing method of Dugdale [DAF⁺94]. From the obtained Fermi surface a nesting vector was determined which was found to be in agreement with the theoretical calculation as well as with experimental results from angle resolved photo-emission spectroscopy. This nesting feature is assumed to be the driving force for the charge density wave ground state.

LuNi₂B₂C

Motivated by the fact that dHvA measurements were unable to determine the Fermi surface topology of the rare earth nickel borocarbide LuNi₂B₂C Dugdale et al. [DAW⁺99] performed a 2D-ACAR investigation on this system and were able to recover its Fermi surface as well as a nesting feature which is conjectured to be the driving mechanism of superconductivity in LuNi₂B₂C. The authors applied the zero-crossing method to determine the contours of the Fermi surface from two maximum entropy filtered 2D-ACAR projections. Due to the limited number of projections a three-dimension reconstruction was not possible. However, the nesting feature of the Fermi surface could be recovered from the projected data and was found to be in good agreement with the Kohn-anomalies found in neutron scattering experiments.

2.3.4. Oxides and exotic materials

The class of oxide materials is of high interest mainly because of its wide range technological applications which span from data storage to laser applications. 2D-ACAR was applied to investigate the electronic structure of these materials either to benchmark theory predictions, like in the case of CrO₂, or to investigate the Fermi surface topology directly which was done for the High- T_C superconductors.

CrO₂

Chromium(IV)-oxide is well known for its usage for in magnetic tape data storage. Due to its high magnetic anisotropy CrO₂ possesses a high coercivity which makes it ideal for magnetic data storage. Theory predicts CrO₂ to exhibit half metallic character [TKSO05]. From the experimental perspective this system is interesting because different theory models (LDA+U or LSDA) result in different Fermi surface topologies. Photo electron spectroscopy measurements on CrO₂ show a high spin polarisation of up to 100% below the Fermi level [DFK⁺02], but suffer from a diminishing signal when the Fermi level is approached. Motivated by this Biasini and Rusz undertook a theoretical assessment for a 2D-ACAR experiment on CrO₂ [BR06, RB07, BR07]. In the course of this investigation the authors developed the idea of magnetic ACAR. It was found that by taking the difference of two ACAR spectra with the sample differently magnetised the probe effects associated with the positron are almost cancelled. Here the authors subsume both electron-positron correlations and positron wave function effects under the term *positron probe effects*. The key to the method of *magnetic ACAR* lies in taking the magnetic difference followed by the application of the LCW-backfolding procedure. The authors found that this way the effects of a non-uniform positron density over the Brillouin zone (i.e. the positron wave function effects) can be avoided. It is concluded that information on the Fermi surface can be obtained by 2D-ACAR which would be inaccessible in a conventional non-magnetic 2D-ACAR measurement. Although the investigations of Biasini and Rusz were limited to half metals they speculate that the scheme of magnetic ACAR could also be applied to generic ferromagnetic systems. In the present work this investigated whether the claims of Biasini are more general in nature by an analysis of the positron effects in ferromagnetic nickel (see chapter 6).

YBa₂Cu₃O_{7-δ}

Once untwinned single crystalline samples became available the high- T_C superconductor YBa₂Cu₃O_{7-δ} naturally attracted much interest from 2D-ACAR experiments since the superconductivity is supposed to be driven by a nesting feature of the Fermi surface [HKR⁺91]. Several features of the Fermi surface could be identified by 2D-ACAR measurements (see [HKR⁺91, PBSM94, MSH⁺95]). However, these features were always related to the electronic structure of the copper oxygen chains and not to the central two CuO₂-planes. In between those two planes the superconducting electron states are expected. A recent detailed theoretical and experimental investigation by Reiner et al. [RGJ⁺15] revealed that due to wave function effects the positron is almost completely excluded from the central CuO₂-planes and practically exclusively samples the outer plane of the CuO-chains. Therefore, the 2D-ACAR studies on this systems have to considered with a grain of salt.

Organics

Organic compounds have also been studied by means of 2D-ACAR. The most prominent example is trans-stilbene, which is used, for example, as a scintillator material or as a gain medium in dye lasers. Trans-stilbene is one of two isomers of the stilbene molecule the other being cis-stilbene. The two isomers can be converted into the other by the absorption of light which makes this compound interesting for the above mentioned optical applications. Due to the aromatic character of the trans-stilbene molecule the delocalized electrons are expected to effectively prevent positronium formation. Selvakumar et al. [SSS12] found experimental proof for this in a 2D-ACAR experiment. The authors did not observe a narrow component in the TPMD which would indicate para-positronium self-annihilation. The authors interpreted the complete absence of the narrow component as missing free volume around the molecule. However, this interpretation may lead to far, although the 2D-ACAR result was found in agreement with positron lifetime measurements [BMS⁺95] the suppressed positronium formation observed can be due to the chemistry of the sample even though open volume is present.

3 Chapter 3.

3 Experimental setup

3.1. Layout of the new 2D-ACAR spectrometer

In this chapter the technical aspects of the experimental setup of the Munich 2D-ACAR spectrometer are presented. The focus is put on the technical design of the spectrometer and its the performance is discussed in terms of resolution and positron transport efficiency.

3.1.1. Overview

The 2D-ACAR spectrometer consists of two main components, the source-sample chamber including the sample environment, and the detector assembly consisting of two Anger-type γ -cameras [AD64], which were obtained from the positron group of Bristol university. A total view of the spectrometer is given in figure 3.1 (A).

In the following the sections the individual components of the spectrometer are discussed in detail. The data acquisition is touched only marginally as this was part of a different project by Weber [Web15].

3.1.2. Detector system

The Anger cameras consist of a large NaI:Tl scintillation crystal with a thickness of 10.5 mm coupled to 61 photomultiplier tubes. The active area is collimated to a diameter of 41.5 cm by a lead ring, in order to exclude the part of the detector where the position response becomes non-linear due to the discontinuity in the light collection efficiency at the borders of the crystal. The position information is obtained from the center of gravity of the light signal produced in the scintillator.

The individual photomultiplier signals are summed up in an analogue weighting resistor network in horizontal and vertical direction and are then divided by the integral signal of all photomultiplier tubes. The resulting x - and y -signals are shaped and amplified before they are fed into the data acquisition system. Parallel to the determination of the center of gravity a logic analyser circuit checks if the integral signal, which corresponds to the energy of the event, lies within a window of about ± 35 keV around the 511 keV photo peak. If this is the case a logic signal is produced and is fed to an analogue coincidence unit. If both cameras produce an appropriate analyser signal, the data acquisition is triggered by the coincidence unit.

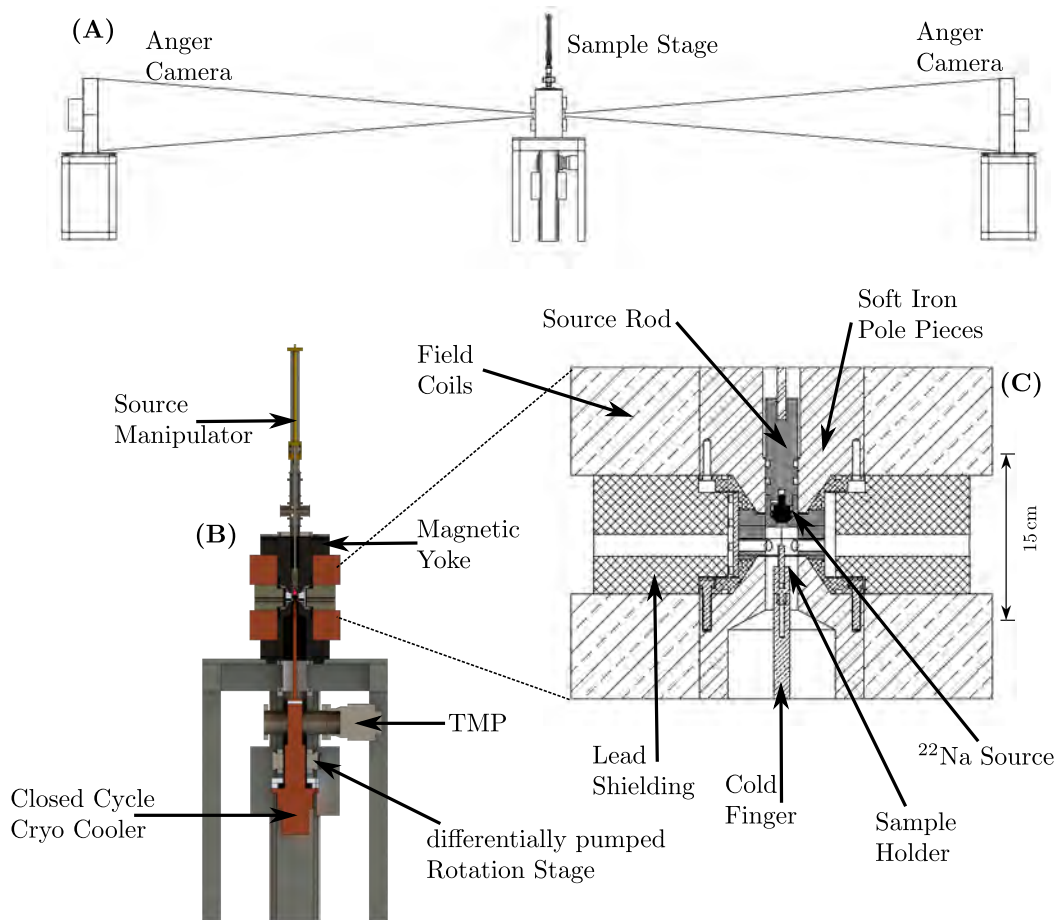


Figure 3.1.: Schematic overview of the 2D-ACAR spectrometer. (A) Total view of the spectrometer, including detectors. The baseline of the Anger cameras is 16.5 m in order to achieve the desired angular resolution. (B) Cut view of the central assembly. The cold finger of the cryostat is fed into the sample chamber from below. (C) Detailed cut view of the source-sample chamber with the custom-built pole piece assembly. Sample and source are positioned symmetrical with respect to the pole pieces.

The two Anger cameras are positioned symmetrically at a distance of 8.25 m to the source-sample chamber. As the typical angular deviation lies in the order of milliradians, a long baseline is needed to resolve such small angles. The angular resolution is limited due to the finite spatial resolution of ≈ 3.9 mm of the Anger cameras. By increasing the baseline the angular resolution could be improved at the expense of the count rate, which decreases quadratically with the length of the baseline. An asymmetric spacing of the detectors relative to the sample chamber would result in a momentum sampling function with flat center [Kru99], which can be beneficial for the data treatment. However, the attainable resolution is always limited by the detector with the shorter distance to the sample. Therefore, a symmetric spacing is chosen in order to achieve the maximum resolution limited by the available space in the experimental hall.

To avoid errors by a transverse pitch and yaw of the Anger cameras their respective axes are aligned collinear with an accuracy of ± 1 mm using a laser positioning system in combination

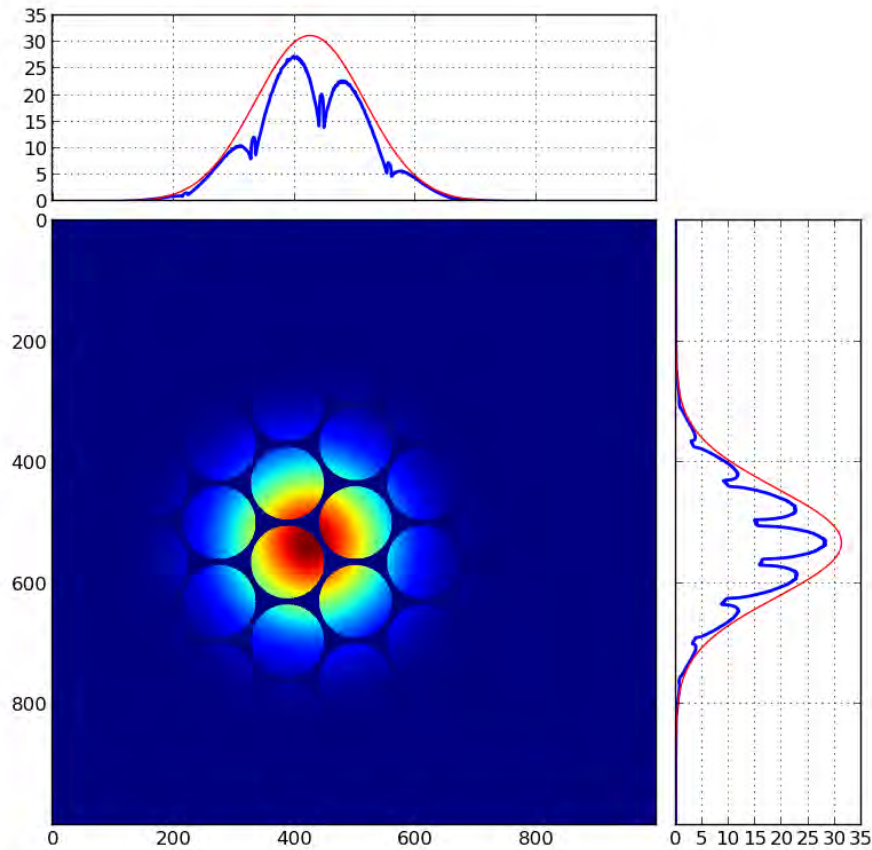


Figure 3.2.: Simulation of the light distribution in an Anger camera for a 511 keV event. On the *top* and on the *left* the projection of the light distribution as it is seen by the Anger camera is shown together with the enveloping projection of the full signal.

with a theodolite. Minor misalignment of the detectors can also be corrected offline in the data, since the positions for each coincident event on the detectors are stored in list-mode. By this it is also possible to correct the data for spatial distortions inherent to the Anger cameras position response [LCW12]. Using this correction procedure the resolution for the 2D-ACAR can be improved by $\approx 10\%$. All values in the context of the present study stem from uncorrected data as this allows a better assessment of the spectrometer performance. Variations and drifts in the gain of the electronics cannot be corrected that easily, therefore, in order to damp temperature fluctuations in the experimental hall, the Anger cameras are housed inside acrylic glass boxes insulated with Styrofoam.

There are certain limits to the achievable detector resolution due to physical and technical reasons. The absolute limit for the detector resolution is given by the range of the photo-electron that is created when a γ -ray interacts with the scintillator crystal. This so-called CSDA-range [BCZC05] is determined by the scintillator material. In the case of 511 keV radiation the range of a photo-electron is about ≈ 0.62 mm. A further physical limitation results from the fact that also multiple Compton scattering followed by a subsequent photo effect of the Compton scattered photon is indistinguishable in the summed up energy signal of the Anger camera from a single photo effect interaction. In the case of NaI the probability for Compton scattering is

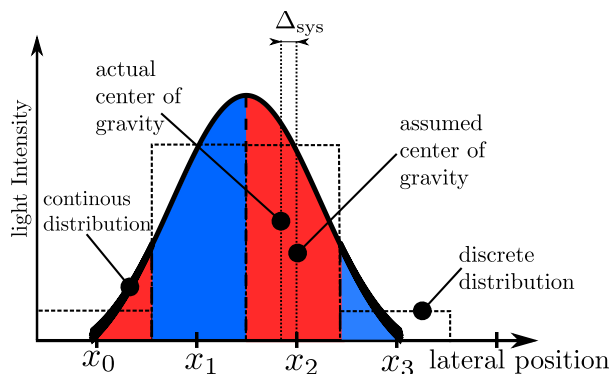


Figure 3.3.: Illustration of the origin of the systematic error that is acquired by the discretisation of a continuous distribution. Without loss of generality the originating light distribution in the example is assumed to be Gaussian. The assumed center of gravity of any bin is always shifted away from the maximum of the distribution.

about 4.5 times higher for 511 keV radiation than for the photo effect. The probability for a subsequent photo effect interaction of the Compton scattered photon is then determined by the mean absorption length and the crystal geometry. For a back scattered photon with an energy of 170 keV the absorption length in NaI is about 6 mm which is the same range as the thickness of the crystal. A double event from backscattering has however no detrimental effect on the resolution as both events lie on the line-of-sight of the detector. The situation is different for photons scattered to smaller angles. If one considers 90° scattering the scattered photon has an energy of about 250 keV and an absorption length of 10 mm, but due to the geometry of the crystal the photon will almost always be interacting inside the crystal. Also at this energy the probability for photo effect is about the same as that for Compton scattering. The effect on the achievable resolution by multiple events can only be fully assessed by Monte-Carlo simulations due to the influence of the crystal geometry, i.e the escape probability of the Compton scattered photon. To give an estimate the transversal projection of the absorption length $l \sin \phi$ as a function of the scattering angle ϕ is averaged from tabulated values assuming that the differential cross section for Compton scattering is constant:

$$\delta x = \frac{1}{\int_0^\pi l(E(\phi))} \int_0^\pi \sin \phi l(E(\phi)) \quad \text{with} \quad E(\phi) = \frac{511 \text{ keV}}{2 - \cos \phi}. \quad (3.1)$$

A value of $\delta x = 0.64 \text{ cm}$ is found, which is comparable to the range of the photo electron. Although in this crude approximation the energy dependence of the branching ratio between Compton scattering and photo effect is not considered this serves as an estimate for the detrimental effect of multiple events on the achievable detector resolution. These two effects discussed here give the hard physical limit for the detector resolution.

Besides the physical limitation for the spatial resolution there are several technical limitations to the operation principle of the Anger camera. The position information is acquired by the center of gravity of the signal amplitudes of the photomultiplier matrix. This discretisation of the light signal from the crystal is accompanied by a further limitation for the spatial resolution. An illustration of the distribution of the light signal is shown in figure 3.2. The light output from the NaI crystal after the absorption of a 511 keV photon via photo effect amounts to about

19400 photons per event. The scintillation light is emitted isotropically but diffuse reflection on the backside of the crystal and total reflection on the front broaden the light distribution. This has also been taken into account for the simulation in figure 3.2. The resulting light distribution is well described by a single Gaussian. The width is strongly dependent on the optical coupling of the photomultiplier tubes to the scintillator. When an air gap between the PMTs and the crystal is taken into account according to the operation manual of the Anger cameras the width of the distribution is about the same as the diameter of the photomultiplier tube. Therefore, two aspects have to be considered: the error of the signal amplitude of each photomultiplier due to photon counting statistics and the systematic error due to the finite size of the multiplier which both factor into the accuracy of the position reconstruction. As stated above the position x of the registered event is determined by the center of gravity of the individual photomultiplier signals

$$x = \frac{\sum_i x_i f(x_i)}{\sum_i f(x_i)} \quad (3.2)$$

from the position of the photomultiplier tubes x_i and the amplitude of the light signal $f(x_i)$. The statistical error of the center of gravity is therefore given by:

$$\Delta x_{\text{stat}} = \sqrt{\sum_i \left(\frac{\partial x}{\partial f(x_i)} \Delta f(x_i) \right)^2} \quad (3.3)$$

$$\frac{\partial x}{\partial f(x_i)} = \frac{x_i \sum_i f(x_i) - \sum_i x_i f(x_i)}{(\sum_i f(x_i))^2}. \quad (3.4)$$

The systematic error originates from the non-uniform light distribution. For the electronic determination of the total center of gravity it is assumed that the light distribution over the photomultiplier tube is uniform. But in reality this is not the case. Therefore the positions x_i of the photomultiplier tubes do not coincide with the center of gravity of the light signal for each photomultiplier. This is illustrated in figure 3.3. The non-uniform light distribution leads to a deviation of the assumed position x_i from the actual center of gravity. For a reasonable number of PMTs and a realistic light distribution this error is maximal when the events occurs directly between two photomultiplier tubes.

Hence, both the statistical error as well as the systematic error depend on the position of the event, the size and spacing of the photomultiplier tubes and on the form of the light distribution. Since the errors can hardly be treated analytically they are estimated by a numerical simulation of the problem. The total photon count in the light distribution is assumed as Gaussian with a fixed integral of 19400 photons and the spacing of the photomultiplier tubes is set to zero. Then the statistical error and the systematic error are calculated for different diameters of the photomultiplier tubes. The width of the tubes (further referenced to as binwidth) is thereby expressed in relative units of the width of the light signal distribution σ . The calculated error budget is shown in figure 3.4 a). The statistical error increases as the binwidth decreases due to the limited number of registered photons while at the same time the systematic error decreases due to the fact that the distribution of the light across one bin becomes more and more uniform. Therefore, a pronounced minimum is found in the total error budget shown in figure 3.4 a). To achieve the best spatial resolution an optimal detector based on the center of gravity method should therefore feature a discretisation pattern of about half the width of the light distribution. This is however not the case for the Anger cameras which have a binwidth of about 1σ . The

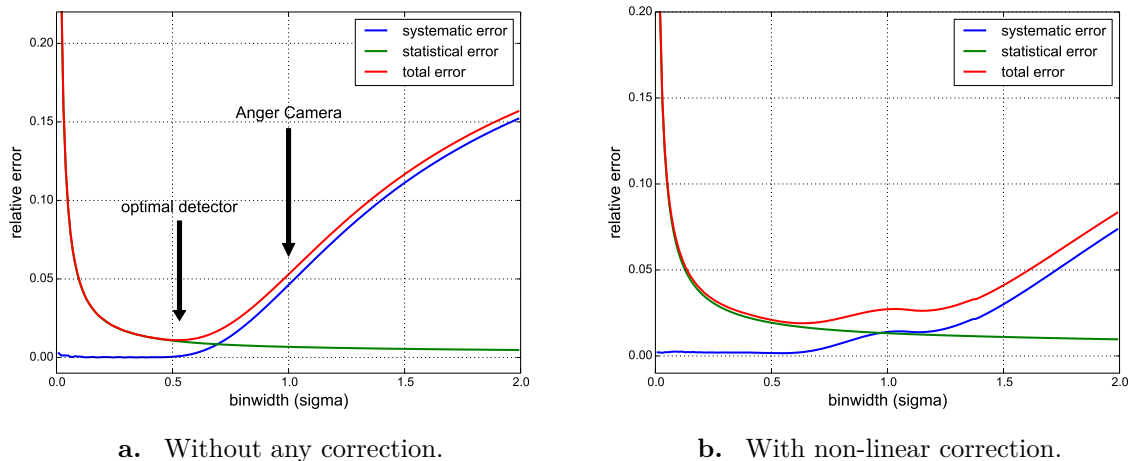


Figure 3.4.: Illustration of the effect of non-linear position correction. Statistical and systematic error as a function of the width of bin. The binwidth is given in relative units in terms of the width σ of the light distribution, e.g. a binwidth of 1 means that 66% of the total light is collected in one bin if the event takes place in the center of a bin.

reason for that is assumed to be mostly of technical and monetary nature as for the same active area a much larger number of photomultiplier tubes and electronics would be necessary.

However, these shortcomings can be partially eluded when a non-linear amplification of the light signal is used. This means, before the center of gravity is determined the individual signals from the tubes $f(x_i)$ are treated by a non-linear amplification function $g(f(x_i))$. Different forms for g are shown in figure 3.5 a). The effect of non-linear amplification on the shape of the registered light distribution is shown in figure 3.5 b). It results in a broadening of the distribution function associated with a decrease of the systematic error due to the non-uniformity of the light distribution as shown in figure 3.4 b).

For this study a non-linear amplification $g(x) = \sqrt{x}$ is assumed but it was found that the exact form of the non-linear amplification is not very important to achieve the desired effect. Using this amplification function it was found that the total error in the position reconstruction could be decreased by a factor of 1.9 (as can be seen in figure 3.4 b)). Within the electronics of the Anger camera the non-linear amplification is realised by a piecewise linear amplification (as shown in figure 3.5 a)).

In these considerations a linear chain of photomultiplier tube was assumed. The effect for the realistic case of of a two-dimensional hexagonal matrix is studies in figure 3.6. Events were distributed along a regular pattern over the photomultiplier matrix and the position were determined according to equation 3.2. As can be seen in figure 3.6 b) the reconstructed position are dragged towards the centers of the photomultiplier tubes. By using the non-linear amplification for the diameter (2.5 in) and the spacing (7 mm) of the photomultiplier tubes the obtained positions now resemble the initial pattern only with minimal distortions. The compensation of the systematic distortions of the obtained positions is crucial. The error due the discretisation of the light signal amounts to $\Delta x_{sys} = 2.4$ mm and $\Delta x_{stat} = 0.3$ mm resulting in a total error of $\Delta x_{dis} = 2.5$ mm. In combination with the physical limitations of the γ -interaction the total resolution of the Anger camera is limited to $\Delta x_{tot} = \Delta x_{dis} + \Delta x_{phys} = 3.1$ mm.

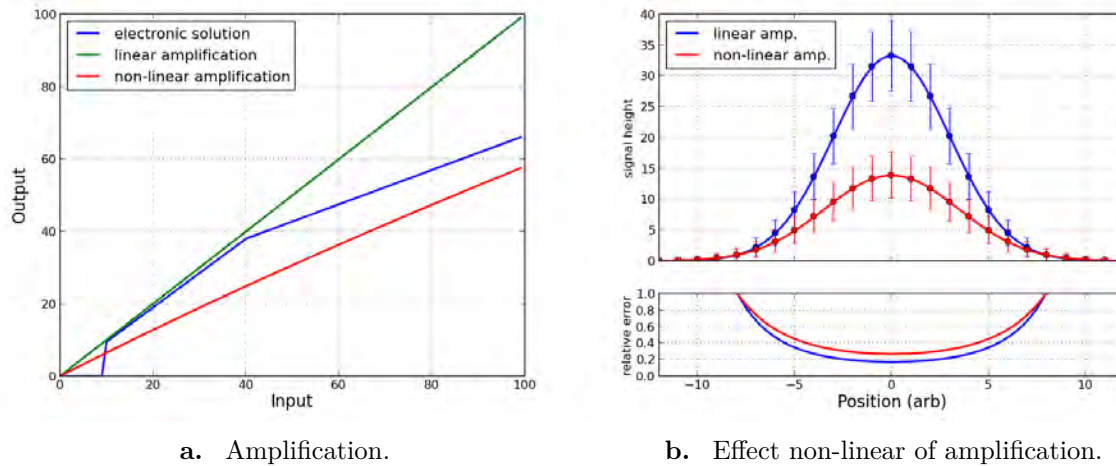


Figure 3.5.: a): Different amplification functions: linear (green), piece-wise linear (blue) and $\propto \sqrt{x}$ (red). b) The effect of non-linear amplification on the shape of the light distribution. A non-linear amplification function broadens the distribution at the expense of statistical precision (lower plot).

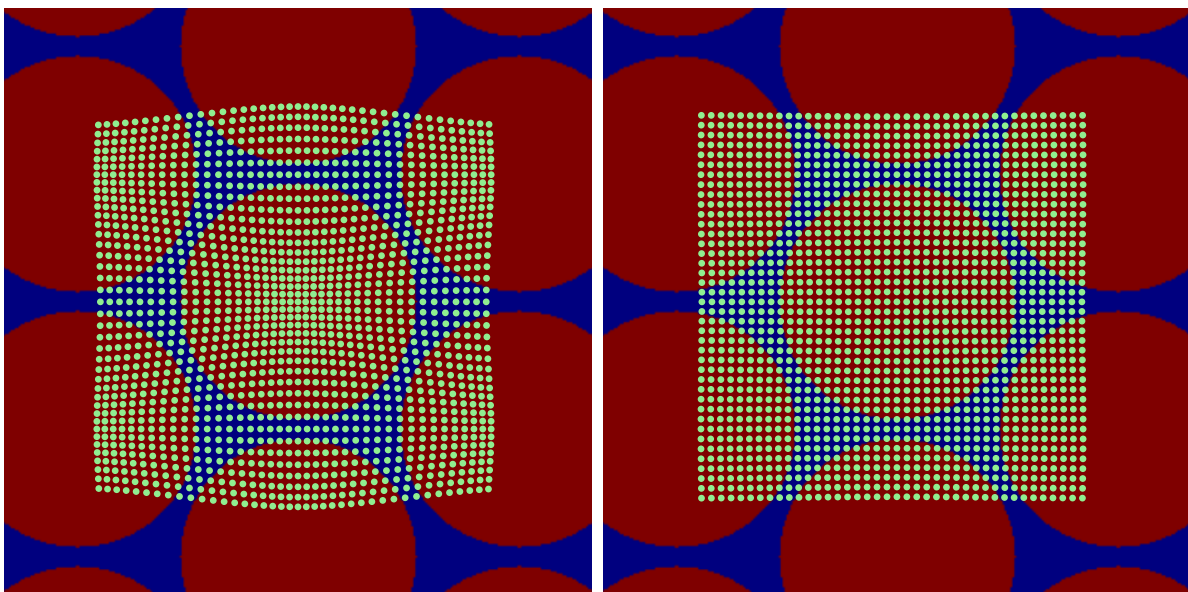


Figure 3.6.: Illustration of the effect of non-linear position correction. The positions are determined by the center of gravity in the x- and y-projections. The reconstructed positions are dragged towards the center of a PMTs (red) the gaps (blue) between the PMTs are chosen similar to the real setup of the Anger camera.

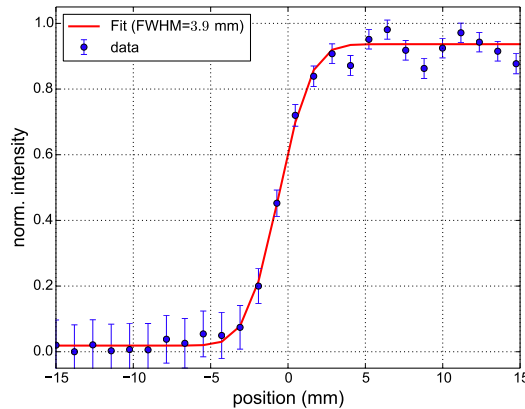


Figure 3.7.: Cut through the detector image with parts of the detector covered by a 10 mm thick $W_{80}Cu_{20}$ absorber. The resulting edge in the detector image is fitted by an error function. A value of 3.9 mm (FWHM) is found to describe the data best which is slightly bigger than the value given by the manufacturer for the spatial resolution of 3.5 mm (FWHM).

This approximation is found to be in satisfactory agreement with the experimental value $\Delta x_{exp} = 3.9$ mm that was determined by covering parts of the detector with tungsten bricks and fitting the recovered edge in the resulting detector image with an error function (see figure 3.7). The result also indicates that there is room for improvement which motivated a detailed experimental study of the Anger camera resolution.

To study the detector resolution in more detail the entire detector was illuminated through a steel grid with holes in a hexagonal pattern. The thickness of the absorber was 8 mm, which amounts to an absorption of 41 % of the 511 keV radiation, the diameter of the holes was 3 mm and the spacing of the holes was 5 mm. A partial image of the resulting detector image is shown in figure 3.8 corrected for low and high frequency noise by convolution of the grid with the difference of two Gaussians to enhance the structure of the grid. This width of the narrow Gaussian is chosen smaller than the hole size to smooth out statical variations from pixel to pixel. The width of the broader Gaussian is chosen accordingly larger than the hole size to compensate variations on larger scales than the grid structure. The positions of the holes are then fitted in the detector image by a two-dimensional Gaussian. It is found that the recovered positions do not follow the hexagonal pattern of the mask (as indicated in figure 3.8 b)). The length scale of these distortions is found to be in the same range as the detector resolution and gives therefore rise to a systematic error for the position reconstruction.

An elegant and computational efficient method to correct these distortions on an event by event basis was developed by Leitner [LCW12] based on the data of this study. From the knowledge of the actual hole pattern a look-up table is calculated in order to correct the measured positions. For this it is necessary that the data is available (in the form of a list of events) for each detector since for the histogrammed ACAR spectrum the event positions from both detectors are required. The problem of finding the distortion vector field was solved by Leitner by formulating a minimisation problem with a regularisation functional. The minimisation problem consists in finding a field f that translates the positions of the hexagonal pattern x to the obtained positions y which are only known to certain accuracy Δy so that the condition

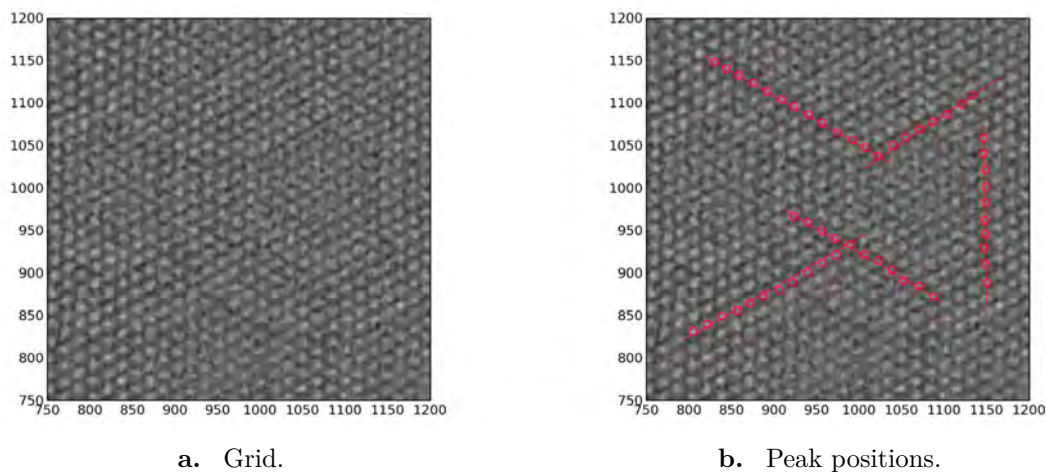


Figure 3.8.: Sections of the detector image when the detector is illuminated through a steel grid. a) Detector image corrected for high and low-frequency noise. b) Expected positions of the holes (red) imaged onto the detector. Small scale distortions can be observed.

$(f(x) - y)^2 / \Delta y^2 = \min$ is fulfilled. An additional regularisation functional, which can be thought of as the potential energy of springs connecting the nearest neighbours, punishes strong deviations from the hexagonal pattern and ensured that the resulting field is smooth (for details see [LCW12]). In order to obtain the undistorted image x the inverse function of $f(x)$ has to be calculated, however the distortion field is only known on the positions of the hexagonal grid which makes an interpolation between the grid points necessary. To avoid the Moiré-effect and to preserve the poisson nature of the data a random number smaller than the bin size used for the histogramming is added to the corrected positions. By use of this method the small scale distortions in the detector image can be corrected. A comparison of the corrected and the uncorrected image is shown in figure 3.9. Leitner et al. [LCW12] also showed that by correcting this distortions the contribution of the detector resolution in an 2D-ACAR measurement could be improved by a factor of 1.7. A detailed discussion on this is given section 3.2.

3.1.3. Data acquisition

In this section the readout of the detectors is discussed. During this thesis the electronic readout of the detectors was fundamentally renewed and improved by Weber [Web15] in his thesis. Details of the complete digital readout and the specifications of the electronics and software are found in the thesis of Weber. However, the principle of the readout will be discussed here and the focus is put on the unchanged parts of the detector electronics. Each detector features a hexagonal matrix of 61 photomultiplier tubes. Each tube is fitted with a charge sensitive pre-amplifier. The coarse gain of these pre-amplifiers is adjusted by the a reference voltage from the MIAMI-board while the integral gain of the detector can be adjusted by a careful variation of the high-voltage that supplies all photomultiplier tubes. The signal from the pre-amplifiers can be checked with an oscilloscope at a test pin on the boards. These signals are individually fed to the so-called PIG-boards that are located on the MIAMI-board. The non-linear amplification of the signal discussed in the previous section occurs at this next step. From the pre-amplifier four signals x_1, x_2, y_1, y_2 are created in the PIG-boards. The x_1 and y_1 signal are subjected to a

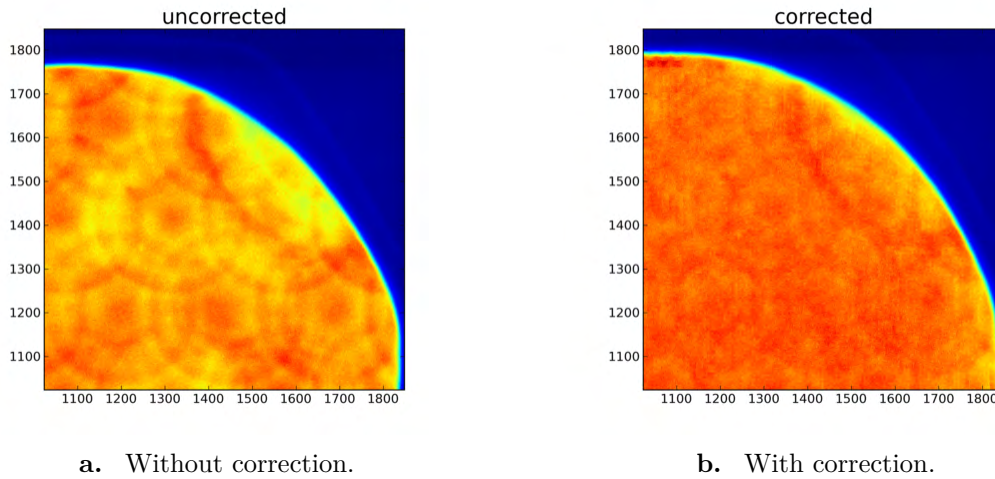


Figure 3.9.: Effect of the correction on the obtained detector image. The corrected image appears smoother and the distortion of the edge are compensated.

non-linear amplification. All x_1 from the same row and all y_1 signals from the same column are fed to high impedance summing amplifiers. The signals from these summing amplifiers are fed to a weighting resistor network with the values of the resistors increasing linear along the rows and columns respectively. The output of the resistor network is then once more integrated by a summing amplifier. A line driver produces the resulting Gaussian shaped weighted x and y signals.

The x_2 and y_2 signals are also summed up in rows and columns but the summed signals are fed to resistor network with equal weighting. The integrated and weighted column and row signals are then also summed up and a line driver produces the resulting Gaussian shaped z signal. The z signal corresponds to the total energy of the event that has been registered by the camera. Therefore, according to equation 3.2 the x and y signal have to be divided by the z signal to to give a value that corresponds to the position of the event on the detector. In the setup that was obtained from the Bristol group this division was done electronically on the so called CANARD-board. Owed to the work of Weber this in not necessary any more. The x, y and z signals from both detectors are connected to a 8-channel 16 bit sampling analogue digital converter (Struck-SIS3302) that is connected to the PC via a optic glass fiber interface. Due to the sampling nature of the ADC the entire Gaussian signals are recorded and the digital value corresponding to the area under the pulse is stored in a digital memory. The advantage compared to a pulse-height-analysis lies in the fact that the area can be determined with higher statistical precision. The digital setup allows for the pile-up rejection and coincidence search in the signals from both detectors and the correction of the x and y signals for the z signal to be carried out online. The singles as well as the coincident events are stored on the hard drive in the form of binary list mode data. The single events are saved with a 64 bit time-stamp from the ADC clock followed by two 32 bit numbers corresponding to the actual x and y positions on the detector and a 32 bit numbers corresponding to the energy of the event (z signal). The coincident events are stored in the form of six 32 bit numbers corresponding to the actual x and y position, the energy of detector one and the actual x and y position and the energy of detector two. The form of these data allows to determine the energy windows for the 511 keV

events in the offline analysis.

3.1.4. Data treatment

In this section the treatment of the data prior to the analysis is discussed. The data is available in the form of lists for the single events on each detector and for the coincident events. The single events are necessary to determine the so-called momentum sampling function that is used to correct the ACAR data for the angle dependent detection efficiency. The coincident events are of course used to calculate the ACAR spectrum.

Data preparation

Here the recipe for preparing the data for a later analysis is given:

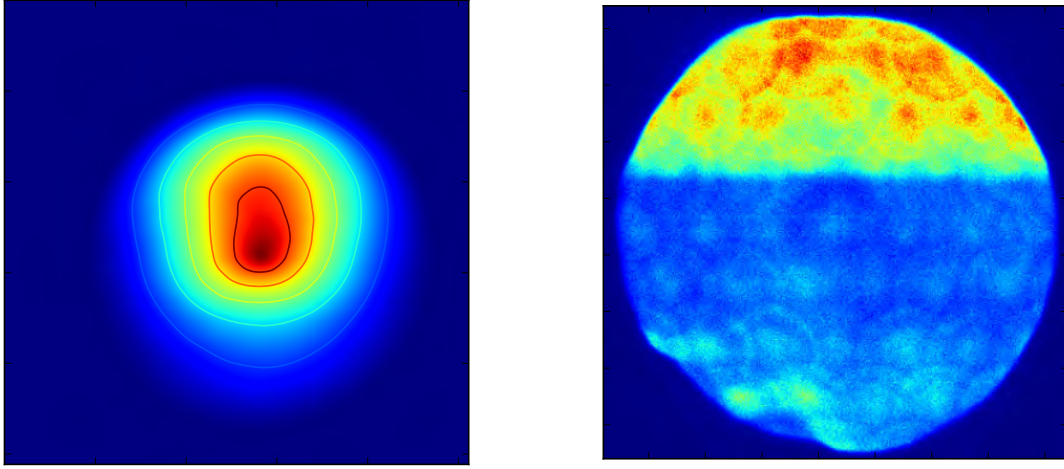
- First, the data is corrected for the spatial distortions using the software package developed by Leitner [LCW12]. The correction software is implemented in the form of a filter so it can be applied directly to the list mode data preserving the list character.
- Second, the position of the energy windows for 511 keV photo peaks are determined from the energy spectra for each detector. This can either be done for the single events or the coincident data.
- Third, these energy windows are used as a filter to find the true events when the data is histogrammed. The histogramming of the singles is straight forward. The ACAR spectrum is calculated from the coincident data according to equations 2.20. Therefore, the size of the two-dimensional histogram for the ACAR data is twice that of the single data.
- Fourth, the ACAR spectrum is corrected for the momentum sampling function that is given by the convolution of the two single spectra. One spectrum has to be flipped on the vertical axis to account for the fact that the detectors are facing each other. Details on the momentum sampling function are discussed below.

Correction for the momentum sampling function

The momentum sampling function describes the detection efficiency for a certain angle in the ACAR spectrum. It is given by the number of positions or pixels on each detector that can be connected under a given angle with respect to the sample position. With the position dependent detection efficiency $\epsilon_1(x_1)$ and $\epsilon_2(x_2)$ of the detectors. The probability of detecting a coincident event with the angular correlation $\theta = x_2 - x_1$ given in the small-angle approximation (without loss of generality x_1 and x_2 are taken in units of the sample detector distance) is found to be

$$P(\theta) = \int \epsilon_1(x_1) \cdot \epsilon_2(\theta - x_1) dx_1. \quad (3.5)$$

Hence, the momentum sampling function is given by the convolution of the two individual detector efficiencies. In the experiment the detector efficiency is given by the geometry (active area), the local detection efficiency and the illumination, i.e. the homogeneity, of the detector image, which is in fact inhomogeneous due to absorption in the sample. It can be easily determined as the normalized single spectra resemble exactly this quantity. The momentum



a. Momentum sampling function.

b. Single detector image.

Figure 3.10.: a) The momentum sampling function obtained for a measurement of tungsten. The asymmetry is due to the absorption inside the tungsten sample. b) One of the single detector images used in the calculation of the momentum sampling function in 3.10 a). The low count rate in the lower half of the detector is due to absorption in the tungsten sample.

sampling function can therefore be acquired by the two-dimensional convolution of the two single camera images $\epsilon_1(\theta_x, \theta_y)$ and $\epsilon_2(\theta_x, \theta_y)$:

$$MSF(\theta_x, \theta_y) = \int \int \epsilon_1(\theta_x - \theta'_x, \theta_y - \theta'_y) \cdot \epsilon_2(\theta'_x, \theta'_y) d\theta'_x d\theta'_y \quad (3.6)$$

The correction of the ACAR spectrum for the momentum sampling is then done by dividing the ACAR spectrum $N(\theta_x, \theta_y)$ by the MSF. An extreme example for a measurement of a tungsten sample is shown in figure 3.10. The momentum sampling function allows for the correction of the partial shadowing of the detector. However, it can not account for the distortions discussed in section 3.1.2.

Adjustment of the photomultiplier gain

The fine gain of the PMTs is set by face-side ten-turn potentiometer on the pre-amplifier boards. An adjustment of the fine gain is usually necessary about once per year in order to ensure a mostly homogeneous detector image. In order to adjust the fine gain all pre-amplifiers are switched off by DIL-switches on the MIAMI-board except for the one to be adjusted. The position compensation (non-linear amplification) is also turned off also by a DIL-switch on the MIAMI-board. Then a ^{22}Na point source is placed directly in front of the active PMT and the resulting energy spectrum is recorded from the energy signal output of the detector. For this it was found that no benefit was achieved by a simultaneous illumination of the entire detector by the ^{22}Na source of the ACAR spectrometer. The fine gain is adjusted in a way that the photo-peak appears at the same position for all photomultiplier tubes. This is done by choosing

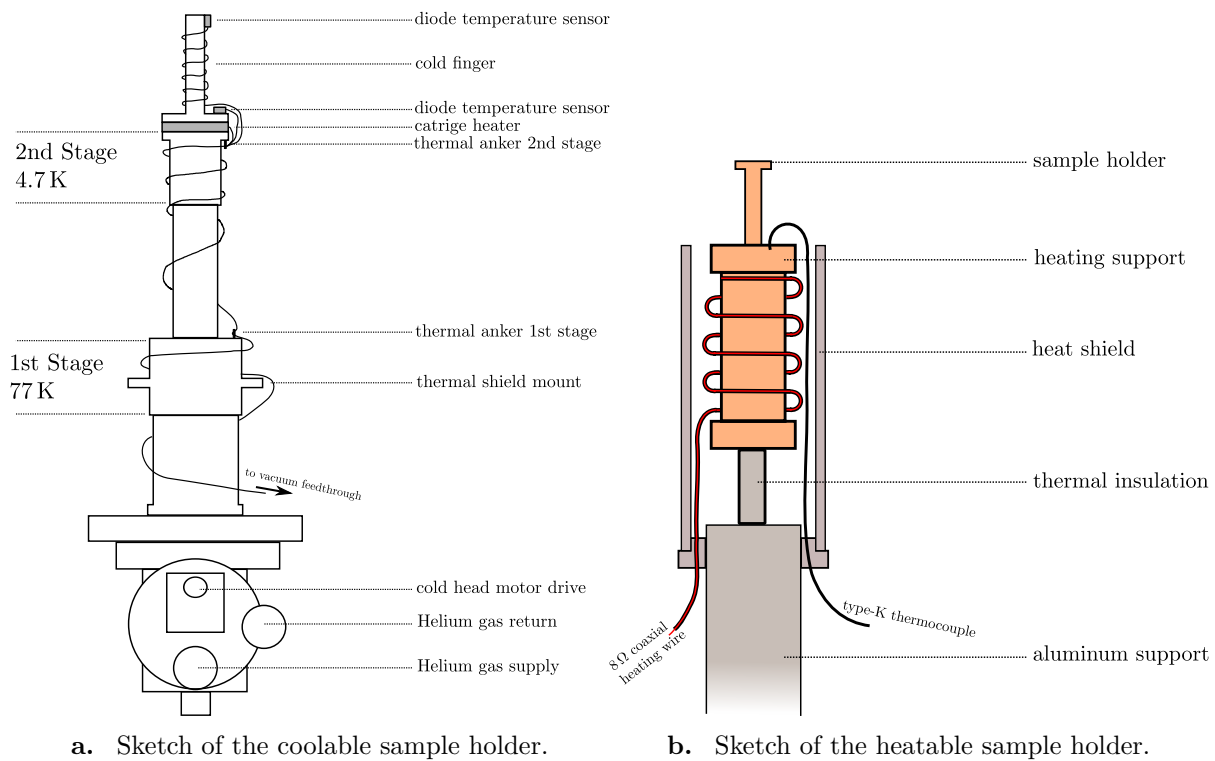


Figure 3.11.: Schematics of the different sample holders.

one reference tube from the center of the camera. This is a tedious work that requires two persons to be carried out efficiently. Special care has to be taken when the gain of the tubes at the corners and edges is adjusted. In order to do so the ^{22}Na source is mounted on a thin metal sheet and carefully moved under the lead ring that covers the the outer part of the detector. Since at these positions usually no clear photo-peak can be observed in the energy signal. So the high energy edge of the obscured photo-peak is used to adjust the gain. Afterwards all pre-amplifiers and the position compensation are switched back on.

3.1.5. Sample environment

Within this thesis a closed-cycle cryostat was purchased and a sample mount was constructed. Furthermore, a alternative heatable sample holder was constructed for measurements at elevated temperatures so that the 2D-ACAR spectrometer features two interchangeable sample holders, for both heating and cooling the sample. Temperatures between 10 K and 650 K can be achieved depending on the sample and hence enable the study of temperature driven effects on the electronic structure.

The sample holder can be cooled by a closed-cycle cryostat (SUMITOMO RDK-415D) with an extended 22 cm long copper cold finger. The temperature is controlled with a PID-controller via two 50 Ω cartridge heaters and a Si diode which are directly coupled to the second stage of the cryostat. Since the temperature at the sample position is slightly different, the sample temperature is separately monitored with an additional temperature sensor which is mounted close to the sample. The wirings for the heating and the temperature measurement are thermally anchored on the first stage of the cryocooler to minimize the external heat flux to the sample.

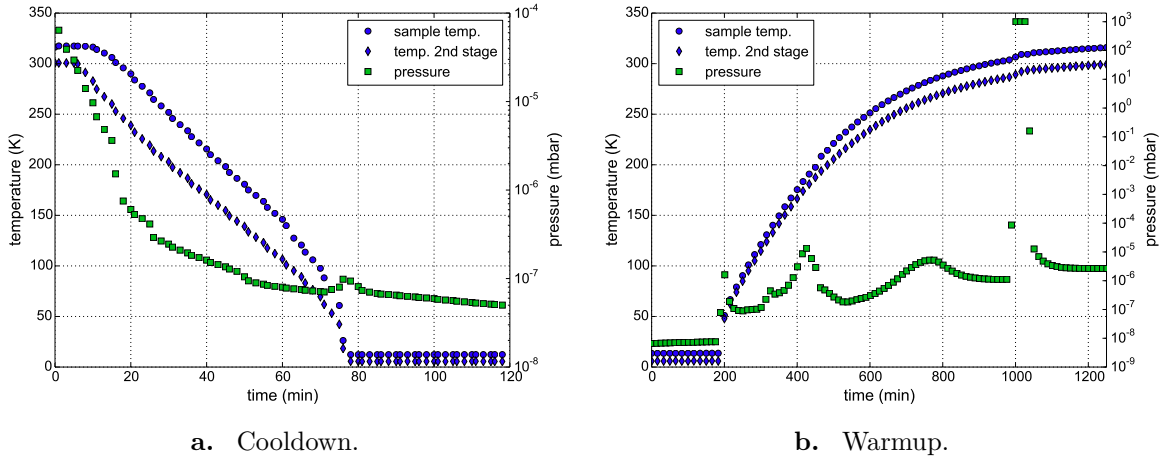


Figure 3.12.: a) Temperature of the sample and at the control point plotted versus time together with the residual pressure in the experimental chamber during the cooldown process and during the warmup process b).

The heatable sample holder is composed of a heating filament in form of a $8\ \Omega$ coaxial heating wire, which is coiled on a copper spindle in order to increase the thermal inertia of the system. The temperature is measured with a standard K-type thermo couple that is fastened to the copper rod close to the sample and controlled with a standard PI-temperature-controller. To minimize the necessary heating power the heater block is decoupled from the vacuum chamber by stainless steel fittings with low thermal conductivity and insulated to the environment by an aluminium heat shield. Sketches of the two sample holder are shown in figure 3.11.

The performance of the coolable sample holder is illustrated in figure 3.12. The cooldown from ambient temperature to about 10 K at the second stage takes about 70 minutes. The offset of about 5 K in the measured temperatures at the second stage of the cryocooler and the sample position is also present at room temperature. It was found that this offset increases over time and was not present when the system was cooled for the first time. This is speculated to be due to radiation damage in the Si-diode due to the irradiation with high energy positrons and γ -radiation from the ^{22}Na source. Therefore the sample temperature is corrected for this offset. As can be seen in figure 3.12 a) the cooling speed increases rapidly below 70 K which is owed to the temperature dependence of the heat capacitance of the copper coldfinger. Also the residual pressure inside the experimental chamber decreases when the cooling is started due to condensation of residual gas on the coldfinger. During the warmup procedure (shown in figure 3.12 b)) the evaporation of atmospheric gases can be observed as peaks in the residual pressure. First argon then nitrogen and oxygen and finally water evaporate from the cold finger. The peak from the water evaporation is strongly pronounced due to the fact that water is pumped very inefficiently by the turbo-molecular pump used in the setup.

3.1.6. Design of the source-sample chamber

The challenges for ACAR lie on the one hand in the maximization of the count rate, and on the other hand in the optimization of the achievable angular resolution, which is given by the spatial resolution of the detectors, their distance, the sample temperature and the positron spot size on

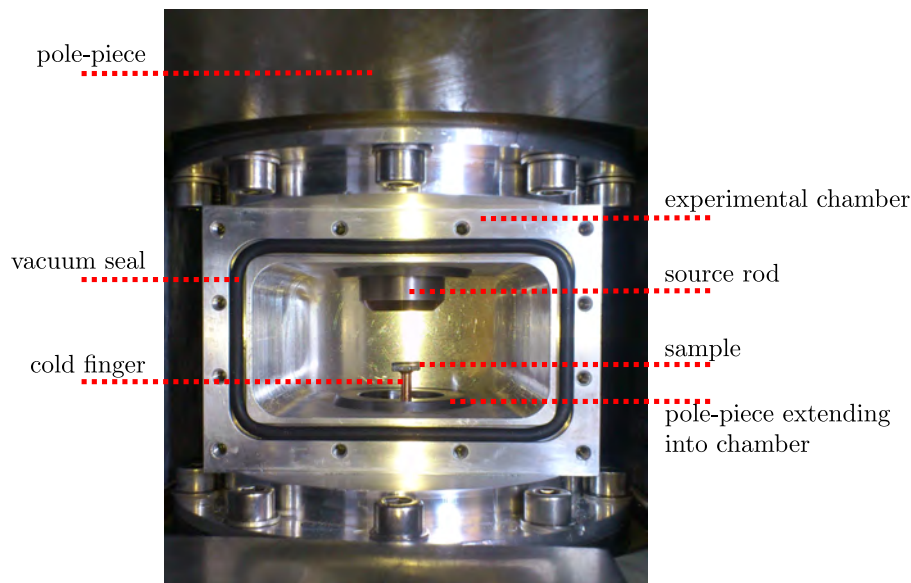


Figure 3.13.: Optical image of the experimental chamber. The tips of the pole-pieces can be seen extending into the chamber. The cold finger mount with sample on top is protruding through the axial bore of the lower pole-piece. The source rod made of elkonite juts through the axial bore of the upper pole-piece. The source rod is fitted with two elastomer caskets to separate the high-vacuum region in the experimental chamber from the fore vacuum section in the source storage.

the sample. In order to improve the resolution the first concern is to minimize the positron spot on the sample. In addition, the sample should be easily accessible, and the spectrometer should enable the study of temperature dependent effects on the electronic structure, such as phase transitions.

All these considerations were taken into account when designing the setup presented in figure 3.1 (B) and (C). The positrons are emitted from a ^{22}Na source deposited on a Ta reflector inside a standard source capsule, which was developed in the positron group of Martin-Luther-Universität in Halle (see figure 2.1). The Ta reflector is used to increase the emission of positrons into the lower half-space.

The source capsule is held inside an $\text{W}_{80}\text{Cu}_{20}$ (elkonite) rod, which is connected to a motorized linear manipulator. The source can be moved into a heavily shielded storage position, for example when the sample is changed. The position of the source capsule and the sample are symmetric with respect to the pole pieces of the electromagnet. The source rod is fitted with two elastomer seals and, when positioned in the measurement position, separates the fore vacuum source storage position from the high-vacuum experimental chamber. This reduces the volume that needs to be pumped by the turbo-molecular pump and allows for lower residual pressures to be reached.

For all considerations presented below a distance between source and sample of 20 mm was chosen (see figure 3.13), as this value turned out to be optimal with regard to the background produced by the source itself and the positron transport from the source to the sample. A larger distance between source and sample would result only in a minor decrease in the background in

the ACAR spectrum, but puts higher requirements to the magnetic guiding field. To produce the guiding field two custom built soft-iron pole pieces are used. The pole pieces have a central bore which allows for the retraction of the source from the sample chamber and for feeding the cold finger of a 4 K closed-cycle cryocooler into the sample chamber. The bore in the base of the lower pole piece is widened so that it can accommodate the heat shield of the cryocooler. The central sample chamber connects the two pole pieces at a fixed distance and also makes them part of the vacuum system. The two pole pieces are therefore an integral part of the sample chamber, which is pumped by a turbo molecular pump from below. This layout frees up space in the central part between the field coils and hence allows the lead shielding to be more compact. The pole piece assembly is placed inside a commercially available electro magnet with a soft iron yoke (GMW model 3473-70). A 5 kW high current power supply ($I_{\max} = 75$ A) is used to generate the magnetic field of up to 1.1 T. The normal conducting copper coils are water cooled. The magnet cooling circuit is separated by the lab cooling water supply for a water-water heat exchanger. This protects the delicate magnet piping from pressure surges of the cooling water supply of the lab and allows to use deionized water in the magnet cooling circuit to protect it from corrosion. The magnet temperature and resistance as well as the cooling water flux are constantly monitored and connected to an interlock system that safely shuts down the magnet in case of for example the loss of cooling water.

The cryocooler is attached to the vacuum system by a motorized differentially pumped rotary platform. This way the orientation of the sample can be changed by $\pm 90^\circ$ with respect to the detector axis without breaking the vacuum or cooling to an accuracy of $\pm 0.1^\circ$. The entire lower section of the spectrometer can be disconnected from the sample chamber and lowered by a hand driven worm gear unit in order to facilitate the change of the sample holder from the coolable option to the heatable.

The annihilation radiation produced in the sample leaves the sample chamber through 1 mm thin aluminium windows. The transmission of these windows is 97.7 % for 511 keV quanta. In order to screen the background contribution in particular the 1275 keV γ -radiation from the source, the sample chamber is enclosed by 25 cm of lead shielding with a 16 mm bore along the line of sight from the sample to the detectors. Hence, apart from the line of sight of the detectors the radiation exposure in the lab is minimized.

3.1.7. Magnetic field configuration

Particular care was taken when designing the pole pieces of the electromagnet. The magnetic field is necessary to transport the positron from the source to the sample otherwise the positron flux on the sample would only be given by the solid angle of the sample as seen by the source. In addition, as mentioned above the positron spot size on the sample also influences the resolution of the ACAR spectrometer.

In the literature [WMW81, BDD⁺82, Kru99, Eck90] several examples of magnet arrangements used for 2D-ACAR spectrometers using ^{22}Na source are found. The apparatus developed by West et al [WMW81] features a normal conduction electromagnet with the source in a fixed pole piece geometry. The source is mounted on the face of one pole piece and the sample is introduced on a coldfinger in radial direction. This makes it difficult to change the sample orientation relative to the detectors without removing the sample from the spectrometer. The setup presented by Kruseman [Kru99] uses also a radial positioning of the sample but the sample holder is fitted with gear drive that allows for the sample orientation to be changed. However, the

positioning accuracy is limited by the complex mechanics. The magnet configuration developed by Eckert [Eck90] is comprised of a split-pair superconducting magnet with an axial bore. Source and sample are positioned asymmetrically inside the magnetic field with a gradient of $\frac{B_{\text{source}}}{B_{\text{sample}}}$ of up to 5 : 1 in order to focus the positrons onto the sample. However, the focus effect is limited by the isotropic emission of the e^+ source. Another apparatus using a superconducting magnet was developed by Bisson et al. [BDD⁺82]. Here the source and the sample are positioned symmetrically at a distance of 5.9 mm through the axial bores inside a cryogenic 2 T magnet. The sample can be cooled via the bath cryostat and the temperature is controlled with an electric heater. The source is mounted at a fixed position inside the magnet and the orientation of the sample can be changed by rotating the sample holder. This symmetrical axial design was partially adopted for the design of the Munich spectrometer. However, as a superconducting split pair magnet was out of the question due to monetary reasons a design based on a normal conducting magnet using soft magnetic pole pieces was devised.

Before designing the pole pieces theoretical calculation of the required field geometry were undertaken. A charged particle like the positron performs a gyration motion due to the Lorentz force when its momentum has a transversal component relative to the magnetic field. The radius of the gyration is given by the strength of the magnetic field B , the positron mass m_e and the transversal component of the positron velocity v_T as

$$r = \frac{m_e v_T}{eB}. \quad (3.7)$$

In figure 3.14 a) the gyration radius is plotted as function of the positron energy for different magnetic fields and in 3.14 b) as function of the field strength for different positron energies (in this case the "transversal" energy). In principle a positron is transported from the source to the sample when the sum of the gyration radius and the radius of the source (2.0 mm) is smaller than the radius of the sample. For a typical sample radius of 2.0 mm a field strength of ≈ 1.2 T is required to transport all positrons from the ^{22}Na spectrum to the sample. This sets the goal for the required field strength.

Also, to ensure a high count rate the magnetic mirror effect due to a gradient in the magnetic field has to be avoided. This effect can be easily derived from the adiabatic invariance of the magnetic flux through the loop of the positron gyration motion

$$\frac{p_{\perp}^2}{B} = \text{const} \quad (3.8)$$

which leads to

$$\frac{v_{\perp}^2}{B(z)} = \frac{v_{0\perp}^2}{B_0} \quad (3.9)$$

and couples the longitudinal and the transversal motion

$$v_{\parallel}^2 = v_0^2 - v_{0\perp}^2 \frac{B(z)}{B_0}. \quad (3.10)$$

Therefore the longitudinal direction will be reversed when the condition

$$\left(\frac{B(z)}{B_0} - 1 \right) > \left(\frac{v_{0\parallel}}{v_{0\perp}} \right)^2 \quad (3.11)$$

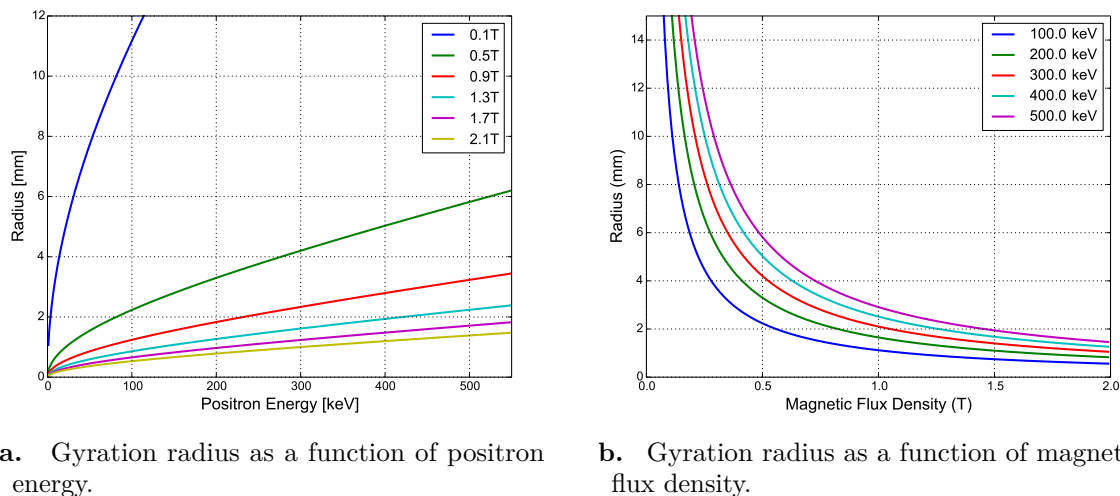


Figure 3.14.: a) Positron gyration radius as a function of positron energy. b) Positron gyration radius as a function of magnetic flux density.

is fulfilled. From this the acceptance angle $\beta = \arctan \frac{v_{0\perp}}{v_{0\parallel}}$, i.e. the emission angle relative to the z -axis, for which positrons are not reflected is determined to

$$\beta = \arctan \frac{1}{\sqrt{\frac{B(z)}{B_0} - 1}}. \quad (3.12)$$

Note that the reflection condition is independent on the particle energy and only depends on the injection angle into the magnetic field. For a homogeneous field the acceptance angle is 90° and for a gradient of $\frac{B(z)}{B_0} = 2$ it is reduced to 45° with an according loss of 50% of positrons emitted into the lower half space. A loss $< 10\%$ corresponding to an acceptance angle of 84° appears acceptable which limits the acceptable gradient in the magnetic field to $\frac{B(z)}{B_0} = 1.01$ and sets the design goal for the inhomogeneity of the magnetic field configuration.

A series of FEM simulations was performed in order to determine layout of the ideal pole piece geometry using the FEM physics simulation toolkit COMSOL [FEM10] before arriving at the final design shown in figure 3.15 a) and in more detail in figure 3.1. Diameter, opening angle and height of the truncated cone shaped pole pieces were optimized in a way that a region with a homogeneous ($< 1\%$ in the direction transverse to the axis between source and sample) flux density is created around the sample and the source (see figure 3.15 a)). The behaviour of the pole piece geometry was tested under realistic conditions in the lab with a 1:7 scale model supporting the results from the FEM simulation.

The simulations and the test measurements revealed that the axial gradient is smaller than $< 1\%$ as desired whereas a radial gradient occurs close to the top of the pole pieces which is due to the central bore in the pole pieces. However, this bore is necessary in order to position the source and the sample. To study the influence of this radial gradient simulations of the positron transport were performed using the results from the FEM simulation. As the positrons are emitted isotropically from the ^{22}Na source with a continuous energy distribution up to the end point energy of 545 keV the entire spectrum and all emission angles have to be considered. The results of this simulation are shown in figure 3.16. The energy spectrum of positrons hitting the

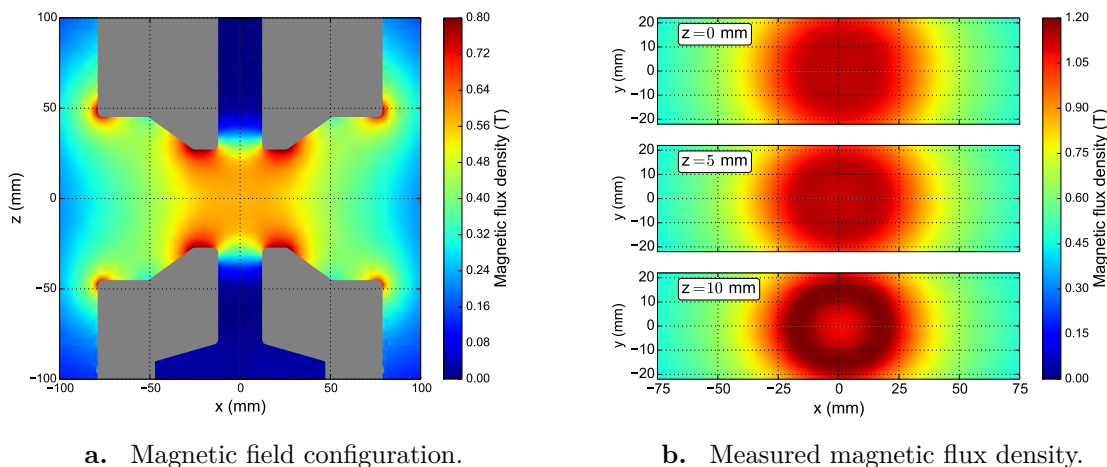


Figure 3.15.: a) FEM Simulation of the magnetic flux density inside the sample chamber. Between the two pole pieces a region with a homogeneous field is created. Sample and source are placed inside this region for optimal positron transport. b) Measured flux density in three planes inside the magnet. The z -position corresponds to the distance to the center of the magnet. The sample is located in the $z = 10$ mm plane.

sample was determined for different nominal magnetic flux densities on the central axis. It was found that for a nominal flux density of 1.0 T almost the complete (98 %) positron spectrum can be mapped onto the sample. For this simulation a source-sample distance of 20 mm, a source diameter of 4 mm and a sample diameter of 10 mm were used. This shows that the magnetic field configuration determined by the pole piece geometry fulfils the design requirements on the basis of the simulations.

The pole pieces were manufactured according to the obtained design parameters from a special sulphur-free magnetic steel (ISO 1.2312). The final magnet assembly of H-frame, pole pieces and coils was rigorously tested in the lab. The field configuration was measured with a Hall probe mounted on a 3-axes stepper motor driven manipulator. In this way, the field throughout the entire sample chamber was mapped out and compared to the FEM simulation shown in figure 3.17 b). Excellent agreement is found concerning the shape of the field distribution. The strength of the magnetic stray field drops rapidly outside the magnetic yoke of the H-frame to values < 1 mT at a distance of more than 40 cm [CWL⁺13].

The field strength was also measured in three planes perpendicular to the z axis: in the plane of the source at $z = 10$ mm, in the central plane of the mirror symmetry at $z = 0$ mm and in between at $z = 5$ mm. The results of these two-dimensional scans are shown in figure 3.15 b) and are found to be in excellent agreement with the simulation shown in figure 3.17 b). The plateau is centred around the sample position and has a diameter (at $1.02 \cdot B_{center}$) of ≈ 20 mm, which is well above the typical sample diameter of 6 – 12 mm. This demonstrated that the design criteria regarding the nominal field strength and the homogeneity have been met. A detailed discussion on the performance under operation conditions of the experiment is given in the next section.

The maximum achievable flux density in the setup is limited by the current through the coils, since the distance of the pole pieces is fixed. Using water cooled copper coils a flux density of

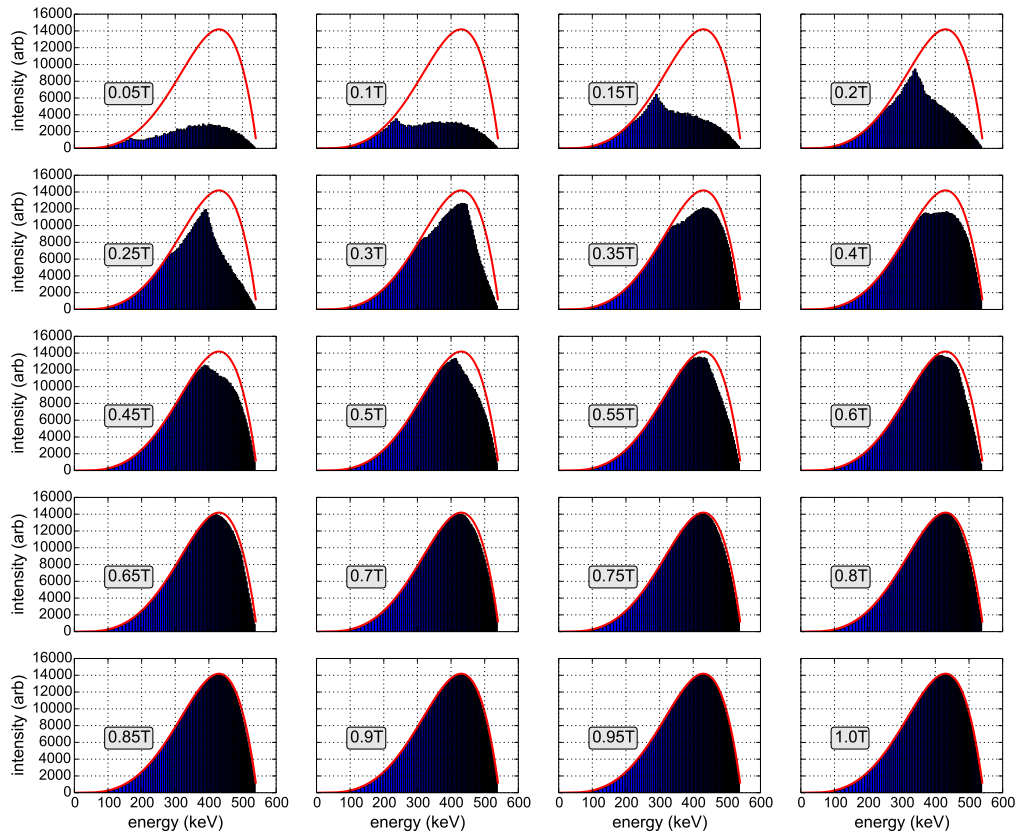


Figure 3.16.: Calculated positron spectrum distribution on the sample, obtained by a Monte-Carlo simulation. For high flux densities almost the full spectrum is mapped onto the sample. The calculations are carried out using the momentum representation $N(p)$ of the positron spectrum, therefore, the binning in the energy representation is not equidistant.

maximal to 1.2 T can be achieved at the central position. However, during routine operation a value of 1.0 T is chosen, as this greatly reduces the heat dissipation in the coils. Also, the soft iron is already beginning to saturate at such high fields (see figure 3.17 a)).

3.2. Performance

As mentioned, a larger distance of the detectors would yield a higher resolution at the expense of count rate. However, the overall performance of a 2D-ACAR spectrometer can be judged by two figures of merit: count rate and resolution. In order to minimize statistical uncertainties, typically 10^8 events are collected in a typical 2D-ACAR spectrum. Therefore, the measurement time is determined by the achieved count rate, which is correlated to the activity of the source and the positron transport efficiency from the source to the sample. The resolution of the spectrometer is, among other contributions, also limited by the spot size on the sample.

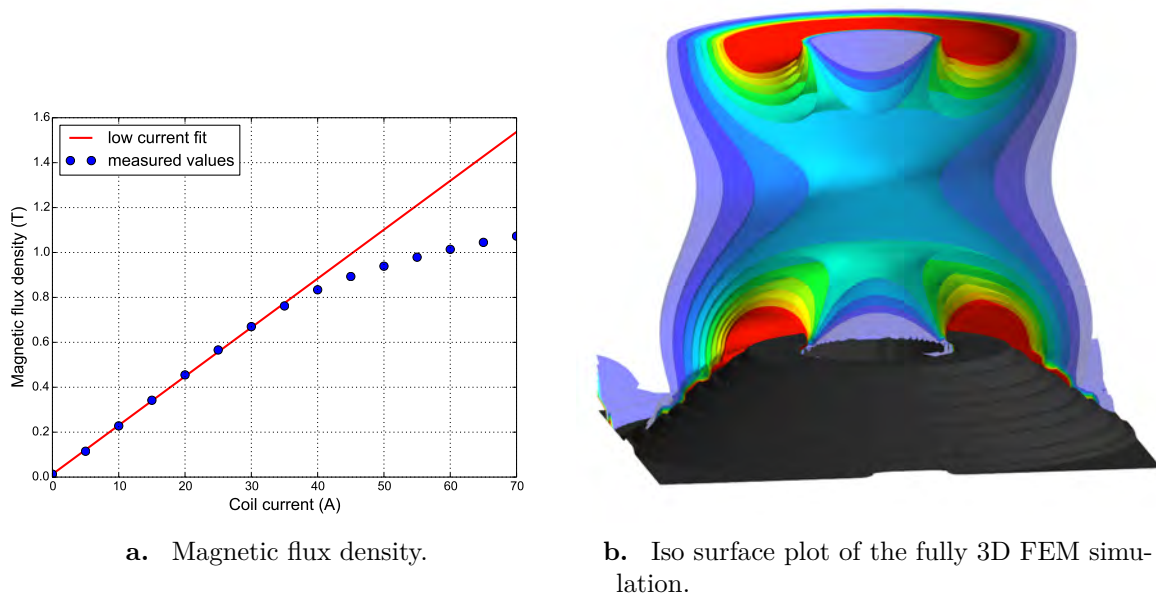


Figure 3.17.: a) Dependence of the magnetic flux density at the sample position on the electric current through the coils. At a current of $I_{\text{coil}} \approx 45$ A the soft iron starts to saturate. b) Three-dimensional representation of the iso-contours of the absolute magnetic flux density. The spacing between the contours is 0.1 T with the central contour at 1.0 T. The lower pole piece is shown as well to illustrate the geometry.

3.2.1. Positron transport efficiency

The coincident count rate C_r in the detectors is given by the source activity A , the branching ratio B_r for β^+ -decay of the source nuclide, the detector efficiencies ϵ_1 and ϵ_2 , the solid angle Ω of the detector with respect to the source, the transmission for 511 keV γ -radiation η and the positron transport efficiency β :

$$C_r = 2 \cdot A \cdot \beta \cdot B_r \cdot \eta^2 \cdot \epsilon_1 \cdot \epsilon_2 \cdot \Omega / 4\pi.$$

The factor of two accounts for the emission of two γ -quanta per annihilation event. The source activity at the time of this study was $A = (1.56 \pm 0.05)$ GBq. The branching ratio for β^+ -decay of ^{22}Na is 90.3% [Fir05]. The positron transport efficiency β accounts for the probability of a positron produced in the source to hit the sample. Also the absorption $1 - \eta = 18.6\%$ of 511 keV quanta in the chamber windows (5 mm in this case) and in the air between the chamber and the detectors has to be taken into account. The individual efficiencies ϵ_1 and ϵ_2 of the detectors can be easily determined by the ratio of the individual single count rates and the coincident count rate. The values are found to be $\epsilon_1 = (7.4 \pm 0.1)\%$ and $\epsilon_2 = (6.6 \pm 0.1)\%$. Finally the solid angle is given by the distance between the detectors and the sample and the active area of the detectors $\Omega = 1.58 \cdot 10^{-4} \cdot 4\pi$. For this estimation the deviation from collinearity of the annihilation quanta is not considered, as only the edge region of the detectors is affected.

For the determination of the count rate a low- Z -material was chosen as target to minimize the effect of positron reflection, in this case a polycrystalline aluminium disc with a diameter of

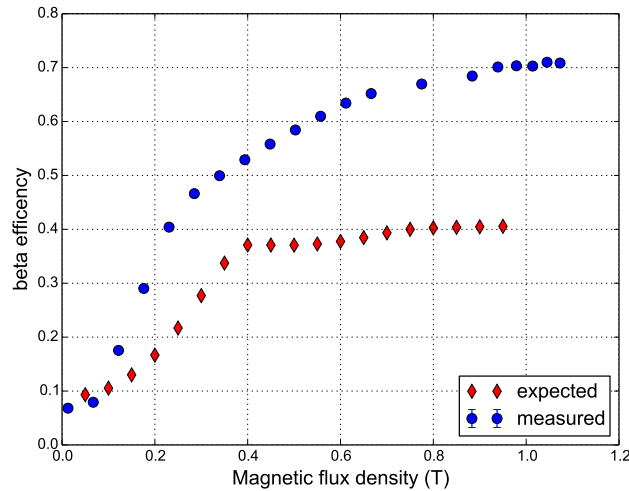


Figure 3.18.: Measured beta efficiency in comparison with the expectation derived from the Monte Carlo simulation. The measured values exceed the expectation indicating that positrons which are emitted into the upper half-space are effectively reflected downwards onto the sample by the Ta reflector.

$d = 10$ mm. With a magnetic flux density of about 1 T a coincident rate of $C_r = 1.0 \cdot 10^3 \text{ s}^{-1}$ was achieved. Therefore, the positron transport efficiency can be calculated to be $\beta = 69\% \pm 4\%$.

This value, meaning that essentially two of three produced positrons hit the sample, appears surprisingly high, as the positron emission from ^{22}Na is isotropic. Only positrons which are emitted into the lower half space can be guided onto the sample, and self absorption inside the source would lead to a reduced positron yield at the sample.

In order to compare the measured positron intensities with calculated ones Monte-Carlo simulations were performed for various magnetic guide fields. The spectra of positrons hitting the sample are shown in figure 3.16 together with the full spectrum from the source.

In figure 3.18 the measured count rate on an aluminium disc with a diameter of $d = 10$ mm is compared with the expected count rate if only emission of positrons into the lower half space is considered. As can be seen, the measured count rate exceeds the expectation for magnetic flux densities higher than 0.1 T. This can be understood in terms of the Ta backening of the source, leading to back reflection of positrons that increases the positron emission into the lower half space.

3.2.2. Determination of the positron spot size

The size of the positron spot on the sample has been measured by moving a guillotine-shaped aluminium target sheet with a thickness of 0.5 mm, which was mounted on a linear translation stage, through the opened sample chamber (see figure 3.19 a)). In this way two orthogonal cuts through the spot profile could be measured simply by flipping the guillotine-shaped target, without having to change the direction of the translation stage [HKR⁺02]. The annihilation radiation of the positron hitting the target was measured with a bismuth-germanate scintillation detector that was collimated to the target. An additional lead collimator was used to block

the radiation from the source. The detector was mounted opposite to the translation stage at a distance of ≈ 1 m to the target. A single channel analyser (ORTEC 551) was used so that only events originating from the 511 keV photo peak are registered. The SCA logic pulses are counted by a standard rate meter read out by a personal computer. The counting time per position 1 mm step was set to 2 s which is sufficient due to the high count rate. By recording the count rate as a function of the target position (see figure 3.19 b)) the beam spot profile can be determined by taking the numerical derivative of the measured integral distribution (see figure 3.19 c)). The measurement was performed for different magnetic fields. The profiles are found to have a shape that can be described by a single Gaussian. An absolute error of ± 0.35 mm is assumed for the limited positioning accuracy of the translation stage corresponding to a translation achieved by 20 steps. This was found to be the typical difference between applied steps and moved steps for moving the stage over the the entire travel range. In combination with the statistical error from the fitting procedure a total error of 0.5 mm appears reasonable. Within the estimated error the values for the FWHM in the two directions are compatible (see figure 3.19 d)). The resulting spot diameter (FWHM) at typical operation conditions (1 T) is found to be (5.4 ± 0.5) mm. Hence, the contribution to the angular resolution in x -direction is given by (0.65 ± 0.06) mrad FWHM for a sample-detector distance of 8.25 m.

3.2.3. Determination of the angular resolution

The ultimate design goal of any spectrometer is that the measurement accuracy or the total error $\Delta_{\text{tot}} = \Delta_{\text{sys}} + \Delta_{\text{stat}}$ of the measurements is dominated by the statistical error and not by the systematic error which has to be carefully assessed. In the case of 2D-ACAR the systematic uncertainty is given by the angular resolution of the spectrometer. It is given by the positron beam spot size, the thermal motion of the positrons and the finite spatial resolution of the detector and the distance between the detectors.

The contribution of the positron spot size can be understood with regard to equation 2.20 if one allows for the annihilation site to differ from $(0|0|0)$ sample position. The y -axis connects the sample and the source and the z -axis connects the sample and the center of the detectors. For a flat sample the positron distribution on the sample is given by the intersection of the emission cone of the positrons with the sample surface plane. By careful alignment of the sample with the sample surface adjusted parallel to the integration direction the positron distribution as seen by the detectors is given by the positron implantation depth along the y -axis and by the projection of the lateral distribution on the x -axis. Therefore, the resolution is always anisotropic. As mentioned the condition is almost completely fulfilled that at the moment of annihilation the positron is in the ground state at $\mathbf{p} = 0$. However, the positron is in thermal equilibrium with the sample which means that that the positron momentum is given by the Maxwell Boltzman distribution:

$$F(\mathbf{p}) = (2\pi m^* k_B T)^{-\frac{3}{2}} \exp^{-\mathbf{p}^2/(2m^* k_B T)} \quad (3.13)$$

with the positron band mass m^* , the temperature T and the Boltzmann constant k_B . The positron band has thereby typical values of $m^* = 1 - 1.6 m_e$ [Kru99]. The contribution of the thermal smearing is then given by the width of the momentum distribution 3.13 to

$$\Delta_{\text{therm}} = 2\sqrt{2 \ln 2 m^* k_B T}. \quad (3.14)$$

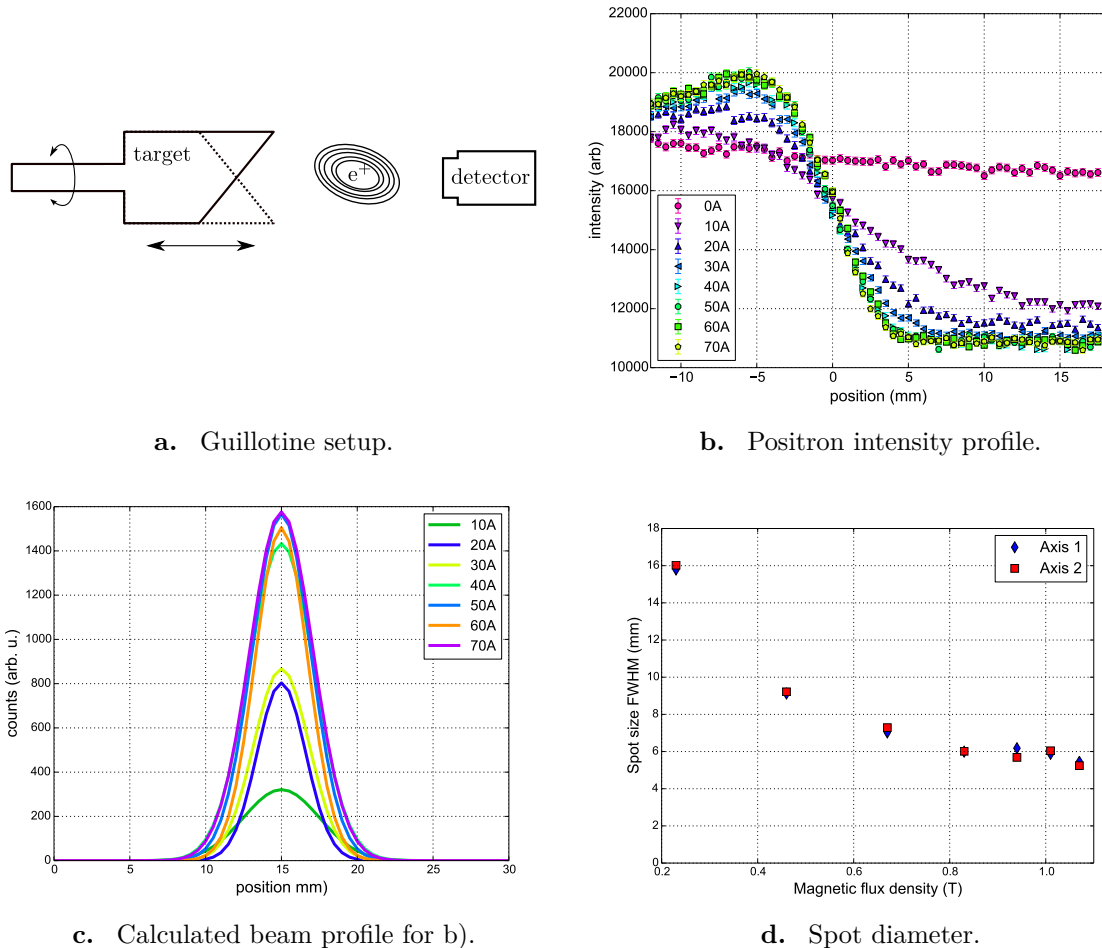


Figure 3.19.: a) Schematics of measurement principle using the the guillotine shaped target. b) Measured profiles of the positron beam at the sample position obtained with guillotine-shaped target that was moved through the experimental chamber for different magnetic flux densities. By flipping the guillotine the intensity profile can be obtained along two independent axis. c) Beam profile along axis 1 obtained by fitting the intensity profiles in b) with an error function. d) Dependence of the spot diameter on the magnetic flux density at the sample position for two arbitrary orthogonal axis.

This results in a value of $\Delta_{\text{therm}} = 0.53$ mrad for $m^* = m_e$ and $T = 300$ K. A further contribution to the angular resolution originates from the limited spatial resolution of the detectors which is discussed in section 3.1.2. The value obtained for the spatial resolution of one detector is $\Delta_x = 3.9$ mm which results in angular resolution of 0.46 mrad. This value has to be multiplied by $\sqrt{2}$ since both detectors factor independently into the ACAR measurement:

$$\Delta_{\text{det}} = \sqrt{2} \frac{3.9 \text{ mm}}{8250 \text{ mm}} = 0.65 \text{ mrad.} \quad (3.15)$$

Since all contributions to the angular resolution (thermal smearing, spot size, detector resolution) are independent, the total angular resolution is given by the sum in quadrature over the individual contributions.

$$\Delta_{\text{sys}} = \sqrt{\Delta_{x,y}^2 + \Delta_{\text{det}}^2 + \Delta_{\text{therm}}^2} \quad (3.16)$$

A way to directly determine the total angular resolution Δ_{sys} is the 2D-ACAR measurement of thermalized para positronium [WMW81, DWM91, BHM77]. The angular correlation of its annihilation radiation is only influenced by the thermal momentum of the positronium itself [Ika79, KS75]. For this study α -quartz is used as sample material, because it shows significant formation of positronium, which is thermalized inside the crystal lattice. According to the periodicity of the lattice the positronium wave function is therefore represented as a delocalized Bloch-state [GMTB70]. This can be confirmed in the ACAR measurement since in the momentum domain the higher order momentum components are observable at the positions of the reciprocal lattice vectors (see figure 3.20 c)). The thermal motion of the positronium atom inside the material leads to a smearing of the momentum distribution. To assess this effect equation 3.14 can be used by replacing m^* with the positronium band mass. It was found by Ikari et al. [IF79] that the band mass of positronium in α -quartz is about $1.6 \cdot 2m_e$. This results in a value of the contribution from thermal smearing of $\Delta_{\text{therm}}^{\text{Ps}} = 0.95$ mrad.

In the perpendicular cross-sections (shown in figure 3.20 a) and figure 3.20 b)) of the 2D-ACAR spectrum (figure 3.20 c)) two features can be distinguished. The narrow component accounts for the para-positronium signal, while the wide component stems from direct positron annihilation and ortho-positronium pick-off annihilation. A superposition of two Gaussians is used to interpret the data.

The width of the narrow component is determined by the angular resolution, which is different for horizontal (x) and vertical (y) direction, since the spot size only contributes to the resolution broadening in the x -direction (see fig. 3.20 a)). The spot size in x -direction is given by the lateral distribution of the positrons on the sample, while the lateral extension in the y -direction (see fig. 3.20 b)) is determined by the implantation depth of the positrons into the sample, which is of the order of $200 \mu\text{m}$ for quartz and therefore can be safely omitted.

A value of (1.53×1.64) mrad² FWHM was achieved at room temperature. Hence, the contribution of the spot size can be extracted, as it is only present in the horizontal component. By taking the values given in figure 3.20 a) and figure 3.20 b) the contribution of the spot size is estimated to be (0.61 ± 0.13) mrad FWHM, which is within the error compatible with the contribution to the resolution that was inferred from the directly measured spot size presented in the previous section. The error of this approximation stems from the statistical accuracy of the fitting procedure.

By correction the values obtained for positronium for the different mass $m_{\text{Ps}}^* = 3.2m_e$ one obtains for the resolution of the spectrometer a value of (1.19×1.34) mrad² FWHM without the

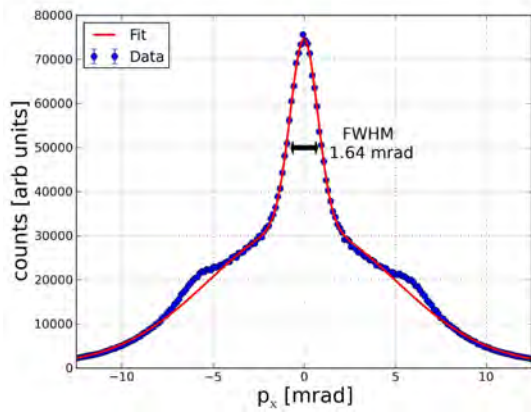
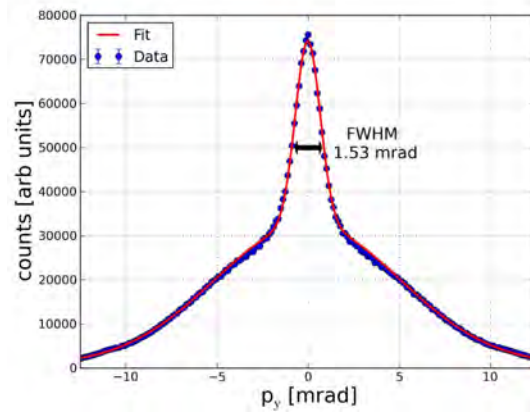
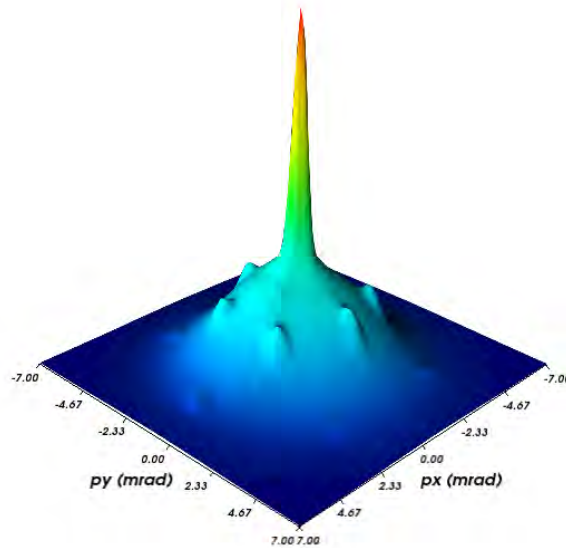
a. Horizontal ($p_y = 0$).b. Vertical cut ($p_x = 0$).c. Surface plot of the 2D-ACAR spectrum for α -quartz.

Figure 3.20.: a) and b) Cuts through the 2D-ACAR spectrum of positron annihilation in single crystalline quartz. c) Surface plot of the 2D-ACAR spectrum single crystalline quartz. The narrow component at $\mathbf{p} = 0$ originates from the self annihilation of para positronium. The higher Umplapp components of the positronium momentum density appear as six-fold symmetric satellite peaks around the central peak.

	$\Delta\Theta_x$ (mrad)	$\Delta\Theta_y$ (mrad)
spacial	1.11	1.11
spot size	0.65	0.0
total (expected)	1.28	1.11
total (measured)	1.34	1.19
positron motion (300 K, $m^* = m_e$)	0.53	0.53
positron motion (10 K, $m^* = m_e$)	0.09	0.09

Table 3.1.: Contribution to the angular resolution.

influence of the positron or positronium motion. This value can be compared to expected value for contributions from the spatial resolution of the detectors and the positron spot size according to equation 3.16. Also, the distortions of the detector image have to be considered (see section 3.1.2). So the contribution of the detectors of 0.65 mrad has to be multiplied by a factor of 1.7 to account for the distortions resulting in a value of $\Delta_{\text{det}} = 1.11$ mrad. Together with the contribution of the positron spot size in x direction this yields value for the expected resolution of (1.11×1.28) mrad². This is in reasonable agreement with the experimental value. As argued by West [WMW81] the slight discrepancy may be due to the fact that the coincident measurement of two photons on the two detectors cannot be considered as two independent measurements and that therefore the factor of $\sqrt{2}$ in equation 3.15 is not justified. However, if a factor of two was considered in 3.15 the resulting value for the spacial resolution would be too high. Another possible explanation could be a slightly different band mass for the positronium. To sum up the resulting contributions to the achieved angular resolution is summarized in table 3.1. The expected resolution is in good agreement with the experimentally observed values which leads to the conclusion that the behaviour of the spectrometer is well understood. When different 2D-ACAR spectrometers are compared in literature usually the values for the para-positronium peak are given as this value resembles a universal standard and a true lower limit for the actual resolution.

In order to improve the resolution the most easy way is to increase the baseline of the detectors at the expense of count rate. The most favourable way is to improve the detector resolution. This may be possible with the Anger cameras by an advanced single multiplier readout used by Morozov et al. [MDE⁺12] or by using a different detector technology like High Density Avalanche Chambers (HIDAC) that are used by the Bristol group [DLU⁺13].

4 Chapter 4.

Determination of the positron polarisation

The polarisation of the positron beam impinging the sample was determined by the magnetic quenching of ortho-positronium in a single crystalline quartz sample. This technique was first used by Nagashima et al. [NCT⁺01] for ACAR and is based in the observation of the magnetic quenching of ortho-positronium in magnetic field in a high pressure argon atmosphere by Obershain et al. [OP62]. The theoretical foundations accordingly have been worked out by Bisi et al. [BFGZ62] and are also presented in this chapter. First the properties and decay modes of free positronium are presented. Then the discussion is extended to positronium in matter and finally the combination of all this is used for the determination of the positron beam polarisation.

4.1. Positronium

Positronium is an exotic hydrogen-like particle consisting of a positron and an electron. It is therefore an ideal model system for theory and attracted much interest from both theoretical and experimental physics. A seminal review on positronium theory was presented by Strocico [Str74] and a detailed review on positronium physics in general and positronium spectroscopy is given by Berko [BP80]. In this section the fundamental properties of positronium are presented to support the discussion of the more complex phenomena of positronium in matter in the following sections.

4.1.1. Properties

One difference to the hydrogen atom lies in the reduced mass of positronium $\mu_{Ps} = \frac{m_e}{2}$ compared to $\mu_H = m_e$ for hydrogen. Therefore, the energy levels of positronium are scaled by a factor of two compared to hydrogen. Also the binding length of the positronium atom is twice that of the hydrogen atom but due to the equal mass the atomic radius is same since the center of gravity is exactly in the middle between electron and positron. A further consequence of the equal mass of positron and electron is that the spin-orbit coupling has about the same strength as the spin-spin coupling. In the hydrogen atom the spin-spin coupling i.e. the hyper-fine interaction is reduced by the mass fraction of electron and proton and by the different gyro-magnetic ratios of electron and proton of $\gamma_e = -2.002$ and $\gamma_p = 5.585$ respectively leading to a factor of about

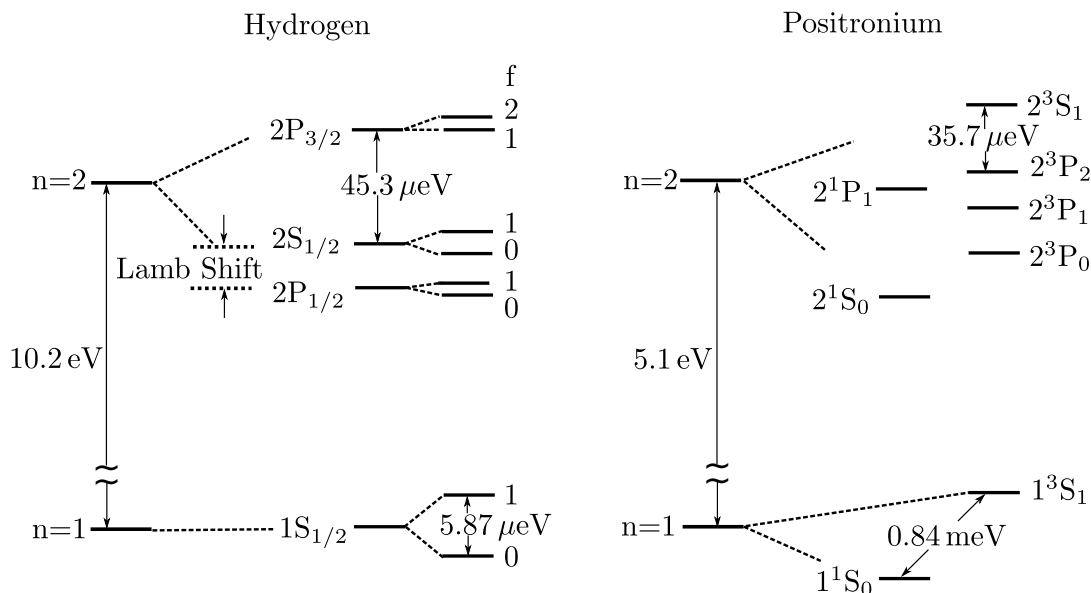


Figure 4.1.: Comparison between the energy levels for the two positronium states: ortho and para-positronium (taken from reference [BP80]).

$(m_e g_e)/(m_p g_p) \approx 1/650$ for the relative strength compared to the positronium atom. Hence the clear hierarchy of the energy levels in the hydrogen atom is not found in the positronium atom. This can be nicely seen in term scheme shown in figure 4.1. In contrast to the hydrogen atom the spectrographic state of the positronium is therefore denoted as $n^{2S+1}l_m$, with the total spin S , the primary quantum number n and the magnetic quantum number m . Two ground states are found for positronium. The singlet state 1^1S_0 is called para-positronium and the triplet state 1^3S_1 is called ortho-positronium. Due to the selection rules for electromagnetic transitions $\Delta l = \pm 1$ the two ground states of positronium can not be translated into each other by an electro-magnetic transition. As the two states do not mix the formation probability from a population of electron and positron with randomly aligned spins is given by the spin multiplicity of the states to $N_{\text{para}}/N_{\text{ortho}} = 1/3$.

4.1.2. Decay modes

The positronium is unstable against the electron positron annihilation via the electro-weak interaction due to the non-zero overlap of the positron and electron wave functions. Ortho- and para-positronium are different eigenstates of the combined charge-parity operator CP and therefore have to annihilate into a different number of photons. For the decay of ortho-positronium an odd number of photons ≥ 3 is necessary to conserve energy, momentum and angular momentum while para-positronium can decay into any even number of photons ≥ 2 so that the conservation laws are preserved in the decay. Due to this fact the life time of free ortho-positronium is longer compared to the para-positronium lifetime since an additional vertex is necessary in the annihilation to couple to the third photon as shown in figure 4.2. This additional vertex is associated with an additional factor of α in the Feynman graph.

The total decay rate λ , which is the inverse of the lifetime, is given according to Fermi's Golden Rule by the number initial and final states and by the transition matrix element. The

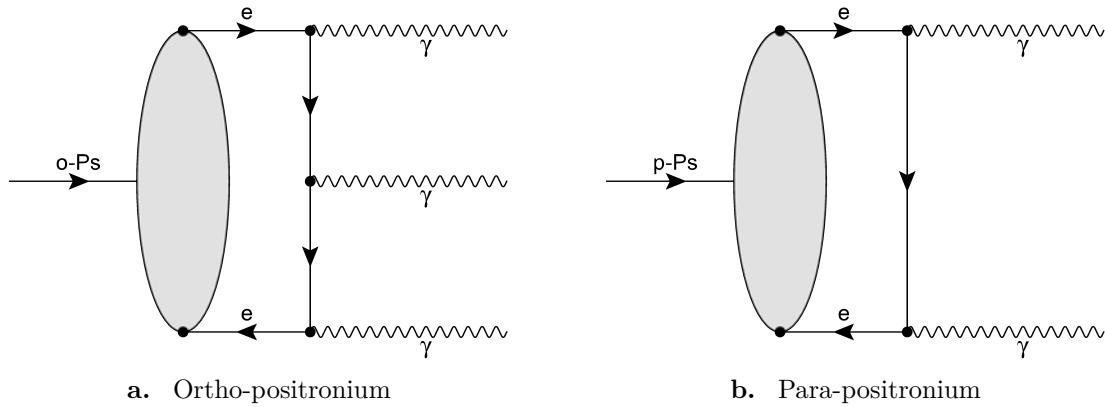


Figure 4.2.: Decay modes of positronium in the lowest order.

matrix element is proportional to the probability of finding both particles at the same position (see [OP49]):

$$|\Psi(r, r)|^2 = \frac{1}{\pi} \left(\frac{\alpha m_e c}{2\hbar} \right)^3 \quad (4.1)$$

Including all higher order corrections the theoretical value for the decay rate of para-positronium (see [CK99]) is found to be

$$\lambda(1^1S_0 \rightarrow \gamma\gamma) = 7989.50(2) \mu\text{s}^{-1} \quad (4.2)$$

which results in a para-positronium lifetime of

$$\tau_{\text{p-Ps}} = 125.164(3) \text{ ps}. \quad (4.3)$$

The calculation of the ortho-positronium decay rate is more complicated, due to the additional vertex in the Feynman graph. A theoretical value including all corrections up to $\mathcal{O}(\alpha^2)$ is given by Adkins et al. [AFS00] to

$$\lambda(1^3S_1 \rightarrow \gamma\gamma\gamma) = 7.03993(1) \mu\text{s}^{-1} \quad (4.4)$$

which results in a ortho-positronium lifetime of

$$\tau_{\text{o-Ps}} = 142.047(1) \text{ ns}. \quad (4.5)$$

Both theoretical values for free positronium are found to be in excellent agreement with the experiment [SAK03, VZG03, ARD94].

4.2. Positronium in matter

For positronium in matter the situation is different to that of free positronium discussed in the previous section. Due to the interaction with the crystal lattice the positronium wave function is modified and due to the presence of electrons in the material the positronium lifetime is reduced by the so-called pick-off process (see figure 4.3). Positronium formation in matter is complex process (a detailed discussion of this effect can be found in [SJ88, BW75, Mog74]) and depends

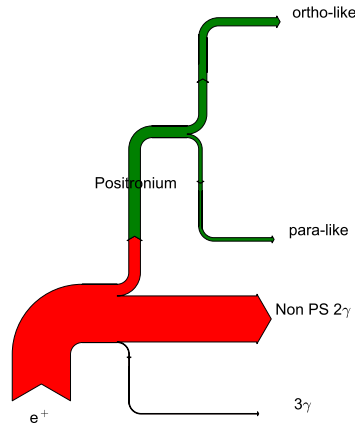


Figure 4.3.: Flowchart illustrating the annihilation channels of a positron in matter. The majority of all positron will undergo two- γ annihilation in the bulk material. In an insulator positronium can be formed in the material. In contrast to free positronium most of the positronium atoms will annihilate under emission of two γ rays either by para-positronium self annihilation or by ortho-positronium pick-off annihilation.

strongly on the electron density in the interstitial volume. Therefore, positronium formation is not observed in metals, since for metals the Wigner Seitz radius, i.e. the radius of a sphere containing one electron at the position of the positron is smaller than the atomic radius of the positronium atom. For insulators the positronium formation is possible inside the crystal lattice if the chemical potential of the electrons is smaller than the binding energy of the positronium atom.

After formation of the positronium atom is thermalized inside the material by inelastic scattering with the atoms. It therefore assumes its ground state in the crystal lattice. The positronium atom is neutral but is easily polarized, hence the interaction potential between the positronium and the crystal atoms can be described by a Yukawa-like potential. Usually this is approximated by a infinite wall potential in order to simplify the calculation of the positronium wave function. For a positronium atom in a spherical well the wave function can be obtained by solving the radial Schrödinger equation [Kru99]

$$\left[\frac{\hbar}{2m} \left(\frac{d}{dr^2} - \frac{l(l+1)}{r^2} \right) + V(r) + E_n \right] \Psi_{Ps} = 0 \quad (4.6)$$

for the energy E_n of the state given by the quantum numbers n and l with the potential

$$V(r) = \begin{cases} 0 & : r < a/2 \\ \infty & : \text{elsewhere} \end{cases} \quad (4.7)$$

for the radius of the potential well $\frac{a}{2}$. The ground state solution for $n = l = 0$

$$\Psi_{Ps} = \frac{1}{\sqrt{4\pi a}} \frac{1}{r} \sin \frac{2\pi r}{a} \cdot \theta\left(\frac{a}{2} - r\right) \quad (4.8)$$

with the heaviside function θ can be used as basis for the solution of a three-dimensional

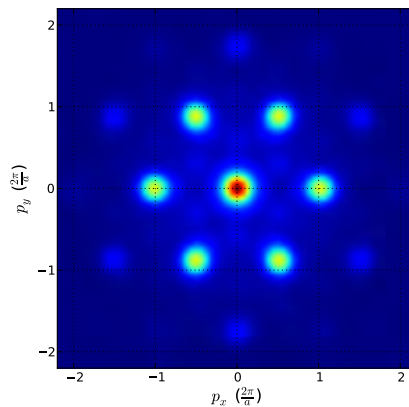


Figure 4.4.: Two-dimensional projection of the positronium momentum density for calculated for hexagonal closed packed array of spherical infinite wall potentials.

hexagonal closed packed arrangement of infinite wall potentials that serves as model for the interstitial volume of a hexagonal lattice. It can be shown that the periodic superposition of the ground state wave function solves the periodic problem by use of the Bloch theorem. The lattice periodic function $\Psi(r) = \Psi(r + a)$ for any lattice vector a given by the Fourier series

$$\Psi(r) = \sum_{\mathbf{G}} C_{\mathbf{G}} \exp^{+i\mathbf{G}r} \quad (4.9)$$

with the coefficients $C_{\mathbf{G}}$ given by the Fourier transform of the wave function over the volume V of the primitive cell

$$C_{\mathbf{G}} = \frac{1}{V} \int_V \Psi(r) \exp^{-i\mathbf{G}r} . \quad (4.10)$$

In principle one has to consider that the periodic wave function does not extend to infinity due to the finite lifetime of the positronium. This can only be accounted for by a more complex time dependent calculation of the transition matrix element. In the static picture it is assumed that the wave function extends only so far that every combination of two points can be connected by a light signal within the lifetime of the para-positronium. The extension of the wave function can hence be approximated by $\frac{1}{2}\tau_{\text{Ps}}c$ which is in the order of centimetres. Therefore, the positronium wave function in the crystal lattice can be safely assumed as a plane wave. The momentum representation of the delocalized positronium wave function inside the periodic potential is then given by the Fourier transform of equation 4.9:

$$\Psi(\mathbf{p}) = \left(\frac{1}{2\pi\hbar} \right)^{\frac{3}{2}} \int \Psi(r) \exp^{-i\mathbf{p}r/\hbar} . \quad (4.11)$$

Then the momentum density is given by

$$N(\mathbf{p}) = \Psi(\mathbf{p})\Psi(\mathbf{p})^* . \quad (4.12)$$

The numerical result for $N(p)$ integrated along one momentum direction (similar to a 2D-ACAR

spectrum) is shown in figure 4.4. In the momentum space representation besides the central peak, which one would obtain when the positronium atom was trapped in a single potential well additional peaks at positions of the reciprocal lattice appear. In the literature these peaks are often referenced as Umklapp or Coussot peaks [BCP69] and are a direct consequence of periodicity of the wave function in real space. The example on a hexagonal lattice was chosen as the interstitial volume of single crystalline quartz resembles this structure. Therefore, self-annihilating para-positronium delocalized in a quartz crystal will exhibit a similar momentum density in the 2D-ACAR experiment. The width of the peaks is determined by the shape of the potential well [Kru99] and by the thermal motion of the positronium. For a well diameter smaller than the lattice spacing the dominating contribution originates from the thermal motion [Kru99]. This discussion applies to ortho- and to para-positronium equally but due to the 3γ self-annihilation of ortho-positronium only para-positronium can be observed in a 2D-ACAR experiment directly. Besides self-annihilation positronium in matter can undergo the so-called pick-off annihilation. In a real crystal the interstitial volume is not bounded by an infinite wall potential. Hence, the positronium wave function will have a non-zero overlap with the electron clouds of the crystal atoms. So the positron is not limited to its binding partner to undergo annihilation. This increases the annihilation rate of ortho-positronium in matter drastically which is described within the Tao-Eldrup [Tao72, ELS81] model as a function of the void radius R :

$$\lambda_R^{\text{matter}} = \frac{(\lambda_{\text{p-Ps}} + 3\lambda_{\text{o-Ps}})}{4} \left[1 - \frac{R}{R + \Delta R} + \frac{1}{2\pi} \sin\left(\frac{2\pi R}{R + \Delta R}\right) \right] \quad (4.13)$$

with the empirically determined parameter $\Delta R = 0.165 \text{ nm}$ and the spin-averaged annihilation rate $\lambda_{\text{p-Ps}} + 3\lambda_{\text{o-Ps}}$. This reduces the lifetime for ortho-positronium in matter to typical values between 0.5 ns and 10 ns [JMS03] and consequently the self-annihilation of ortho-positronium by $\frac{\lambda_{\text{o-Ps}}}{\lambda_R^{\text{matter}}}$. In the annihilation by the pick-off process the branching ratio between 3γ and 2γ can be expected to be the same as for a positron immersed in an electron gas of 1/373. For this reason the pick-off process is observable in 2D-ACAR measurement. The resulting momentum distribution is broader than that for para-positronium self annihilation since the momentum distribution of the electron that participates in the pick-off process is determined by the Fermi distribution and not by the thermal momentum of the positronium atom. Summarizing the most important facts:

- The momentum distribution of self-annihilating para-positronium in matter is determined by the thermal motion of the positronium atom and the lattice effects (as shown in figure 4.4).
- 3γ self-annihilation of ortho-positronium can not be observed in a 2D-ACAR experiment.
- In matter the pick-off annihilation process reduces the ortho-positronium lifetime.
- Pick-off annihilation of ortho-positronium can be observed in a 2D-ACAR experiment and gives rise to a broad component in the momentum distribution.

4.3. Positronium in an external magnetic field

The effect of a magnetic field on the positronium atom was extensively discussed in the seminal work by Major (see reference [C⁺00]). In this section a brief overview is given and the main

focus is put on the discussion of the formation of mixed para-positronium and ortho-positronium states in a magnetic field, which is necessary to the understanding of the magnetic quenching of positronium presented in the next section. For a positronium atom in a magnetic field the free Hamilton operator

$$\hat{H} = \frac{\hat{\mathbf{p}}^2}{m_e} - \frac{\alpha\hbar c}{r} \quad (4.14)$$

is modified by the so-called hyper-fine Hamiltonian (see Major in [C⁺00])

$$\hat{H}_{\text{HF}} = \frac{1}{2}\hbar\gamma_e B_{\text{ext}}\sigma_{e^+}^z - \frac{1}{2}\hbar\gamma_e B_{\text{ext}}\sigma_{e^-}^z + \frac{1}{4}\Delta E_{o-p}\sigma_{e^-}\sigma_{e^+} \quad (4.15)$$

which is used to treat the influence of the external magnetic field B_{ext} as a small perturbation to the Hamilton operator in equation 4.14 with the Pauli spin matrices σ , the gyro-magnetic ratio γ_e and the hyper-fine splitting energy between the ground states of ortho and para-positronium $\Delta E_{o-p} = 0.8412$ meV. In an external magnetic field the eigenstates $|S, m\rangle$ with the total spin quantum number S and the magnetic quantum number m of the perturbed Hamilton operator

$$\hat{H}_{\text{pert.}} = \hat{H} + \hat{H}_{\text{HF}} \quad (4.16)$$

can be found in the base of the unperturbed eigenstates $|\uparrow\downarrow\rangle$ and $|\downarrow\uparrow\rangle$ of the Hamilton operator in equation 4.14. Note, for the unperturbed Hamilton operator the states $|\uparrow\downarrow\rangle$ and $|\downarrow\uparrow\rangle$ are degenerate. For a zero external field the eigenstates of 4.16 are

$$|0, 0\rangle = \frac{1}{\sqrt{2}} (|\uparrow\downarrow\rangle - |\downarrow\uparrow\rangle)$$

for the 1S_0 singlet state of para-positronium and

$$\begin{aligned} |1, 0\rangle &= \frac{1}{\sqrt{2}} (|\uparrow\downarrow\rangle + |\downarrow\uparrow\rangle) \\ |1, 1\rangle &= |\uparrow\uparrow\rangle \\ |1, -1\rangle &= |\downarrow\downarrow\rangle \end{aligned}$$

for the 3S_1 triplet states of ortho-positronium. When the external field is non-zero ($B_{\text{ext}} > 0$) the first two terms in 4.15 have also to be considered. The eigenstates of the full Hamiltonian are then expressed in the product base of the ortho and para-positronium states

$$\begin{aligned} |1\rangle &= \sqrt{\text{sech } \gamma} \left(-\sinh \frac{\gamma}{2} |0, 0\rangle + \cosh \frac{\gamma}{2} |1, 0\rangle \right) \\ |2\rangle &= |1, 1\rangle \\ |3\rangle &= |1, -1\rangle \\ |4\rangle &= \sqrt{\text{sech } \gamma} \left(\cosh \frac{\gamma}{2} |0, 0\rangle + \sinh \frac{\gamma}{2} |1, 0\rangle \right) \end{aligned}$$

with the dimensionless parameter

$$\gamma = \text{arsinh} \left(\frac{2\hbar\gamma_e B_{\text{ext}}}{\Delta E_{o-p}} \right) = \text{arsinh} \left(\frac{B_{\text{ext}}}{\kappa 3.6 \text{ T}} \right)$$

. The so-called electron-positron contact density in the material κ defined as the ratio of the the electron-positron overlap in matter to that of free positronium:

$$\kappa = \frac{|\Psi_e(0)|^2}{|\Psi_e^0(0)|^2}$$

. As can be seen the $m = 0$ states mix in the para-like state $|1\rangle$ and in the ortho-like state $|4\rangle$ dependent on the strength of the external magnetic field. Consequently the ortho-like state can undergo 2γ annihilation when it oscillated into the para state which has a much higher annihilation rate. Therefore, depending on the oscillation amplitude, i.e. the probability of finding ortho-like positronium in the para-positronium state, the annihilation rate of the ortho-like positronium is increased. This effect is called magnetic quenching of ortho-positronium [Mil75] and can be used to determine the polarisation of a positron beam as discussed in the next section.

4.4. Magnetic quenching of ortho-Positronium

For a random orientation of the positron spin the occupation of the positronium states in a magnetic field is equal to $\langle i|i\rangle = \frac{1}{4}$. If one considers now a polarisation P of the positron beam defined as the projections of the positron spins \vec{s}_i on the direction of the magnetic field:

$$P = \frac{1}{N} \sum_k^N \frac{\vec{s}_k \cdot \vec{B}_{\text{ext}}}{|\vec{B}_{\text{ext}}|} \quad (4.17)$$

Mills [Mil75] found that the occupation is given by

$$\begin{aligned} \langle 1|1\rangle &= \frac{1}{8(1+\gamma^2)} \left[(1+\gamma)^2(1-P) + (1-\gamma)^2(1+P) \right] \\ \langle 2|2\rangle &= \frac{1}{4}(1+P) \\ \langle 3|3\rangle &= \frac{1}{4}(1-P) \\ \langle 4|4\rangle &= \frac{1}{8(1+\gamma^2)} \left[(1-\gamma)^2(1-P) + (1+\gamma)^2(1+P) \right]. \end{aligned}$$

The states $|2\rangle$ and $|3\rangle$ do not oscillate into a state that is subjected to two-photon-decay and therefore do not have to be considered in the calculation of the two-photon-annihilation intensity from positronium self-annihilation. The $|1\rangle$ resembles the para-like states and $|4\rangle$ the ortho-like state.

The intensity of the two photon self-annihilation signal I is determined by the branching ratio for two photon decay $Br_{2\gamma}$ for each state multiplied by the occupation. The branching ratio for two photon decay is given by the ratio between the two photon annihilation rate $\lambda_{2\gamma} = \lambda_{\text{pPs}}$, which is given by the para-positronium annihilation rate, and the total annihilation rate of the state. The total annihilation rates λ_1 for the para-like state $|1\rangle$

$$\lambda_1 = \kappa \frac{\gamma^2 \lambda_{\text{oPs}} + \lambda_{\text{pPs}}}{1 + \gamma^2} \quad (4.18)$$

and the total annihilation rate λ_4 for the ortho-like state $|4\rangle$

$$\lambda_4 = \kappa \frac{\lambda_{\text{oPs}} + \gamma^2 \lambda_{\text{pPs}}}{1 + \gamma^2} \quad (4.19)$$

were evaluated by Nagashima et al. [NH90]. Using these annihilation rates to calculate $Br_{2\gamma}$ one obtains for the two photon intensity of the para-like positronium state

$$I_1 = \underbrace{\frac{\lambda_{\text{pPs}}}{\lambda_1} \frac{1}{1 + \gamma^2}}_{Br_{2\gamma}} \cdot \langle 1|1\rangle \quad (4.20)$$

and for the two photon intensity of the ortho-like positronium state

$$I_4 = \underbrace{\frac{\lambda_{\text{pPs}}}{\lambda_4} \frac{\gamma^2}{1 + \gamma^2}}_{Br_{2\gamma}} \cdot \langle 4|4\rangle. \quad (4.21)$$

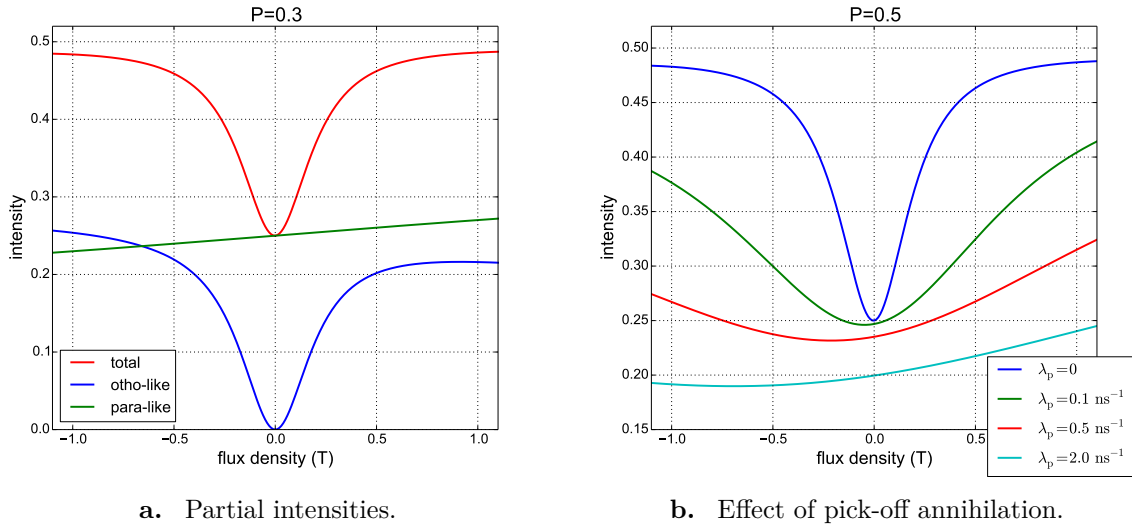
The total intensity of the two-photon-annihilation signal from the self annihilation of positronium is therefore dependent on the magnetic field, the positron polarisation and the electron positron contact density:

$$I_{2\gamma}^{\text{self}}(B) \propto I_1 + I_4. \quad (4.22)$$

As shown in section 4.3 the signal from positronium self-annihilation can be clearly distinguished from the from the pick-off annihilation signal by the shape of the associated momentum distribution in the 2D-ACAR spectrum. However, as can be seen in figure 4.5 a) the total Intensity of the two photon annihilation from the self annihilation of positronium as a function of the magnetic field is symmetric. This is due to the fact the sum of the occupations of the ortho-like and the para-like positronium is conserved, since in vacuum all terms linear in γ are cancelled. For positronium in matter the pick-off annihilation rate has to be included as an additive term $\lambda_{\text{pick-off}}$ in equations 4.18 and 4.19. The pick-off process act as a additional loss term and mainly reduces the contribution of I_4 as can be seen from equation 4.21 due to the lower self-annihilation rate from the ortho-like state. The resulting signal from positronium self-annihilation shows then an asymmetry upon reversal of the magnetic field (see figure 4.5 b)).

Hence, the positron polarisation can be determined by measuring the intensity of the self-annihilation signal of positronium as a function of the magnetic field. The only additional free parameter in the analysis is the electron positron contact density κ when the pick-off annihilation rate is determined in a separate positron lifetime experiment.

Even without the possibility to directly distinguish between self-annihilation and pick-off annihilation as it is the case for DBAR the determination of the polarisation is possible. This was successfully demonstrated by Nagai et al. [NNK⁺00]. In this case the total two-photon annihilation rate. The ratio of positronium self-annihilation to total two-photon annihilation is then found to be proportional to the so-called S-Parameter (for a definition of the S-Parameter see section 7.2).



a. Partial intensities.

b. Effect of pick-off annihilation.

Figure 4.5.: a) Plot of the calculated partial and total two photon annihilation intensities for a positron polarisation of $P = 0.3$ versus the magnetic field. The total intensity is symmetric upon reversal of the magnetic field. b) The effect of pick-off annihilation studied on the total two-photon-annihilation intensity for a positron polarisation of $P = 0.5$ for different pick-off annihilation rates. Due to the higher relative probability for pick-off annihilation from the ortho-like state an asymmetry of the intensity upon reversal of the magnetic field is expected.

4.5. Experimental determination of the positron polarisation

This section deals with the experimental procedure and data evaluation for the determination of the positron polarisation by measuring the asymmetry in the signal of positronium self-annihilation upon reversal of the external magnetic field.

4.5.1. Experimental procedure

A $1.2 \times 0.8 \text{ cm}^2$ single-crystalline α -quartz sample with a high positronium yield is used as a production target. In order to avoid systematic errors in the determination of the polarisation one has to make sure that the transport efficiency is uniform. Therefore, a large sample is chosen and a detailed study of the transport field was performed (see the results of the FEM simulations shown in figure 3.17 b)). The transport is considered to be uniform when it shows no field dependence. In a first approximation this is the case when the sum of the source size and the positron gyration radius is smaller than the sample dimensions. This is safely the case when the field exceeds $B = 0.4 \text{ T}$ and therefore that data was taken only at higher fields.

The degree of polarisation of positrons emitted from a β^+ source in the direction of emission is given by the momentum in forward direction $\frac{v}{c}$, which is a measure of how many reference frames can be found in which the helicity of the positron, the projection of the positron spin on the momentum, is conserved. The overall polarisation P of positrons emitted in a cone with opening angle ϑ relative to the emission direction is then given by $P = \frac{1}{2} \frac{\langle v \rangle}{c} (1 + \cos \vartheta)$. In zero magnetic field ϑ is given by the solid angle Ω as $\Omega = 2\pi(1 - \cos \vartheta)$. However, in a 2D-ACAR experiment a magnetic field is applied in order to deliver more positrons from the source to the sample [CWL⁺13]. This means that the net polarisation of the positrons hitting the sample

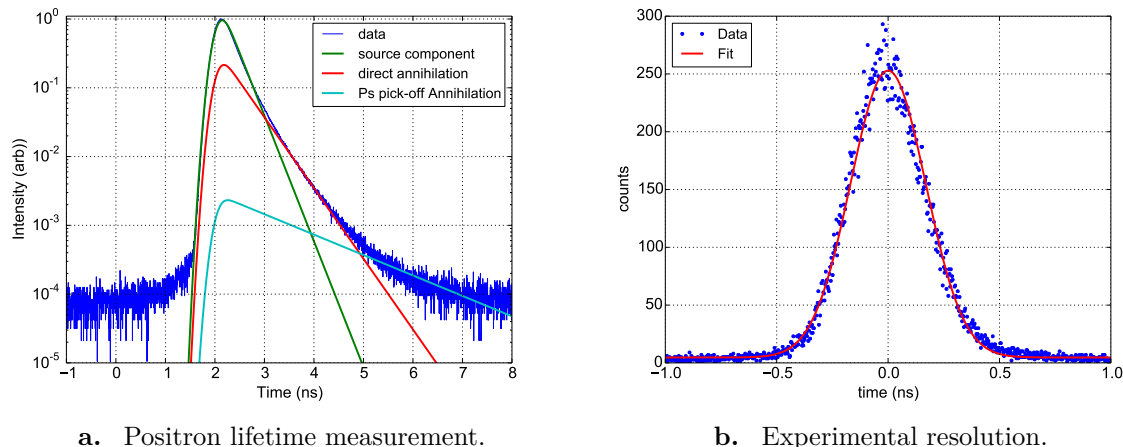


Figure 4.6.: a) Positron lifetime spectrum of the α -quartz sample. Three lifetime components according to annihilation in the source, as free positron annihilation and positronium pick-off annihilation can be identified. b) Experimental resolution of the lifetime spectrometer at the time of the measurement fitted with a single Gaussian from the prompt coincidence. The FWHM of the distribution is ≈ 0.40 ns.

cannot be calculated from simple geometric considerations. In addition, the source-capsule that is used in the experiment is equipped with a tantalum backing on which the ^{22}Na is deposited. For this reason the positron polarisation is lowered by positron back-reflection and has to be determined in a dedicated experiment.

The sample is orientated with the integration direction chosen along the c -axis. Therefore, the resulting 2D-ACAR spectrum exhibits the six-fold symmetry of the quartz lattice. A 2D-ACAR spectrum of single crystalline quartz is shown in figure 3.20 c) together with horizontal and vertical cuts through the distribution in figures 3.20 a) and 3.20. The narrow component is due to positronium self-annihilation and the broad component originates from pick-off annihilation and annihilation of free positrons inside the quartz sample.

As discussed in the previous section the intensity of the self annihilation signal is necessary to determine the polarisation. Therefore the spectra are modelled by the super-position of two two-dimensional Gaussian distributions and a constant background:

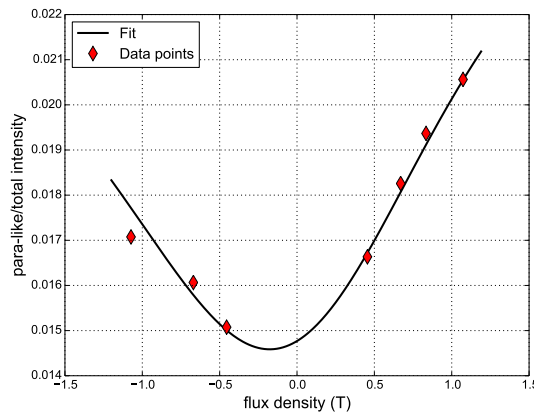
$$f_i(x, y) = \sum_i^{N,B} I_i \exp\left(\frac{-(x - x_0)^2}{2\sigma_{i,x}^2} + \frac{-(y - y_0)^2}{2\sigma_{i,y}^2}\right) + const. \quad (4.23)$$

The values obtained by the fits of the individual spectra are presented in table 4.1. As can be seen the width of the broad component is symmetric while the narrow component has an elliptical profile due to the anisotropic resolution function. The variation of the observed widths for the narrow as well as for the broad component is the same range as the statistical precision. Hence, no dependence of the width on the magnetic field is observed. The relative intensity of the self-annihilation signal is determined by the ratio of the volume of the narrow Gaussian to the volume of the broad Gaussian distribution.

The pick-off annihilation rate was determined to $\lambda_{\text{pick-off}} = 0.69(1) \text{ ns}^{-1}$ in a dedicated positron lifetime experiment. The resolution of the lifetime spectrometer was determined by

Table 4.1.: Table of the values obtained from fitting the individual spectra.

B_{ext} (T)	N_{tot} 10^6 counts	σ_x^B (mrad)	σ_y^B (mrad)	I_B 10^3	σ_x^N (mrad)	σ_y^N (mrad)	I_N 10^3	$\frac{V_N}{V_B}$
1.073	65.0	5.56(2)	5.59(2)	20.0	0.79(4)	0.71(4)	22.8	0.0206
0.834	78.1	5.58(2)	5.60(2)	24.3	0.80(4)	0.70(4)	26.0	0.0194
0.67	76.7	5.69(2)	5.60(2)	23.9	0.83(4)	0.70(4)	24.2	0.0183
0.455	194.1	5.60(1)	5.61(1)	60.8	0.90(2)	0.69(2)	55.9	0.0166
-0.455	67.8	5.60(2)	5.61(2)	21.4	0.88(4)	0.68(4)	17.8	0.0151
-0.67	152.4	5.59(1)	5.61(1)	49.4	0.82(2)	0.69(2)	43.8	0.0161
-1.073	93.7	5.57(2)	5.61(2)	31.4	0.77(3)	0.70(3)	29.6	0.0171

**Figure 4.7.:** Relative strength of the para-like positronium signal as a function of the magnetic flux density. The asymmetry is a result of the positron polarisation.

the width of the prompt coincidence to ≈ 400 ps (FWHM)(see figure 4.6 b)). This is sufficient to obtain three lifetime components from the spectrum: the pick-off lifetime, lifetime for free positron annihilation and the source component together with the lifetime for para-positronium self-annihilation. The latter two are not separated in the analysis. The lifetime spectrum together with the fit of the lifetime components is shown in figure 4.6.

4.5.2. Results and discussion

For the analysis the scheme proposed by Nagashima et al. [NH90] was adopted by fitting equation 4.22 with a free scale factor to the data of table 4.1. Hence, the fit has three free parameter: the positron polarisation, the electron positron contact density and a scale parameter. The MINUIT-package [JR75] was used to perform a χ^2 fit of the theoretical function to the data. A value of

$$P = 0.31 \pm 0.04$$

for the positron polarisation was found to describe the data best. This value agrees with the results from other groups for similarly constructed source capsules [KMF⁺11]. The best-fit value for the electron positron contact was found to be

$$\kappa = 0.68 \pm 0.07$$

and in fair agreement with value obtained by Nagai et al [NNK⁺00] also obtained for signal crystalline quartz (the error is given by the statistics). The statistical error of the data points in figure 4.7 are small compared to the symbols. This is due to the high statistical precision in the determination of the self-annihilation intensity. The uncertainty in the final value results from the limited amount of available data points for different magnetic fields. However, the precision of the value for the polarisation is sufficient for the analysis of spin-polarized ACAR spectra.

5 Chapter 5.

The electronic structure of chromium studied by temperature-dependent 2D-ACAR

Of the three metals in the chromium group: chromium, molybdenum and tungsten which all crystallize in the body centred structure chromium exhibits the most interesting properties. In contrast to molybdenum and tungsten, which are both paramagnetic in the ground state, chromium shows an incommensurate spin density wave ground state with a Néel temperature of $T_N = 311\text{ K}$ [Faw88]. The phase diagram of chromium is shown in figure 5.1. Below T_N chromium shows a transversal polarized spin density wave. At $T_S = 121\text{ K}$ a spin-flip transition occurs and the spin density wave changes to a longitudinally polarized form. The periodicity of the spin density wave is found to be incommensurate with a reciprocal lattice vector. Therefore, theoretical prediction of the Fermi surface in the spin density wave state are difficult due to the non-local nature of the electronic correlations which give rise to this effect. The Fermi surface of paramagnetic chromium however can be calculated. A three-dimensional illustration is given in figure 5.2. The Fermi surface of chromium is comprised of four sheets, two electron-like and two hole-like sheets. The electron sheets are centred at the Γ -point on the Brillouin zone and form an octahedral structure with almost spherical nobs at the corners, the so-called electron jack. The second electron sheet in the form of ellipsoidal lenses is located inside the electron jack. One hole-like sheet is centred at the H -point, the so-called hole-octahedron. The second hole-like sheet of ellipsoidal form and is situated at the N -point. Parallel sections of the H -hole octahedron and the Γ -electron jack can be connected by a common spanning vector which gives rise to Fermi surface nesting. Below T_N this nesting results in an instability of the system, due to the high number of electron and hole states that can be coupled leading to the opening an energy gap as shown in figure 2.8. Due to the fact that the electron surface at Γ is slightly smaller than the H -hole sheet the nesting vector is not commensurate to the reciprocal lattice. This results in an effective cancellation of the H -hole and parts of the Γ -electron Fermi surface sheets leaving the electron nobs and the N -hole ellipsoids to form the Fermi surface of the spin density wave state as illustrated in figure 5.9. The nesting vector defines the propagation direction of the spin density wave along the $[100]$ -direction. By cooling the sample in a high magnetic field from the paramagnetic state a single domain (single- q) state can be achieved. The traditional experimental method for studying the Fermi surface by the de Haas-van Alphen effect is limited to low temperatures, and therefore cannot be utilized for the

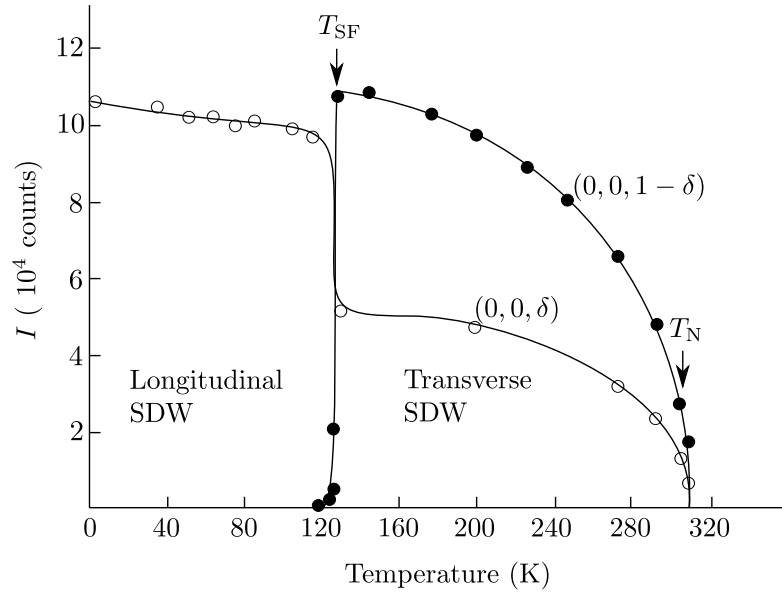


Figure 5.1.: Magnetic neutron scattering intensity as a function of temperature (adapted from [Faw88]) illustrating the magnetic phases of Cr. The transition to the paramagnetic state is found at the Néel temperature $T_N = 311 \text{ K}$. Chromium undergoes a spin flip transition at $T_S = 121 \text{ K}$ from a transversal polarised (AF_1) to the longitudinal polarized (AF_2) SDW state.

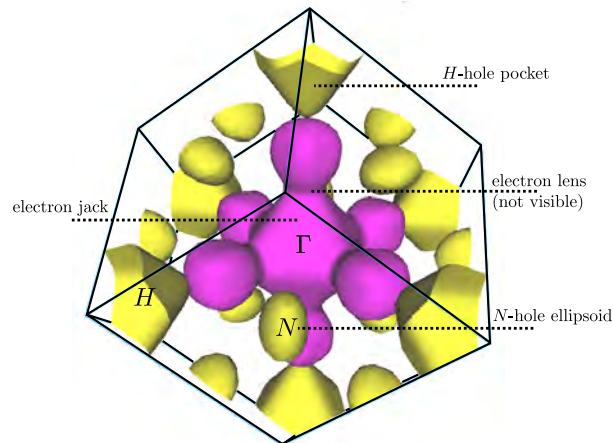


Figure 5.2.: Three dimensional illustration of the Fermi surface of chromium (rendered from calculated data taken from [CNC⁺00]). The central structure (pink) is called the electron jack. Inside the electron jack an additional electron surface the so-called electron lens is found. The electron lens is usually considered to be too small to be resolved by 2D-ACAR. There are two hole-like sheets (yellow) present the H -hole octahedra and the N -hole ellipsoids

study of the paramagnetic phase of chromium. For this reason, several ACAR investigations, both experimental [SOS⁺77, SMW88, FDH⁺98] and theoretical [SS83, SKS92, RST02] have been performed on paramagnetic chromium. A summary and discussion of these investigations is given in section 2.3.1. Studying the fermiology of the paramagnetic phase of chromium allows to gain insight to the driving mechanism of the anti-ferromagnetic ordering below 311 K, since a nesting feature of the Fermi surface is expected to be strongly related to the magnetic phase transition. However, several 2D-ACAR investigations performed in the paramagnetic [DFH⁺98, Bia00] phase of chromium revealed significant discrepancies between the measured and the calculated two-photon-momentum distribution which cannot be explained in terms of the topology of the Fermi surface. These discrepancies are most probably due to electron-positron correlations and/or many-body effects not accounted for by theory. Recently, an experimental approach to this problem, the utilisation of a state-dependent enhancement has been presented in [LHAD10]. With this method the enhancement is directly obtained by fitting the contribution of the individual bands to the data. This way, the Fermi surface nesting vector was deduced via the computation of the static susceptibility from the fitted LMTO calculations. In this study the focus is put on the differences in the Fermi surface topology between paramagnetic and anti-ferromagnetic chromium.

Two related investigations of the electronic respective magnetic structure of chromium have been performed. In a first approach the differences in the electronic structure of chromium in the paramagnetic and a anti-ferromagnetic multi- q spin density wave state are investigated. The obtained ACAR spectra are compared with different theory calculations performed with the DMFT and in the LSDA. Based on that an investigation of the single- q state is performed with the focus on the identification of the symmetry breaking of the electronic structure from the cubic symmetry of the paramagnetic state to a orthorhombic and respectively a tetragonal symmetry in the spin density wave state.

5.1. Study of the magnetic phase transition of multi- q chromium

5.1.1. Temperature-dependent measurements

A disc 10 mm in diameter with a thickness of 2 mm was cut from a single crystalline Cr rod used in neutron scattering experiments by spark erosion. The sample surface is orientated perpendicular to the [100] direction with an accuracy better than 0.5° , which was checked by means of Laue diffraction. The sample surface was polished in order to remove surface defects which may trap positrons. Positron lifetime measurements on the sample were performed and revealed a single lifetime component. However, it shall be noted that due to the strong source component the identification of the bulk lifetime was not possible. For the measurements of the spin density wave state the sample was mounted on the coolable sample holder and two measurements were performed: at 10 K and at room temperature, respectively 2D-ACAR spectra were recorded with the integration direction along [001]. Afterwards the sample holder was changed for the heatable option and two measurements were performed: one at room temperature and one at 45°C . An excess of 10^8 counts was collected in each spectrum. Additional single spectra with about $50 \cdot 10^6$ counts were recorded for each measurement for the determination of the momentum sampling function. At the time this measurements were performed the distortion correction was not available, therefore the resolution is about 10% worse than for the single- q spectra [CWH⁺13]. Two of the four measurements were performed at room temperature in

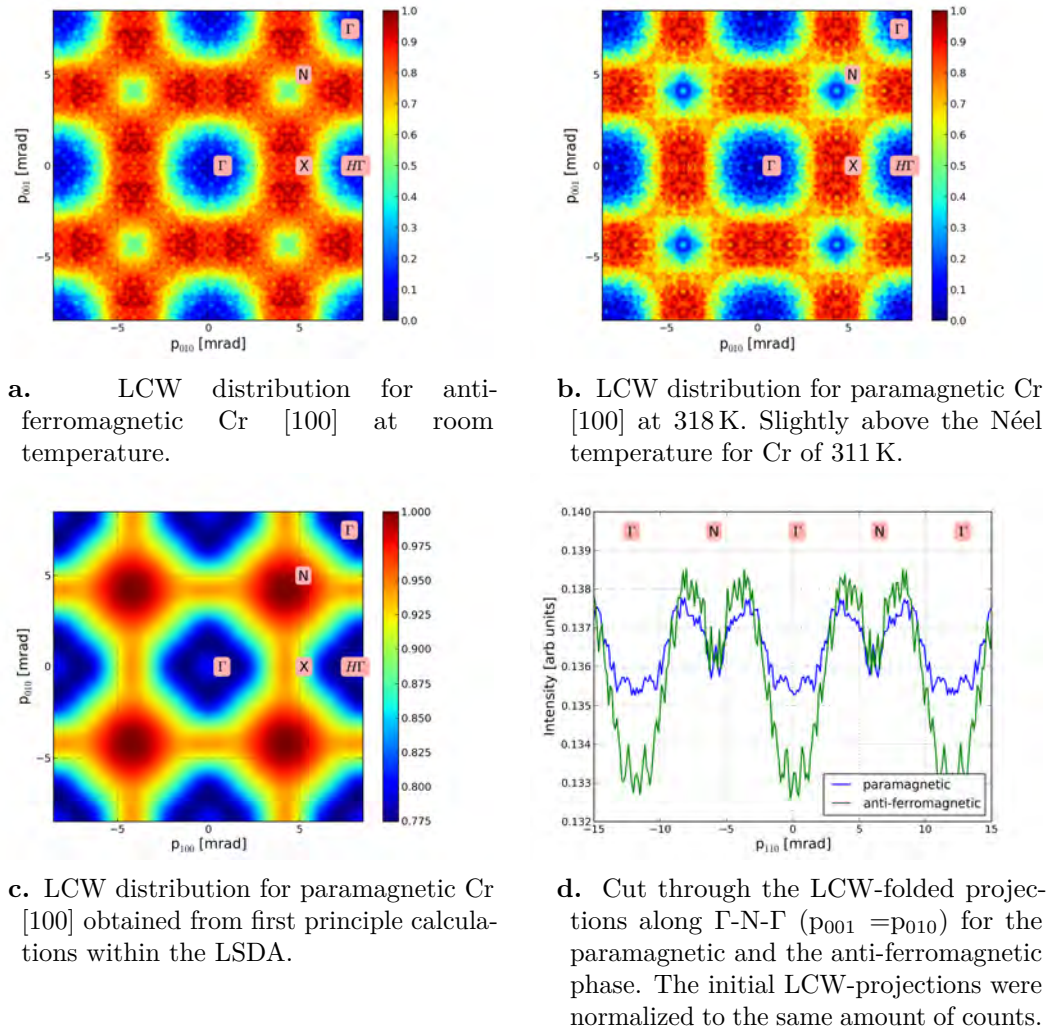


Figure 5.3.: Analysis of the Cr LCW-distribution and comparison with theory.

order to check if the ACAR spectra are consistent before and after the change of the sample holder. Since both spectra are compatible within the statistical limits only the spectrum with the higher statistics is presented here (see figure 5.3 a)). The comparison of the low temperature and the room temperature spectra shows the effect of decreasing resolution with increasing temperature. However, besides the lower resolution in the room temperature measurement both spectra are similar and hence only one is shown.

5.1.2. Results from the LCW analysis and comparison to theory

The features at the N -points appear to be occupied in the SDW phase (High symmetry points of the Brillouin zones of both phases, *simple cubic* for the SDW phase and *bcc* for the paramagnetic phase are indicated in figures 5.3). This picture changes when the sample temperature is increased above the Néel temperature (see figure 5.3 b)). A small difference in temperature drives the sample into the paramagnetic state and yields a drastic change in the LCW-folded data. The N -hole pockets become more pronounced, which can be seen

comparing cuts along Γ - N - Γ for both phases (see figure 5.3 d)). Furthermore, the electron pocket structure at the X -points connecting the N -points is smaller than in the anti-ferromagnetic phase. Generally, the agreement with previous 2D-ACAR results (see reference [DFH⁺98]) on paramagnetic chromium is considerable. However, the discrepancies between the present data and the SPRKKR [EKM11] calculations are quite substantial. This has also been reported from different laboratories [DFH⁺98, Bia00]. The relative intensities in the calculation for the occupied and the unoccupied states can not be reproduced in the LCW-folded data (see figure 5.3 c)).

The experimental resolution of our spectrometer lies between 1.54 mrad and 1.64 mrad [CWL⁺13], which is only slightly less than the extent of the N -point features in the data. However, the changes in the LCW-folded data when the sample is driven over the magnetic phase transition cannot be attributed to resolution effects, since a temperature increase of 20 K results in a degradation of the overall resolution of less than 0.01 mrad.

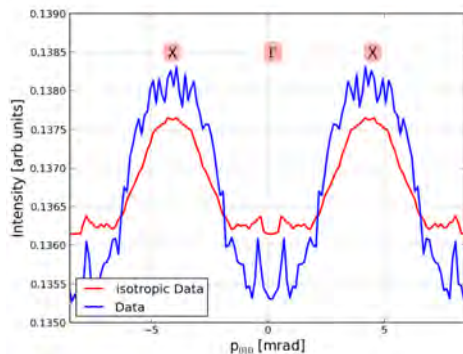


Figure 5.4.: Cut through the LCW-folded data along $X\Gamma X$ ($p_{001} = 0$) in comparison with the same cut for a LCW-folding of the isotropic data. The position of high symmetry points is indicated.

The LCW-folding was applied to the isotropic data, which was obtained by azimuthal averaging of the original data. The isotropic data does not contain the full information on the Fermi surface topology. With the isotropic data alone features at the X -point, similar to those described above, can be produced by the LCW-folding, as can be seen in figure 5.4.

A possible explanation would be that the positron annihilation with electrons of a flat band close to the Fermi energy is strongly enhanced as discussed in literature, but this was not found to be the case in the study of Laverock et al. [LHAD10]. It has to be considered that the application of the LCW-theorem is only valid if the positron wave function can be characterized as a plane wave, which is, however, not true if strong electron-positron correlation effects are present, as it is the case for chromium [RM84]. If this is the case, the strong lattice effects of the electron-positron correlations would also obscure the Kahana-like momentum dependence of the enhancement which is consistent with the fact that the Jarlborg-Singh enhancement model also used by Laverock et al. gives an inferior description of the data than the state-dependent enhancement [LHAD10].

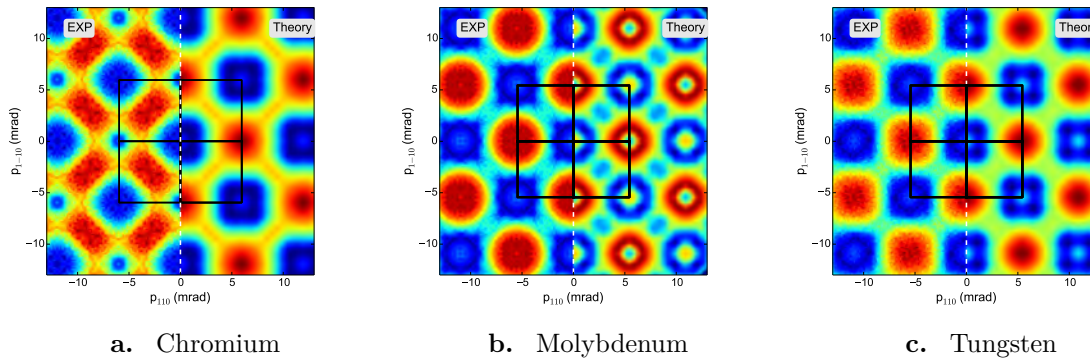


Figure 5.5.: Comparison of the experimental LCW folded data for the paramagnetic phase with calculations obtained in the LSDA for the chromium group metals chromium, molybdenum and tungsten. According to the Lomer [Lom62] picture the Fermi surfaces of these three elements are similar. It can be seen that the agreement with theory is satisfactory for molybdenum and excellent for tungsten while there are distinct discrepancies for chromium. This indicates that the theory model is in principle capable of describing the data but fails for chromium. The reason for that are most probably non-local effects introduced either by electron-electron and/or positron-electron correlations that are present in chromium.

5.1.3. Comparison with Mo and W

In order to check the validity of the calculation scheme discussed above additional measurements on the chromium group metals molybdenum and tungsten are performed and compared. This way it is possible to assess the predictive power of the theory calculations.

The tungsten crystal was obtained from a commercial vendor (Mateck) and the molybdenum crystal was supplied by the Bristol group. Both measurements on tungsten and molybdenum were performed at 10 K in order to benefit from the improved resolution at lower temperatures. Both crystals are orientated with the [110] plane perpendicular to the sample surface. The accuracy of the orientation for the tungsten crystal is given by the manufacturer to be better than 0.1° . The orientation of the molybdenum crystal was checked by Laue diffraction and confirmed to be better than 0.5° . In both measurements the integration direction is chosen along [110] similar to the chromium measurement. The measurement on molybdenum was straight forward. In the case of tungsten however the strong absorption of the annihilation radiation in the sample lead to a highly non-symmetric momentum sampling function as shown in figure 3.10 a). This required great care for the correction initial spectra.

The calculations are carried out with the SPRKKR package [EKM11] with the same general input parameters besides the lattice parameter as have been used in the calculation of the chromium spectra. The calculated spectra and the experimental data are compared in terms of the LCW folded projections similar to the chromium study. As can be seen the agreement between theory and experiment is satisfactory in the case of molybdenum (see figure 5.5 b)) and excellent in the case of tungsten (see figure 5.5 c)). This leads to the conclusion that the strong electron-electron correlations present in the chromium system are not accounted for by the LSDA calculations (see figure 5.5 a)). In all cases the calculations were carried out in the independent particle model, i.e. no electron-positron correlation was considered. The tungsten and the molybdenum data suggest that these electron-positron play a minor role but it was

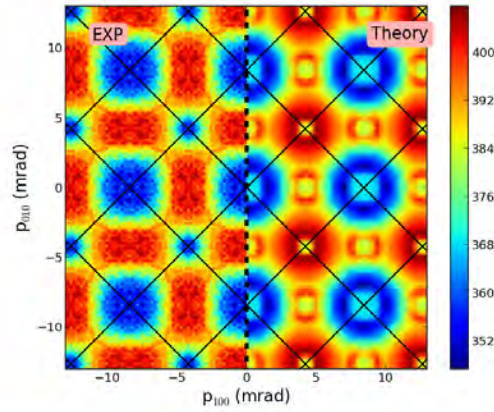


Figure 5.6.: Comparison between the LCW-folded experimental data and the calculations obtained within the DMFT for paramagnetic chromium projected along [001]. The discrepancies of the LSDA can be partially resolved.

found by Jensen et al. [JW90] that the behaviour of the positron in chromium is fundamentally different than in the other elements of this group.

5.1.4. Discussion

The results from previous measurements on paramagnetic chromium were successfully reproduced. It was found that the 2D-ACAR spectrum is drastically different in the anti-ferromagnetic and in the paramagnetic phase [DFH⁺98]. However, the interpretation of the data with respect to the calculations within the LSDA remains unsatisfactory. This is partially resolved by recent calculations performed within the DMFT by the theory group from Augsburg [Chi14]. The comparison with the data is shown in figure 5.6. In this case the electron-electron correlation were included which results in a much better description of the data. However, several features present in the experimental data cannot be accounted for by the calculations. The most striking difference is found at the N -point similar to the LSDA calculations. Here a low density is found in the experiment while the theory predicts a significant electron like structure. Since the inclusion of electron-electron correlations does not resolve this issue it can be concluded that this effect is due to strong electron-positron correlations. Apart from the k -space analysis in terms of the LCW folded data a comparison of the anisotropies of the experimental data and the theoretical calculations is shown in figure 5.7. The DMFT calculation describe the details found in the experiment well especially in the low momentum region.

Since at present it is not possible to include these effects into the calculations one has to resort to the investigation of properties of the electronic structure that can be accessed without the backup of theoretical calculations for the study of chromium. Therefore, this study was extended to the investigation of the symmetry breaking of the electronic structure in the spin density wave state of single- q chromium.

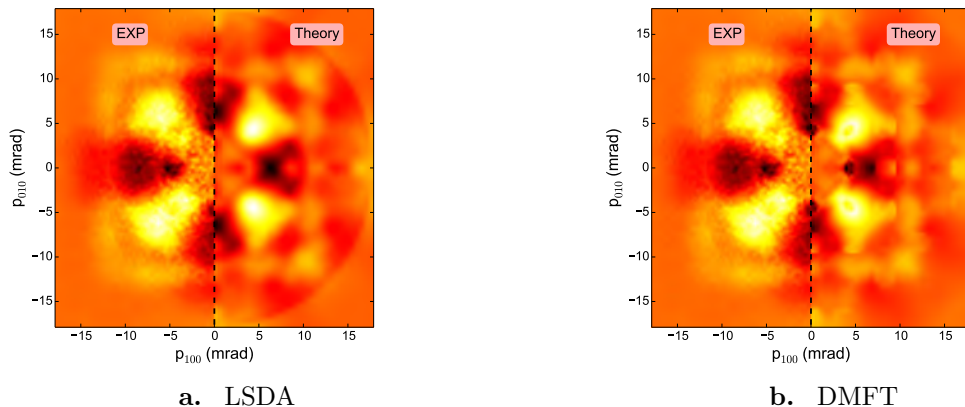


Figure 5.7.: Comparison of the anisotropy in the 2D-ACAR spectrum for the paramagnetic state with the calculations obtained within the LSDA (a) and the DMFT (b). As can be seen the DMFT calculation describes the data well. This gives further credit to the presence of strong electronic correlations in chromium, as these are accounted for by the DMFT calculations.

5.2. Investigation of the symmetry breaking in single- q chromium

It is known from quantum oscillation measurements [FAG⁺94, SSM⁺69, SFB⁺72] that the electronic structure of single- q chromium in the spin density wave state exhibits not the same space group symmetry as the bcc crystal lattice. This is illustrated in figure 5.8. The transversal polarised state (AF_1) shows an orthorhombic symmetry whereas the longitudinal state (AF_2) shows tetragonal symmetry. In dHvA measurements [FAG⁺94] the tetragonal symmetry was directly observed as the planes perpendicular to the q -vector were found to be no mirror planes to the electronic structure. This means that the only four-fold axis is along the q -vector.

5.2.1. Experimental procedure

The aim of this study is to identify this symmetry breaking in the electronic structure due to the magnetic interactions in the AF_1 and AF_2 state by means of 2D-ACAR. Therefore, the sample was field cooled in a magnetic field of 14 T [Bra13]. The magnetisation direction was chosen in-plane along the [100] direction. In the notation of this study the [010] denoted the out-of-plane axis. During transport and storage the sample was kept at temperatures around 0 °C in order to preserve the single- q SDW state. The mounting of the sample onto the sample holder was also performed in the freezer. In order to facilitate the orientation of the sample a marking of the [100] direction was engraved on the side face before it was magnetized. The sample was mounted in the spectrometer on the pre-cooled cryostat to ensure no loss of the single- q state during the orientation of the sample in the spectrometer.

As illustrated in figure 5.10 two measurements were performed in each state (AF_1 and AF_2) with the q -vector aligned parallel, denoted as q_{\parallel} and perpendicular, denoted as q_{\perp} to the ingratiation direction. The measurement in the AF_1 state was performed at 150 K and the measurement in the AF_2 state was performed at the lowest achievable temperature of 10 K. In each spectrum an excess of 10^8 counts were collected and single spectra for the calculation of the momentum sampling functions with $50 \cdot 10^6$ were recorded. Both, the ACAR data as

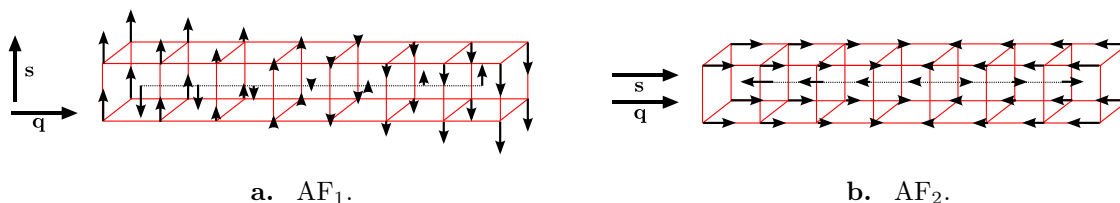


Figure 5.8.: Spin polarisation of the different spin density wave states to illustrate the different symmetries of the electronic structure. The transversal state AF_1 shows an orthorhombic symmetry whereas the longitudinal state AF_2 exhibits tetragonal symmetry.

well as the single spectra were corrected for the distortions of the detector according to the scheme discussed in section 3.1.2 which improves the resolution by $\approx 10\%$ compared to the multi- q study. The draw back of having the q -vector in-plane is the fact that the resolution in the in-plane direction is lower than perpendicular to the sample surface due to the anisotropic contribution to the resolution from the positron beam spot. Therefore, great care was taken in order to align the sample surface perpendicular to the integration direction. One measure was to mount the sample on the sample holder using a special yoke in order to compensate a slight miss cut of the sample backside during the glueing process. A misalignment of the sample surface results in different lateral dimensions of the projection of the positron spot on the sample and therefore in a different resolution function for the different alignments of the q -vector. This effect was directly assessed from that data and discussed in detail below.

5.2.2. Results

The anisotropies of the data for the measurement in the AF_1 phase are shown in figures 5.11 a) and 5.11 b). By naked eye no significant differences in the spectra can be observed. The same is true for the measurements of the AF_2 phase shown in figures 5.11 c) and 5.11 d). Due to the lower sample temperature of the AF_2 phase measurement the resolution is slightly better and from the consideration of section 3.2.3 an improvement of the resolution by ≈ 0.14 mrad is expected.

In principle the measurement with the q -vector aligned perpendicular to the integration direction should slightly deviate from the four-fold symmetry of the $[100]$ plane. However, as stated above due to the anisotropic resolution function the four-fold symmetry is always broken down to a two-fold symmetry.

In order to reveal the any systematic change in the spectra the difference spectra of the full data of the q -vector parallel and perpendicular are analysed as shown in figure 5.13 a) and 5.12 a) for the AF_1 phase and for the AF_2 phase respectively. As can be seen no distinct anisotropy only a strong isotropic contribution is observed. This means that in fact the resolution function is different for both measurements. This is can be well described by the difference of two Gaussians as shown in figures 5.13 b) and 5.12 b). From the fit values it is found that the resolution changed by 2.18(2) % in the two measurements for the AF_1 phase and by 2.20(2) % for the AF_2 phase measurements between q_{\parallel} and q_{\perp} . Both values are consistent within the error which confirms the repetition accuracy of the rotation stage of the spectrometer. With the considerations presented in section 3.2.3 this can be converted to a change in the alignment of the sample surface of $1.26(6)^\circ$ between the measurements. An illustration of the origin of the

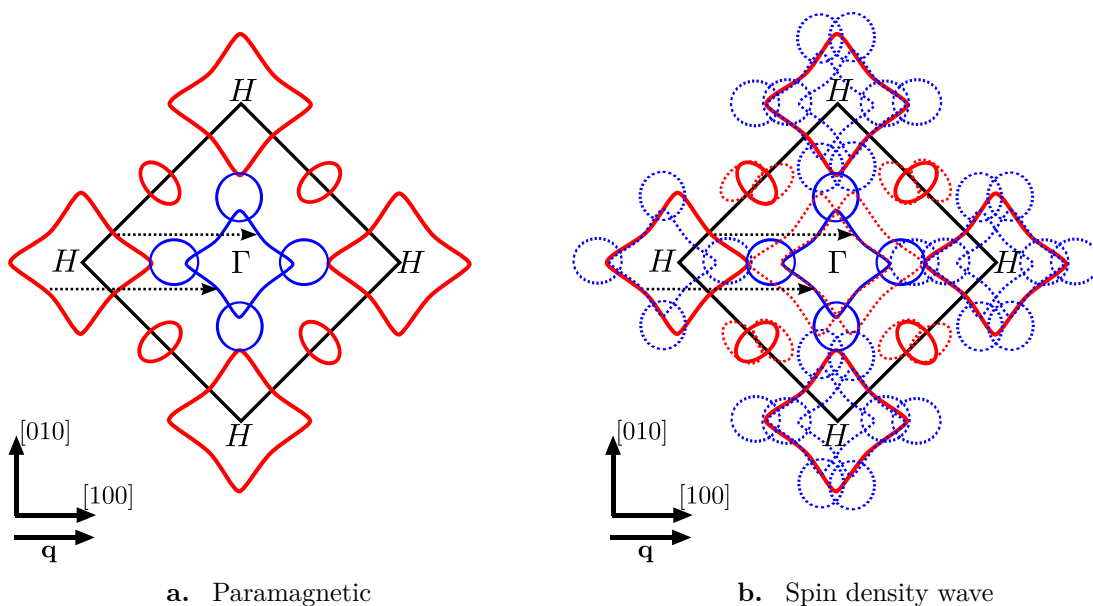


Figure 5.9.: a) Cuts through the Fermi surface of chromium in the basal plane (inspired by [KS08b]) to illustrate the formation of the spin density wave. Fermi surface sheets on the H -hole octahedron can be connected to the octahedral structure of the Γ -centred electron jack by a spanning vector q . The Γ -octahedron is slightly smaller than the H -hole octahedron therefore the length of the spanning vector differs by a small fraction δ from a reciprocal lattice vector. b) This results in the formation of an incommensurate spin density wave ground state where the H -hole and the Γ -electron sheets cancel each other by the opening of an energy gap.

changes resolution function due to the apparent change of the projected lateral dimensions of the positron spot on the sample is given in figure 5.14. This effect is considered as a systematic error of the determination of the symmetry breaking.

In order to assess the effect of the symmetry breaking, i.e the transition from cubic to tetragonal respective orthorhombic symmetry, two approaches are undertaken. In the first approach the \mathbf{p} -space data in the extended zone scheme is considered as it appears in the 2D-ACAR spectra. In the second approach the data is folded back into \mathbf{k} -space using the LCW transform and analysed for the symmetry breaking.

For the \mathbf{p} -space data the anisotropies of the individual measurements are compared using an affine transformation in the form of the linear transformation tensor ϵ . The general assumption behind this is that the symmetry breaking is small and can be described as shear along the direction of the q -vector. In the case of two-dimensional data \vec{X} , where \vec{X} denotes the positions of the data points ϵ has the form of:

$$\epsilon = \begin{pmatrix} \epsilon_{xx} & \epsilon_{xy} \\ \epsilon_{yx} & \epsilon_{yy} \end{pmatrix}.$$

The sheared positions are then given by $\epsilon \otimes \vec{X}$. In order to avoid a rotated shear the off-diagonal elements are set to zero and in order to compare the sheared density of the measurement with the q -vector parallel to the integration to the one with the q -vector perpendicular the data has to be evaluated on a regular grid. This makes an interpolation between the sheared grid

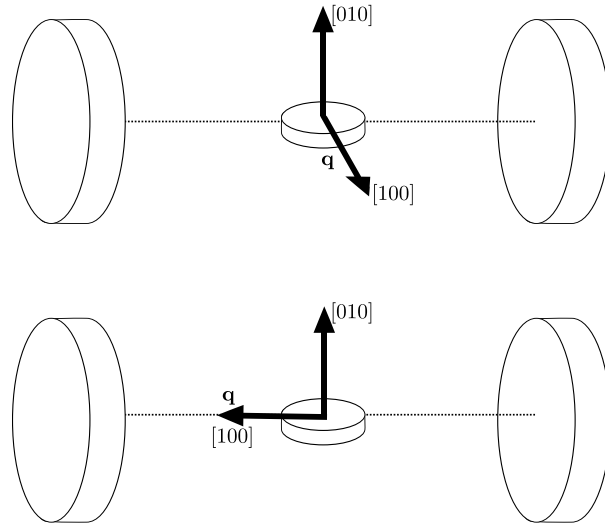


Figure 5.10.: Principle of the 2D-ACAR measurement for the investigation of the symmetry breaking in the electronic structure in the single- q SDW state. Two measurements are performed in the AF_1 and the AF_2 state with the q -vector aligned parallel and anti-parallel to the integration direction given by the line of sight of the detectors

points and regular grid necessary. Therefore, the discretisation of the data is performed on a grid with 2048×2048 pixels and the position are linearly interpolated. The components of the deformation tensor are determined by a least-squares fit by minimizing the difference between the sheared anisotropy spectrum with the q -vector parallel and the anisotropy spectrum with the q -vector perpendicular. The origin of \vec{X} is chosen to coincide with the rotational center on the data. For the measurement in the AF_1 phase the following deformation tensor was obtained:

$$\epsilon_{AF_1} = \begin{pmatrix} 1.0137(1) & 0 \\ 0 & 1.0012(1) \end{pmatrix}.$$

and for the measurement in the AF_2 phase:

$$\epsilon_{AF_2} = \begin{pmatrix} 1.0139(1) & 0 \\ 0 & 1.0008(1) \end{pmatrix}.$$

. The components ϵ_{xx} denote the distortion in-plane parallel to the q -vector and ϵ_{yy} out of plane. The values are found to be in reasonable agreement for both measurements. The errors are given by the statistical accuracy. The systematic error due to the tilt of the sample determined above add an additional value of ± 0.0104 to the error budget. Hence, both diagonal components of the deformation tensor are compatible with unity. The deviation from unity of the in-plane component of 0.32σ cannot be considered to be significant.

A method to circumvent the shortcomings of the direct analysis presented above is the analysis of the \mathbf{k} -space data by using an geometrical model to describe the observed densities. This analysis focuses on the structure obtained at the N -points of the LCW-folded data (shown in figure 5.15). As can be seen in figure 5.2 the N -hole ellipsoids located on the basal plane of the Brillouin zone are stacked onto each other and rotated by 90° in the 2D-ACAR measurement

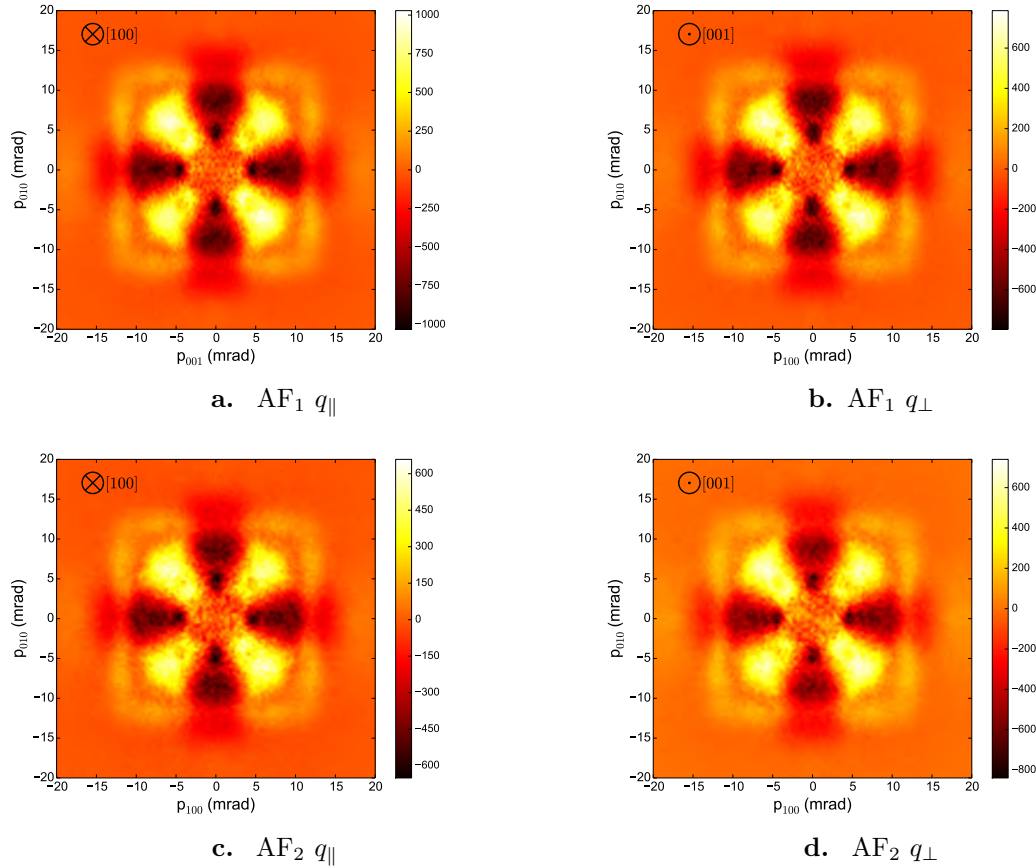


Figure 5.11.: Anisotropy of the 2D-ACAR spectra for the longitudinal AF_1 state obtained at 150 K with the q -vector aligned parallel (*a*) and perpendicular to the integration direction (*b*) Anisotropy of the 2D-ACAR spectra for the longitudinal AF_2 state obtained at 10 K with the q -vector aligned parallel (*c*) and perpendicular to the integration direction (*d*). In all cases the spectra shows a deviation from the four-fold symmetry of the $[100]$ -plane due to the anisotropic resolution function. Compare for example the hole-like structures at $(0|\pm 5$ mrad) and $(\pm 5$ mrad|0)

with the integration direction chosen along $[110]$. Using a geometrical model similar to Biasini et al. [Bia00] the expected LCW density can be calculated. Here the N -hole ellipsoids are modelled according to Ketterson et al. [KKS75] with a diameter of 0.35 mrad and a semi-axis of 0.54 mrad. The modelled ellipsoids are then stacked according to the reciprocal lattice and the density is projected onto the $[100]$ -plane. In the spin density wave state the incommensurate q -vectors lead to the formation of infinite chains of ellipsoids along q . This was found in de dHvA measurements (for details see [Faw88] and references therein). An illustration of this infinite chain Fermi surface is given in figure 5.16 a). It is a direct result of the Fermi surface nesting shown in figure 5.9.

For the measurements parallel and perpendicular to the q -vector the density is either integrated along q which makes it indistinguishable from the stack of the ellipsoids or perpendicular to q which results in a modified LCW density. The expected densities from this geometrical model are shown in 5.16 c) together with the same densities convoluted with the experimental resolution.

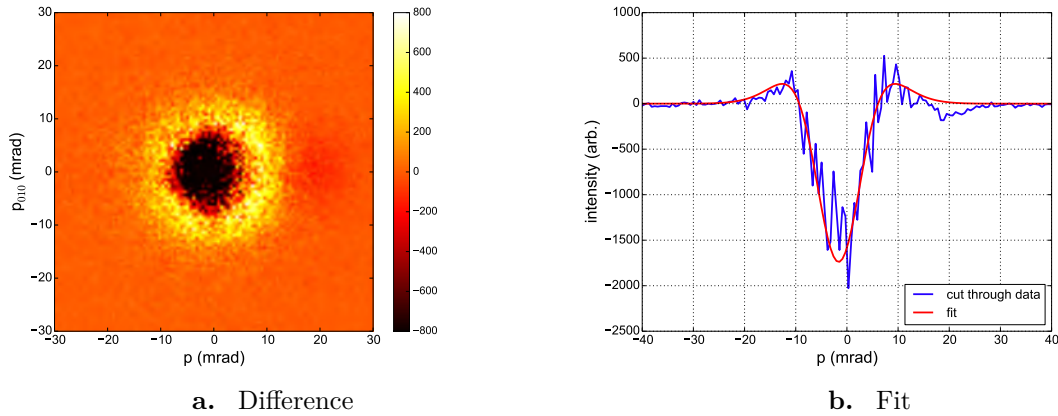


Figure 5.12.: a) Difference of the two measurements with the q -vector aligned parallel and perpendicular to the integration direction for the AF₂ state. No distinct anisotropic contribution can be observed in the spectrum. b) Cut through the difference spectrum fitted with the difference of two Gaussians in order to assess the effects of a systematic error due to a slight misalignment of the sample. The resulting spectrum is well described by the Fit.

Even with the effect of the resolution the expected densities can be distinguished. By comparing the expected densities obtained from the simplified geometrical model to the LCW densities from the measurements shown exemplary in figure 5.16 b) the effect of the symmetry breaking can be estimated. Here the expected densities are described by a two-dimensional Gaussian with different widths along each axis as the effect of the resolution function obscures the details in the initial densities. A ratio of the widths for the measurements with q perpendicular and parallel to the integration direction that differs from unity would be a direct hint for the symmetry breaking. In the AF₁ phase ratios of 1.0(1) in plane and 1.04(17) out-of-plane were found. For the AF₂ phase value ratios of 0.96(12) in plane and 1.11(10) out-of-plane were obtained, respectively. Hence, high statistical error makes an assessment of the symmetry breaking impossible. It is concluded that the loss of information in the LCW transformed data cannot be compensated by using this geometrical model to describe the expected density.

5.2.3. Conclusion

The observation of the symmetry breaking in the electronic structure of chromium in the spin density wave state turned out to be a difficult task. The analysis of the \mathbf{p} -space data however represents the most promising approach as the information content in the \mathbf{k} -space data is insufficient given the current resolution of the spectrometer in order to determine the structure of the N -hole ellipsoid with the required precision.

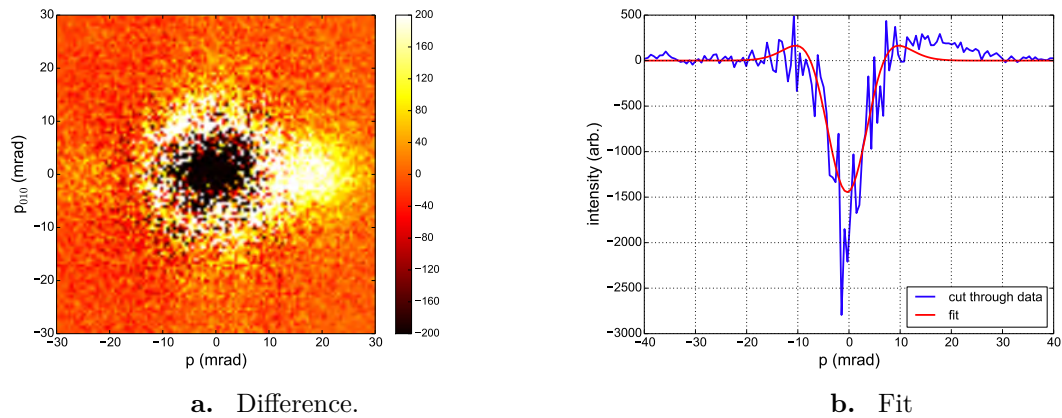


Figure 5.13.: a) Difference of the two measurements with the q -vector aligned parallel and perpendicular to the integration direction for the AF_1 state. An anisotropy is found in the difference which cannot be accounted for by a change in the resolution function. However, due to the absence of inversion symmetry this cannot be due to a symmetry breaking in the electronic structure. A possible explanation can be layer of frozen residual gas on the sample which may lead to positronium formation. b) Cut through the difference spectrum fitted with the difference of two Gaussians in order to assess the effects of a systematic error due to a slight misalignment of the sample. The value obtained by the fitting coincides with those obtained for the AF_2 state measurement.

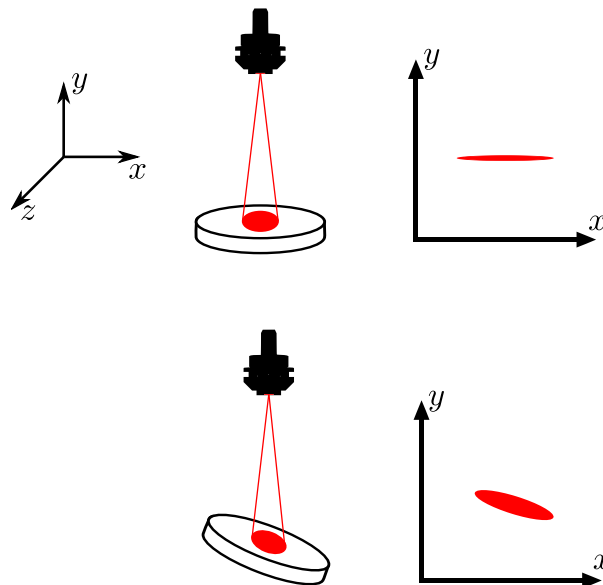


Figure 5.14.: Illustration of a source for a systematic error in the determination of the symmetry breaking in the electronic structure. The sample has to be turned by 90° , therefore a slight misalignment of the sample in the spectrometer changes the apparent shape of the positron spot size on the sample which results in a modified resolution function.

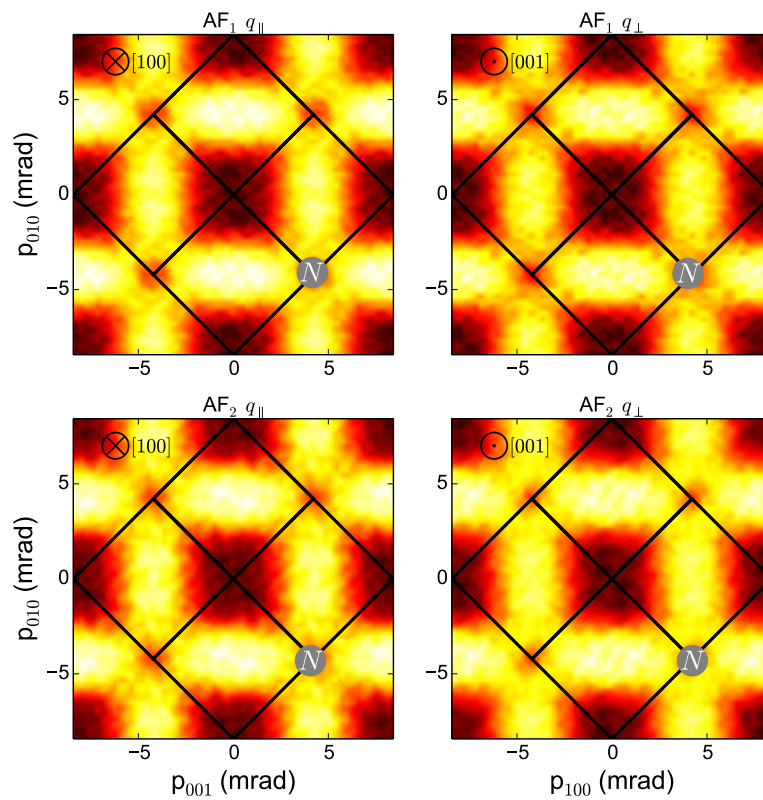
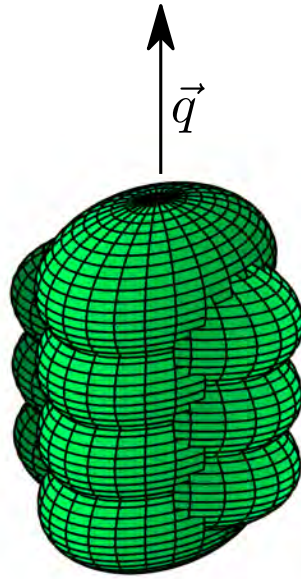
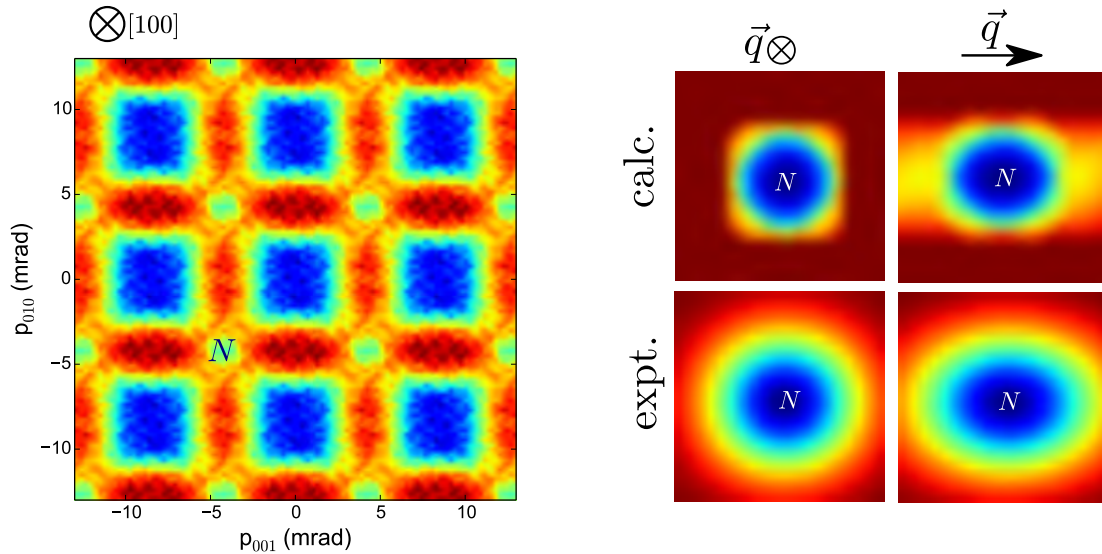


Figure 5.15.: LCW folded data for the transversal (AF_1) and the longitudinal (AF_2) with the q -vector aligned parallel and perpendicular to the integration direction.



a. The infinite chain of N -hole ellipsoids that form parallel to the Q -vector is responsible for this symmetry breaking.



b. The LCW folded ACAR spectrum in the region around the N -hole ellipsoid is described by a simplified geometrical model.

c. Illustration of the analysis procedure after the convolution with the experimental resolution most of the information is lost. The extent of the plotted density is $(1.5 \times 1.5) \text{ mrad}^2$.

Figure 5.16.: a) Illustration of the infinite chain structure of the N -hole ellipsoids. b) Experimentally determined projection of the momentum density obtained by LCW-folding of the data. c) Calculated projection of the momentum density obtained from the geometrical model before and after convolution with the resolution function. The symmetry breaking can still be observed from the different widths of the distributions.

6 Chapter 6.

Spin-polarized 2D-ACAR measurements on Nickel

Nickel is one of the most prototypical d electron system and therefore attracted great interest from both theory and experiment. Electronic properties of narrow-band materials, such as the d -shell transition-metal series and their compounds, cannot be entirely explained within a one-electron picture, because of the presence of significant local correlations between electrons in the partially filled d band [IFT98]. From a theoretical point of view the realistic description of the band structure has to contain an accurate treatment of many-body electron-electron interactions to account for the mixed itinerant and localized behaviour of the valence states [IFT98, GK96, KSH⁺06].

From an experimental point of view high resolution techniques are needed to identify many-body effects of the electronic excitations. The classical approach using quantum oscillation techniques is very challenging in ferromagnetic systems [Tsu67], since the variation of the magnetisation of the Landau-levels is superimposed with the magnetisation of the material itself. Hence, most investigations on the electronic structure and correlations in nickel relied on photo-electron emission spectroscopy [AKO⁺96, SPK⁺96]. Braun et al. [BME⁺12] could show the importance of local correlations in nickel using the magnetic dichroism in photo-emission for a spin-resolving measurement. The importance of local electron-electron correlations on the correct description of the band structure of nickel was recognized by Wang and Callaway [WC77]. However, it was found in different photo emission studies (see for example [EHK78, HKE79, EP80, HCS⁺09, BME⁺12]) that the correct prediction of the exchange splitting and the width of the d -band are beyond the capabilities of the LSDA approach. In fact, it was found in the experiment that the $3d$ -band width is about 30% narrower than that obtained from local spin density approximation calculations. In addition, the magnetic exchange-splitting is overestimated by LSDA calculations compared with the experimental data.

Besides the apparent discrepancies in the predicted band widths the dominant correlation effect in nickel predicted by LSDA+DMFT is the well known satellite situated at 6 eV below the Fermi level which is also found in the photo-emission data [HKE79, BME⁺12], and which however, can also not be explained by pure LSDA calculations. An improved description of correlation effects for the $3d$ electrons via the LSDA+DMFT gives the width of the occupied $3d$ bands of nickel properly reproduces the exchange splitting and the 6 eV satellite structure in the valence band [LKK01].

In this study the influence of the local correlations calculated within the LSDA+DMFT

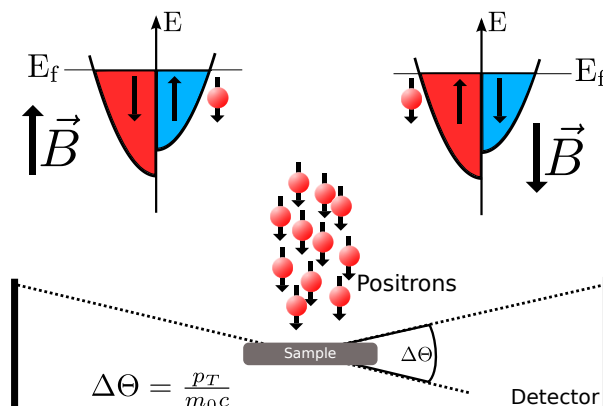


Figure 6.1.: Schematic view of the principle of spin polarized 2D-ACAR. By magnetizing the sample the singlet electron positron annihilation is preferred either for electrons spin minority or majority direction, depending on if the magnetisation is parallel or anti-parallel to the emission direction of the positrons. For clarity the positron polarisation is set to 1.

framework on the electronic structure is assessed by spin polarized 2D-ACAR. In the calculation the value for the local electron-electron repulsion, the so-called Hubbard U , is varied and the resulting 2D-ACAR spectra are compared to the experimental data. In the analysis the effects of the positron wave function and the the electron-positron correlations (enhancement) are investigated.

6.1. Introduction to spin-polarized 2D-ACAR

Two-dimensional projections of the TPMD are measured for different external magnetic fields at room temperature. The sample is 10 mm in diameter and 0.5 mm high. It was obtained from Mateck GmbH with the [110] direction out of plane. In the case of Ni the [110] direction coincides with the magnetic easy axis. The accuracy of the orientation was chosen better than 0.1° . The sample surface is polished to 50 nm surface roughness. An external magnetic field using the electromagnet of the spectrometer (flux density of ≈ 1.1 T) was applied parallel (anti-parallel) with respect to the crystallographic [110] direction of the sample which coincides with the emission direction of the positrons, i.e. the polarisation direction of the positron beam. The β^+ spectrum of ^{22}Na , which served as positron source, has an end-point energy of 545 keV with a mean energy of about 210 keV. This corresponds to a beam polarisation of 71 % for forward emission. The geometry of the source and the magnetic transport field (higher acceptance angle) leads to a lower net polarisation of the beam. Still a significant, non-zero polarisation of the beam is expected, which was determined to 31(4) % in a dedicated experiment (see section 4.5).

Spin polarized ACAR is one of the few experimental methods that can probe the momentum distribution of the electron in the bulk with respect to the spin direction. It was successfully applied to pure [GMWP91] as well as compound systems [HM86, HMRB90] and implicitly by Haynes et al. [HWL⁺12]. It relies on two facts, the non-zero net polarisation of positrons emitted from a radioactive source and the preferred singlet annihilation of electrons and positrons.

Due to the conservation of angular momentum the two-photon annihilation of an electron and a positron is only allowed when the annihilation pair is in a singlet configuration with

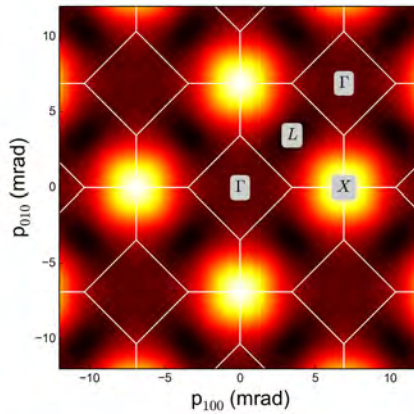


Figure 6.2.: Experimental spin-averaged LCW-folded momentum density of nickel with the integration direction chosen along [001]. The extent of the Brillouin zone are indicated by the solid lines.

their spins orientated anti-parallel. Furthermore, positrons emitted from a β^+ source such as ^{22}Na are longitudinally polarized due to parity violation in the weak interaction. The degree of polarisation in the direction of emission is given by the momentum in forward direction $\frac{v}{c}$, which is a measure of how many reference frames can be found in which the helicity of the positron, the projection of the positron spin on the momentum, is conserved [ZVHRG79]. The overall polarisation P of positrons emitted in a cone with opening angle ϑ relative to the emission direction is then given by $P = \frac{1}{2} \langle \frac{v}{c} \rangle (1 + \cos \vartheta)$. In an experiment the emission direction is defined by the line-of-sight between source and sample. It was shown experimentally that the positron polarisation is to a high degree conserved until the moment of annihilation, although the positron undergoes multiple scattering during thermalisation [KS75, SMB87].

In ferromagnetic materials the degeneracy between the two spin states is relieved and the densities in the individual spin channels are different, resulting in the formation of a majority and a minority spin population. When an external magnetic field is applied parallel or anti-parallel to the emission direction, i.e. the direction of the positron spin, the positrons will predominantly annihilate either with electrons from the majority spin direction or the minority spin direction. A sketch of this concept is shown in figure 6.1.

The momentum distribution of the annihilating pair is conserved in the two-photon momentum distribution of the annihilation quanta and is given by:

$$\rho_i^{\text{M(m)}}(\mathbf{p}) = \left| \int e^{-i\mathbf{p}\mathbf{r}} \Psi_+(\mathbf{r}) \Psi_i^{\text{M(m)}}(\mathbf{r}) \sqrt{\gamma(\mathbf{r})} d^3\mathbf{r} \right|^2 \quad (6.1)$$

with Ψ_+ the positron wave function, $\Psi_i^{\text{M(m)}}$ the electron wave function in the i th majority (M) or minority (m) band and the momentum dependent enhancement factor γ . As shown in figure 6.1 the direction of the electron spins in the majority band is anti-parallel to the external magnetic field, i.e. the magnetisation while the direction of the positron spins is fixed.

By contrast to Compton scattering, where all electrons have a more or less equal weight, a 2D-ACAR spectrum is no simple summation over all i electron states $N_i^{\text{M(m)}}(p_x, p_y)$ [KMF⁺11,

KMF⁺12, KFM⁺13]. Instead, in any positron annihilation experiment in general and in a 2D-ACAR experiment in particular the electron states are weighted with the overlap of the positron and the electron wave functions.

Therefore, the contribution $N_i^{M(m)}(p_x, p_y)$ of each electron from the majority (minority) band to the 2D-ACAR spectrum is given by integrating equation 6.1 along one momentum direction. The experimental 2D-ACAR spectrum for the magnetisation aligned anti-parallel (+) or parallel (−) to the positron polarisation is then given by

$$N_{\pm}(p_x, p_y) = \frac{\lambda_s}{4} \sum_i^{occ} \left[\frac{(1 \pm P)N_i^M(p_x, p_y)}{\lambda^{\downarrow\downarrow}} + \frac{(1 \mp P)N_i^m(p_x, p_y)}{\lambda^{\uparrow\downarrow}} \right] \quad (6.2)$$

with the singlet annihilation rate $\lambda_s = 4\pi r_e^2 c$, r_e the classical electron radius and the net longitudinal polarisation of the positrons P . The terms $\lambda^{\downarrow\downarrow(\uparrow\downarrow)}$ denote the *total* positron annihilation rate for positrons with spins aligned parallel ($\downarrow\downarrow$) to the magnetisation direction of the sample and for positrons with spins aligned anti-parallel ($\uparrow\downarrow$) to the magnetisation direction of the sample (the first arrow indicates the magnetisation direction and the second arrow the direction of the positron spins).

$$\lambda^{\downarrow\downarrow(\uparrow\downarrow)} = \frac{1}{2} \sum_i^{occ} \left(\lambda_s \omega_i^{M(m)} + \lambda_t (\omega_i^{M(m)} + 2\omega_i^{m(M)}) \right) \quad (6.3)$$

with the triplet annihilation rate $\lambda_t = \lambda_s(4\alpha/9\pi)[\pi^2 - 9] \approx 1/1115\lambda_s$ and the overlap $\omega_i^{M(m)}$ of positron and the electron from the i th majority (minority) band:

$$\omega_i^{M(m)} = \int \rho_i^{M(m)}(\mathbf{p}) d^3\mathbf{p}. \quad (6.4)$$

From above equations it can be seen that, unless the positrons are completely polarized an 2D-ACAR spectrum will contain contributions of both, the majority and the minority bands. In the analysis of a spin polarized ACAR measurement the difference of the two ACAR spectra $\Delta N(p_x, p_y)$ is taken, which is given by

$$\Delta N(p_x, p_y) = N_+(p_x, p_y) - N_-(p_x, p_y) \quad (6.5)$$

$$= \frac{\lambda_s P}{2} \sum_i^{occ} \left[\frac{N_i^M}{\lambda^{\downarrow\downarrow}} - \frac{N_i^m}{\lambda^{\uparrow\downarrow}} \right] \quad (6.6)$$

It was found possible by Berko [BM71] and co-workers to relate the physically interesting property $N^M - N^m$ connected to spin dependent momentum density of the material to the above mentioned difference ΔN of two 2D-ACAR spectra measured with the magnetisation vector parallel and anti-parallel to the positron polarisation:

$$\begin{aligned} \sum_i^{occ} [N_i^M(p_x, p_y) - N_i^m(p_x, p_y)] &\propto \\ &\propto \Delta N(p_x, p_y) + P \frac{\lambda^{\downarrow\downarrow} - \lambda^{\uparrow\downarrow}}{\lambda^{\downarrow\downarrow} + \lambda^{\uparrow\downarrow}} \sum N_{\pm} \\ &\approx \Delta N(p_x, p_y) + \delta F^{3\gamma} \sum N_{\pm} \end{aligned} \quad (6.7)$$

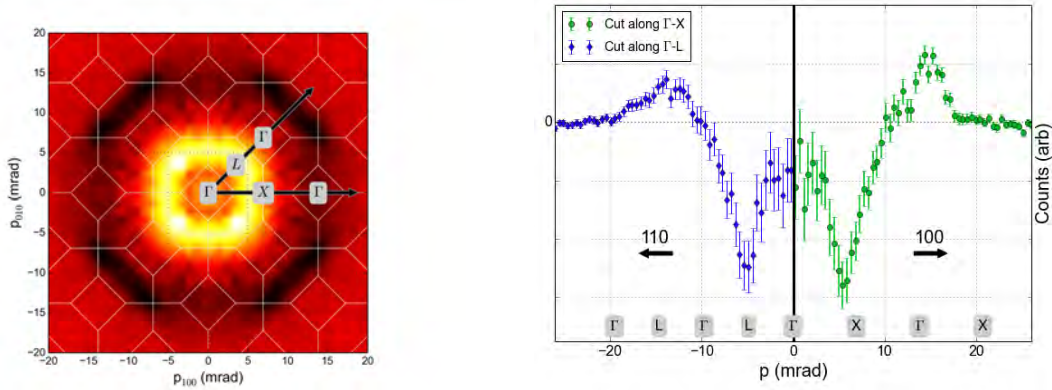


Figure 6.3.: Difference between two ACAR spectra when the magnetic field is reversed: (a) 2D spectrum with the integration direction along the [001], and (b) cut through the momentum density along high symmetry directions for $p_{100} = 0$ and $p_{110} = 0$.

the fraction of $3\text{-}\gamma$ annihilation $\delta F^{3\gamma}$ is on the order of $(1 - P)/1115$ and therefore can be safely neglected in a first order approximation in most cases. Therefore, the difference of the ACAR spectra $\Delta N(p_x, p_y)$ (magnetic ACAR) is directly related to the difference in the occupation of the spin majority and minority bands and is only linked by a proportionally constant.

6.2. Fundamentals of the theoretical calculations

Amongst the basic methods to measure momentum densities are 1D and 2D-ACAR and Compton scattering experiments. These spectroscopic quantities are routinely computed within the Density Functional Theory (DFT) [HK64, KS65, Koh99]. Within the present project collaborators from Universität Augsburg and Ludwig Maximilians Universität have computed the electronic structure and the 2D-ACAR for the perfect Ni bulk lattice using the LSDA of DFT for the electron exchange and correlation effects [CWB⁺15]. Electronic correlations beyond the LSDA were included using the DMFT [MV89, KV04]. The electronic Green's function $G_e^X(\mathbf{r}, \mathbf{r}', E_e)$ is obtained within the standard multiple scattering formalism [Gon92] of the Korringa-Kohn-Rostoker method [EKM11]. The positions \mathbf{r}, \mathbf{r}' are sites within the unit cell and E_e is a specific energy contour integration variable; X denotes the calculation procedure: LSDA or LSDA+DMFT. The ground state properties of the positron are obtained from the two-component DFT. In practice the Schrödinger equation is solved in real space and the lowest lying positron band is used to obtain the positronic Green's function $G_{p+}(\mathbf{r}, \mathbf{r}', E_p)$. Details on the implementation can be found in the thesis of D. Bena [Ben04].

$$G_{\sigma\sigma'}^X(\mathbf{p}_e, \mathbf{p}_p, E_e, E_p) = \frac{1}{N\Omega} \int d^3\mathbf{r} \int d^3\mathbf{r}' \phi_{\mathbf{p}_e\sigma}^{e\dagger}(\mathbf{r}) \text{Im} G_e^X(\mathbf{r}, \mathbf{r}', E_e) \phi_{\mathbf{p}_e\sigma}^e(\mathbf{r}') \phi_{\mathbf{p}_p\sigma'}^{p\dagger}(\mathbf{r}) \text{Im} G_{p+}(\mathbf{r}, \mathbf{r}', E_p) \phi_{\mathbf{p}_p\sigma'}^p(\mathbf{r}'), \quad (6.8)$$

(\mathbf{p}_e, σ) , and (\mathbf{p}_p, σ') are the momenta and spin of electron and positron, respectively. Here $G_{\sigma\sigma'}^X$ is computed for each energy point on the complex energy contour, providing the electron-positron momentum density:

$$\rho_{\sigma}^X(\mathbf{p}) = -\frac{1}{\pi} \int dE_e G_{\sigma\sigma'}^X(\mathbf{p}_e, \mathbf{p}_p, E_e, E_p). \quad (6.9)$$

Since the positron is considered to be in the ground state the integration over the positron energies E_p is not required and $\sigma' = -\sigma$ at the annihilation. The momentum carried off by the annihilation quanta is equal to that of the two particles up to a reciprocal lattice vector, accounting for the fact that the annihilation takes place in a crystal. Hence an electron with wave vector \mathbf{k} contributes to $\rho_\sigma^X(\mathbf{p})$ not only at $\mathbf{p} = \mathbf{k}$ but also at $\mathbf{p} = \mathbf{k} + \mathbf{K}$, with \mathbf{K} a vector of the reciprocal lattice. The spin resolved integrated momentum density $N_\sigma^X(p_x, p_y) = \int \rho_\sigma^X(\mathbf{p}) dp_z$ enters in the formula for computing the 2D-ACAR spectra – the integral of the total momentum density along a given p_z direction:

$$N_{2D-ACAR}^X(p_x, p_y) = \int [\rho_m^X(\mathbf{p}) + \rho_M^X(\mathbf{p})] dp_z = Tr_\sigma N_\sigma^X(p_x, p_y) \quad (6.10)$$

In order to assess the influence of the presence of the positron, the electronic momentum density has been computed from the Green's function in the momentum representation, as used in the calculations of the Compton profiles [CWB⁺15]:

$$G_{\sigma\sigma'}^X(\mathbf{p}_e, \mathbf{p}_e, E_e) = \frac{1}{N\Omega} \int d^3\mathbf{r} \int d^3\mathbf{r}' \phi_{\mathbf{p}_e\sigma}^{e\dagger}(\mathbf{r}) Im G_e^X(\mathbf{r}, \mathbf{r}', E_e) \phi_{\mathbf{p}_e\sigma}^e(\mathbf{r}'), \quad (6.11)$$

which formally corresponds to equation 6.8 from which the positronic Green's function is removed. The spin projected momentum density is obtained according to the formula:

$$\tilde{\rho}_\sigma^X(\mathbf{p}) = -\frac{1}{\pi} \int dE_e G_{\sigma\sigma'}^X(\mathbf{p}_e, \mathbf{p}_e, E_e). \quad (6.12)$$

The electron positron correlations are explicitly included in the calculation in form of the Boronski-Nieminen (BN) functional [BN86] parametrized for vanishing positron density and for electron densities in the typical range of transition metals $r_s \approx 2$ as described in section 2.2.2. As shown the BN parametrisation does not include any explicit momentum dependence. The advantage of this functional is that it can be directly included in KKR formalism as the functional is parametrized in term of the local density in real space. It was found that in the case of Doppler or ACAR spectra the shape of the of the momentum densities is only slightly changed compared to the IPM when the BN functional is employed. However, the agreement between theory and experiment is improved and similar to that of different parametrisations of γ like the LDA(E) (see [KSS14a, KSS14b] for an extensive discussion).

6.3. Experimental results

The measurement is performed in the p -space, however to proceed in the natural way when comparing with Fermi surface structures, the transformation into the k -space is required. This is done by use of the LCW-procedure [LCW73]. The LCW folded distribution is shown in figure 6.2. In the LCW folded momentum distribution the contribution from completely filled bands is cancelled out to a good approximation and the Fermi surface information is enhanced. Therefore, the characteristics of the Fermi surface (in this case spin averaged) can be conjectured.

The LCW-folded projections already contain much valuable information on the Fermi surface. However, by taking advantage of the positron polarisation additional information on the

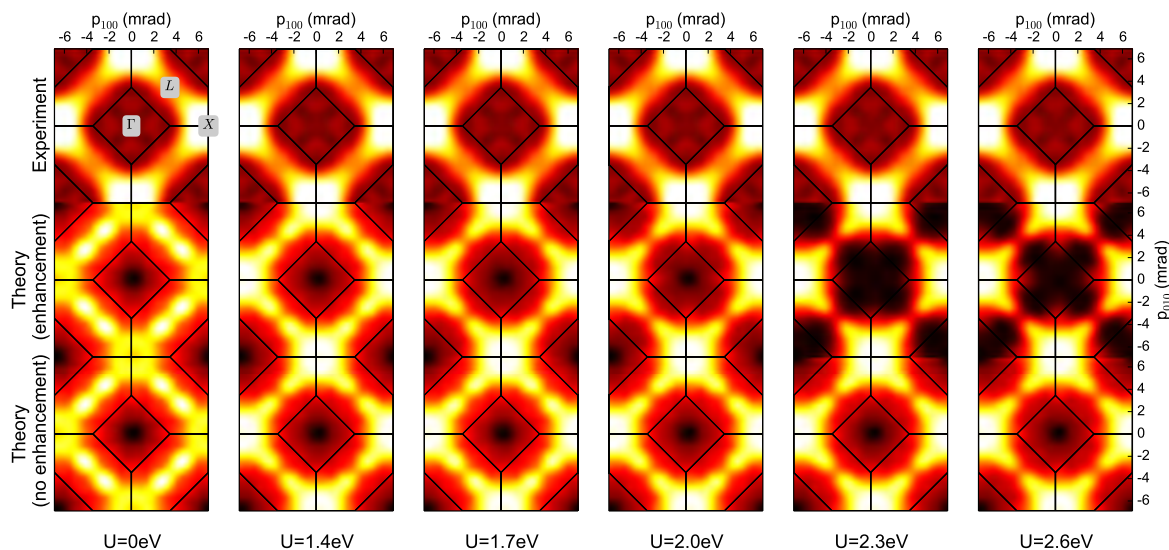


Figure 6.4.: Experimental magnetic LCW spectra (*top*) compared to theory convolved with experimental resolution (*bottom*). The free parameter in the theory is the so called Hubbard U , the electron-electron exchange correlation energy. Judging by naked eye one may find the best agreement for U in the range of 2.0-2.3 eV. To find the best agreement a more quantitative analysis is necessary.

individual spin channels of the Fermi surface can be obtained. Two electron-positron momentum distributions were measured with the magnetic field pointing parallel and parallel to the positron polarisation. In figure 6.3 the raw spin-difference of the 2D-ACAR measurement of nickel is presented. The integration direction was chosen along the [001] direction. The 4-fold symmetry is clearly observable even with limited statistics in the difference spectrum. In each spectrum an excess of 250 millions counts was collected and the data was corrected for the momentum sampling function in the usual way. In addition, a cut through the momentum density for $p_{100} = 0$ and $p_{110} = 0$ is shown in figure 6.3, which is in good agreement with the study of Genould et al. [GMWP91]. It shall also be noted that the difference spectrum contains almost no anisotropic contribution.

The difference between the two measurements with parallel and anti-parallel magnetisation for the LCW-folded distributions is shown in figure 6.4. Before subtraction the individual spectra were normalized to an equal amount of counts. A renormalisation due to the effect of the 3γ decay was omitted since the effect of the correction in the case of nickel [BM71] is negligible compared to the statistical noise. The LCW-folded difference spectrum is later used to draw a comparison with the two theory frameworks LSDA and LSDA+DMFT that have been evaluated in this study.

6.4. Comparison between theory and experiment

In order to compare the experimental results with the theoretical calculations first the theoretical data is convoluted with the experimental resolution function. This is illustrated in figure 6.4 for

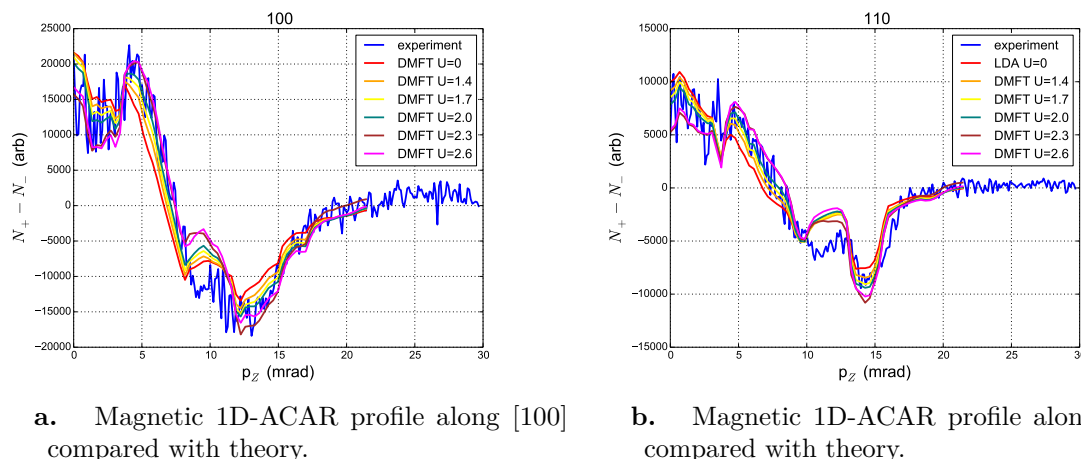


Figure 6.5.: Comparison of different magnetic 1D-ACAR profiles with theory. Due to the two-fold integration the statistical noise is greatly reduced, however, at the expense of information that is lost with the further integration.

the 2D LCW folded projection. For the sake of completeness also the LCW densities calculated without the BN enhancement are shown. The following discussion is based on the comparison of the calculated spectra including the enhancement and the experimental data. A two pronged approach is chosen to assess the degree of agreement between experimental data and theory. For one thing the one-dimensional magnetic ACAR profiles (similar to Compton profiles) to the theoretical data (see figure 6.5) are compared. The advantage of the twice integrated profiles lies in the great reduction of statistical noise. However, valuable information is lost due to the integration of the two-dimensional profiles along one momentum direction. Additionally, the two-dimensional magnetic LCW projection are compared to the theory (see figure 6.4). The middle and bottom rows shows the evolution of the calculated magnetic LCW with the changing correlation strength U . It can be clearly seen that with increasing U a gap opens at the L -points of the Brillouin zone. These gaps are associated with the necks in the Fermi surface of nickel. The LSDA alone underestimates the density at the X -point, while the density near the L -point is exaggerated. In the LSDA+DMFT the highest density is found at the X -point like in the experimental data. However, the structure connecting the X and L -points is not as clearly pronounced in the experimental data than it is in the DMFT calculations.

The scaling factor that was fitted to the data and found to agree for all theory models within the error limits and the offset was close to zero. The resulting values for χ^2 from the one-dimensional as well as for the two-dimensional analysis are shown in figure 6.6. As can be seen a distinct minimum is found for $U = 2.0$ eV. This minimum is less pronounced in the one-dimensional data. This means that although the difference spectrum appears rather isotropic the information is less in the one-dimensional profiles. The same analysis was carried out for the calculations within the independent particle model (without enhancement) and is shown in figure 6.6. As can be seen the calculations with and without the enhancement functional obtained within the LSDA are practically indistinguishable. However, for higher values of U the agreement between theory and experiment is stronger when the enhancement is included. The found minimum with enhancement is also in accordance with the evaluation of Compton scattering experiments [BMC⁺12] where values of $U = 2.0$ eV and $U = 2.3$ eV were

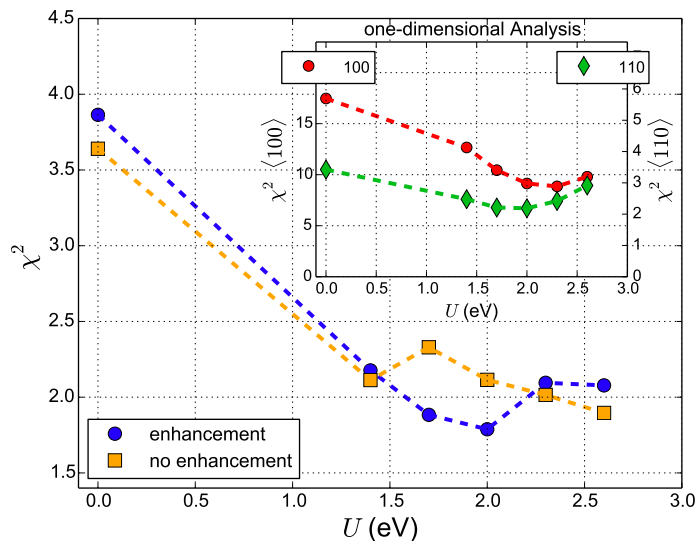


Figure 6.6.: Calculated χ^2 between theory and experimental data as a function of Hubbard U for the two-dimensional data. The strength of the electron-electron correlations is increasing with increasing U . A pronounced minimum of the χ^2 value is found in the analysis of the two-dimensional data when electron positron enhancement is included. The inset shows the same analysis carried out for the one-dimensional data including the enhancement.

found to describe the experimental data best.

6.5. Spin decomposition of 2D-ACAR spectra

According to equation 6.6 the knowledge of the polarisation P makes it possible to determine the momentum densities in the individual spin channels. However, the different $3-\gamma$ fractions have to be treated as equal. This appears justified with regard to the very small total contribution of $3-\gamma$ events, which was determined by Berko and Mills to be 0.0012(9) in the case of nickel [BM71]. This method of extracting the individual contributions was first used by Minjarends et al. for the study of NiMnSb [HMRB90]. In our case the polarisation was determined to $P = 0.31(4)$ in a dedicated experiment (see section 4.5), by exploiting the magnetic quenching of ortho-positronium in single-crystalline quartz. From equation 6.6 it follows:

$$N_M \propto \frac{1+P}{2P}N_- - \frac{1-P}{2P}N_+ \quad (6.13)$$

$$N_m \propto \frac{1+P}{2P}N_+ - \frac{1-P}{2P}N_- \quad (6.14)$$

For $P = 1$ the measured spectra represent the individual contribution directly. However, for $P < 1$ the individual contributions are obtained by a non-linear superposition of the measured spectra. According to equations 6.13 and 6.14 the difference between the measured spectra N_+ , N_- and the spin-averaged (non-magnetic) distribution is enhanced. This strength of this enhancement as well as the difference in the spectra are both $\mathcal{O}(P)$.

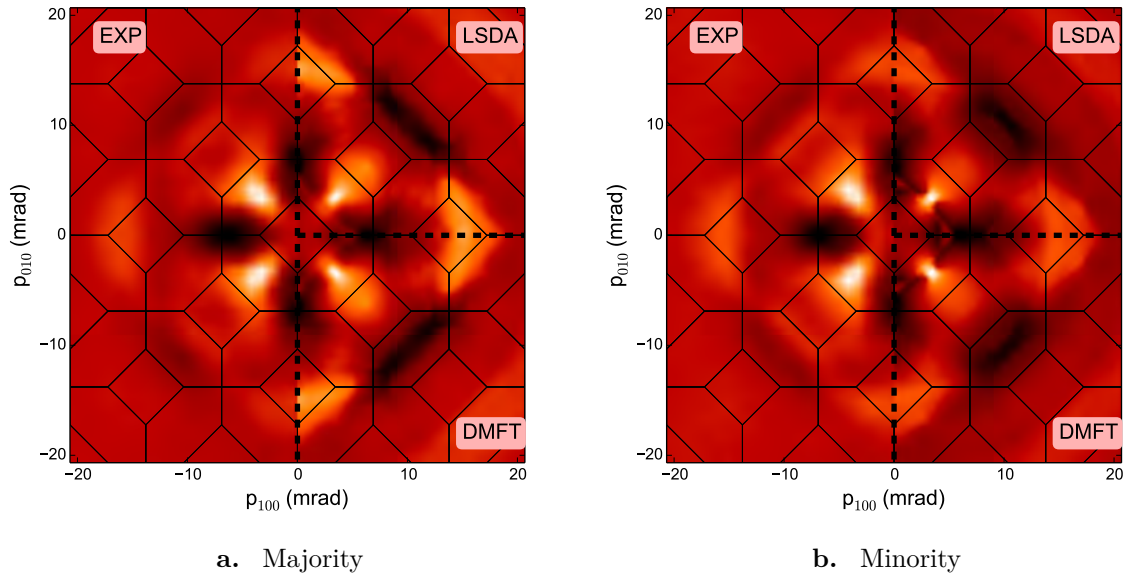


Figure 6.7.: Comparison of the anisotropies between the experimental data and the theory predictions (LSDA and LSDA+DMFT) for the individual spin channels. The experimental data was obtained by decomposing the measured 2D-ACAR spectra for the contribution from the spin majority and spin minority channels. For details see text.

The full power of this spin decomposition lies in the fact that the individual spin channels can be analysed separately. In the DMFT the electron-electron correlations leads to the formation of a satellite peak in the DOS 6 eV below the Fermi level for nickel, as discussed above. However, this satellite is only predicted in one spin channel. In order to estimate the predictive power of the theory models the anisotropy of the data is calculated for the majority density N_M and the minority density N_m (see figures 6.7 b) and 6.7 a)) which have been decomposed from N_+ and N_- according to 6.13 and 6.14. Then the value for χ^2/ndf between the measured and the calculated anisotropy is determined for the positron polarisation $P = 0.31$.

For $P = 0.31$ the χ^2/ndf value for the DMFT is smaller than for the LSDA (see figure 6.8). However, since all χ^2/ndf are significantly bigger than one we still see systematic differences between theory and experiment that cannot be accounted for by the experimental error. This is also supported by the fact that the calculated minima in χ^2/ndf as a function of the positron polarisation (as shown in figure 6.8) for the LSDA and also for the DMFT are not found at the experimentally determined value for $P = 0.31$. For the LSDA a value of $P = 0.46(8)$ and for the DMFT a value of $P = 0.70(22)$ is found respectively. As can be seen in the inset of figure 6.8 the minima are extremely shallow resulting in a high uncertainty for P . The discrepancies between theory and experiment are found to be most striking in the high momentum region with $|p| > 10$ mrad(1.4 a.u.) (see figures 6.7 b) or 6.7 a)). At this point is difficult to assess the source of these discrepancies, albeit it can be speculated that this is due to a momentum dependent enhancement, i.e. electron-positron correlations, that are not included in the theory models. The findings of Babiellini and co-workers [BHP⁺97] support this assumption, the authors showed that the independent particle model (IPM) the low momentum region is under-represented with respect to the high momentum region. If this is also the case for the BN enhancement model

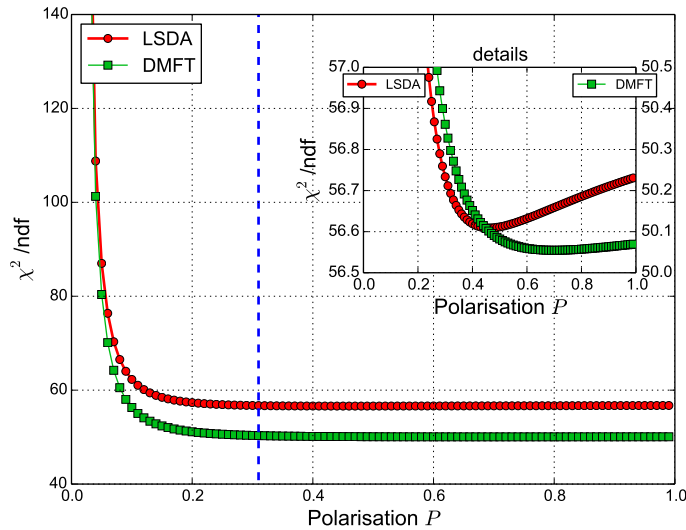


Figure 6.8.: χ^2/ndf between theory and experimental data as a function of polarisation P of the positron beam. The singularity at $P = 0$ can be understood with regard to equations 6.13 and 6.14. The dotted line marks the positron polarisation in the present experiment.

remains an open question.

6.6. Discussion

6.6.1. Positron probe effects in Ni

In order to assess the probe effects introduced by the positron the TPMD was calculated within the LSDA and DMFT including the positron wave function and the enhancement effects, including only the wave function effects and in complete absence of the positron. In figure 6.9 a) the results of the LSDA calculations including the positron wave function and the BN enhancement (left column) and in the absence of the positron right column are shown. Without the positron “bonds” along the $[110]$ directions in both spin channels. In the presence of the positron a significant reduction of the “bonds” take place for the majority spin channel. The presence of strong bonds for the spin down electrons causes the discrepancy in comparison with the experimental data.

Figure 6.9 b) presents the electronic momentum densities obtained within the LSDA+DMFT method. The calculations have been performed using the parameters $U=2.0$ eV $J=0.9$ eV and a temperature $T=400$ K.

The effect of electronic correlations leads to weaker “bonds” along the $[110]$ directions in both spin channels and hence to a better agreement with the experimental measurements.

Several cuts along the symmetry directions in the Brillouin zone are analysed. As the positron affects the spin channels differently the spin-contrast $n_M(\mathbf{k}) - n_m(\mathbf{k})$ computed in the LSDA and the DMFT is shown in figure 6.10. Basically all features of the momentum density are qualitatively reproduced in the spin-difference with and without the presence of the positron.

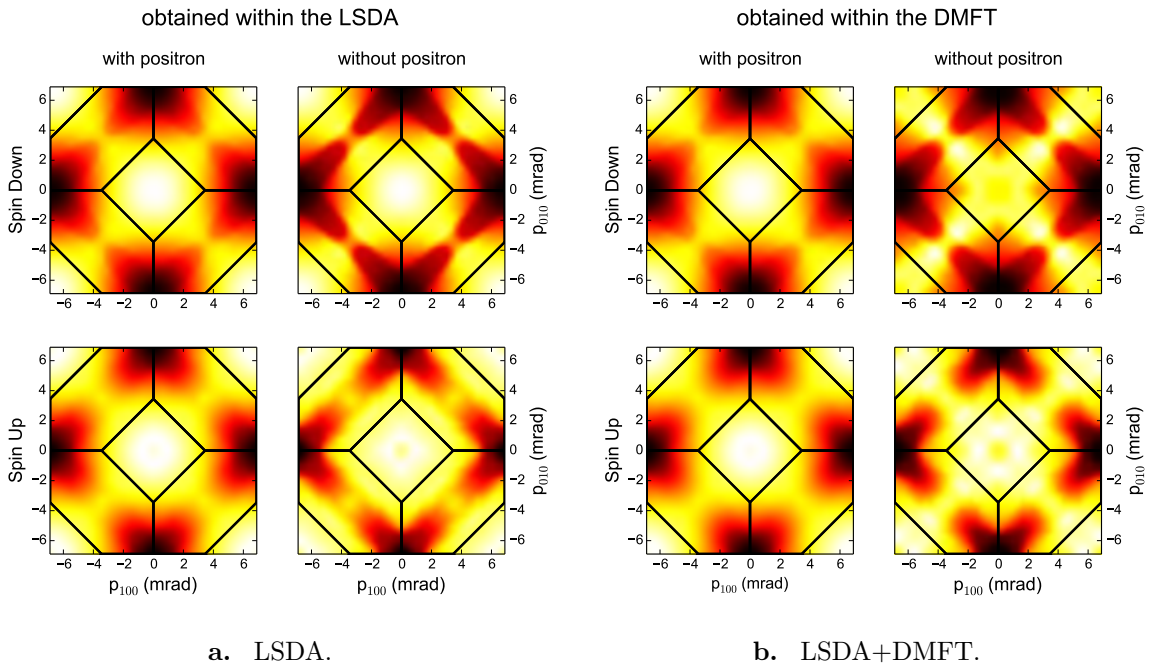


Figure 6.9.: *a)* Study of the positron wave function effects within the pure LSDA and *b)* LSDA+DMFT spin-resolved electronic momentum densities.

One can observe in figure 6.10 a) that in the absence of dynamic electronic correlations the spin-contrast remains essentially the same along the symmetry lines in the Brillouin zone. By contrast, electronic correlations captured by DMFT lead to a clear distinction between the momentum resolved spin-contrast in the presence or absence of the positron.

This supports the qualitative claim of Biasini et al. [BR06, RB07] that in the spin-difference the influence of the positron should be small. Here, it is also shown that the effect of electronic correlations accounted for within the LSDA+DMFT results in an electron momentum density that is a clearly distinguishable from the respective momentum densities obtained within the LSDA. This also holds in the \mathbf{k} -space representation in terms of the LCW-folded projections of the electron momentum density with or without the presence of the positron. The question whether electron-electron correlation effects can be observed within the \mathbf{k} -space representation of positron data is thereby answered positively. We also note that the effects of electron-electron correlations within the LSDA+DMFT on the electron density are anisotropic and therefore go beyond a strictly isotropic Lam-Platzmann [LP74] correction of the LSDA data.

6.6.2. Can polarised positrons be used as a workaround to the enhancement problem?

As stated above Biasini et al. [BR06, RB07] proposed that spin polarized ACAR can be used to avoid positron probe effects in ferromagnetic materials. However, the authors limited their discussion on half metals where only one spin channel is occupied at the Fermi level. Within the investigation of Ni it is tried to assess whether the claims of Biasini et al. are more general in nature. The term "positron probe effects" subsumes the positron wave function and the electron positron correlation effects. Biasini and co-workers demonstrated by means of an exemplary

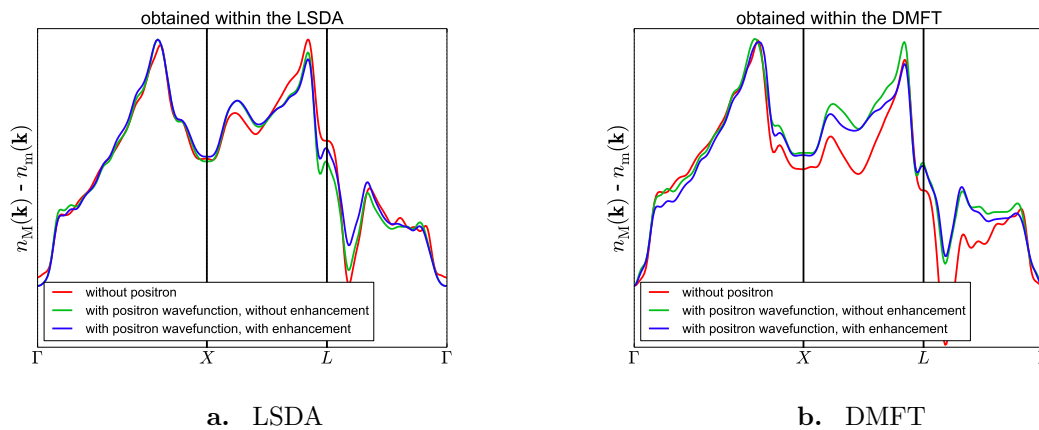


Figure 6.10.: Cut through the magnetic LCW densities along major symmetry points. The effects of the positron wave function alone and the combined influence of the positron wave function together with the electron positron correlations (enhancement) on the magnetic LCW is studied in comparison with pure electron density.

study that by taking the spin difference at least for half metallic materials the positron probe effects can be partially avoided. As the contributions of all paired electrons are cancelled out one ends up only with the signal of all unpaired electrons. These electrons are located at the Fermi surface and are highly mobile. Biasini et al. also proposed to apply a magnetic LCW back-folding procedure to compare the theory model to the experimental data. In this case, magnetic LCW simply means that the difference of the individual LCW-projections [LCW73] for spin up and spin down is taken. As the LCW-procedure is a linear transformation this is equivalent to applying the LCW to the spin-difference spectrum.

Electron positron correlation effects are due to the screening of the positron charge when it is immersed in an electron gas. In general the more mobile electrons, which predominantly take part in the screening of the positron charge, are located near the Fermi surface. As a result, these electrons are more likely to participate in electron-positron annihilation, which again leads to an over-representation of said electrons. From the theoretical point of view this problem is difficult to tackle since a true many-particle description of the electron and positron density is necessary to calculate the enhancement. Different ways to parametrize the enhancement factor have been proposed in literature, with the most successful having been developed by Jarlborg and Singh [SJ85, JS87] as well as by Boronski and Nieminen [BN86] in the 1980s. A more recent treatment of the enhancement problem by Laverock et al. [LHAD10] extends the Jarlborg-Singh approach by a state-dependent component so that electronic states with different angular momentum can be treated separately. A way to solve the many-body problem of electron-positron correlation directly was presented by Makkonen [MESH14] et al. and a comprehensive overview of the theoretical treatment can be found in references [KSS14b] and [KSSB12].

It is maintained, that in 2D-ACAR the state-dependent nature of the enhancement has always to be taken into account. By taking the magnetic difference of two measurements, one with the sample magnetisation aligned parallel to the positron spin orientation and one with the sample magnetisation aligned anti-parallel, the effects of all paired electrons not contributing to the magnetism are cancelled out. The remaining signal originates only from the unpaired electrons.

Considering, for example, an energy dependent enhancement proposed by Jarlborg and Singh [JS87] or Mijnders and Singru [MS79] it can be argued that the energy difference for the paired electrons in the majority/minority bands is given by the Stoner splitting and hence, the enhancement can be assumed to be constant and the strong electron-positron correlation effects present in nickel [KSSW⁺75] could be eluded. However, this is only the case either when the splitting is small or the distance of the band to the Fermi energy is constant. In the present study it is apparent in the variation of χ^2 (as can be seen in figure 6.6) that the enhancement cannot be treated as constant in magnetic ACAR. Having said that, the claims of Biasini cannot be extended to arbitrary ferromagnetic materials. However, with regard to the present results at least the effects of the non-uniform sampling of the electrons by the positron wave function plays a minor role in magnetic ACAR.

6.7. Conclusion

It has been shown that spin-polarized 2D-ACAR is a powerful tool to investigate the electronic structure of ferromagnetic systems. By use of this technique major issues with the interpretation of 2D-ACAR data due to probe effects of the positron could be avoided. Moreover, the strength of magnetic 2D-ACAR becomes apparent due to the higher information content of the two-dimensional data than in Compton scattering. Electron-electron correlation effects in Ni were clearly observed in the 2D-ACAR spectra. The Hubbard U could be determined quantitatively by variation of the electron-electron correlation strength in DMFT calculations and the comparison with the experimental results. For Ni, a value for $U = 2.0$ eV was found to give the best agreement between data and theory.

7 Chapter 7.

Defect studies

7.1. Time dependent radiation damage in SiO₂

Defect studies are readily conducted by applying positron annihilation techniques such as positron annihilation lifetime spectroscopy or Doppler broadening of the annihilation radiation spectroscopy. This is due to the fact that the positron as a probe particle is very sensitive to imperfections in the crystalline structure of the sample material. These techniques are usually considered as a non-destructive method, as the incident positron energies as well as the typical positron flux is too low to cause detectable damage in the sample. However, during 2D-ACAR measurements that were performed on single crystalline quartz to determine the angular resolution as described in 3.2.3, dark traces could be observed on several specimens of the measured quartz samples after the samples were taken out of the spectrometer as can be seen in table 7.1 and in detail in figure 7.2. However, the dark traces did not appear on every sample. Traces were found and the artificially grown samples SiO₂-001, SiO₂-002, SiO₂-003 and on the natural grown quartz sample SiO₂-005, so it can be concluded that the growing procedure plays no role in this case. These dark traces were also observed in a study on electron beam irradiation damage by Das et al. in 1974 [DM74].

A detailed inspection of the 2D-ACAR data taken on the freshly polished sample SiO₂-001 (see figure 7.2), which showed the highest average positronium yield determined by the relative intensity of the narrow peak in the 2D-ACAR spectrum. It revealed that the positronium fraction in the spectrum exhibits a time dependence, as can be seen in figure 7.1. The data was taken in list mode and divided into spectra with 3 hours accumulation time each. Then the individual 2D-spectra were fitted with two elliptical two-dimensional Gaussians which as shown for a cut through the data in figure 7.1 a). As expected, the two components of the broad Gaussian are identical within the error limits since the anisotropy of the resolution function is negligible in this regime. As can be seen in figure 7.1 b) the overall intensity of the narrow component decreases with time while its width stays constant. The intensity of the narrow component decreases within the first 24h by 8.1(1)% until it reaches its saturation value of 0.137(3).

The damage caused in quartz by irradiation with light charged particles such as electrons or positrons is assumed to be twofold: (i) displacement of individual atoms which causes the black marks and (ii) ionisation damage which produces amorphous regions within the crystal lattice [DM74]. Weissmann and Nakajima go even further and attribute the black colouring to

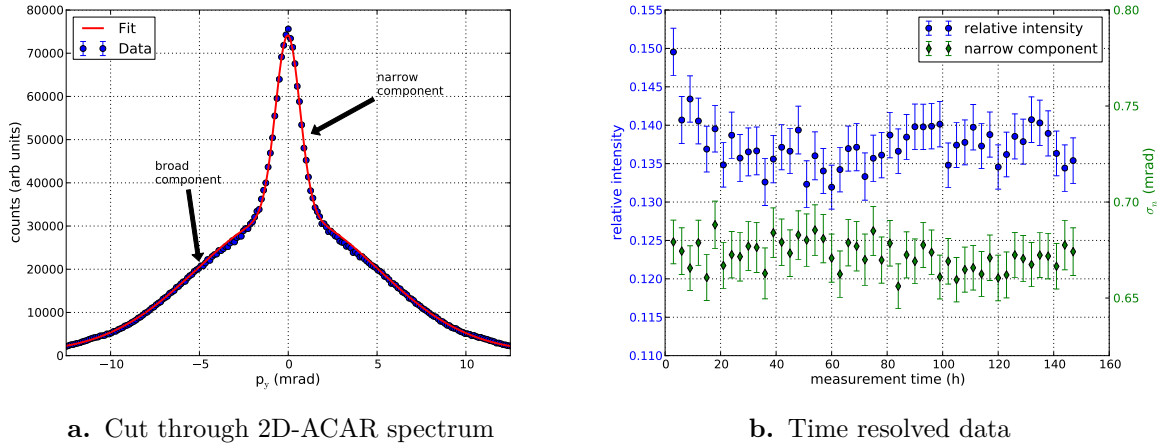


Figure 7.1.: a) Cut through the 2D-ACAR spectrum along $p_x = 0$ together with the fit of the data. b) Results of the time dependent analysis of the 2D-ACAR spectrum of the single crystalline SiO_2 sample 001 shown in figure 7.2. The relative intensity together with the width of the narrow component is plotted against the measurement/irradiation time.

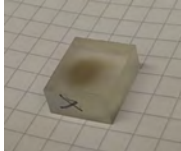
silicon enriched interstitial clusters [WN63]. In a 2D-ACAR experiment both damage types, displacements and ionisation, lead to a reduced positronium formation. Displacement type defects act as trapping centers for the positrons and thus capture thermalized positrons before they can form positronium. Ionisation decreases the long-range order of the crystal and therefore prevents the positronium to form a delocalized Bloch-state in the crystal. The subsequent annihilation of positronium from the localized bulk-state leads to a broader contribution in the 2D-ACAR spectrum. Hasegawa et al. showed that this contribution can be clearly distinguished from the self annihilation in the delocalized state [HTF⁺96].

In the present case no significant change in the width of the narrow component was observed (see figure 7.1 b)). This clearly shows that ionization damage only plays a minor role. Moreover, the decrease of the intensity in the narrow component corresponds to less formation of positronium. Hence, it is concluded that the main defect type created by irradiation of quartz with positrons from a ^{22}Na source are or vacancy-like defects.

This is supported by kinematic considerations for elastic scattering of high energetic positrons on SiO_2 . The formation of silicon or oxygen vacancies with a formation energy $E_{\text{vac}} \approx 8$ eV is only possible for positron energies higher than $E_{e^+} > 59$ keV for oxygen and in case of silicon for energies $E_{e^+} > 103$ keV. The values for the dislocation formation energies found in literature (see for example [PI97]) vary by ± 2 eV so this consideration serves as a rough estimate. The mean positron energy of the ^{22}Na spectrum is 215 keV so the formation of vacancies is energetically possible.

When the positron atom scattering cross section is considered constant an exponential distribution of the vacancies is expected which approaches zero at $\approx 700 \mu\text{m}$ below the surface. After $\approx 700 \mu\text{m}$ the positron energy is below the dislocation formation threshold due to the continuous energy loss in the material. The observation that the decrease saturates after ≈ 30 h suggests that mainly the surface region is affected by the irradiation damage. In order to further investigate this phenomenon depth dependent Doppler broadening and positron lifetime experiments are desirable.

Table 7.1.: Single crystalline α -Quartz samples.

Sample number	Counts	positronium yield	observable radiation damage	optical image
SiO ₂ -001	$458.5 \cdot 10^6$	13.7(3) %	yes	
SiO ₂ -002	$127.0 \cdot 10^6$	7.4(1) %	yes	
SiO ₂ -003	$131.6 \cdot 10^6$	3.2(1) %	yes	
SiO ₂ -004	$210.9 \cdot 10^6$	7.1(1) %	no	
SiO ₂ -005	$52.9 \cdot 10^6$	6.0(3) %	yes	
SiO ₂ -006	$10.7 \cdot 10^6$	5.2(4) %	no	crystal broken
SiO ₂ -007	$186.9 \cdot 10^6$	3.4(2) %	no	
SiO ₂ -008	$54.7 \cdot 10^6$	11.6(2) %	no	

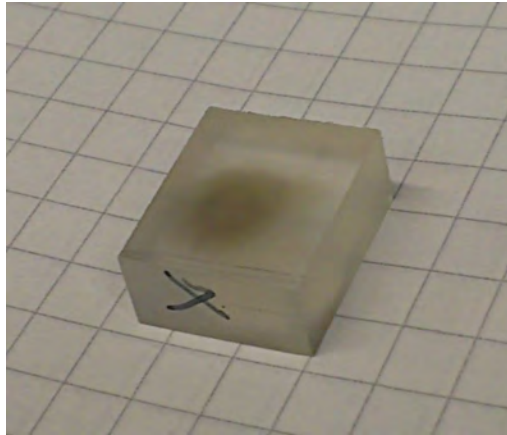


Figure 7.2.: Optical image of the single crystalline SiO₂-001 sample. A dark region can be observed in the sample surface which was created during the irradiation with high energy positrons. The marked side is perpendicular to the c-axis.

7.2. Defects in Heusler compounds studied with DBAR and 2D-ACAR

As discussed in section 2.2 the longitudinal component of the momentum of the annihilating pair results in a Doppler shift of the 511 keV annihilation energy. Due to the limited energy resolution of the high-purity germanium detectors used for DBAR which is typically in the order of 1.4 keV contribution from delocalized electrons, like conduction and valence electrons, cannot be distinguished. However, it is possible to differentiate the delocalized electrons from the more tightly bound core electrons which exhibit a larger Doppler shift. In a DBAR measurement the contributions from the valence and the core electrons are assessed by a line-shape parameter of the annihilation line, the so-called S-parameter. It is defined by the ratio of two regions of the annihilation line as $S = \frac{A}{A+B}$ as shown in figure 7.3. An increasing S-parameter corresponds to an increasing defect concentration in the most simple case. When a positron is trapped in an open-volume defect the overlap of the positron with core electrons is reduced while the probability of annihilating with a valence electron is enhanced. This way the average measured Doppler shift is less when the positron annihilates from a defect site which leads to higher S-parameter. For details on the technique of DBAR see references [Pik12] and [Sta08]. For the study of the Heusler crystals Fe₂TiSn and Ni₂MnGa the Doppler spectrometer at the NEPOMUC beamline was used [SHS08]. This spectrometer uses a monoenergetic positron beam which allows the variation of the implantation energy between 1 keV and 30 keV and also features a heatable sample holder which can achieve temperatures of up to 600 °C [RPH13]. By varying the implantation energy the evolution of the S-parameter from the surface to the bulk can be studied by so-called S(*E*)-profiles, which are related to the positron mobility in the sample. From the transition from the bulk to the surface value the positron diffusion length can be determined which can in turn be converted into a quantitative estimate for the defect concentration. Due to the high intensity of the NEPOMUC beam these S(*E*)-profiles can be measured in-situ while heating the sample. It was demonstrated by Oberdorfer et al. [OSS⁺10] that this can be used to study the annealing process of bulk materials in-situ. Reiner et al. [RPH12] further refined this method to study the annealing in thin metallic films. Fe₂TiSn

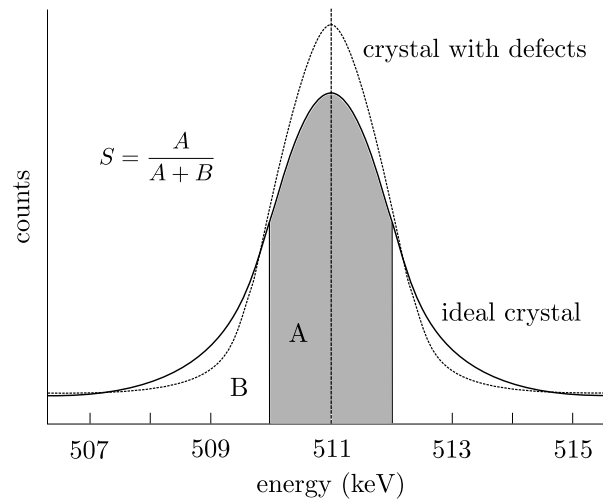


Figure 7.3.: Illustration of the determination of the S-parameter of the annihilation line. To minimize the statistical error the regions A and B are defined in a way that $S = 0.5$. (Illustration adapted from reference [Sta08])

and Ni_2MnGa both show remarkable features in their temperature dependent behaviour which is discussed in the following.

7.2.1. Fe_2TiSn

Introduction

The Heusler compound Fe_2TiSn is of high interest for both theoretical and experimental reasons [GFP11]. Fe_2TiSn is a strong candidate for zero-gap semiconducting behaviour [DBS⁺02] in a transition metal compound at the border of a ferromagnetic quantum critical point. Density functional band structure calculations for an ordered crystal yield a non-magnetic ground state and a pseudogap at the Fermi level [Sle06]. A temperature dependent defect study on a stoichiometric, single-crystalline Fe_2TiSn sample was performed applying the DBAR technique. The S-Parameter of the annihilation line serves as a relative measure for the electron momentum density at the positron annihilation site. The variation of the S-Parameter from the surface to the bulk value allows the calculation of the positron diffusion length, which is a very sensitive measure for the defect concentration in the sample. Both, the surface to the bulk value of the S-Parameter are characteristic for a sample in a given state.

Investigation of the annealing behaviour

The Fe_2TiSn sample was supplied by A. Neubauer [Neu11] from the crystal growth group of E21 Physics Department at TUM. The crystal was grown using an optical float zoning technique [NBB⁺11]. The side of the sample facing the positron beam was polished to ≈ 10 nm surface roughness. This is crucial for Doppler measurements at a positron beam. Due to the limited implantation depth one has to be sure that the surface signal is not affected by unwanted defects caused by sample cutting and preparation. The sample was cleaned for 20 min in 1 M hydrochloric acid and afterwards cleaned with isopropanol. The time between cleaning and

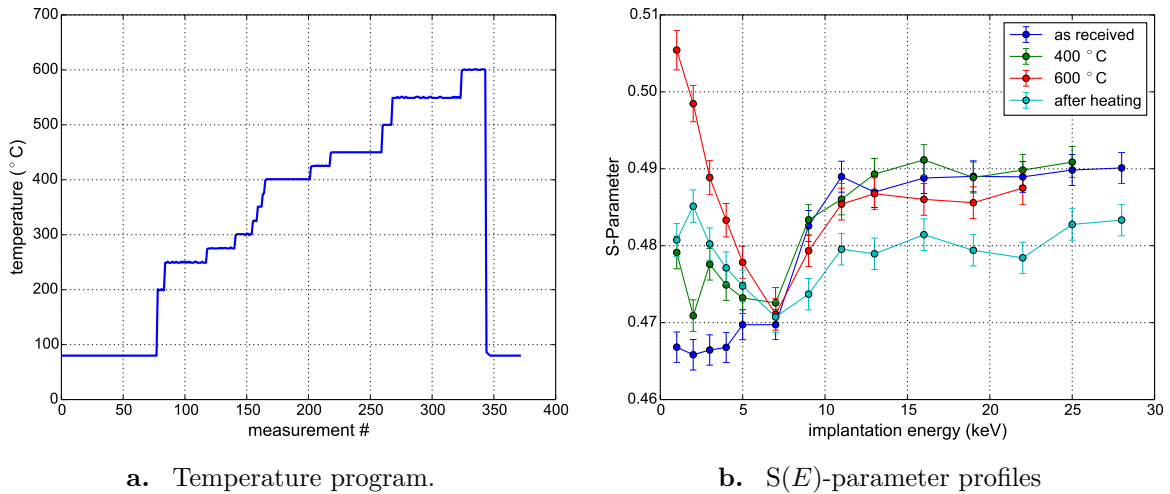


Figure 7.4.: a) Temperature cycle that was performed during the measurement of Fe_2TiSn . b) Comparison of the $S(E)$ -profiles before and after the tempering process. While before the heating cycle no variation in S is observable, a typical $S(E)$ -profile is found after the heating cycle with a decreasing $S(E)$ -Parameter from the surface to the bulk.

mounting the sample inside the vacuum chamber was less than 3 min before a vacuum better than 10^{-2} mbar was achieved. The vacuum during the experiment was in the range of 10^{-7} mbar.

While measuring the surface and bulk S -parameter the sample was heated. The temperature program is shown in figure 7.4 a). The surface and bulk S -parameter were measured alternately at least four times each at every temperature step. In addition full $S(E)$ -profiles of the available energy range between 1 – 28 keV have been measured before and after the heating cycle and at two different elevated temperatures 400 °C and 600 °C (see figure 7.4 b)).

The obtained spectra were analysed in the usual way regarding background correction and the definition of the energy windows for the calculation of the S -parameter. Figures 7.5 a) and 7.5 b) show the evolution of the surface and bulk S -parameter during the heating cycle.

While the bulk S -parameter returns to a value even below its original value after heating, the surface S -parameter shows a hysteresis as the final value is higher than initial value. At around 400° the bulk S -parameter drops significantly. At the same temperature the surface S -parameter begins to steeply increase with increasing temperature. As can be seen in figure 7.4 b) the initial $S(E)$ profile exhibits a monotone transition from the lower surface to the higher bulk value. After the temper process the $S(E)$ -profile shows a non-monotone transition with a local minimum which cannot be explained in a two-state model with only a surface and bulk S -parameter.

In addition, the hysteresis in the S -parameter is only present for the surface value (see figure 7.5 a)). This behaviour is attributed to a structural change or a variation in the composition only at the surface of the crystal. It is known from magnetisation measurements with differently treated samples that iron-rich precipitates are formed at grain boundaries or at the surface of a Fe_2TiSn crystal [Neu11].

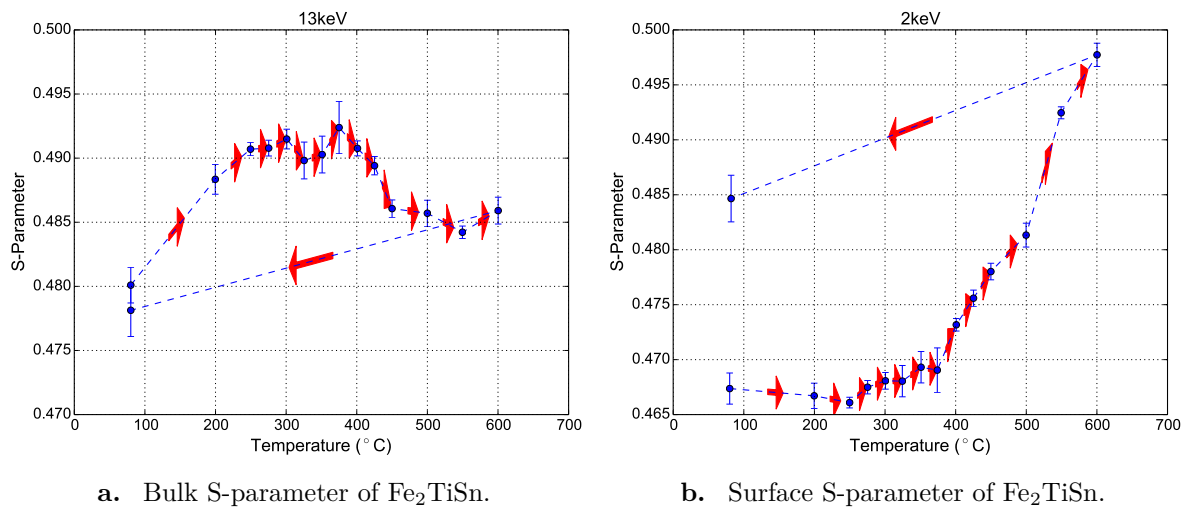


Figure 7.5.: a) Evolution of the bulk S-parameter of Fe₂TiSn obtained at an implantation energy of 13 keV as a function of temperature. Note the significant breakdown in the S-parameter at 400 °C. b) Evolution of the surface S-parameter of Fe₂TiSn obtained at an implantation energy of 2 keV as a function of temperature. Note the significant increase in the S-parameter up to 600 °C which is due to thermally activated positronium formation at the surface.

Comparison with 2D-ACAR measurements

The 2D-ACAR measurements on Fe₂TiSn were performed with the ACAR spectrometer at TU Delft. This spectrometer combines a conventional 2D-ACAR setup with ²²Na source (see section 3.1) with the POSH positron beam [Kru99]. This way, due to the different implantation characteristics (see figure 7.8 b)) the ACAR signal originates to 99 % from the bulk for the conventional setup and up to 35 % from the surface or sub-surface region for the 7.5 keV POSH beam. The implantation profiles were calculated using Markovian implantation profiles. The combination of these two methods allows for the separation of surface and bulk effects.

For the 2D-ACAR measurements the sample was cut from the same rod as that was used for the DBAR studies, however it was not subjected to any annealing procedure or heat treatment. The crystal was cut in a way that the [110] direction faces towards the positron beam and was orientated using Laue diffraction in a way that the integration direction is along [100]. This direction corresponds to a four-fold symmetry, which is expected in the data. For the measurements with the Posh beam $72 \cdot 10^6$ counts were collected over the course of two weeks with 5.5 days of active data taking. After the reactor was shut down for the summer break the sample was switched to the conventional setup and ca. $20 \cdot 10^6$ were collected with 12 days of active data taking.

Afterwards the data was corrected for the momentum sampling function and the isotropic part was subtracted in order to study the anisotropy. The two- and one-dimensional anisotropies for the surface region obtained with the POSH beam are shown in figure 7.6 and the two- and one-dimensional anisotropies for the bulk data are given in figure 7.7. The relative strength of the anisotropic contribution to the overall spectrum is about a factor of 100 times lower than for comparable Heusler systems [HBB⁺15] which hints at an elevated defect concentration but still lower than the saturation trapping threshold of $\approx 2 \cdot 10^{-3} \frac{1}{\text{atom}}$ [KRL99].

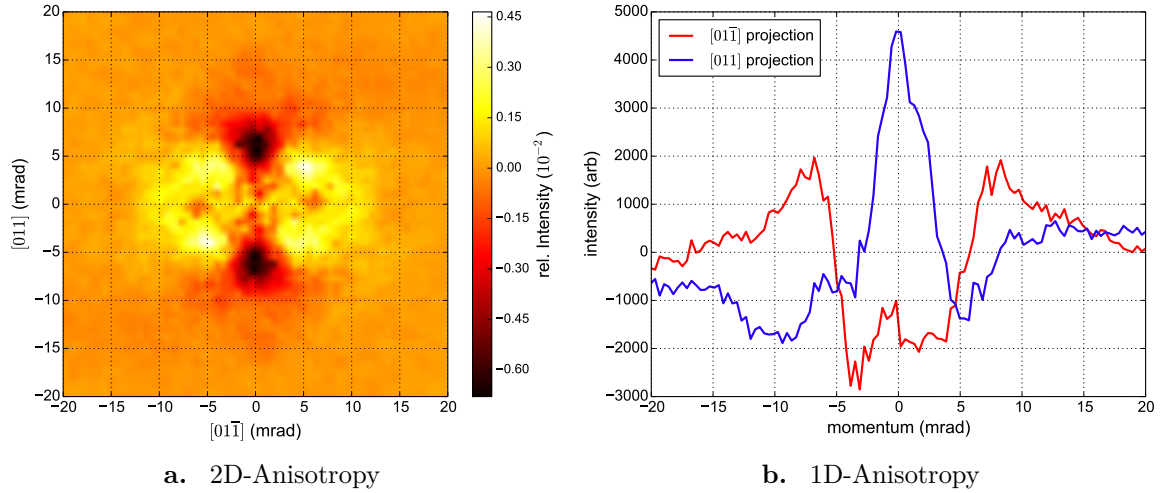


Figure 7.6.: a) Two-dimensional anisotropy of Fe_2TiSn obtained with the POSH beam at an implantation energy of 7.5 keV. b) Anisotropy integrated along major symmetry directions. With the expected symmetry of the $[100]$ direction the two projection should be equivalent.

Note that even by eye the POSH data appears clearly two-fold symmetric while in the two-dimensional bulk data a stronger four-fold symmetry seems to be present. However, with regard to the one-dimensional profiles (see figure 7.7 b)), which should be equivalent besides a small deviation from the asymmetric resolution function, also the bulk data exhibits not the full expected four-fold symmetry. One has to keep in mind that the two-dimensional projection will always exhibit a two-fold symmetry due to the inversion symmetry which is always given. In order to get a quantitative estimate on this symmetry breaking by the normalized autocorrelation for the data D as a function of the rotation angle α is calculated by the sum over the quadratic distance between the original and the rotated data according to:

$$E(\alpha) = 1 - \frac{\sum_{i,j} (D_{i,j} - \text{rot}(\alpha, D)_{i,j})^2}{\sum_{i,j} (D_{i,j} - \text{rot}(0, D)_{i,j})^2}. \quad (7.1)$$

When the rotation transform is applied to data with square shape, this is easily possible for rotation angles multiple of 90° . For different angles one has to rely on interpolation methods. In this case a bi-cubic interpolation is used and at each step the conservation of the integral number of counts is checked and, if necessary, corrected by scaling. The results of this analysis are given in figure 7.8 a). For a system with inherent n -fold symmetry one expects maxima in $E(\alpha)$ for $\alpha = k \cdot \frac{2\pi}{n}$ with $0 < k \leq n$. Due to the asymmetric resolution function any discrete rotational symmetry for $n \geq 2$ is broken. To assess this effect perfectly four-fold symmetric data is artificially generated by summing over four discrete 90° rotations. This data is then convoluted with an elliptic two-dimensional Gaussian kernel with $\sigma_x = 0.47$ mrad and $\sigma_y = 0.60$ mrad (values from [Fal02]) according to the asymmetric resolution function. With this a value of $E(90^\circ) = 0.88$ is found which is further assumed to give the upper limit for $E(90^\circ)$ for the real data. As can be seen in figure 7.8 the bulk value for E is with $E_{\text{bulk}}(90^\circ) = 0.56$ significantly larger than the surface value of $E_{\text{surface}}(90^\circ) = 0.17$. Systematic effects from misalignment of the sample cannot account for this strong deviation, especially as the sample was orientated and

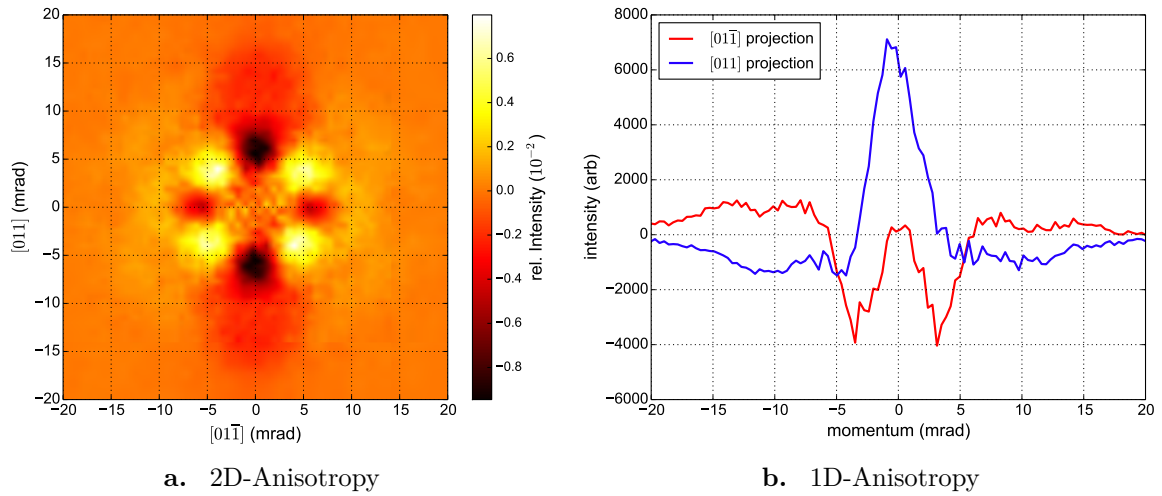


Figure 7.7.: a) Two-dimensional anisotropy of Fe_2TiSn obtained with the conventional ACAR setup. In this case the mean implantation energy of the ^{22}Na source is 215 keV. b) Anisotropy integrated along major symmetry directions. With the expected symmetry of the $[100]$ direction the two projections should be equivalent.

mounted in the same way in both sample chambers. A surface value about three times lower than the bulk value indicates that the expected four-fold symmetry of the electronic structure is broken in particular at or near the surface.

When these results are put into perspective by comparison with the DBAR results of section 7.2.1 it appears more the justified to assume the surface of the Fe_2TiSn crystal is susceptible to changes in the composition and or structure, although in the Laue diffraction no deviation from the expected $L2_1$ diffraction pattern was observed. In the Doppler $S(E)$ -profiles the most prominent change appears in the surface region and also this change is more pronounced when the material is heated to higher temperatures (see figure 7.4 b)). The fact that the surface S -parameter shows a hysteresis is also a strong hint that a structural change occurs at the surface (see fig7.11 a)). Using the $S(E)$ -profiles the depth of the affected region can be calculated from the implantation profiles. This systematic effect is observable for implantation energy up to 8 keV which corresponds to a mean depth of 320 nm. This also explains the fact that the ACAR spectrum that was obtained at the beam for an implantation energy of 7.5 keV cannot be decomposed into a linear combination of a bulk spectrum and an arbitrary two-fold symmetric spectrum. From the implantation profile (see figure 7.8 b)) one would assume a combination of 35 % surface and 65 % bulk respectively. However, this decomposition fails as the ACAR spectrum contains practically no bulk contribution.

A. Neubauer [Neu11] found by means of EDX and SEM that in the growth of Fe_2TiSn crystals an iron-rich phase is formed at the grain boundaries. This phase was identified with $\text{Fe}_{68}\text{Ti}_{25}\text{Sn}_7$ and also gives rise to a strong signal in magnetisation measurements. The magnetisation signal also appears for single crystals but can be suppressed when the sample is etched and kept under vacuum. When the sample is kept in air the magnetisation signal attributed to the foreign phase reappears. The sample that was measured in Delft with 2D-ACAR was kept in air most of the time so it safe to assume that this foreign phase was formed on the surface in the time

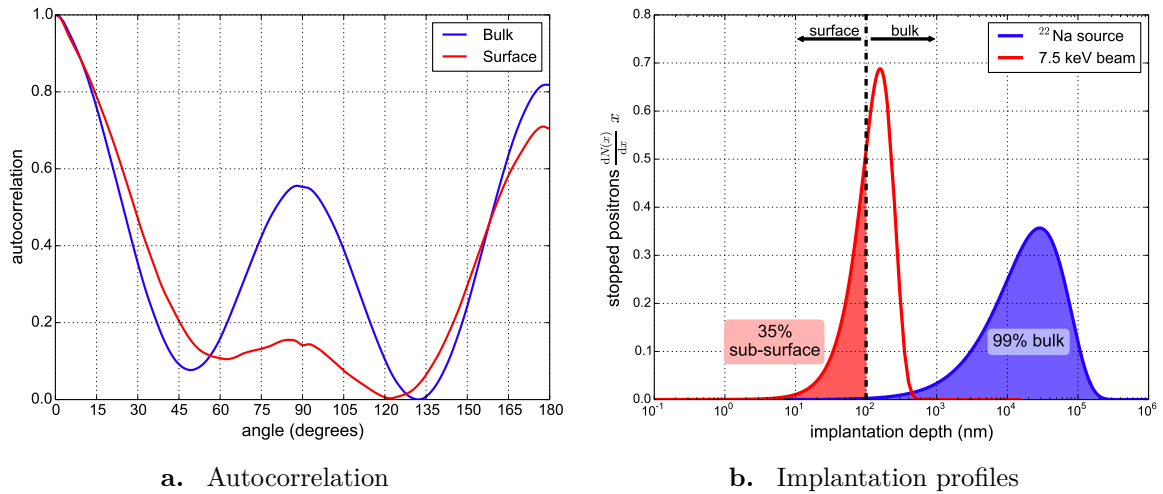


Figure 7.8.: a) Autocorrelation of the anisotropy for the data obtained with the POSH and the conventional setup. For 4-fold symmetric data the maxima are expected to occur in intervals of 90° . This behaviour is more pronounced in the conventional data. b) Comparison of the implantation profiles for the POSH beam and the conventional setup using a ^{22}Na source. The criterion to distinguish between surface and bulk is chosen at 100 nm according to the typical positron diffusion length in a perfect crystal. The probability to diffuse back to the surface is practically zero for positrons which are implanted deeper than 100 nm.

(≈ 2 weeks) after polishing the sample. In the first DBAR measurement (see figure 7.4 b)) the effect of the foreign phase is not observed as this sample was etched right before mounting in the spectrometer.

Conclusion

Doppler broadening spectroscopy and ACAR measurements were applied to study the crystal quality and the electronic structure of Fe_2TiSn . It was found that the properties at the surface and in a near surface region to a depth of up to 320 nm are affected by the growth of an iron-rich foreign phase. This foreign phase is formed when the sample is subjected to air as well as in vacuum at higher temperatures.

From the temperature dependent Doppler measurements it is found that first changes at the surface appear at $\approx 400^\circ\text{C}$. This means that the standard procedure of recrystallisation at elevated temperatures when dealing with defect rich Fe_2TiSn samples has to be reconsidered. As the material decomposes at higher temperatures annealing is out of the question, therefore it is crucial to obtain defect free samples directly from the growth.

By a fit of the $S(E)$ profiles (see figure 7.9) the positron diffusion length can be obtained [HBB⁺15] which can be used to determine a quantitative value for the defect concentration. In the present case Hugenschmidt et al. [HBB⁺15] determined the defect concentration in the Fe_2TiSn samples using estimated values for the positron lifetime. A positron diffusion length of 13 nm respectively 19 nm was found. Using an estimation for the bulk positron lifetime of 120(20) ps this corresponds to a defect concentration in the range of $1.6 \cdot 10^{-4}$ to $1.6 \cdot 10^{-3}$ per atom.

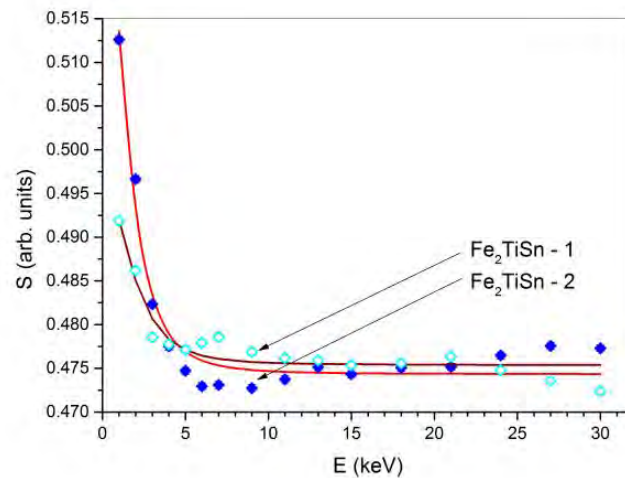


Figure 7.9.: Measured $S(E)$ profile fitted with a theoretical positron diffusion model (taken from [HBB⁺15]). The curve labelled $\text{Fe}_2\text{TiSn-1}$ corresponds to the sample that was subjected to the heat treatment. The curve labelled $\text{Fe}_2\text{TiSn-2}$ corresponds to the sample that was investigated by means of 2D-ACAR.

7.2.2. Ni_2MnGa

Introduction

Ni_2MnGa is a magnetic shape memory alloy and has therefore attracted attention from both theory and experiment [UHK⁺96]. Further knowledge on the properties of this system is needed in order to make it applicable for industrial use [MGP⁺13]. One aspect is the role of the electronic structure, i.e. the shape of the Fermi surface, at the martensitic phase transition which is sought to be accountable for the strong magnetic field induced strain. 2D-ACAR measurements are the method of choice for this investigation at the transition occurs at temperatures up to 110 °C [HWL⁺12]. The transition temperature has a strong dependence on the stoichiometry of the sample.

However, the growth of stoichiometric, defect-free crystals that are essential for ACAR is challenging. Therefore, one has to rely on annealing in order to get high quality single crystals. In this study the behaviour of Ni_2MnGa is studied during a heating cycle by means of temperature dependent DBAR measurements.

Doppler study of the annealing process

The Ni_2MnGa sample was supplied from the metal physics group at E13 at the physics department of TUM. The sample was prepared, as usual for 2D-ACAR measurements, by polishing the [110] cut surface to 50 nm surface roughness. Subsequently the sample was electro-chemically etched and kept sealed until the measurement.

The DBAR study of the annealing behaviour was carried out at the Doppler spectrometer at MLZ. As described in section 7.2.1 this spectrometer is particularly well suited for the study of annealing processes. The general procedure for this measurement was almost analogue to

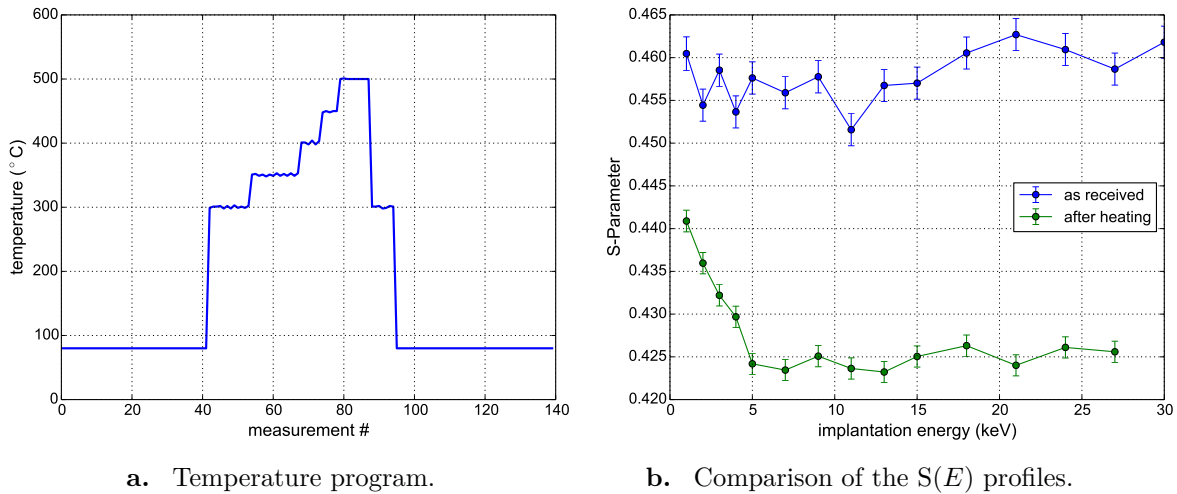


Figure 7.10.: a) Temperature cycle that was performed during the measurement of Ni_2MnGa . b) Comparison of the $S(E)$ -profiles before and after the tempering process.

the Fe_2TiSn measurement. Full $S(E)$ -profiles were recorded at the begin and at the end of the heating cycle and single S -parameter measurements of the bulk at 21 keV and of the surface at 4 keV were made throughout the heating cycle four times at each temperature point and in an alternating order. For technical reasons it was not possible to measure $S(E)$ -profiles at temperatures above 500°C . The temperature steps in this measurement were wider than for Fe_2TiSn (see figure 7.4 a) and figure 7.10 a)) because no significant effect was expected below the B2 transition where the Mn and the Ga atoms become fully disordered and therefore the diffusive mobility for vacancy-type defects is increased. From calorimetric measurements the temperature for this $L2_1$ to B2 transition was expected in the vicinity of 600°C [MGP⁺13].

Although temperatures above 500°C could not be reached even at lower temperatures interesting effects could be observed. The evolution of the bulk (see figure 7.11 b)) and the surface S -parameter (see figure 7.11 a)) shows the same trend. No change in the S -parameter is observed until a temperature of 450°C was reached then both the surface and bulk value drop significantly and then basically stays constant for the rest of the temper program. When cooling the sample back to room temperature the S -parameter decrease slightly. However, the variation from 500°C to 30°C is about three times larger than the variation in the S -parameter between 30°C and 500°C .

This is also reflected in the $S(E)$ -profiles taken before and after the heating cycle (see figure 7.10 b)). A virtually constant $S(E)$ -profile before the heating means that practically no positron diffusion takes place which gives rise to the assumption of a very high defect concentration. After the heating cycle the $S(E)$ -profile shows the typical monotonous transition from the surface to the bulk value.

From changes in the S -parameter alone it is difficult to draw conclusions on the processes that occur in the sample during the heating process. Therefore, the so called W -parameter (W stands for wing), which is defined by the ratio between the wing region and the total, is taken. In the analysis the windows for the W -parameter were defined in such a way that statistical error for both parameters are approximately equal. From the combined information in the S

and W-parameter one can infer to shifts of the higher momenta of the annihilation line. This is done by so-called S-W-plots where both parameters are plotted against each other. A detailed example of such an analysis can be found in reference [RPH14]. These higher momenta of the annihilation line are characteristic for annihilation from a specific defect site so that a change in the S-W-slope gives strong evidence for the formation or disappearance of a positron trapping site.

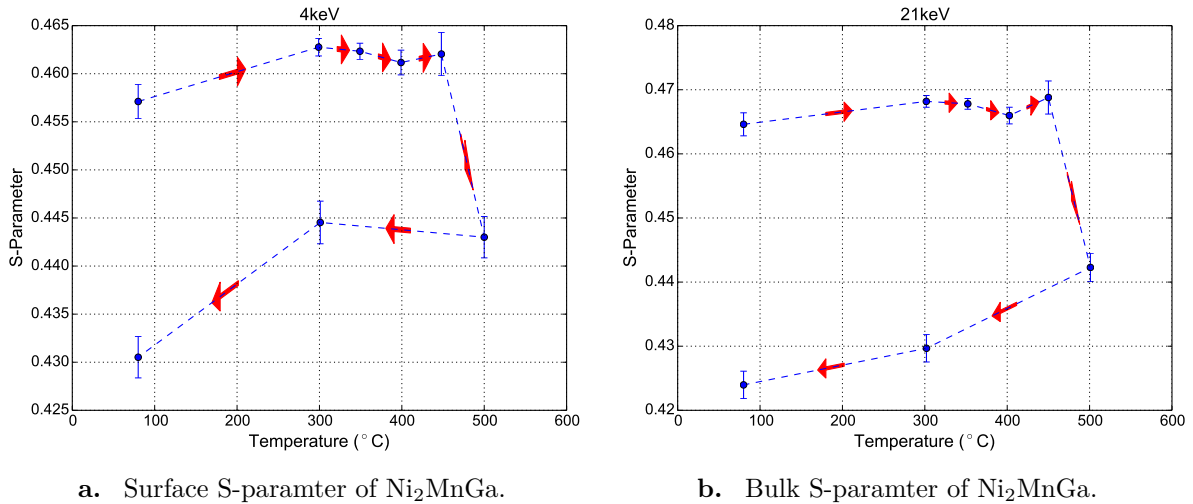


Figure 7.11.: a) Evolution of the surface S-parameter of Ni₂MnGa obtained at an implantation energy of 4 keV as a function of temperature. Note the significant breakdown in the S-parameter at 500 °C. b) Evolution of the bulk S-parameter of Ni₂MnGa obtained at an implantation energy of 21 keV as a function of temperature. Note the similar significant breakdown in the S-parameter at 500 °C.

In figure 7.12 a plot of the S-parameter against the W-parameter is shown for the bulk and the surface values. Two almost linear regimes can be identified for the surface as well as for the bulk measurements. The first extends from room temperature up to 450 °C and the second linear regime connects the value at 450 °C to a different room temperature value after heating. The increase in the first regime is interpreted as a combined effect of thermal lattice expansion and thermally activated positronium formation at the surface. This is supported by the fact that the change of the W-parameter is stronger for the surface value. The second regime associated with a decrease of S and an increase in W is attributed to annealing of defects close to the B2 transition temperature.

The transition occurs around 450 °C, due to the coarse temperature steps a more precise determination is not possible. The fact that the transition occurs in the bulk as well as in the surface region gives strong evidence that the state of the entire sample is changed. If this was due to out gassing of Mn from the surface one would first expect for the surface to be affected before the bulk and second that the effect at the surface is stronger. In contrast to this behaviour the relative change in the S and W-parameter is about 23% stronger in the bulk. This also shows that the observed behaviour is clearly a bulk and not a surface effect.

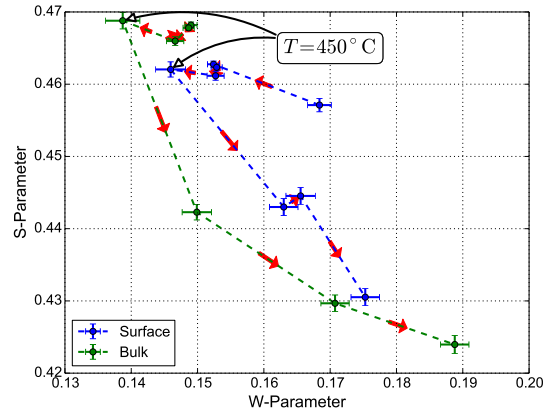


Figure 7.12.: The S-parameter plotted against the W-parameter for the bulk measurements at 21 keV and the surface measurements at 4 keV. The arrows indicate the progress in the the temperature program (see 7.10 a)). At 450 °C the slope changes drastically and even revert its sign.

Conclusion

The behaviour of Ni_2MnGa at elevated temperature differs to that of Fe_2TiSn . This is due to the different kinetics in the Ni_2MnGa system [EMI⁺07]. It was found by Erdélyi et al. [EMI⁺07] that the diffusion speed of gallium in the ordered $L2_1$ phase is strongly temperature dependent and about a factor of four lower than in the disordered B2 phase. This supports the findings of this study: although the sample was not driven over the B2 transition ($T_{B2} \approx 600^\circ\text{C}$) the behaviour of the S versus the W-parameter, i.e. the drastic drop at 450 °C indicates the kinetics in the sample are accelerated which results in an annealing of vacancy-like defects.

8 Chapter 8.

8 Summary and Outlook

Within the course of this work a new 2D-ACAR spectrometer was set up and successfully brought into operation in the experimental hall of the Maier-Leibnitz Laboratory in Garching. The spectrometer has a baseline of 16.5 m and uses standard Anger camera detectors with a spatial resolution of 3.9 mm at 511 keV. It features a unique newly developed magnetic pole piece geometry, which allows for high positron transport efficiency and at the same time accommodates a versatile sample environment in order to vary the sample temperature from 10 K to 650 K. The overall angular resolution of the spectrometer was found to be (1.53×1.64) mrad² FWHM which is in good agreement with the expected estimated value.

In 2D-ACAR the angular correlation of electron positron annihilation radiation is measured. Due to the fact that the positron is fully thermalized at the moment of annihilation the angular correlation originated mainly from the electron momentum. The obtained 2D-ACAR spectra represent a projection of the electron momentum density along one momentum component. Hence, 2D-ACAR is a powerful tool for the investigation of the bulk electronic structure even at elevated temperatures.

The new 2D-ACAR spectrometer was first used to perform temperature dependent measurements of the electronic structure on paramagnetic and SDW state chromium, as the paramagnetic phase is unreachable in quantum oscillation experiments. A thorough investigation of the LCW-folded ACAR data revealed that the most striking change in the electronic structure between the paramagnetic and magnetically ordered system can be associated with the *N*-hole ellipsoid structure of the Fermi surface of chromium. Theoretical calculations in the LSDA resulted in an unresolvable difference between theory and experiment which can be partially improved by accounting for electron-electron correlations. A subsequent investigation of the iso-electronic systems molybdenum and tungsten revealed that in these systems the theory predictions are very accurate, which gives rise to the conclusion that positron probe effects are very strong in chromium and nearly absent in tungsten. A further investigation of a field cooled chromium sample with a single *q*-vector was undertaken in order to find proof for the subtle symmetry breaking of the electronic structure in the magnetically ordered state. However, no significant effect could be observed in either **k**-space or **p**-space analysis which is due to a systematic uncertainties resulting from a change in the anisotropic resolution function.

Since a ²²Na source is used the positrons are partially polarized. The degree of polarisation was determined in a dedicated experiment by measuring the field asymmetry of para-positronium self annihilation in single crystalline quartz which results from the magnetic quenching of

ortho-positronium. This way the degree of polarisation was determined to 0.31 ± 0.04 which is slightly lower than expected for emission into one half space because of positron back reflection from the tantalum backing of the source capsule.

The availability of polarized positron motivated spin-polarized study of the electronic structure on ferromagnetic nickel, which is known for strong electron-electron correlation effects. In this study the spin polarized ACAR data was compared to theoretical calculations within the DMFT where the value for U the local Coulomb repulsion between the electrons was changed. It was found that a value of $U = (2.0 \pm 0.1)$ eV describes the data best. The value is found to be in excellent agreeable with results from Compton scattering experiments. As a main asset of spin polarized ACAR it was found that in magnetic ACAR measurements the positron probe effects of the positron wave function and the electron positron correlation can be partially avoided which allows for the unambiguous determination of U . This shows that spin resolved 2D-ACAR spectroscopy in particular can serve a a powerful benchmark for theoretical calculations.

In the future this method will be used to determine the electronic structure of more complex systems such as Heusler alloys or heavy fermion systems. The unique features of spin polarized ACAR will allow for the determination of the individual sheets of the Fermi surface for majority and minority electron bands.

Once the new experimental hall east at the MLZ is available the spectrometer will be moved there. In the new hall the baseline can be extended to 24 m which will improve the resolution to a level where also the individual Fermi surface sheets of Ni can be observed. The improved resolution will also allow to revisit the investigation in single- q chromium. Also, the NEPOMUC beam will be available in the new experimental hall which will allow for depth resolved measurements of the electronic structure. This adds a whole new quality to the 2D-ACAR measurement since this way the evolution of the electronic structure from the surface to the bulk can be studied as well as multi-layered systems. Hence the long standing issue between ARPES and quantum oscillations whether the electronic structure at the surface represents the bulk properties can be finally resolved.

A

Appendix A.

Determination of the source activity

After the ^{22}Na source (PS168) was delivered the first task was to determine the actual activity of the source to see if the source activity is the same as claimed by the manufacturer (iThemab Labs). In principle this measurement is trivial: by measuring the count rate for the 1275 keV prompt gamma line of ^{22}Na and comparing it to a known reference the source activity can be estimated. As it turned out the precise absolute measurement of such high rates using a gamma spectrometer is not as trivial as initially thought.

Measurements

To determine the activity A of the new ^{22}Na source PS168 two spectra are recorded: one of PS168 and one of a reference source with a known activity A_{ref} . Under the assumption, that the photo-peak efficiency and the branching ratios are the same, which is always the case when the same nuclide is used, the activity is given by:

$$A_{PS168} = A_{\text{ref}} \cdot \frac{\Omega_{\text{ref}}}{\Omega_{PS168}} \cdot \frac{C_{PS168}}{C_{\text{ref}}} \quad (\text{A.1})$$

with Ω_{PS168} and Ω_{ref} the solid angle of the respective detector setup and C_{PS168} and C_{ref} the count rate in the chosen energy window (either 511 or 1275 keV). The solid angle $\Omega = \frac{A_{\text{det}}}{4\pi d^2}$, with the active area of the detector A_{det} and the distance d between source and detector, has to be considered since for practical reasons the distance of the detector to the source could not be kept constant. The used sources are tabulated in table A.1. A schematic view of the setup is shown in figure A.1 and some photographic images are shown in figure A.2. Two different detector types were used: a high purity germanium semi-conduction detector (HPGe) and a BGO scintillation detector. The detector pulses were amplified using an Ortec 972 shaping amplifier and the amplified signal was then digitized using a FastComtec 2020 ADC. So in each measurement the energy spectra of the gamma radiation were recorded. The multi channel analyser that is used to obtain the spectra (FastComtec WebMCA) is matched to the Wilkinson-type ADC which uses a fixed dead time correction of 500 ns per event. The count rate is then determined by the sum under the respective peaks which are corrected by an experimentally determined background spectrum and the live time, the time during which the ADC is not busy, of the measurement. This turned out to be the crucial point of this measurement and will be discussed in the following. The background corrected spectra are shown in figure A.3. As can be seen the

Source	Nuclide	(nominal) Activity
PS168	^{22}Na	1.949 GBq
PS134	^{22}Na	0.605 MBq
PS99	^{22}Na	0.273 MBq
PS87	^{60}Co	94.3 kBq

Table A.1.: Used sources

HPGe has a significantly better energy resolution than the BGO.

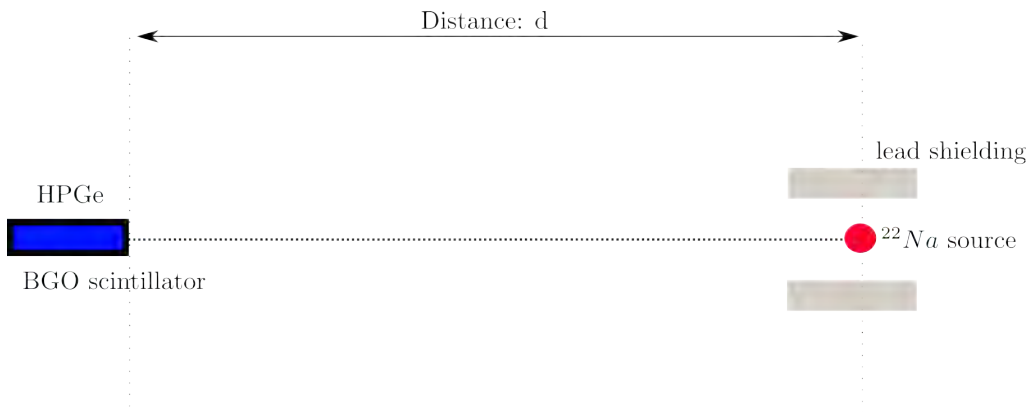


Figure A.1.: Schematics of the measurement setup.

Results of the count rate measurements

The count rate C including the background correction is given by:

$$C = \frac{\int_{E_1}^{E_2} \left(N(E) - \frac{t_{\text{live}}}{t_{\text{BG}}} N(E)_{\text{BG}} \right) dE}{(E_2 - E_1) \cdot t_{\text{live}}}$$

the integral over the respective peak in the gamma spectrum $N(E)$ in the energy window $[E_2 - E_1]$ divided by the live time t_{live} of the detector system. The source activity is then be calculated using equation A.1. The positioning of the energy windows is indicated in figure A.3. The results for the different detectors are shown below.

Scintillator

The values obtained with the scintillation detector are tabulated in table A.2. Using these values the activity of PS168 is by a factor of 4993 ± 7 higher than the activity of PS99, for an energy window around 511 keV and the activity of PS168 is by a factor of 4896 ± 14 higher than the activity of PS99, for an energy window around 1275 keV.

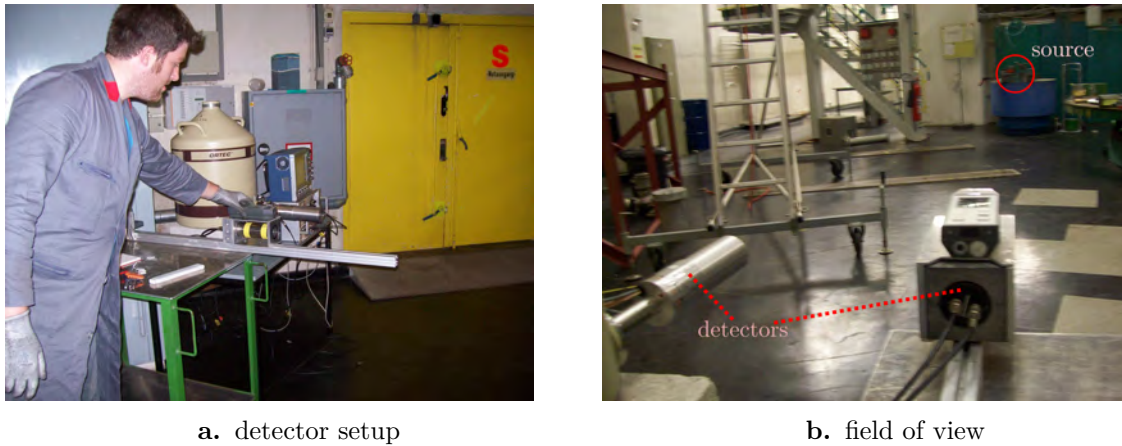


Figure A.2.: Image of the experimental setup in the atomic egg.

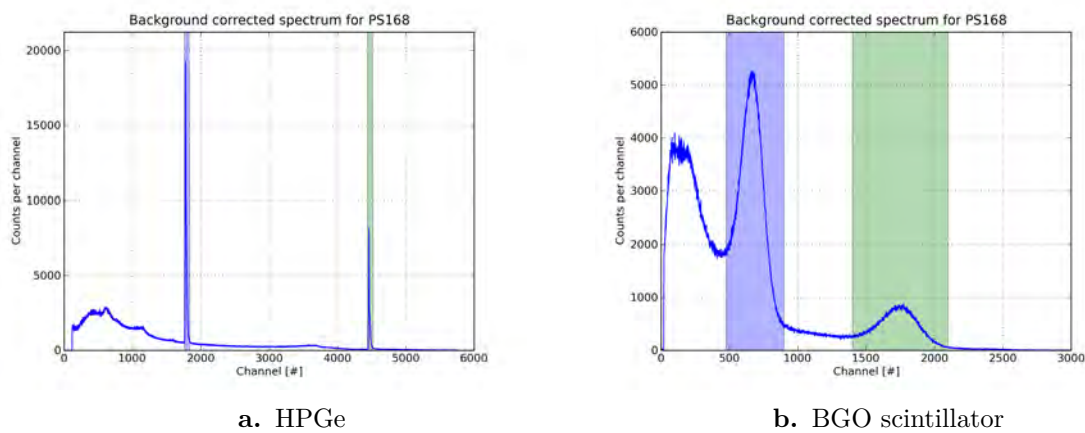


Figure A.3.: Comparison of the spectra recorded with the HPGc and the scintillation detector. The windows used in the analysis are indicated by the shaded areas (511 keV: blue, 1275 keV: green).

HPGe

The values obtained with the HPGc detector are tabulated in A.3. Using these values the activity of PS168 is by a factor of 4331 ± 26 higher than the activity of PS99, for an energy window around 511 keV and the activity of PS168 is by a factor of 4553 ± 51 higher than the activity of PS99, for an energy window around 511 keV.

Preliminary conclusion

The combined results from both detector types lead to an activity of PS168 of : (1.28 ± 0.09) GBq. This value is far off the value given by the manufacturer of 1.95 GBq. The discrepancy cannot be explained by the absorption in air which is about 7.2 % for 1275 keV and about 10.6 % for 511 keV for a baseline of 9.8 m. This can either be explained by the fact that (i) the activity of the source is indeed too low, (ii) the activity of the reference is higher than assumed, (iii) the detector efficiencies has changed between the measurement of the source and the reference or by

PS168		
Energy (keV)	distance (mm) d	count rate [1/s]
511	9800	4002.26 ± 3.66
1275	9800	1059.33 ± 1.88
PS99		
Energy (keV)	distance (mm) d	count rate [1/s]
511	1000	76.99 ± 0.08
1275	1000	20.78 ± 0.05

Table A.2.: Measured count rates with the scintillation detector.

PS168		
Energy (keV)	distance (mm) d	count rate [1/s]
511	8300	1916.31 ± 3.10
1275	8300	569.53 ± 1.69
PS99		
Energy (keV)	distance (mm) d	count rate [1/s]
511	250	405.22 ± 0.64
511	500	116.07 ± 0.34
511	1000	30.54 ± 0.18
1275	250	111.21 ± 0.33
1275	500	31.75 ± 0.18
1275	1000	8.62 ± 0.09

Table A.3.: Measured count rates with the HPGe detector.

(iv) an erroneous dead time correction. First (ii) the activity of the reference was determined in a gamma spectrometer calibrated by the PTA Berlin. The value for the activity of the reference was found to be in accordance with the assumed one. Next (iii) the detection efficiency was checked by a measurement of the references in the atomic egg where the PS168 source was stored rather than in lab. The only reason for the efficiencies to be different using the same setup could be different electronic noise in the lab and in the atomic egg. The efficiency is determined in terms of the photo peak, i.e. the probability of detecting a gamma event by photo electric interaction with the detector. The photo-peak efficiency f for all gamma lines and all detector setups was determined, using

$$f = \frac{C}{\Omega A}$$

with A the nominal source activity and Ω the solid angle of the source relative to the detector setup. The obtained values are tabulated in tables A.4 and A.5. As can be directly seen in figure A.4 the photo-peak efficiency is significantly lower only for the PS168 source using the nominal activity of 1.95 GBq. This left the conclusion that either the activity of PS168 is lower or the dead time correction of the spectrometer is erroneous. The investigation of the latter is presented in the next section*.

Nuclide	Energy (keV)	Source id	d (mm)	f
^{22}Na	511	PS99	249	0.259
^{22}Na	511	PS99	499	0.298
^{22}Na	511	PS99	999	0.315
^{22}Na	511	PS99	2000	0.346
^{22}Na	511	PS134	500	0.325
^{22}Na	511	PS134	1000	0.332
^{22}Na	511	PS134	2000	0.345
^{22}Na	511	Ps168	8300	0.191
^{22}Na	1275	PS99	249	0.129
^{22}Na	1275	PS99	499	0.148
^{22}Na	1275	PS99	999	0.161
^{22}Na	1275	PS99	2000	0.167
^{22}Na	1275	PS134	500	0.160
^{22}Na	1275	PS134	1000	0.165
^{22}Na	1275	PS134	2000	0.173
^{22}Na	1275	Ps168	8300	0.103

Table A.4.: Photo-peak efficiency f for the HPGe

Nuclide	Energy (keV)	Source id	f
^{22}Na	511	PS98	0.867
^{22}Na	511	PS99	0.966
^{22}Na	1275	PS98	0.403
^{22}Na	1275	PS99	0.520
^{60}Co	1183	PS87	0.600
^{22}Na	511	PS168	0.676
^{22}Na	1275	PS168	0.324
^{22}Na	511	PS168b	0.768
^{22}Na	1275	PS168b	0.366

Table A.5.: Photo-peak efficiency f for the BGO scintillator (d=1000mm)

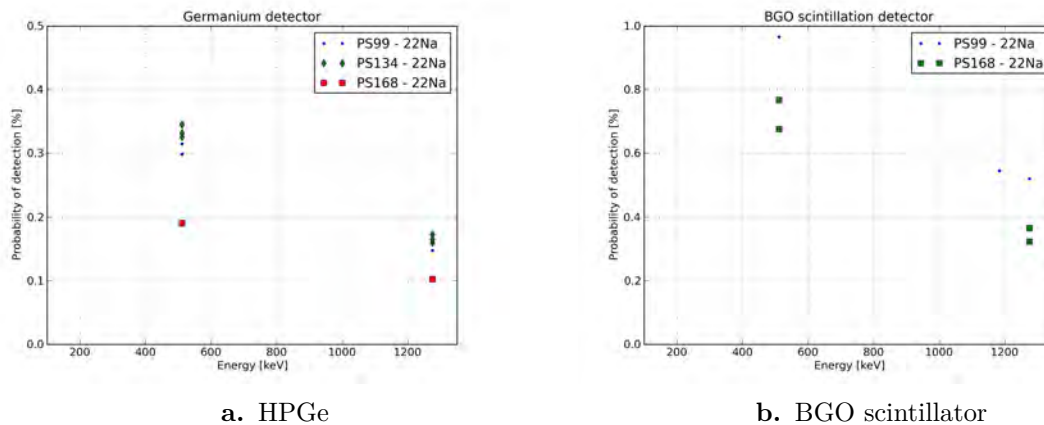


Figure A.4.: Detection probability for the two different detectors. When the nominal activity for PS168 probability is assumed the calculated detection probability appears to be lower for all considered energies.

Dead time correction error

In order to determine the correctness of the dead time correction a series of the following measurements have been performed. A signal generated by tail pulse generator is fed to the test input of the HPGe pre-amplifier. Therefore, this investigation is limited to the HPGe detector. The shape of the signal is matched to the HPGe signal pulses and the frequency of tail pulses was adjusted to 1000.0 Hz. The amplitude was chosen in a way that the arising peak in the spectrum appears far left of the 1275 keV peak. Then a ^{22}Na reference source is placed at different distances in front of the detector. By varying the distance of the source the count rate and with it the dead time can be changed. The signal from the tail pulse generator serves as a clock which allows to precisely determine the live time of the setup by integrating the resulting peak. In figure A.5 the measured number of tail pulses is plotted together with the measured number of 1275 keV events from the reference source relative to the expected number of events versus the distance between source and detector as well as a function of the measured dead time. As can be seen for short distances, i.e. high dead times, the ratio drops below one. This is a direct hint that the dead time correction of the ADC/MCA combination works unsatisfactorily. By normalizing the measured 1275 keV to the tail pulse events and considering the solid angle (as shown in figure A.6) the ratio between measured and expected counts is found to be constant for all distances. The reason for this is the fixed dead time correction of the ADC. The FastComtec 2020 is a Wilkinson-type ADC, which means it works by measuring the time it takes for the voltage levels at the input and at a capacitor which is charged by constant current to be equal. During this process the ADC is dead and cannot accept new pulses. The dead time, however, depends on the duration of the charging process and therefore varies with the pulse height. This means that for higher levels at the input the conversion takes longer. This is no problem as long as the input pulses keep the same height with increasing count rate. As a matter of fact, for higher count rates the baseline of the signals from the detector can have an offset voltage due to pile-ups in the detector. This means that one pulse is generated on the falling tail of the predecessor pulse.

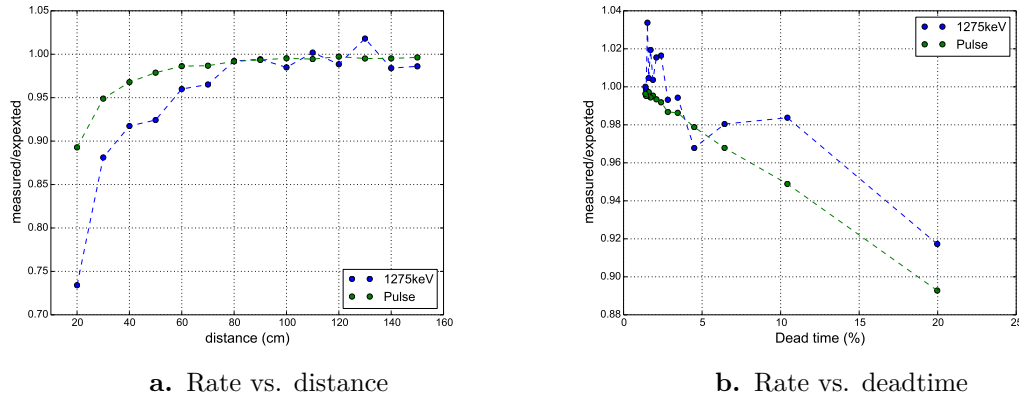


Figure A.5.: Ratio between measured and expected number of counts plotted versus the distance between source and detector (*left*) and versus the dead time (*right*) for the 1275 keV and for tail pulse generator. The number of expected counts is calculated from the frequency of the pulser and from the known activity of the reference in combination with the solid angle.

Final results

In order to correct the faulty dead time correction a correction function is determined by fitting the ratio of measured to expected events for the 1275 keV signal with a linear function (as shown in figure A.7). The obtained correction as a function of the relative dead time D measured with the ADCs is given by

$$f(D) = 1.0030(98) - D \cdot 0.00561(53).$$

Using this correction the activity of the ^{22}Na source PS168 is found to be

$$A_{PS168} = (1898 \pm 6) \text{ MBq}.$$

This value is in good accordance with the value given by the manufacturer of 1.95 GBq, also, when the absorption in air is considered. This analysis showed that for high count rates the dead time correction of standard ADC cannot be trusted and that even a rather trivial measurement can turn out to be rather tricky.

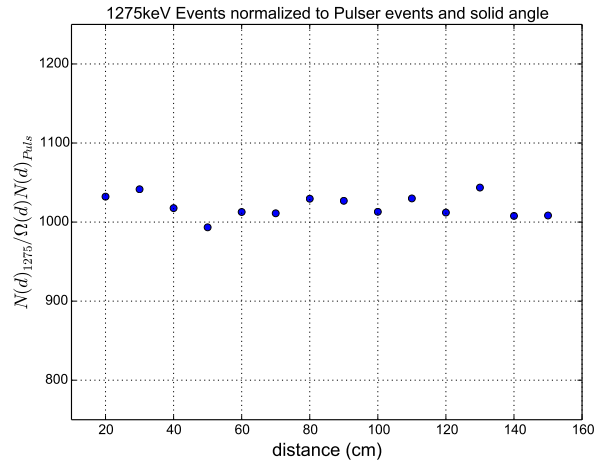


Figure A.6.: Corrected pulsar rate.

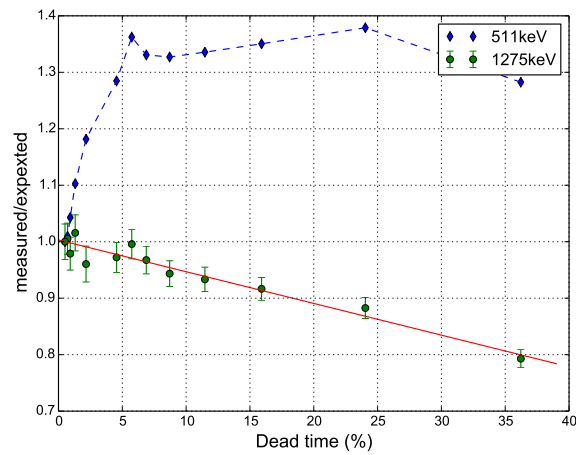


Figure A.7.: Ratio of measured to expected rate plotted versus the deadtime. A clear linear trend is observed for the 1275 keV events. The behaviour for the 511 keV is not understood, it may be due to the higher number of pile-ups resulting from the higher detection efficiency or by variations in the Compton background originating from the 1275 keV line in the analysis window of the 511 keV photo-peak events.

B Appendix B.

A GEM-based gamma camera prototype for 2D-ACAR

The most relevant characteristic of any 2D-ACAR spectrometer is the achievable angular resolution. In principle, the resolution can be improved easily by placing the detectors further apart. However, the coincidence count rate scales with the inverse square of the detector detector distance l while the angular resolution only scales with the linear with $1/l$. Hence, a detector with high intrinsic spatial resolution is desirable in order to maximize the count rate.

In this work a new type of gas detector for the use a gamma camera was developed together with Martin Rutzinger, who carried out the experiments. The concept for this type of gamma detector is based on the high density avalanche cambers (HIDAC) developed by Jeavons [JCS75]. The incident gamma radiation is converted by a high density converter into electrons either by Compton scattering or by the photo effect. The electrons are then detected in a multiwire drift chamber, which has a very high detection efficiency for charged particles. By measuring the distribution of the electrons with a segmented anode readout the position of the interaction point between the incident gamma and the converter can be inferred. In 1978 Jeavons et al. [Jea78] demonstrated the capabilities of such a detector for positron emission tomography and for 2D-ACAR and in 1981 West et al [WMW81] set up the first 2D-ACAR spectrometer using this type of detector in Bristol followed by the Geneva group in 1982 [BDD⁺82]. The HIDAC technology was subsequently improved by Townsend [TFJ⁺87] and Jeavons [JCD99] to sub-millimetre resolution and a detection efficiency of 12 % for 511 keV. Consequently, this type of detector has been implemented in the Bristol 2D-ACAR spectrometer [DLU⁺13]. The spatial resolution of the Bristol detector is 0.96 mm, which is more than three times better than the typical resolution of an Anger camera (≈ 3.5 mm). For two facts, the high spatial resolution and the high efficiency, the HIDAC technology is of high interest for 2D-ACAR spectroscopy. However, due to the complexity of the multiwire chamber a high amount maintenance is needed to operate it, hence this type of detector is only rarely used in practice and is not commercially available any longer (former manufacturer Oxford Positron Systems Ltd.). Therefore, the HIDAC principle of a high density converter and a gas detector was adopted to build a new detector replacing the multiwire chamber by a modern gas electron multiplier (GEM) detector. The GEM detector has been developed at CERN (see [Sau01] and references therein) and is still under active development (see for example [KWP⁺04]).

A GEM detector uses so called GEM foils for gas electron multiplication. These Kapton[®] foils have a thickness of 50 μm and are coated with 5 μm copper on both sides. By a photo-

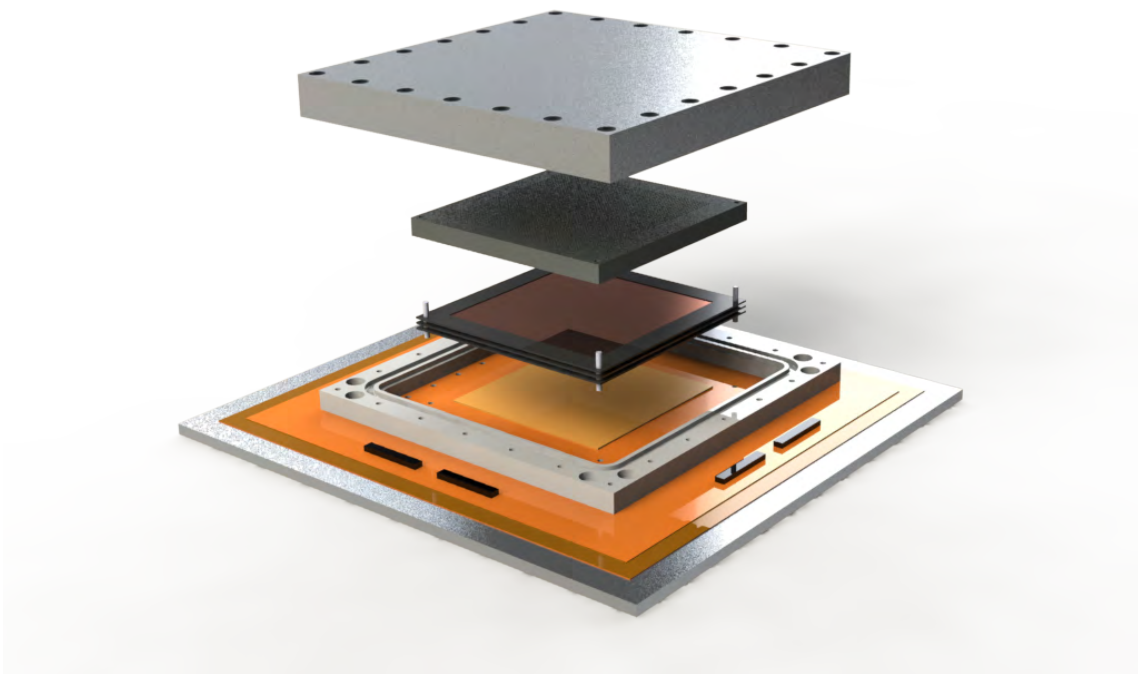


Figure B.1.: Explosion view of the CAD model for the GEM based gamma camera. From top to bottom: 0.2 mm lid, lead converter, GEM-stack, read-out plane, support-frame and ground plate. For details please see reference [Rut12].

lithographic process holes with a bore of $70\ \mu\text{m}$ and a pitch of $140\ \mu\text{m}$ on a hexagonal pattern are etched into the foils. The electron multiplication takes place inside the holes. By applying a voltage of typically 350 V between the top and the bottom of the foils the electrons from the primary event are accelerated in electric field gradient inside the holes and generate secondary electrons. The gain of one foil is in the range of $10^2 - 10^3$. By using multiple foils (up to three) in series the total gain can range up to $2 \cdot 10^4$ [Sau01]. As a counting gas a 70/30 mixture of argon and carbon dioxide is used. Similar to multiwire chambers GEM detectors are used to detect charged particles [ACD⁺02] but also have been considered for the detection of soft x-ray radiation [BKK⁺02, ABB⁺07].

The setup of prototype combining the HIDAC principle with a GEM detector is shown in figure B.1. The γ -radiation is converted into electrons in a lead converter and the charge created in the gas by the electrons is amplified by a triple-GEM and then registered on a strip-readout connected to a charge sensitive pre-amplifier. Several materials and geometries, i.e. monolithic and perforated, were investigated for the converter. Among the tested converter materials iron, copper, silver, tungsten and lead the latter showed the highest conversion probability for a monolithic converter. In the case of a monolithic converter the thickness of the converter showed no significant effect on the achievable conversion rate. Rutzinger [Rut12] found that the highest

efficiency could be achieved with a perforated lead converter which consists of five Pb layers with a thickness of 0.5 mm separated by layers of FR4 (fibre glass) with a thickness of 140 μm . Holes with a diameter 0.8 mm were drilled into the converter in a hexagonal pattern with a pitch of 1.4 mm. The FR4 layers are used to insulate the Pb layers electrically so that a voltage can be applied over the Pb stack in order to drift the secondary electrons through the holes. A drift voltage between the Pb sheets of 100 V was chosen, similar to the voltage used in for the perforated multi layer converters in HIDAC cameras. A total efficiency of 1.56 % could be achieved which is comparable to the efficiency of a single HIDAC module. It was also found that the time resolution of this setup is 68 ns which gives a sufficiently low coincidence resolving time in order to avoid random coincidences.

Tests of the spatial resolution have also been carried out. Rutzinger was able to demonstrate that the position of a collimated γ -beam of 511 keV can be reconstructed from the signals registered on the strip readout. Due to the limited number of available pre-amplifiers not all strips could be read out simultaneously, therefore, the achieved value for the spatial resolution of 7.8 mm (FWHM) is an upper bound for the actual achievable spatial resolution. Using a finer read out pattern with a simultaneous readout of the strips (like it was used in reference [ABDS⁺04]) may allow to achieve a better spatial resolution. Another way to improve the resolution of the readout may be the application of a so-called backgammon-readout, which use a sophisticated pattern of the anode but only requires the measurement of four charge signals in order to determine the position of the event (for details see [MAI⁺92]).

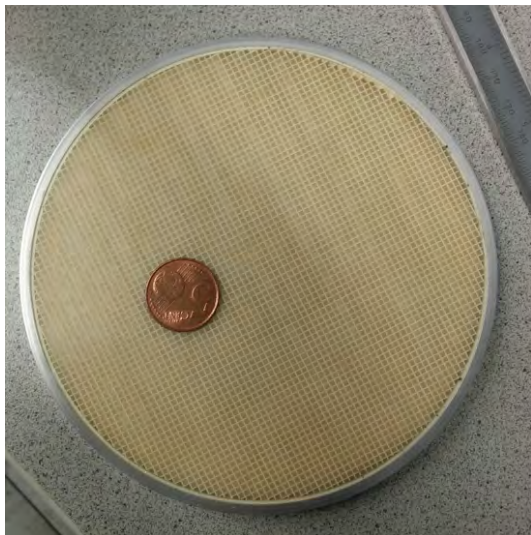
In order to deliver a performance comparable to a HIDAC camera the GEM γ -detector would have to consist of multiple (up to eight) modules. By contrast to the HIDAC modules, which need only one readout for two converters, the GEM detectors are limited to one converter per readout.

Regarding the results obtained with the prototype the use of a GEM detector as gamma camera appears feasible for future applications in 2D-ACAR spectroscopy.

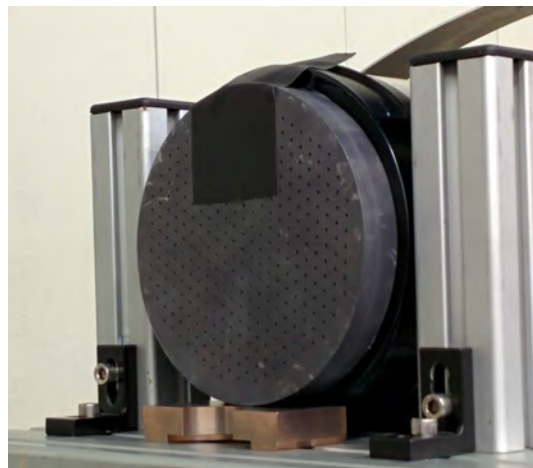
C Appendix C.

Study of position-sensitive PMTs as gamma cameras for 2D-ACAR

In this study the applicability of the Hamamatsu-R3292 series photo-multiplier for 2D-ACAR experiments is investigated. This special type of photo multiplier tube features intrinsic spatial resolution by use of a twelve stage coarse mesh dynode array and a segmented anode consisting of 28×28 crossed anode wires. It has a diameter of 13.2 cm with an active area of 10 cm in diameter. It is used for example for medical imaging (for details see ref.[WMK⁺98] and references therein) and in neutron small-angle scattering experiments. The aim is to determine



a. Scintillator.



b. Collimator.

Figure C.1.: a) Photographic image of the used CsI scintillator. The dimensions of the scintillator pillars are $1.4 \times 1.4 \times 5 \text{ mm}^3$. No optical coupling agent is used between the scintillator and the PMT. b) Photographic image of the used collimator placed in front of the detector.

the spatial resolution for the γ -energy of 511 keV which is relevant for 2D-ACAR experiments.

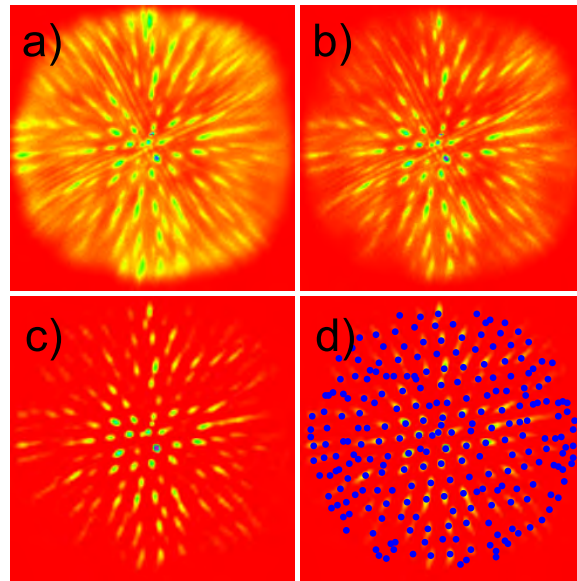


Figure C.2.: a) Image of the lead collimator obtained without energy filter. b) Image of the lead collimator obtained with an energy window centred around 511 keV. c) Image after subtraction of low and high frequency noise. d) Positions of the collimator holes obtained by a localized center-of-gravity analysis.

Experimental setup

A segmented CsI scintillator is placed on the PMT. The physical dimensions of the scintillator pillars are $1.4 \times 1.4 \times 5 \text{ mm}^3$ and the pillars are optically decoupled from each other by a thin barium-sulfide coating (see figure C.1). To avoid inhomogeneities due to air bubbles no optical grease was used to couple the scintillator to the photo multiplier tube. The x and y anode lines are connected in parallel and summed up on both ends by a charge-sensitive pre-amplifier. The four ends of the individual lines are connected to the ADC which was custom built by the FZJ[ECR⁺02]. Hence, the lateral position is given as $x \propto (x_1 - x_2)/(x_1 + x_2)$ and for y analogously. The energy of the event is given by $E \propto x_1 + x_2 + y_1 + y_2$. Since the position is obtained by center-of-gravity method in general a non-linear correction is necessary. However, since the segmentation of the scintillator is smaller than the spacing of the anode wires the influence of the light distribution on the cathode can be omitted. The x, y and E signal are recorded in list mode for off-line analysis. A 20 mm lead collimator with a hexagonal bore pattern with diameter of 1 mm and a pitch of 6 mm is placed directly in front of the scintillator (see figure C.1). The whole setup is placed 1.4 m from the sample chamber in the line-of-sight of the Anger cameras in the ACAR spectrometer. This way the spatial resolution and the efficiency is measured.

Results

The raw detector image integrated over all energies is shown in figure C.2. When the energy filter is applied the spots corresponding to the holes in the collimator appear more pronounced.

For the analysis the high and low frequency noise is subtracted by convolving the energy filtered data with a Mexican hat kernel. Then the positions of the peaks are determined by a localized center-of-gravity analysis. The measured peak positions are then compared with their expected positions. The shape of the distribution of the deviations serves as measure for the spatial resolution of the setup (see figure C.3). By fitting the shape with a single Gaussian a resolution of

$$\Delta x_{\text{FWHM}} = (1.98 \pm 0.03^{\text{stat}} \pm 0.4^{\text{sys}}) \text{ mm}$$

is obtained. The systematic error is estimated by the parallax of the incident gamma radiation.

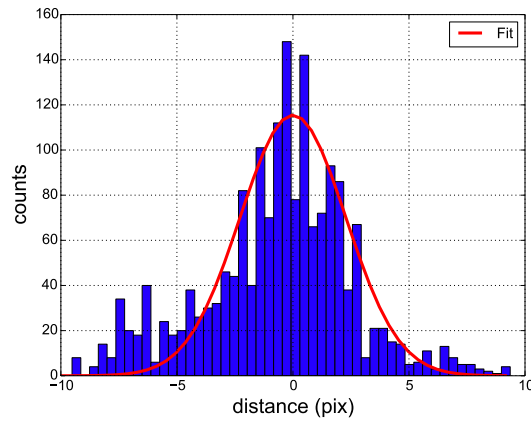


Figure C.3.: Histogram of the distances between the expected position of the collimator holes and the positions obtained from the analysis. A single Gaussian is used to describe the distribution. The width of this Gaussian gives an estimate for the spatial resolution of the setup.

Conclusion

While the spatial resolution of the test setup is $\approx 40\%$ better than that of a typical Anger camera, at the same time the angular field-of-view is about four times lower and the photo peak efficiency is $\approx 50\%$ that of an Anger camera. The current limitations concerning the base line of the experiment pose no limit for the positioning of PMT cameras since the optimum position would be 6.60 m from the sample. This is the closest distance where no clipping of the 2D-ACAR spectrum occurs. At this position the achievable momentum resolution was 1.1 mrad, about 30 % better than with the current Anger camera setup. However the achievable count rate would be reduced by a factor of ≈ 20 compared to the current system.

D Design study for integration of the 2D-ACAR spectrometer to the NEPOMUC positron source

The concept presented in this chapter might prove to be useful in the future when the east hall will be available at the FRM II. In order to operate a 2D-ACAR machine at a positron beamline several design criteria have to be met [CWH⁺14]. To minimize the effect of anisotropic angular resolution the positron beam spot size on the sample has to be as small as possible. This could be easily achieved by using of apertures in the positron beam at the expense of count rate. Also, the sample needs to be coolable, which allows the study of temperature dependent effect and also further improves the angular resolution as the thermal smearing of the positron momentum is decreased.

To meet these criteria two possible options lie are obvious: magnetostatic or electrostatic focussing of the positron beam. Magnetic beam focussing has the advantage that the positron beam has not to be extracted from the guiding field. However, to change the implantation energy the positrons need to be electrostatically accelerated in the magnetic field without creating too much transversal momentum, which is by itself not trivial and also requires the sample and its surroundings to be set to high voltage. Therefore, magnetostatic focussing of a slow positron is unfavourable compared to electrostatic focussing.

Both methods have their advantages and disadvantages when it comes to focussing a slow positron beam (see [C⁺00] and references therein). Since the sample needs to be mounted on a cryostat, which sets strong constraints to the design of a magnetic lens system and also with regard to the intended physics program of the spectrometer, i.e. measurements in zero magnetic field, an electrostatic beam focussing is chosen. Based on designs of Stadlbauer [SHS08] and Strasser [Str02] a positron beam optics has been developed which fulfils the requirements to operate a 2D-ACAR spectrometer at a slow positron beam. In the following the results of this design study are presented together with an outlook on future measurements.

Requirements for the positron beam optics

In order to focus a positron beam electrostatically the positrons first have to be extracted from the magnetic field. One has to make sure that this process is strongly non-adiabtic, because

otherwise the positrons would follow the magnetic flux lines into the field termination. Therefore, two things are required: a long gyration length $l_g = 2\pi \frac{p_L}{qB}$ and a steep gradient in the magnetic flux density with $\frac{\nabla B}{B} \gg 1/l_g$. This is achieved by accelerating the positrons and by choosing a small aperture for the field termination. A very elegant way to increase $\frac{\nabla B}{B}$ was implemented by Piochacz [PKE⁺08], he uses magnetic vanes inside the termination aperture to increase the gradient proportional to the number of vanes.

In the present setup as less elaborate setup is used, the field termination consists of a soft magnetic disk with a bore of 25 mm which is placed inside a ISO-CF-100 flange, which is also soft magnetic (see figure D.1). It is held by three ceramic insulators to create an air gap of 1 mm so an electric potential can be applied to the inner disk. A FEM simulation of the magnetic flux density is shown in figure D.3. The NEPOMUC guiding field, which has strength of ≈ 70 G is terminated in the soft magnetic flange ($\mu_r = 5000$) and fed back via mu-metal pipes. The residual flux density after the termination is lower than 0.1 G.

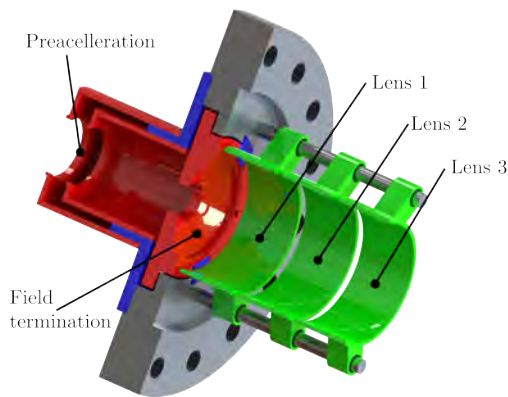


Figure D.1.: Layout of the beam optics. *Red:* Magnetic field termination with preacceleration. *Green:* Einzel lens for electrostatic focussing. *Blue:* Insulator elements.

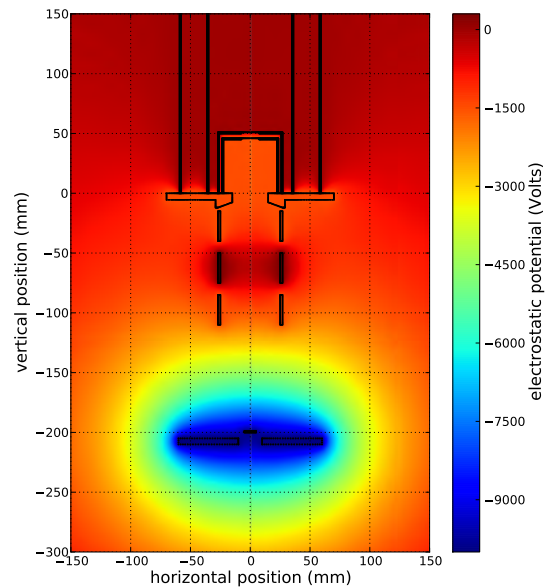


Figure D.2.: FEM Simulation of the electrostatic potentials exemplary for an implantation energy of 10 keV. The potential at the field termination and the preacceleration is -1 kV

The positron beam is accelerated between two fine meshed grids with a distance of 5 mm about 50 mm in front of the field termination. This way it is ensured that the positrons do not acquire additional transverse momentum by $E \times B$ drift, since the electrical and magnetic field lines are parallel within the acceleration gap and the region in the vicinity of the field termination (high $\frac{\nabla B}{B}$) is electrical field free (see figure D.2). In this study the accelerating potential was chosen such as the positron enter the field termination with about 1 keV kinetic energy.

The next component of the beam optics is an Einzel lens which images the beam at the exit of the magnetic field termination. The Einzel lens is designed to operate in decel-accel mode as

this offers higher refractive power compared to accel-deccel mode. The zoom of the Einzel lens is adjusted by ratio $\frac{U_3}{U_2}$ of the potentials at the elements 3 and 2 while lens element 1 is kept at the same potential as the magnetic field termination. The lens elements have a tubular geometry with an inner diameter of the lens $D = 50$ mm and a length of $l = 25$ mm. The diameter D is chosen to be about 10 times the expected beam diameter to minimize spherical aberrations as the beam travels closer to the optical axis. Also, the focal length f can be tuned in a wider range. For $\frac{eU_2}{E_{e+}} = 1$ (when the potential at lens element 2 matches the beam energy) the lens has its highest refractive power with $f \approx 2D$ (for $U_1 = U_3$). By changing U_3 the focus can be fine tuned.

The drag field which is created by the sample potential and also defines the implantation energy shifts the focal plane towards the sample. The sample itself is elevated 10 mm above a metal plate, which is kept at the same potential. This way the field of view of the detectors remains unobstructed and the electrical field between the lens system and the sample is nearly homogeneous close to the optical axis. With increasing sample potential the focal plane of the Einzel lens has to be moved further away from the sample by decreasing $\frac{U_3}{U_2}$.

Estimated performance

Particle tracing calculations using the electric and magnetic fields from the FEM simulation show that a positron beam with realistic parameters ($p_{\perp}/p_L \leq 0.05$ and $200 \text{ eV} \leq E \leq 1000 \text{ eV}$) can reliably be extracted from the magnetic guiding field (exemplary shown in fig D.4 for a 300 eV beam). However, the additional transverse momentum that is acquired in the field termination limits the achievable beam focus on the sample. This is due to the fact that in a cylindrical symmetric configuration the canonical momentum $p_{\Phi} = mr^2\dot{\Phi} + qB\frac{r^2}{2}$, which is a conservative of motion, couples the longitudinal and the transverse motion. A positron which is created in a magnetic field with $B = 70 \text{ G}$ at a distance R from the symmetry axis is extracted to $B = 0$ at a distance r will acquire a transverse energy of $E_{\perp} = \frac{1}{2}m(\frac{1}{2}\omega_g R)^2(\frac{R}{r})^2$ (with the gyration frequency $\omega_g = \frac{qB}{m}$) which results in this case for $R = r = 3.5 \text{ mm}$ to $E_{\perp} = 13.2 \text{ eV}$. Therefore, even a monoenergetic beam will experience a smearing of the longitudinal energy which then lead to an imperfect focussing due to chromatic aberrations of the lens system.

However, a beam spot diameter of $(5.0 \pm 1.0) \text{ mm}$ for a sample potential of -10 kV is readily achieved depending on the initial divergence p_{\perp}/p_L of the beam.

Conclusion

The extraction and focussing assembly devised for this study resembles a fusion of different known and applied concepts in positron beam optics. The strength of our design lies in the electrostatic preacceleration prior the extraction of the beam from the magnetic guiding field in combination with a simple yet versatile electrical lens system. The simulations showed that this assembly works under realistic conditions and fulfils the requirements to operate a 2D-ACAR spectrometer at a slow positron beam.

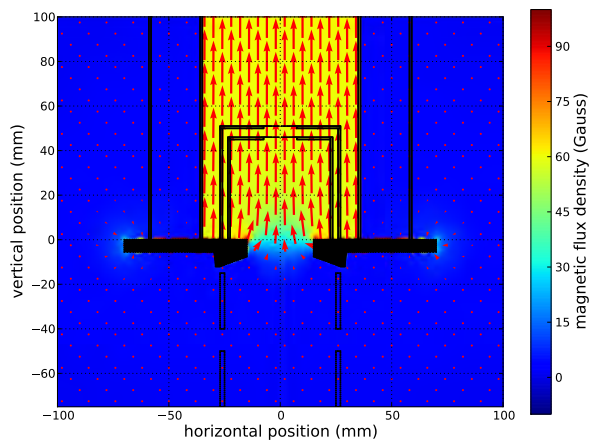


Figure D.3.: FEM Simulation of the magnetic flux density at the field termination calculated for the nominal operation conditions of the NEPOMUC beamline (≈ 70 G). The absolute value of the magnetic flux density is color coded, the arrows indicated its strength and direction. The strength of the field drops rapidly after the field termination. While the guiding field is homogeneous the field exhibits a significant radial component in the field termination. A way to improve with would be the magnetic vane design by Piochacz.

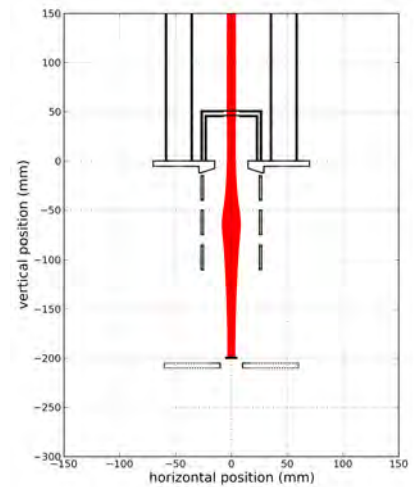


Figure D.4.: Particle tracing simulation of a 300 eV positron beam with divergence corresponding to $p_{\perp}/p_L = 0.05$. The diameter of the primary beam is assumed to be 7 mm. The diameter of the beam spot on the sample is in the range of (5.0 ± 1) mm depending on the initial conditions, i.e. the initial beam divergence.

E Appendix E.

Experimental Parameters

- **High voltage supply detector 1:**
 $U_{\text{Det1}} = +1010 \text{ V}$
- **High voltage supply detector 2:**
 $U_{\text{Det2}} = +1060 \text{ V}$
- **Pre-vacuum pressure**
 $p = 1.8 \cdot 10^{-2} \text{ mbar}$
- **Residual pressure in experimental chamber**
 $p \simeq 10^{-7} \text{ mbar}$
- **Source-sample distance**
 $d_{\text{source}}^{\text{sample}} = 20 \text{ mm}$
- **Detector-detector distance**
 $d_{\text{Det1}}^{\text{Det2}} = 16.587 \text{ m}$
- **Typical magnet current**
 $I_{\text{mag}} = 60 \text{ A}$
- **Magnet cooling water flow rate**
 $f_{\text{mag}} \approx 7.5 \frac{1}{\text{min}}$
- **Magnet cooling water pressure loss**
 $\Delta p_{\text{mag}} \approx 3 \text{ bar}$
- **Cryostat cooling water flow rate**
 $f_{\text{cryo}} \approx 15 \frac{1}{\text{min}}$
- **Width of the coincidence time window**
 $\Delta t_{\text{coin.}} < 500 \text{ ns}$

F Appendix F.

Technical drawings

Technical drawings of the following components of the 2D-ACAR spectrometer:

- overview of the source-sample chamber
- upper pole piece
- lower pole piece
- source holder and shielding
- source manipulator

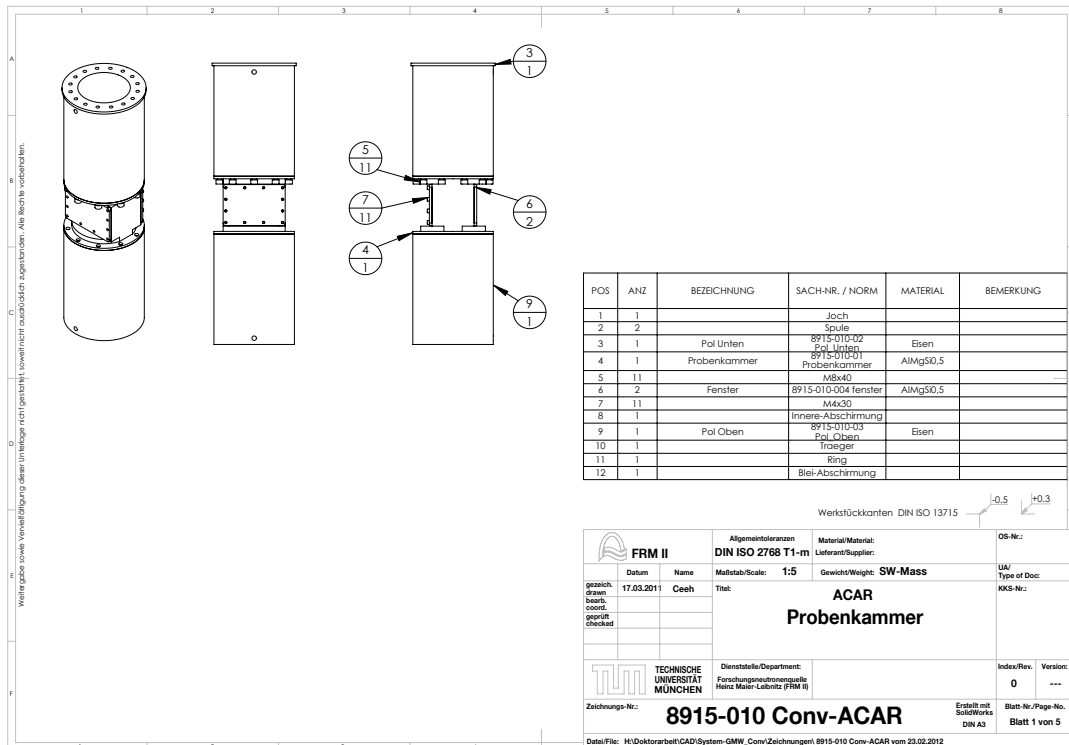


Figure F.1.: Overview of the sample chamber and pole-piece geometry

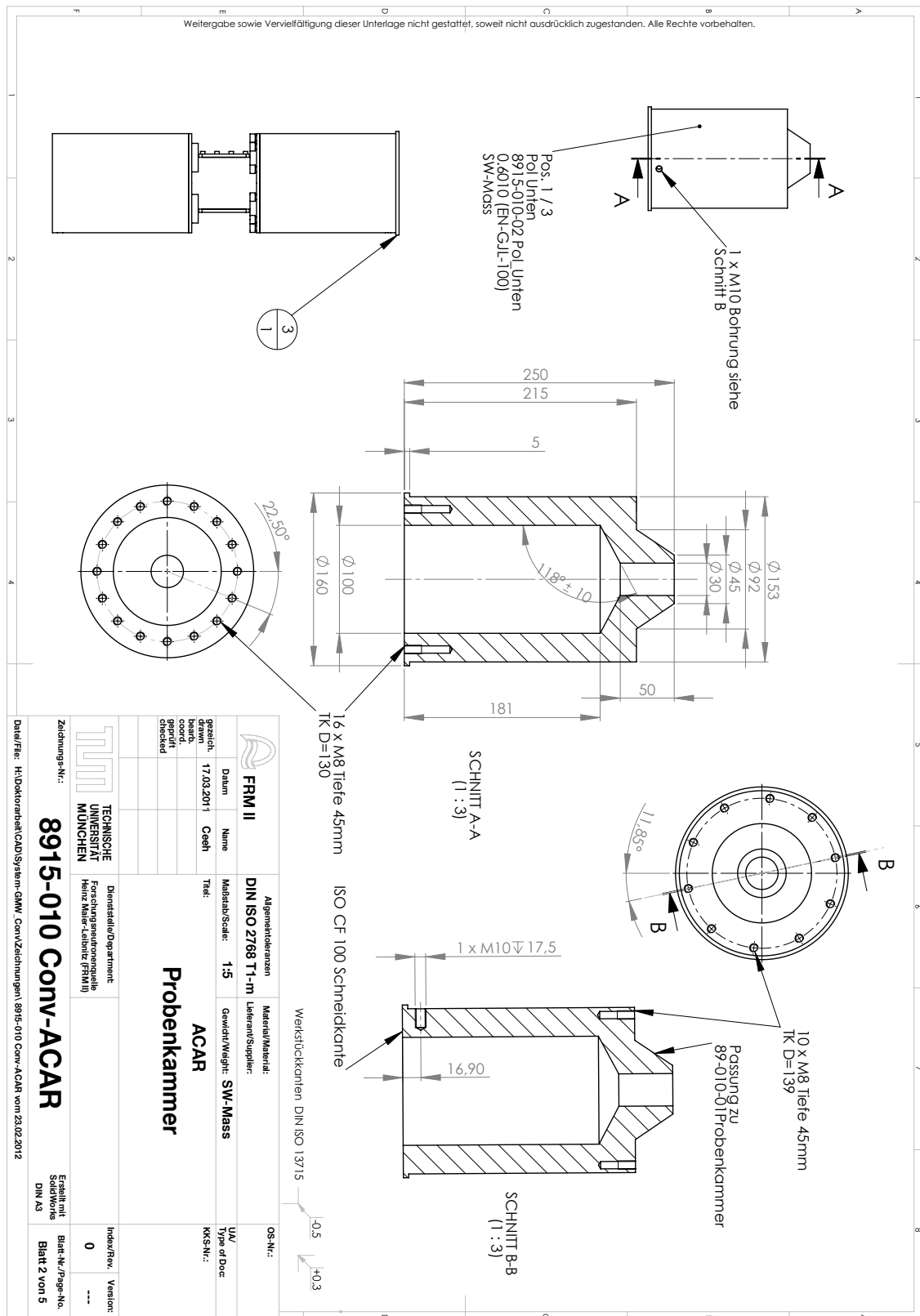


Figure F.2.: Details of the pole-piece. The outer dimensions of the upper and the lower pole-piece are identical. In order to increase the absorption for the 1275 keV radiation from the source, the central bore in the upper pole-piece is reduced to 30 mm.

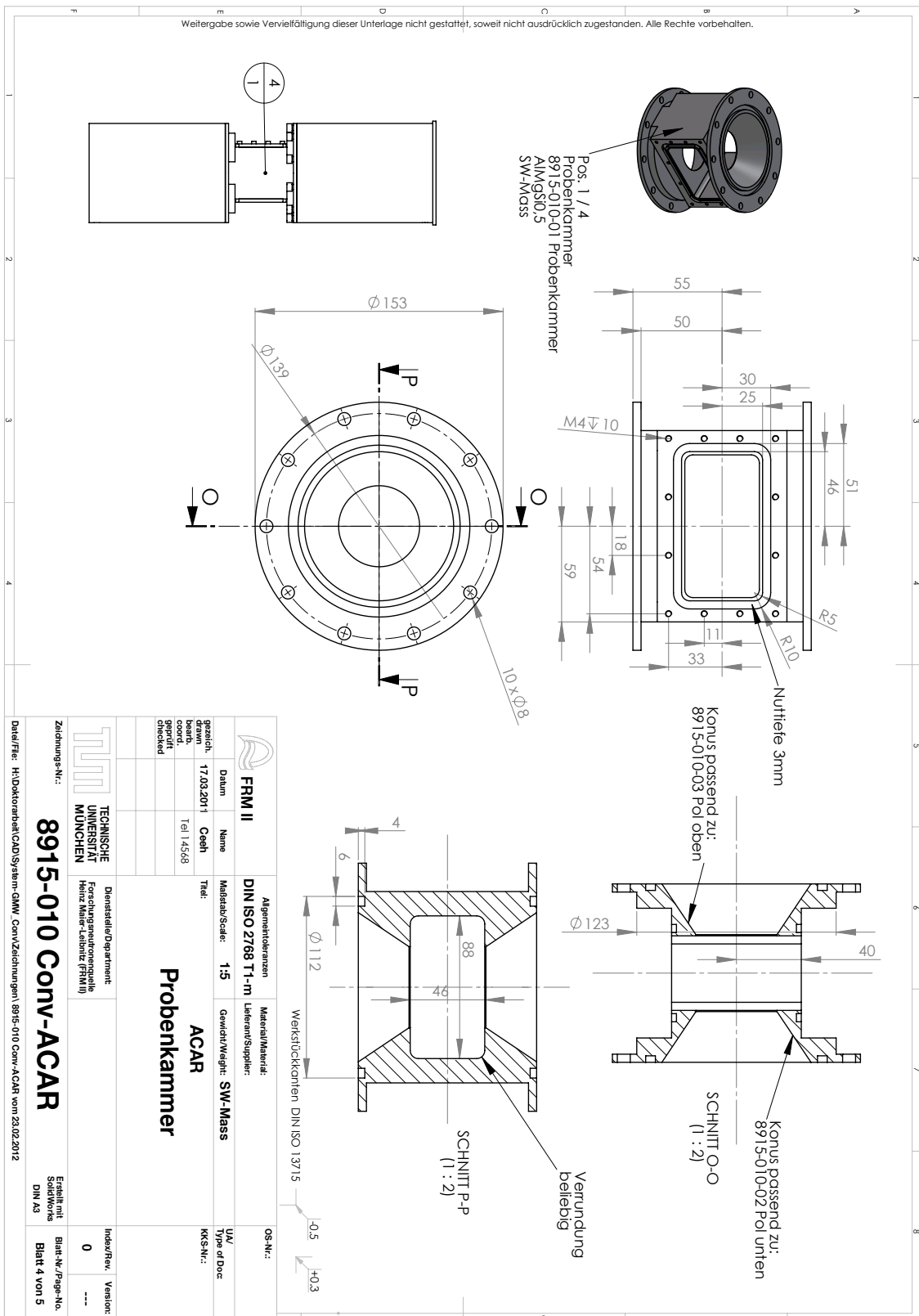


Figure F.3.: Schematics of the source sample chamber. The chamber connects the upper and the lower pole-piece. An elastomer o-ring fitting is used to in between the pole-pieces and the chamber.

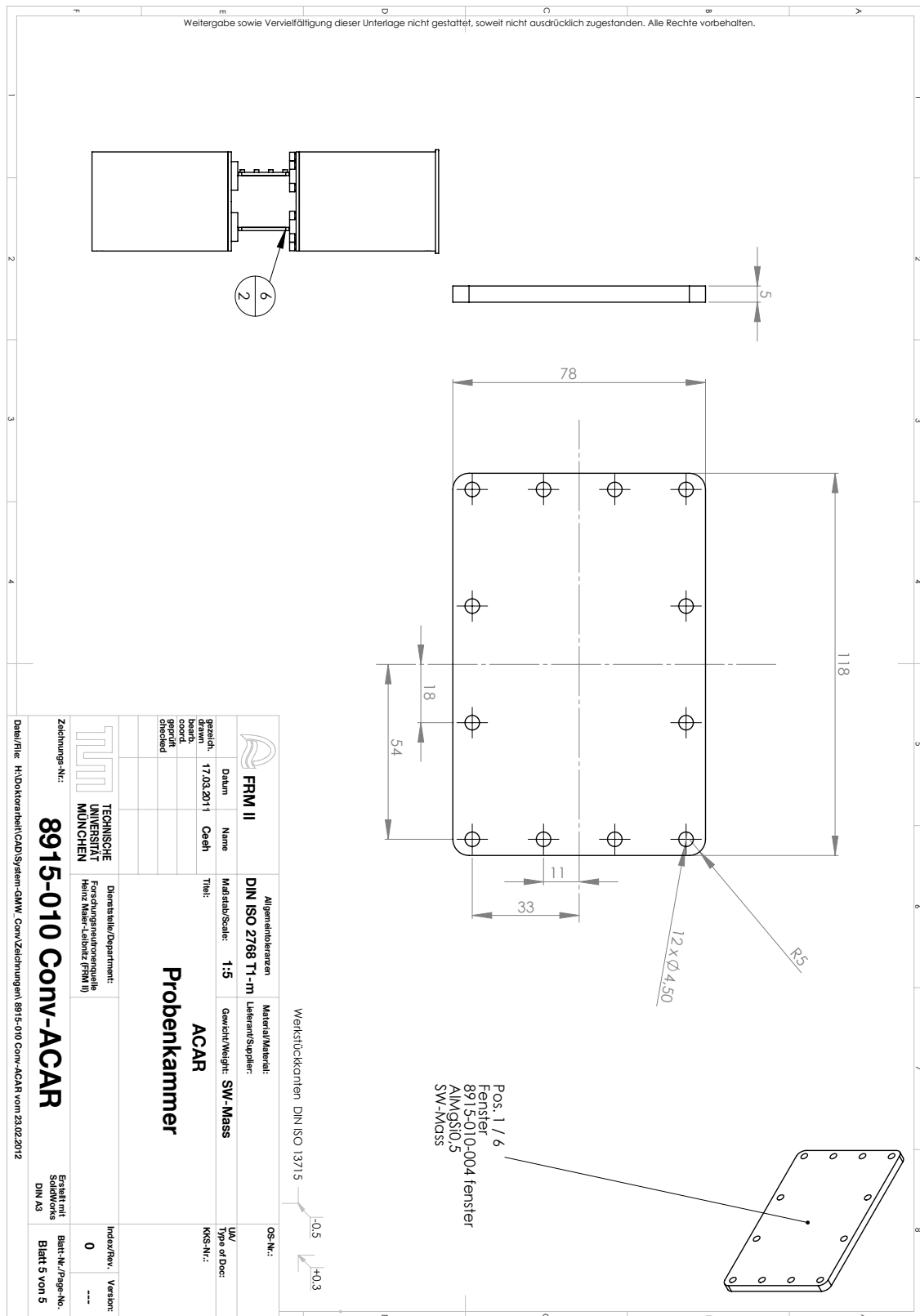


Figure F.4.: The windows for the sample chamber. In the revised version the windows are milled down to 1 mm in the line-of-sight of the detectors.

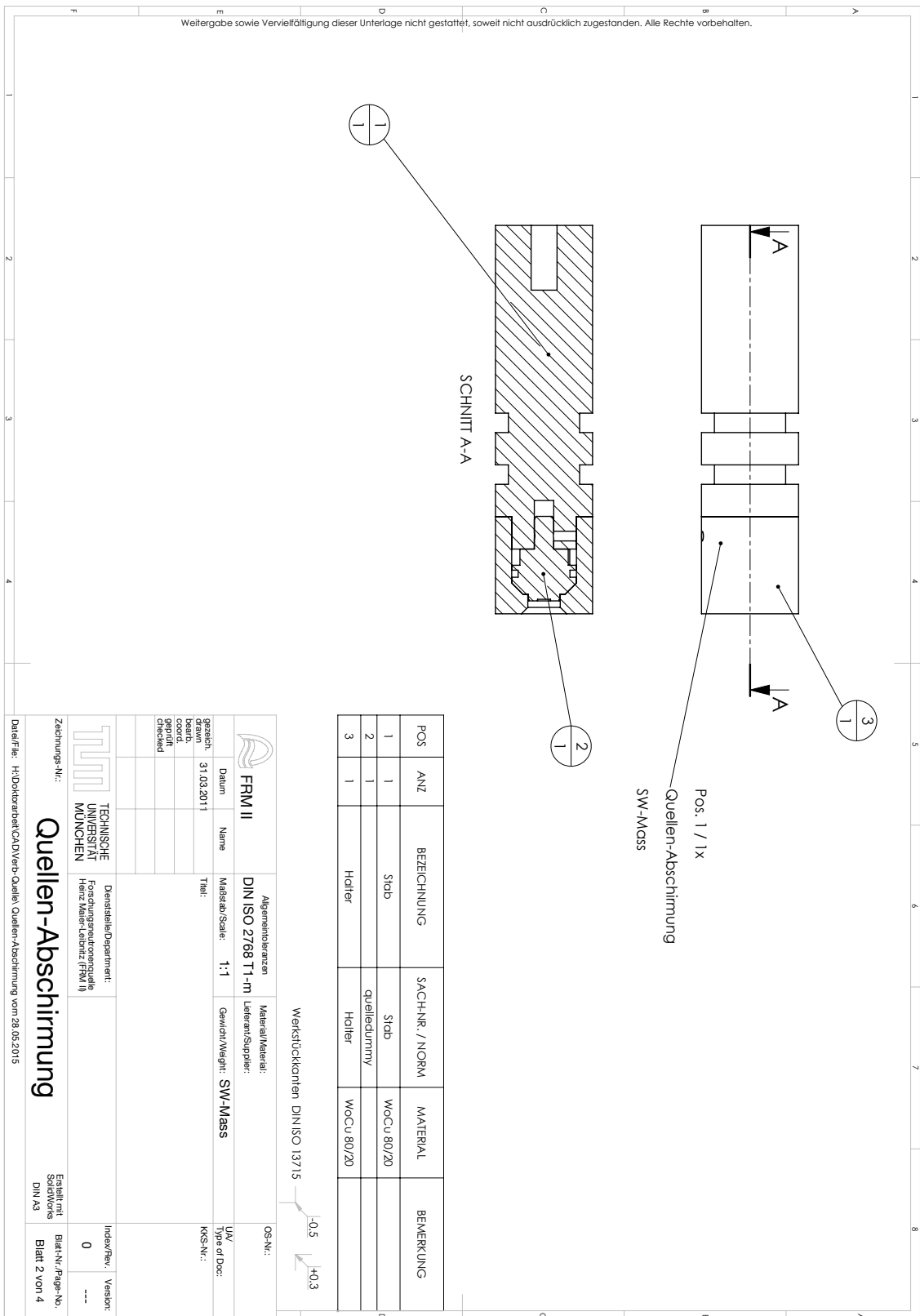


Figure F.5.: Details of the source holder made from a $W_{80}Cu_{20}$ alloy.

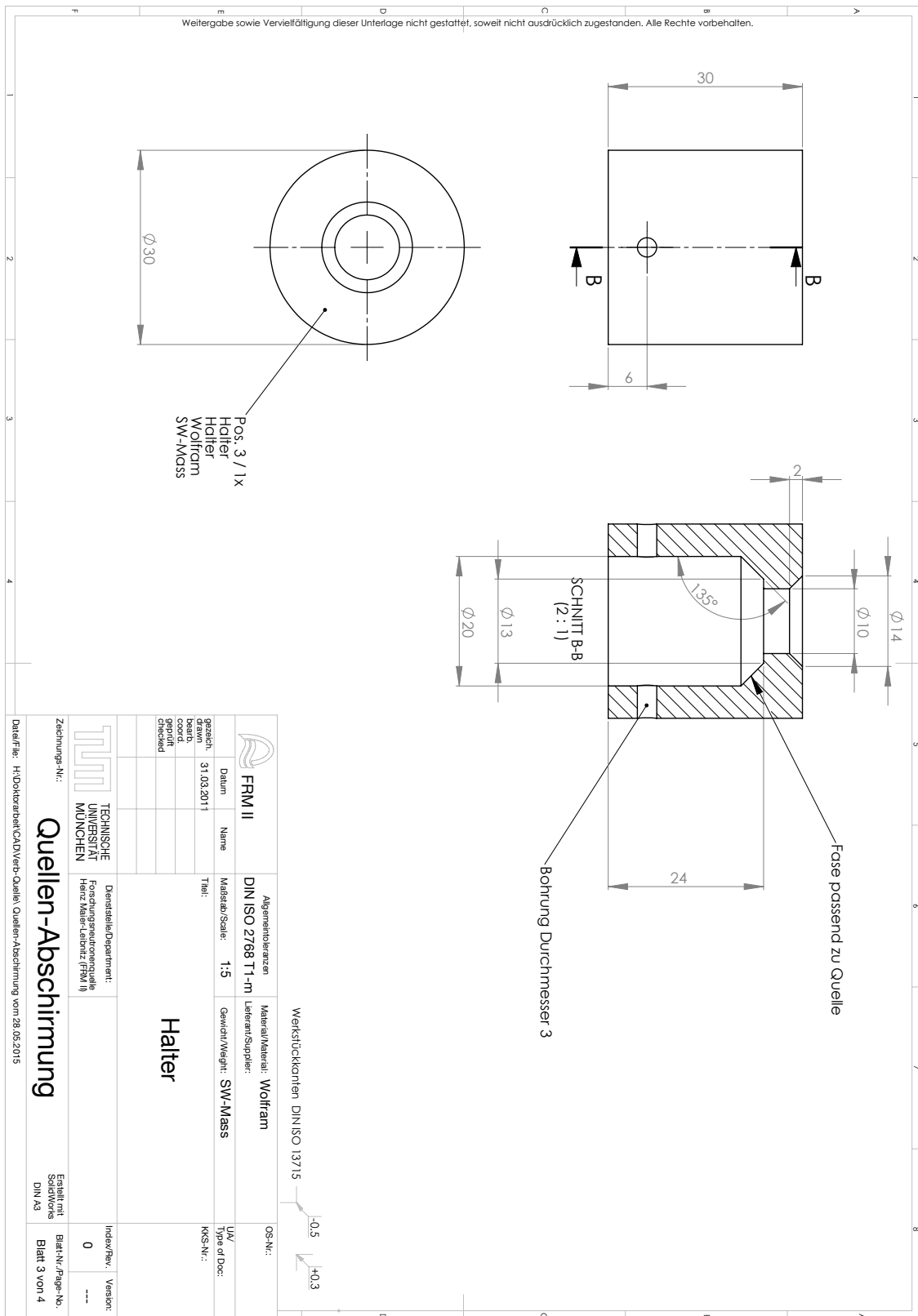


Figure F.6.: Cap of the source holder made from a $W_{80}Cu_{20}$ alloy .

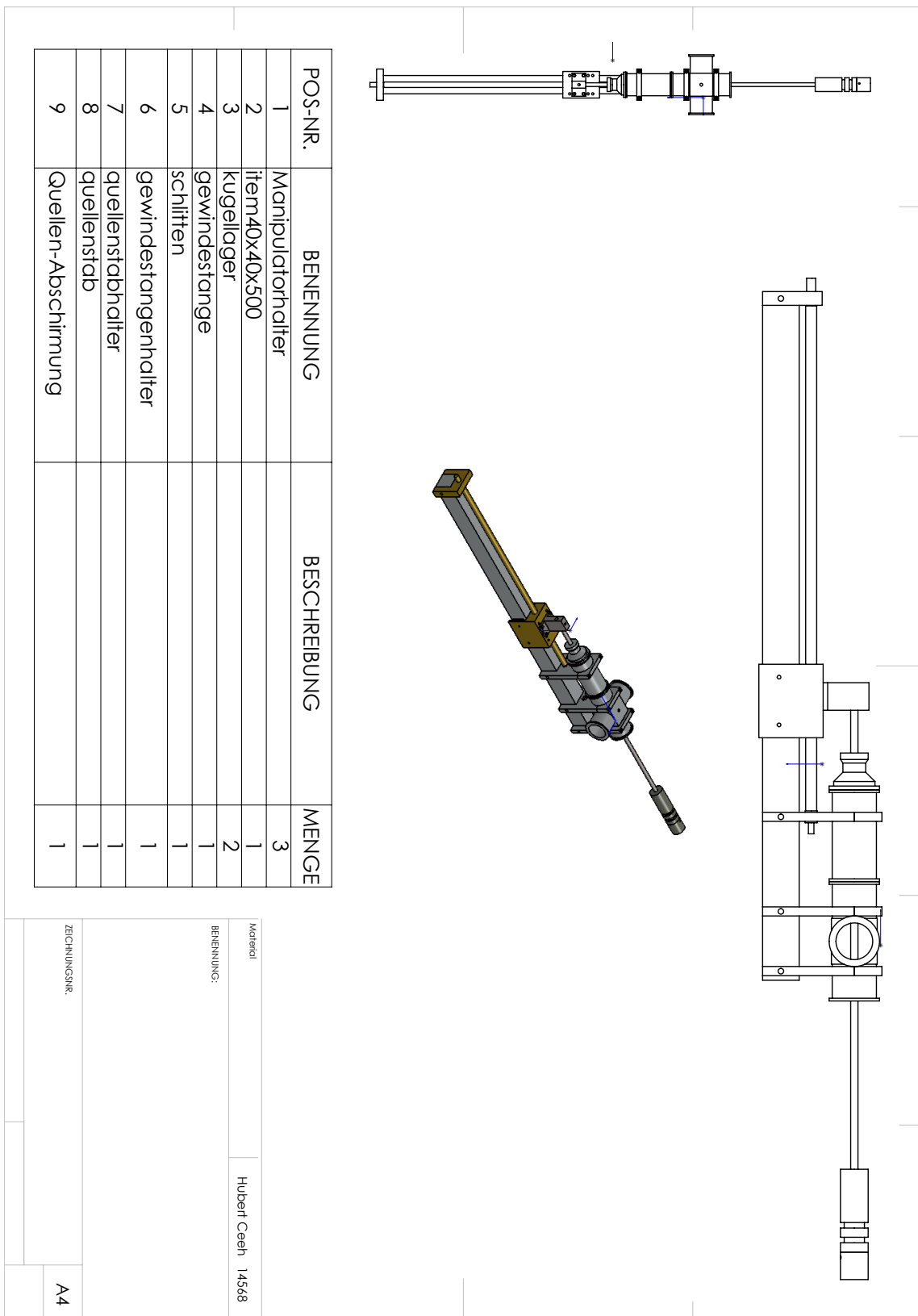


Figure F.7.: Overview of the source manipulator which is used to retract the source from experimental chamber into the storage position by a motorized gear drive.

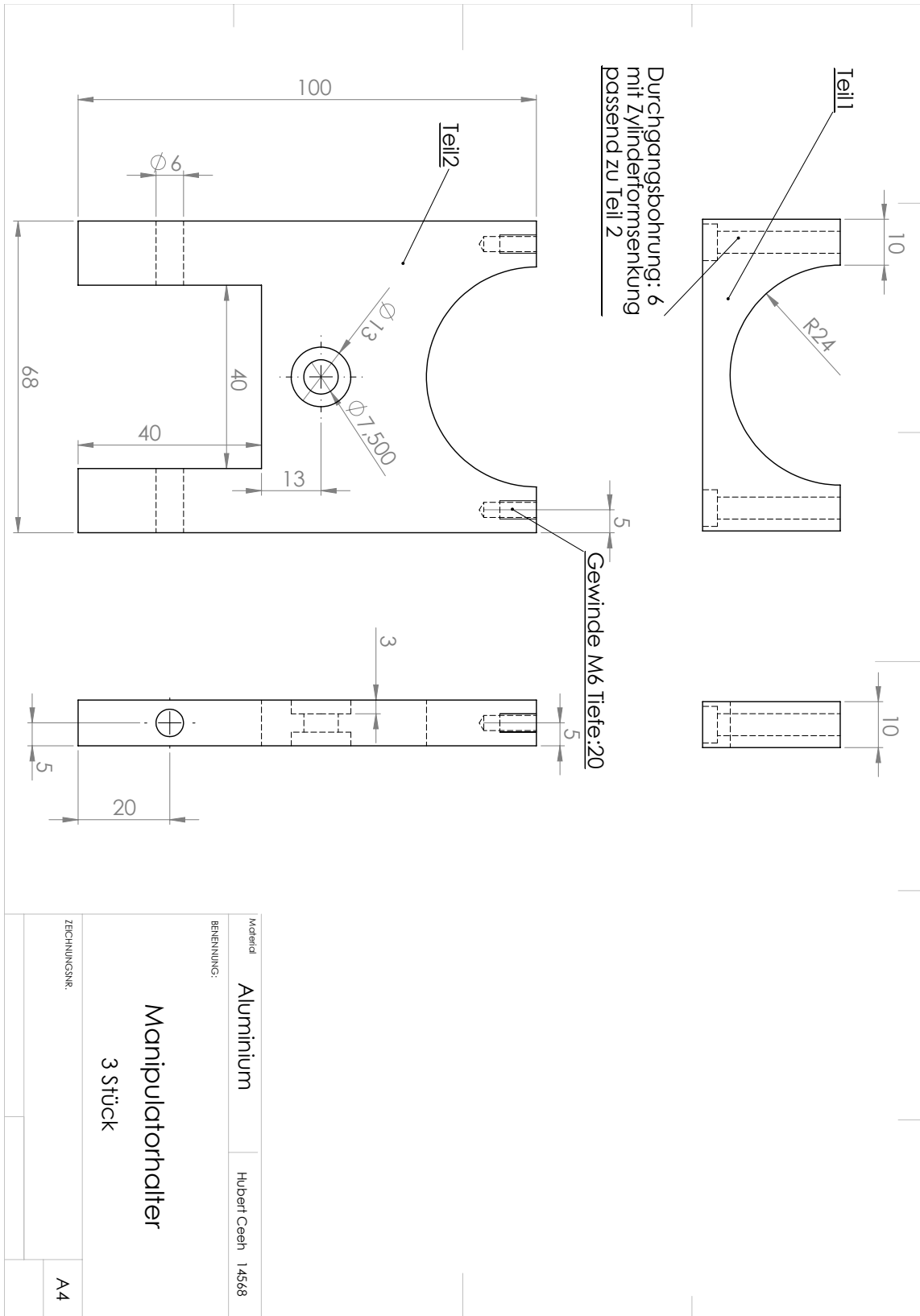


Figure F.8.: Holding clamps for the vacuum system of the source manipulator.

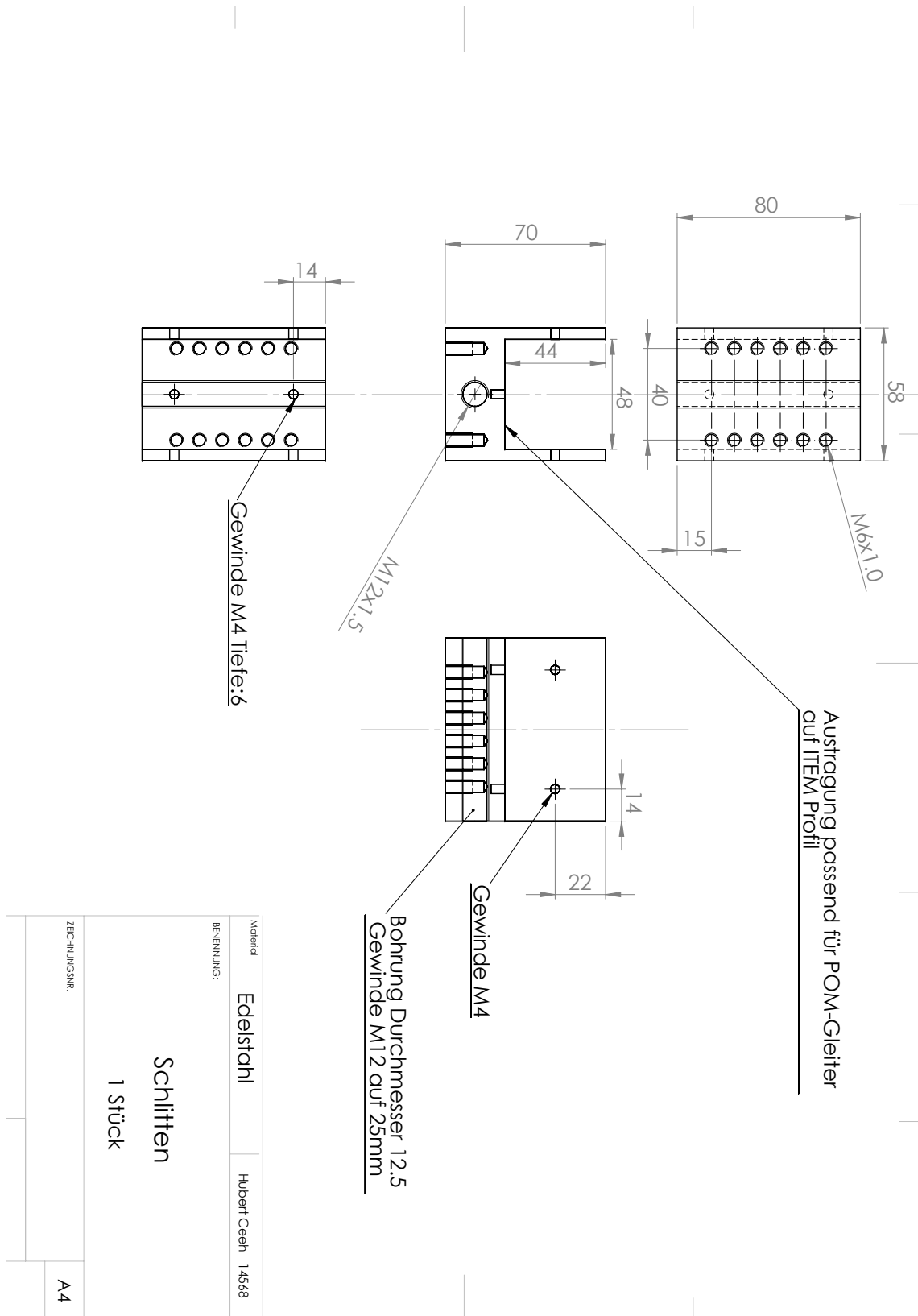


Figure F.9.: Carriage mounted on the gear drive.

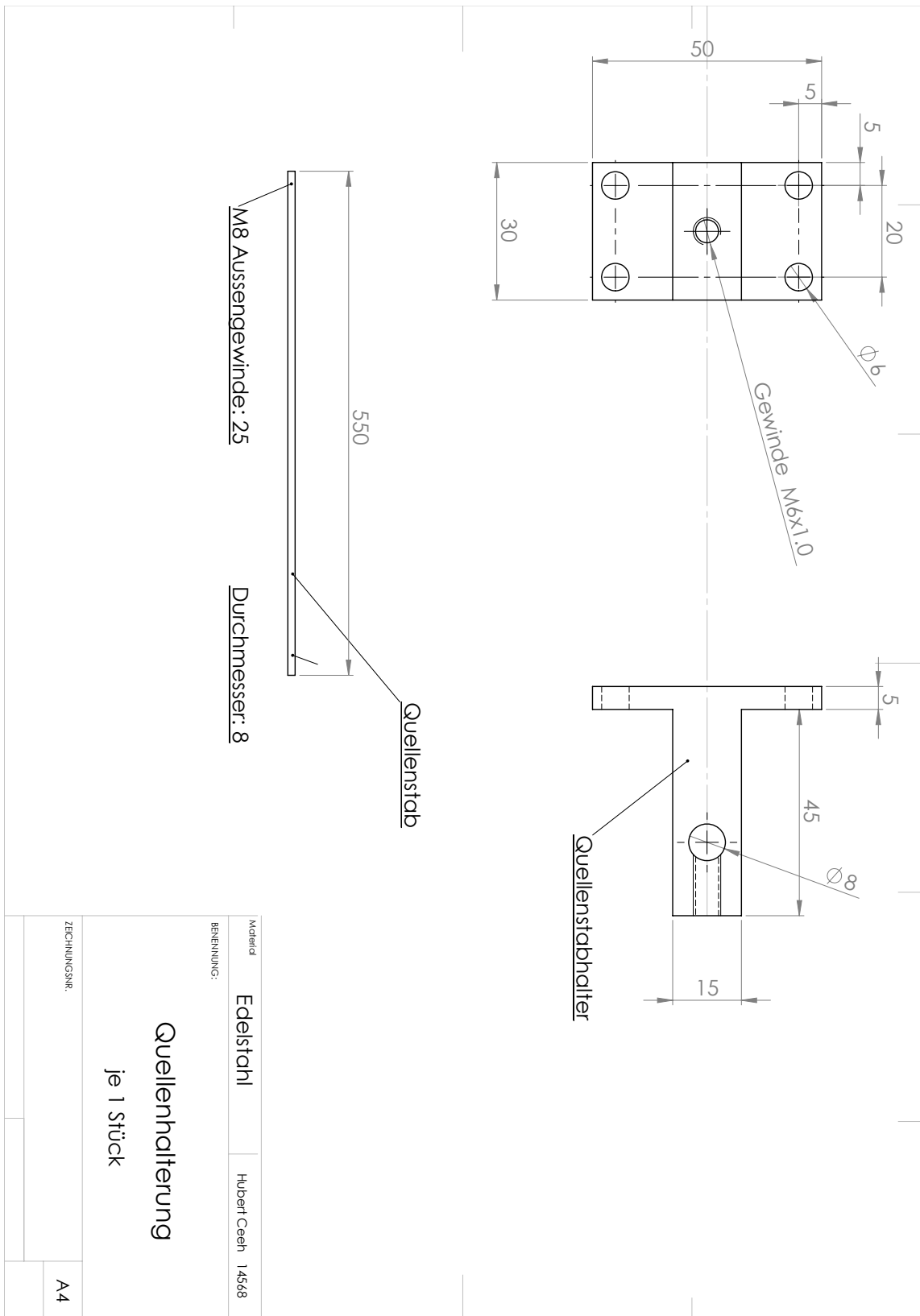


Figure F.10.: Holder for the source rod connecting the source to the movable carriage.

Abbreviations

ACAR	Angular Correlation of Annihilation Radiation
ADC	Analogue Digital Converter
ARPES	Angle Resolved Photo Emission Spectroscopy
DBAR	Doppler Broadening of Annihilation Radiation
BML	Bloch-Modified Ladder
bcc	Body Centred Cubic
CP	Charge Parity
CSDA	Continuous Slowing Down Approximation
dHvA	de-Haas van Alphen
DMFT	Dynamical Mean Field Theory
EMD	Electron Momentum Distribution
fcc	Face Centred Cubic
FEM	Finite Element Method
FLAPW	Full Potential Linearized Augmented Plane Wave
FS	Fermi Surface
FWHM	Full Width Half Maximum
GGA	Generalized Gradient Approximation
HIDAC	High Density Avalanche Chambers
IPM	Independent Particle Model
LCW	Lock Crisp West
LDA	Local Density Approximation
LMTO	Linearized Muffin Tin Orbitals
LSDA	Local Spin Density Approximation
MCA	Multi Channel Analyser
MIAMI	Mixer And Mother Interface
PALS	Positron Annihilation Lifetime Spectroscopy
PID	Proportional Integral Differential
PIG	Programmable Interface and Gate
PMT	Photo Multiplier Tube
SdH	Shubnikow de-Haas
TPMD	Two Photon Momentum Distribution

List of Publications

- 2011** Ceeh H., Gärtner S., Hugenschmidt C., Schreckenbach K., Schwalm D. and Thierolf P., Status report on the setup for the decay rate measurement of the negative positronium ion, *Journal of Physics: Conference Series* 262, 012011
- 2011** Ceeh H., Hugenschmidt C., Schreckenbach K., Gärtner S. A., Thierolf P. G., Fleischer F. and Schwalm D., Precision measurement of the decay rate of the negative positronium ion Ps^- , *Physical Review A*, 84, 062508.
- 2013** Ceeh, H., Weber, J. A., Leitner, M., Boni, P. and Hugenschmidt, C., The source-sample stage of the new two-dimensional angular correlation of annihilation radiation spectrometer at Technische Universität München, *Review of Scientific Instruments*, 84, 043905-043905.
- 2013** Ceeh H., Weber J., Hugenschmidt C., Leitner M. and Böni, P., First measurements with the Munich 2D-ACAR spectrometer on Cr, *Journal of Physics: Conference Series* , 443, 012094
- 2014** Ceeh H., Weber, J. A., Hugenschmidt C., Leitner M., Böni P., Positron beam optics for the 2D-ACAR spectrometer at the NEPOMUC beamline, *Journal of Physics: Conference Series*, 505, 012041
- 2015** H. Ceeh, J.A. Weber, P. Böni, M. Leitner, D. Benea, L. Chioncel, D. Vollhardt, H. Ebert, J. Minar, C. Hugenschmidt, (15), Electron-electron interaction strength in ferromagnetic nickel determined by spin-polarized positron annihilation, arXiv:1501.02584

List of co-authored Publications

- 2012** Leitner M., Ceeh H. and Weber J. A., Eliminating spatial distortions in Anger-type gamma cameras, *New Journal of Physics*, 14, 123014
- 2012** Hugenschmidt C., Ceeh H., Gigl T., Lippert F., Piochac, C., Pikart P. and Zimnik S., The Upgrade of the Neutron Induced Positron Source NEPOMUC, *Journal of Physics: Conference Series*, 443, 012079
- 2013** Weber, J. A., Böni, P., Ceeh, H., Leitner, M. and Hugenschmidt, C., First 2D-ACAR Measurements on Cu with the new Spectrometer at TUM., *Journal of Physics: Conference Series* , 443, 012092
- 2014** Hugenschmidt Christoph, and Hubert Ceeh, "The Free Volume in Dried and H₂O-Loaded Biopolymers Studied by Positron Lifetime Measurements.", *The Journal of Physical Chemistry B*, 118.31 , 9356-9360.
- 2014** Weber, J. A., Ceeh H., Hugenschmidt C., Leitner M., Böni P., The effect of regularization on the reconstruction of ACAR data. *Journal of Physics: Conference Series*, 505, 012047

- 2014** Hugenschmidt, C., Ceeh H., Gigl T., Lippert F., Piochacz C., Reiner M., Zimmnik S., Positron Beam Characteristics at NEPOMUC Upgrade, Journal of Physics: Conference Series, 505, 012029
- 2014** Hugenschmidt C., Bauer A., Böni P., Ceeh H., Eijt S. W. H., Gigl T., Weber J., Quality of Heusler Single Crystals Examined by Depth Dependent Positron Annihilation Techniques, Applied Physics A, 119.3, 997-1002
- 2015** Leitner M., Ceeh H. and Weber J. A., Fermi surface determination from momentum density projections, arXiv:1505.02572

Parts of the present thesis have been published in the above stated references.

Bibliography

- [ABB⁺07] ANULLI, F; BALLA, A; BENCIVENNI, G; CORRADI, G; D'AMBROSIO, C; DOMENICI, D; FELICI, G; GATTA, M; MORONE, MC; MURTAS, F u. a.: A triple GEM gamma camera for medical application. *Nuclear Instruments and Methods in Physics Research Section A: Accelerators, Spectrometers, Detectors and Associated Equipment* 572 (2007), 1, 266–267
- [ABDS⁺04] ALFONSI, M; BENCIVENNI, G; DE SIMONE, P; MURTAS, F; LENER, M P.; BONIVENTO, W; CARDINI, A; DEPLANO, C; RASPINO, D ; PINCI, D: High-rate particle triggering with triple-GEM detector. *Nuclear Instruments and Methods in Physics Research Section A: Accelerators, Spectrometers, Detectors and Associated Equipment* 518 (2004), 1, 106–112
- [ACD⁺02] ALTUNBAS, C; CAPÉANS, M; DEHMELT, K; EHLERS, J; FRIEDRICH, J; KONOROV, I; GANDI, A; KAPPLER, S; KETZER, B; DE OLIVEIRA, R u. a.: Construction, test and commissioning of the triple-gem tracking detector for compass. *Nuclear Instruments and Methods in Physics Research Section A: Accelerators, Spectrometers, Detectors and Associated Equipment* 490 (2002), 1, 177–203
- [AD64] ANGER, Hal O.; DAVIS, Donald H.: Gamma-Ray Detection Efficiency and Image Resolution in Sodium Iodide. *Review of Scientific Instruments* 35 (1964), 6, 693–697. DOI 10.1063/1.1746695
- [AFS00] ADKINS, G. S.; FELL, R. N. ; SAPIRSTEIN, J.: Order α^2 Corrections to the Decay Rate of Orthopositronium. *Physical Review Letters* 84 (2000), 22, 5086–5089
- [AKO⁺96] AEBI, P.; KREUTZ, T. J.; OSTERWALDER, J.; FASEL, R.; SCHWALLER, P. ; SCHLAPBACH, L.: k-Space Mapping of Majority and Minority Bands on the Fermi Surface of Nickel below and above the Curie Temperature. *Physical Review Letters* 76 (1996), 1150–1153. DOI 10.1103/PhysRevLett.76.1150
- [AP79] ARPONEN, J; PAJANNE, E: Electron liquid in collective description. III. Positron annihilation. *Annals of Physics* 121 (1979), 1-2, 343–389. DOI 10.1016/0003-4916(79)90101-5
- [ARD94] AL-RAMADHAN, A.H.; D.W.GIDLEY: New Precision Measurement of the Decay Rate of Singlett Positronium. *Physical Review Letters* 72 (1994), 11, 1932
- [BCP69] BRANDT, Werner; COUSSOT, Gérard ; PAULIN, Robert: Positron Annihilation and Electronic Lattice Structure in Insulator Crystals. *Physical Review Letters* 23 (1969), 522–524. DOI 10.1103/PhysRevLett.23.522

- [BCZC05] BERGER, M.J.; COURSEY, J.S.; ZUCKER, M.A. ; CHANG, J.: STAR, PSTAR, and ASTAR: Computer Programs for Calculating Stopping-Power and Range Tables for Electrons, Protons, and Helium Ions (version 1.2.3). *National Institute of Standards and Technology, Gaithersburg, MD* Available: <http://physics.nist.gov/Star> [2012/6/15] (2005)
- [BDD⁺82] BISSON, PE; DESCOUTS, P; DUPANLOUP, A; MANUEL, AA; PERREARD, E; PETER, M ; SACHOT, R: A high angular resolution 2-D correlation apparatus for positron annihilation studies. *Helvetica Physica Acta* 55 (1982), 100
- [Ben04] BENEÀ, Diana A.: *Theoretical description of magnetic Compton scattering and magnetic properties of Cr-chalcogenide compounds*. 2004
- [BFC03] BIASINI, M.; FERRO, G. ; CZOPNIK, A.: Fermi-surface topology of the heavy-fermion antiferromagnetic superconductor CeIn₃. *Physical Review B* 68 (2003), 094513. DOI 10.1103/PhysRevB.68.094513
- [BFGZ62] BISI, A.; FIORENTINI, A.; GATTI, E. ; ZAPPA, L.: Magnetic Quenching of Positronium in Solids and Positron Helicity. *Physical Review* 128 (1962), 2195–2199. DOI 10.1103/PhysRev.128.2195
- [BFKSC02] BIASINI, M.; FERRO, G.; KONTRYM-SZNAJD, G. ; CZOPNIK, A.: Fermi surface nesting and magnetic structure of ErGa₃. *Physical Review B* 66 (2002), 075126. DOI 10.1103/PhysRevB.66.075126
- [BHM77] BERKO, S.; HAGHGOOIE, M. ; MADER, J.J.: Momentum density measurements with a new multicounter two-dimensional angular correlation of annihilation radiation apparatus. *Physics Letters A* 63 (1977), 3, 335–338. DOI 10.1016/0375-9601(77)90922-7
- [BHP⁺97] BARBIELLINI, B.; HAKALA, M.; PUSKA, M. J.; NIEMINEN, R. M. ; MANUEL, A. A.: Correlation effects for electron-positron momentum density in solids. *Physical Review B* 56 (1997), 7136–7142. DOI 10.1103/PhysRevB.56.7136
- [Bia00] BIASINI, Maurizio: Study of the Fermi surface of molybdenum and chromium via positron annihilation experiments. *Physica B: Condensed Matter* 275 (2000), 4, 285–294
- [BKK⁺02] BACHMANN, S; KAPPLER, S; KETZER, B; MÜLLER, Th; ROPELEWSKI, L; SAULI, F ; SCHULTE, E: High rate X-ray imaging using multi-GEM detectors with a novel readout design . *Nuclear Instruments and Methods in Physics Research Section A: Accelerators, Spectrometers, Detectors and Associated Equipment* 478 (2002), 1-2, 104–108. DOI 10.1016/S0168-9002(01)01719-3
- [BKSM⁺01] BIASINI, M.; KONTRYM-SZNAJD, G.; MONGE, M. A.; GEMMI, M.; CZOPNIK, A. ; JURA, A.: Fermi Surface and Magnetic Structure of TmGa₃. *Physical Review Letters* 86 (2001), 4616–4619. DOI 10.1103/PhysRevLett.86.4616
-

- [BM71] BERKO, S.; MILLS, A. P.: SPIN DISTRIBUTION STUDIES IN FERROMAGNETIC METALS BY POLARIZED POSITRON ANNIHILATION EXPERIMENTS. *Journal de Physique Colloques* 32 (1971), C1–287–C1–289. DOI 10.1051/jphyscol:1971197
- [BMC⁺12] BENEÀ, D.; MINÁR, J.; CHIONCEL, L.; MANKOVSKY, S. ; EBERT, H.: Magnetic Compton profiles of Fe and Ni corrected by dynamical electron correlations. *Physical Review B* 85 (2012), 085109. DOI 10.1103/PhysRevB.85.085109
- [BME⁺12] BRAUN, J.; MINÁR, J.; EBERT, H.; CHAINANI, A.; MIYAWAKI, J.; TAKATA, Y.; TAGUCHI, M.; OURA, M. ; SHIN, S.: Correlation effects, circular dichroism, and Fermi surfaces of bulk nickel from soft x-ray angle-resolved photoemission. *Physical Review B* 85 (2012), 165105. DOI 10.1103/PhysRevB.85.165105
- [BMS⁺95] BOKOR, M; MAREK, T; SÜVEGH, K; THEQE, I K. ; VERTES, A: A positron annihilation study on phase transitions in trans-stilbene single crystal. *Journal of radioanalytical and nuclear chemistry* 200 (1995), 3, 265–275
- [BN86] BORONSKI, E.; NIEMINEN, R. M.: Electron-positron density-functional theory. *Physical Review B* 34 (1986), 3820–3831. DOI 10.1103/PhysRevB.34.3820
- [BP80] BERKO, S; PENDLETON, H N.: Positronium. *Annual Review of Nuclear and Particle Science* 30 (1980), 1, 543–581. DOI 10.1146/annurev.ns.30.120180.002551
- [BPK⁺96] BARBIELLINI, B.; PUSKA, M. J.; KORHONEN, T.; HARJU, A.; TORSTI, T. ; NIEMINEN, R. M.: Calculation of positron states and annihilation in solids: A density-gradient-correction scheme. *Physical Review B* 53 (1996), 16201–16213. DOI 10.1103/PhysRevB.53.16201
- [BPTN95] BARBIELLINI, B.; PUSKA, M. J.; TORSTI, T. ; NIEMINEN, R. M.: Gradient correction for positron states in solids. *Physical Review B* 51 (1995), 7341–7344. DOI 10.1103/PhysRevB.51.7341
- [BR06] BIASINI, M.; RUSZ, J.: LETTER TO THE EDITOR: Cancellation of probe effects in measurements of spin-polarized momentum density by electron positron annihilation. *Journal of Physics: Condensed Matter* 18 (2006), L289–L295. DOI 10.1088/0953–8984/18/22/L03
- [BR07] BIASINI, M.; RUSZ, J.: Fermi surface and momentum spin density of the half metal CrO₂. *physica status solidi (c)* 4 (2007), 10, 3875–3878. DOI 10.1002/pssc.200675867
- [Bra13] BRANDL, Georg: Private Communication. (2013)
- [BT03] BIASINI, M.; TROC, R.: Fermi surface of UGe₂ in the paramagnetic phase. *Physical Review B* 68 (2003), 245118. DOI 10.1103/PhysRevB.68.245118
- [BW75] BRANDT, Werner; WILKENFELD, Jason: Electric field dependence of positronium formation in condensed matter. *Physical Review B* 12 (1975), 2579–2587. DOI 10.1103/PhysRevB.12.2579
-

- [C⁺00] COLEMAN, Paul G. u. a.: *Positron beams and their applications*. World Scientific, 2000
- [CDM⁺04] CROWE, S. J.; DUGDALE, S. B.; MAJOR, Zs.; ALAM, M. A.; DUFFY, J. A. ; PALMER, S. B.: Electronic topological transitions, magnetic ordering and the Fermi surfaces of Y and the heavy rare earths. *Europhysics Letters* 65 (2004), 2, 235
- [Chi14] CHIONCEL, Liviu: Private Communication. (2014)
- [CK65] CARBOTTE, J. P.; KAHANA, S.: Positron Annihilation in an Interacting Electron Gas. *Physical Review* 139 (1965), A213–A222. DOI 10.1103/PhysRev.139.A213
- [CK99] CZARNECKIA, Andrzej; KARSHENBOIMB, SavelyG.: Decays of Positronium. *arXiv:hep-ph/9911410v1* (1999)
- [CKGL03] CHIONCEL, L.; KATSNELSON, M. I.; GROOT, R. A. ; LICHTENSTEIN, A. I.: Nonquasiparticle states in the half-metallic ferromagnet NiMnSb. *Physical Review B* 68 (2003), 144425. DOI 10.1103/PhysRevB.68.144425
- [CNC⁺00] CHOY, TS; NASET, J; CHEN, J; HERSHFIELD, S ; STANTON, C: A database of fermi surface in virtual reality modeling language (vrml). *Bulletin of The American Physical Society* 45 (2000), 1, L36–42
- [CWB⁺15] CEEH, Hubert; WEBER, Josef-Andreas; BÖNI, Peter; LEITNER, Michael; BENEÄ, Diana; CHIONCEL, Liviu; VOLLHARDT, Dieter; EBERT, Hubert ; HUGENSCHMIDT, Jan Minar C.: Electron-electron interaction strength in ferromagnetic nickel determined by spin-polarized positron annihilation. *arXiv:1501.02584* (2015)
- [CWH⁺13] CEEH, Hubert; WEBER, Josef; HUGENSCHMIDT, Christoph; LEITNER, Michael ; BÖNI, Peter: First measurements with the Munich 2D-ACAR spectrometer on Cr. *Journal of Physics: Conference Series* 443 (2013), 1, 012094. DOI 10.1088/1742-6596/443/1/012094
- [CWH⁺14] CEEH, H; WEBER, J A.; HUGENSCHMIDT, C; LEITNER, M ; BONI, P: Positron beam optics for the 2D-ACAR spectrometer at the NEPOMUC beamline. *Journal of Physics: Conference Series* 505 (2014), 1, 012041
- [CWL⁺13] CEEH, Hubert; WEBER, Josef A.; LEITNER, Michael; BÖNI, Peter ; HUGENSCHMIDT, Christoph: The source-sample stage of the new two-dimensional angular correlation of annihilation radiation spectrometer at Technische Universität München. *Review of Scientific Instruments* 84 (2013), 4. DOI 10.1063/1.4801454
- [DAF⁺94] DUGDALE, S B.; ALAM, M A.; FRETWELL, H M.; BIASINI, M ; WILSON, D: Application of maximum entropy to extract Fermi surface topology from positron annihilation measurement. *Journal of Physics: Condensed Matter* 6 (1994), 31, L435
- [Dan89] DANIUK, S: A local-density study of the electron-positron interaction in transition metals by positron annihilation. *Journal of Physics: Condensed Matter* 1 (1989), 32, 5561
-

- [DAW⁺99] DUGDALE, S. B.; ALAM, M. A.; WILKINSON, I.; HUGHES, R. J.; FISHER, I. R.; CANFIELD, P. C.; JARLBORG, T. ; SANTI, G.: Nesting Properties and Anisotropy of the Fermi Surface of $\text{LuNi}_2\text{B}_2\text{C}$. *Physical Review Letters* 83 (1999), 4824–4827. DOI 10.1103/PhysRevLett.83.4824
- [DBS⁺02] DORDEVIC, S. V.; BASOV, D. N.; SLEBARSKI, A.; MAPLE, M. B. ; DEGIORGI, L.: Electronic structure and charge dynamics of the Heusler alloy Fe_2TiSn probed by infrared and optical spectroscopy. *Physical Review B* 66 (2002), 075122. DOI 10.1103/PhysRevB.66.075122
- [DFA⁺97] DUGDALE, S. B.; FRETWELL, H. M.; ALAM, M. A.; KONTRYM-SZNAJD, G.; WEST, R. N. ; BADRZADEH, S.: Direct Observation and Caliper of the “Webbing” Fermi Surface of Yttrium. *Physical Review Letters* 79 (1997), 941–944. DOI 10.1103/PhysRevLett.79.941
- [DFH⁺98] DUGDALE, S B.; FRETWELL, H M.; HEDLEY, D C R.; ALAM, M A.; JARLBORG, T; SANTI, G; SINGRU, R M.; SUNDARARAJAN, V ; COOPER, M J.: Fermiology of Cr and Mo. *Journal of Physics: Condensed Matter* 10 (1998), 46, 10367
- [DFK⁺02] DEDKOV, Yu. S.; FONINE, M.; KÖNIG, C.; RÜDIGER, U.; GÜNTHERODT, G.; SENZ, S. ; HESSE, D.: Room-temperature observation of high-spin polarization of epitaxial $\text{CrO}_2(100)$ island films at the Fermi energy. *Applied Physics Letters* 80 (2002), 22, 4181–4183. DOI 10.1063/1.1482142
- [DHS03] DAMASCELLI, Andrea; HUSSAIN, Zahid ; SHEN, Zhi-Xun: Angle-resolved photoemission studies of the cuprate superconductors. *Review of Modern Physics* 75 (2003), 473–541. DOI 10.1103/RevModPhys.75.473
- [Dir30] DIRAC, Paul A.: A theory of electrons and protons. In: *Proceedings of the Royal Society of London A: Mathematical, Physical and Engineering Sciences* Bd. 126 The Royal Society, 1930, 360–365
- [DLU⁺13] DUGDALE, S B.; LAVEROCK, J; UTFELD, C; ALAM, M A.; HAYNES, T D.; BILLINGTON, D ; ERNSTING, D: The Bristol HIDAC 2D-ACAR Spectrometer. *Journal of Physics: Conference Series* 443 (2013), 1, 012083
- [DM74] DAS, Gopal; MITCHELL, T. E.: Electron irradiation damage in quartz. *Radiation Effects* 23 (1974), 1, 49–52. DOI 10.1080/00337577408232044
- [DWM91] DAI, G.H.; WEEBER, A.W. ; MIJNARENS, P.E.: Reconstructed intensity distribution of the positron source used in two-dimensional measurements of the angular correlation of annihilation radiation. *Nuclear Instruments & Methods in Physics Research, Section A: Accelerators, Spectrometers, Detectors, and Associated Equipment* 306 (1991), 1-2, 261–266. DOI 10.1016/0168-9002(91)90330-S
- [Eck90] ECKERT, A.: *Electron Momentum Distribution of LiMg Alloys by Positron Annihilation 2D-ACAR*, Hochschule der Bundeswehr München, Diss., 1990
- [ECR⁺02] ENGELS, R; CLEMENS, U; RONGEN, H; BUSSMANN, N; KEMMERLING, G; REINARTZ, R ; SCHELTEN, J: A flexible data acquisition board for nuclear detectors. *Nuclear Science, IEEE Transactions on* 49 (2002), 1, 318–320
-

- [EHK78] EASTMAN, D. E.; HIMPSEL, F. J. ; KNAPP, J. A.: Experimental Band Structure and Temperature-Dependent Magnetic Exchange Splitting of Nickel Using Angle-Resolved Photoemission. *Physical Review Letters* 40 (1978), 1514–1517. DOI 10.1103/PhysRevLett.40.1514
- [EKM11] EBERT, H; KÖDDERITZSCH, D ; MINÁR, J: Calculating condensed matter properties using the KKR-Green’s function method—recent developments and applications. *Reports on Progress in Physics* 74 (2011), 096501. DOI 10.1088/0034-4885/74/9/096501
- [ELS81] ELDRUP, M.; LIGHTBODY, D. ; SHERWOOD, J.N.: The temperature dependence of positron lifetimes in solid pivalic acid . *Chemical Physics* 63 (1981), 1-2, 51–58. DOI 10.1016/0301-0104(81)80307-2
- [EMI⁺07] ERDÉLYI, G; MEHRER, H; IMRE, AW; LOGRASSO, TA ; SCHLAGEL, DL: Self-diffusion in Ni₂MnGa. *Intermetallics* 15 (2007), 8, 1078–1083
- [EP80] EBERHARDT, W.; PLUMMER, E. W.: Angle-resolved photoemission determination of the band structure and multielectron excitations in Ni. *Physical Review B* 21 (1980), 3245–3255. DOI 10.1103/PhysRevB.21.3245
- [EVS⁺06] EIJT, Stephan W. H.; VEEN, Anton van; SCHUT, Henk; MIJNARENDS, Peter E.; DENISON, Art B.; BARBIELLINI, Bernardo ; BANSIL, Arun: Study of colloidal quantum-dot surfaces using an innovative thin-film positron 2D-ACAR method. *Nature Materials* 5 (2006), 1, 23–26
- [FAG⁺94] FAWCETT, E; ALBERTS, HL; GALKIN, V Y.; NOAKES, DR ; YAKHMI, JV: Spin-density-wave antiferromagnetism in chromium alloys. *Reviews of modern physics* 66 (1994), 1, 25
- [Fal02] FALUP, Claudiu V.: *The Delft intense slow positron beam 2D-ACAR facility for analysis of nanocavities and quantum dots*, TU Delft, Diss., 2002
- [Faw88] FAWCETT, Eric: Spin-density-wave antiferromagnetism in chromium. *Review of Modern Physics* 60 (1988), 209–283. DOI 10.1103/RevModPhys.60.209
- [FDA⁺99] FRETWELL, H. M.; DUGDALE, S. B.; ALAM, M. A.; HEDLEY, D. C. R.; RODRIGUEZ-GONZALEZ, A. ; PALMER, S. B.: Fermi Surface as the Driving Mechanism for Helical Antiferromagnetic Ordering in Gd-Y Alloys. *Physical Review Letters* 82 (1999), 3867–3870. DOI 10.1103/PhysRevLett.82.3867
- [FDH⁺98] FRETWELL, H M.; DUGDALE, S B.; HUGHES, R J.; BRADER, J; ALAM, M A. ; RODRIGUEZ-GONZALEZ, A: Fermi surface callipering of chromium alloys. *Journal of Physics: Condensed Matter* 10 (1998), 46, 10375
- [FEM10] FEMLAB: COMSOL Multiphysics Version 4.0 released. *Sealing Technology* 2010 (2010), 7, 4. DOI 10.1016/S1350-4789(10)70335-4
- [FHO72] FUJIWARA, Kunio; HYODO, Toshio ; OHYAMA, Jun ichi: Enhancement of Annihilation Rate of Electron-Positron pairs in Periodic Fields. *Journal of the Physical Society of Japan* 33 (1972), 4, 1047–1059. DOI 10.1143/JPSJ.33.1047
-

- [Fir05] FIRESTONE, R.B.: Nuclear Data Sheets for. *Nuclear Data Sheets* 106 (2005), 1, 1–88. DOI 10.1016/j.nds.2005.10.003
- [GFP11] GRAF, Tanja; FELSER, Claudia ; PARKIN, Stuart S.: Simple rules for the understanding of Heusler compounds. *Progress in Solid State Chemistry* 39 (2011), 1, 1–50
- [GKKR96] GEORGES, Antoine; KOTLIAR, Gabriel; KRAUTH, Werner ; ROZENBERG, Marcelo J.: Dynamical mean-field theory of strongly correlated fermion systems and the limit of infinite dimensions. *Review of Modern Physics* 68 (1996), 13–125. DOI 10.1103/RevModPhys.68.13
- [GKS01] G. KONTRYM-SZNAJD, R.N. W. H. Sormann S. H. Sormann: Fermi Surface of Yttrium. *Materials Science Forum* 363-365 (2001), 558–560
- [GMSW98] GERHARDT, U.; MARQUARDT, S.; SCHROEDER, N. ; WEISS, S.: Bayesian deconvolution and analysis of photoelectron or any other spectra: Fermi-liquid versus marginal Fermi-liquid behavior of the 3d electrons in Ni. *Physical Review B* 58 (1998), 6877–6891. DOI 10.1103/PhysRevB.58.6877
- [GMTB70] GREENBERGER, A.; MILLS, A.P.; THOMPSON, A. ; BERKO, S.: Evidence for positronium-like Bloch states in quartz single crystals. *Physics Letters A* 32 (1970), 2, 72–73. DOI 10.1016/0375–9601(70)90093–9
- [GMWP91] GENOUD, P; MANUEL, A A.; WALKER, E ; PETER, M: Spin-polarized 2D ACAR in nickel across the Curie temperature. *Journal of Physics: Condensed Matter* 3 (1991), 23, 4201
- [Gon92] GONIS, Antonios: *Green functions for ordered and disordered systems*. 1992
- [HBB⁺15] HUGENSCHMIDT, C.; BAUER, A.; BÖNI, P.; CEEH, H.; EIJT, S.W.H.; GIGL, T.; PFLEIDERER, C.; PIOCHACZ, C.; NEUBAUER, A.; REINER, M.; SCHUT, H. ; WEBER, J.: Quality of Heusler single crystals examined by depth-dependent positron annihilation techniques. *Applied Physics A* 119 (2015), 3, 997–1002. DOI 10.1007/s00339–015–9058–7
- [HCG⁺13] HUGENSCHMIDT, C; CEEH, H; GIGL, T; LIPPERT, F; PIOCHACZ, C; PIKART, P; REINER, M; WEBER, J ; ZIMNIK, S: The Upgrade of the Neutron Induced Positron Source NEPOMUC. *Journal of Physics: Conference Series* 443 (2013), 1, 012079
- [HCG⁺14] HUGENSCHMIDT, C; CEEH, H; GIGL, T; LIPPERT, F; PIOCHACZ, C; REINER, M; SCHRECKENBACH, K; VOHBURGER, S; WEBER, J ; ZIMNIK, S: Positron Beam Characteristics at NEPOMUC Upgrade. *Journal of Physics: Conference Series* 505 (2014), 1, 012029
- [HCS⁺09] HOFMANN, A.; CUI, X. Y.; SCHÄFER, J.; MEYER, S.; HÖPFNER, P.; BLUMENSTEIN, C.; PAUL, M.; PATTHEY, L.; ROTENBERG, E.; BÜNEMANN, J.; GEBHARD, F.; OHM, T.; WEBER, W. ; CLAESSEN, R.: Renormalization of Bulk Magnetic Electron States at High Binding Energies. *Physical Review Letters* 102 (2009), 187204. DOI 10.1103/PhysRevLett.102.187204
-

- [HDM⁺04] HUGHES, R. J.; DUGDALE, S. B.; MAJOR, Zs.; ALAM, M. A.; JARLBORG, T.; BRUNO, E. ; GINATEMPO, B.: Evolution of the Fermi surface and the oscillatory exchange coupling across Cr and Cr-based alloys. *Physical Review B* 69 (2004), 174406. DOI 10.1103/PhysRevB.69.174406
- [HK64] HOHENBERG, P.; KOHN, W.: Inhomogeneous Electron Gas. *Physical Review* 136 (1964), B864–B871
- [HKE79] HIMPSEL, F. J.; KNAPP, J. A. ; EASTMAN, D. E.: Experimental energy-band dispersions and exchange splitting for Ni. *Physical Review B* 19 (1979), 2919–2927. DOI 10.1103/PhysRevB.19.2919
- [HKR⁺91] HAGHIGHI, H.; KAISER, J. H.; RAYNER, S.; WEST, R. N.; LIU, J. Z.; SHELTON, R.; HOWELL, R. H.; SOLAL, F. ; FLUSS, M. J.: Direct observation of Fermi surface in YBa₂Cu₃O_{7- δ} . *Physical Review Letters* 67 (1991), 382–385. DOI 10.1103/PhysRevLett.67.382
- [HKR⁺02] HUGENSCHMIDT, C; KÖGEL, G; REPPER, R; SCHRECKENBACH, K; SPERR, P ; TRIFTSHÄUSER, W: First platinum moderated positron beam based on neutron capture. *Nuclear Instruments & Methods in Physics Research, Section B: Beam Interactions with Materials and Atoms* 198 (2002), 3-4, 220–229. DOI 10.1016/S0168-583X(02)01527-6
- [HKR⁺04] HUGENSCHMIDT, C.; KÖGEL, G.; REPPER, R.; SCHRECKENBACH, K.; SPERR, P.; STRASSER, B. ; TRIFTSHÄUSER, W.: The neutron induced positron source at Munich – NEPOMUC. *Nuclear Instruments and Methods in Physics Research Section B: Beam Interactions with Materials and Atoms* 221 (2004), 160–164
- [HLM⁺08] HUGENSCHMIDT, C.; LÖWE, B.; MAYER, J.; PIOCHACZ, C.; PIKART, P.; REPPER, R.; STADLBAUER, M. ; SCHRECKENBACH, K.: Unprecedented intensity of a low-energy positron beam. *Nuclear Instruments and Methods in Physics Research Section A: Accelerators, Spectrometers, Detectors and Associated Equipment* 593 (2008), 3, 616–618
- [HM86] HANSEN, K. E. H. M.; MIJNARENDS, P. E.: Positron-annihilation study of the half-metallic ferromagnet NiMnSb: Theory. *Physical Review B* 34 (1986), 5009–5016. DOI 10.1103/PhysRevB.34.5009
- [HMRB90] HANSEN, K. E. H. M.; MIJNARENDS, P. E.; RABOU, L. P. L. M. ; BUSCHOW, K. H. J.: Positron-annihilation study of the half-metallic ferromagnet NiMnSb: Experiment. *Physical Review B* 42 (1990), 1533–1540. DOI 10.1103/PhysRevB.42.1533
- [HSTT88] HOFFMANN, L; SINGH, A K.; TAKEI, H ; TOYOTA, N: Fermi surfaces in Nb₃Sn through positron annihilation. *Journal of Physics F: Metal Physics* 18 (1988), 12, 2605
- [HTF⁺96] HASEGAWA, M.; TABATA, M.; FUJINAMI, M.; ITO, Y.; SUNAGA, H.; OKADA, S. ; YAMAGUCHI, S.: Positron annihilation and ESR study of irradiation-induced
-

- defects in silica glass. *Nuclear Instruments and Methods in Physics Research Section B: Beam Interactions with Materials and Atoms* 116 (1996), 1-4, 347–354. DOI 10.1016/0168-583X(96)00070-5
- [HU04] HAMID, A. S.; UEDONO, A.: Spin-dependent momentum density distribution and Fermi surface of Ho via 2D-ACAR measurements. *physica status solidi (b)* 241 (2004), 4, 856–863. DOI 10.1002/pssb.200301949
- [HUM⁺11] HAMID, A. S.; UEDONO, A.; MAJOR, Zs.; HAYNES, T. D.; LAVEROCK, J.; ALAM, M. A.; DUGDALE, S. B. ; FORT, D.: Electronic structure and Fermi surface of the weak ferromagnet Ni₃Al. *Physical Review B* 84 (2011), 235107. DOI 10.1103/PhysRevB.84.235107
- [HWL⁺12] HAYNES, T D.; WATTS, R J.; LAVEROCK, J; MAJOR, Zs; ALAM, M A.; TAYLOR, J W.; DUFFY, J A. ; DUGDALE, S B.: Positron annihilation study of the Fermi surface of Ni₂MnGa. *New Journal of Physics* 14 (2012), 3, 035020
- [IF79] IKARI, Hiroshi; FUJIWARA, Kunio: Positronium in α -Quartz. I. Observed Temperature Dependence of the Positronium Effective Mass and the Probability of Annihilation from Singlet Positronium State. *Journal of the Physical Society of Japan* 46 (1979), 1, 92–96. DOI 10.1143/JPSJ.46.92
- [IFT98] IMADA, Masatoshi; FUJIMORI, Atsushi ; TOKURA, Yoshinori: Metal-insulator transitions. *Review of Modern Physics* 70 (1998), 1039–1263. DOI 10.1103/RevModPhys.70.1039
- [Ika79] IKARI, Hiroshi: Positronium in α -Quartz. II. Possible Effect of Damping of Positronium Quasiparticle on the Momentum Distribution. *Journal of the Physical Society of Japan* 46 (1979), 1, 97–101. DOI 10.1143/JPSJ.46.97
- [JCD99] JEAVONS, AP; CHANDLER, RA ; DETTMAR, CAR: A 3D HIDAC-PET camera with sub-millimetre resolution for imaging small animals. *Nuclear Science, IEEE Transactions on* 46 (1999), 3, 468–473
- [JCS75] JEAVONS, Alan P.; CHARPAK, Georges ; STUBBS, RJ: The high-density multiwire drift chamber. *Nuclear Instruments and Methods* 124 (1975), 2, 491–503
- [Jea78] JEAVONS, Alan P.: The high-density proportional chamber and its applications. *Nuclear Instruments and Methods* 156 (1978), 1, 41–51
- [JMS03] JEAN, YC; MALLON, PE ; SCHRADER, David M.: *Principles and applications of positron and positronium chemistry*. World Scientific, 2003
- [JR75] JAMES, F; ROOS, MINUIT: Minuit-a system for function minimization and analysis of the parameter errors and correlations. *Computer Physics Communications* 10 (1975), 6, 343–367
- [JS87] JARLBORG, T.; SINGH, A. K.: Local-density approach for calculation of electron-positron enhancement in transition metals. *Physical Review B* 36 (1987), 4660–4663. DOI 10.1103/PhysRevB.36.4660
-

- [JW90] JENSEN, Kjeld O.; WEISS, A.: Theoretical study of the application of positron-induced Auger-electron spectroscopy. *Physical Review B* 41 (1990), 3928–3936. DOI 10.1103/PhysRevB.41.3928
- [Kah63] KAHANA, S.: Positron Annihilation in Metals. *Physical Review* 129 (1963), 1622–1628. DOI 10.1103/PhysRev.129.1622
- [KFM⁺13] KAWASUSO, A; FUKAYA, Y; MAEKAWA, M; MOCHIZUKI, I ; ZHANG, H: Spin-polarized positron annihilation spectroscopy for spintronics applications. *Journal of Physics: Conference Series* 443 (2013), 1, 012084
- [KKN⁺91] KUBOTA, T.; KONDO, H.; NAKASHIMA, H.; MURAKAMI, Y. ; TANIGAWA, S.: Study on Momentum Density and Fermi Surface in Paramagnetic Cr and W by Positron Annihilation. *physica status solidi (b)* 168 (1991), 1, 179–191. DOI 10.1002/pssb.2221680117
- [KKN⁺92] KONDO, H; KUBOTA, T; NAKASHIMA, H; KAWANO, T ; TANIGAWA, S: Spin-dependent three-dimensional electron momentum density studies in ferromagnetic Co by means of full-scale use of a two-dimensional angular correlation of polarized positron annihilation radiation. *Journal of Physics: Condensed Matter* 4 (1992), 19, 4595
- [KKN⁺93] KONDO, H.; KUBOTA, T.; NAKASHIMA, H.; MURAKAMI, Y. ; TANIGAWA, S.: Study on the Three-Dimensional Electron Momentum Density and the Fermi Surface in Cu by Positron Annihilation. *physica status solidi (b)* 177 (1993), 2, 345–360. DOI 10.1002/pssb.2221770210
- [KKS⁺75] KETTERSON, J. B.; KOELLING, D. D.; SHAW, J. C. ; WINDMILLER, L. R.: Parametrization of transition-metal Fermi-surface data. *Physical Review B* 11 (1975), 1447–1459. DOI 10.1103/PhysRevB.11.1447
- [KMF⁺11] KAWASUSO, Atsuo; MAEKAWA, Masaki; FUKAYA, Yuki; YABUCHI, Atsushi ; MOCHIZUKI, Izumi: Spin-polarized positron annihilation measurements of polycrystalline Fe, Co, Ni, and Gd based on Doppler broadening of annihilation radiation. *Physical Review B* 83 (2011), 100406. DOI 10.1103/PhysRevB.83.100406
- [KMF⁺12] KAWASUSO, A.; MAEKAWA, M.; FUKAYA, Y.; YABUCHI, A. ; MOCHIZUKI, I.: Doppler broadening of annihilation radiation measurements on 3d and 4f ferromagnets using polarized positrons. *Physical Review B* 85 (2012), 024417. DOI 10.1103/PhysRevB.85.024417
- [Koh61] KOHONEN, T.: Contributions to the study of life times of positrons in solids. *Annals Academiae Scientiarum Fennicae A VI* (1961), 1–79
- [Koh99] KOHN, W.: Nobel Lecture: Electronic structure of matter—wave functions and density functionals. *Review of Modern Physics* 71 (1999), 1253–1266
- [KRL99] KRAUSE-REHBERG, Reinhard; LEIPNER, Hartmut S.: *Positron annihilation in semiconductors: defect studies*. Bd. 127. Springer, 1999
-

- [Kru99] KRUSEMAN, A. C.: *Two-dimensional ACAR and low-background DBAR on materials with defects*, Delft University of Technology, Diss., 1999
- [KS65] KOHN, W.; SHAM, L. J.: Self-Consistent Equations Including Exchange and Correlation Effects. *Physical Review* 140 (1965), A1133–A1138
- [KS75] KUBICA, P.; STEWART, A. T.: Thermalization of Positrons and Positronium. *Physical Review Letters* 34 (1975), 852–855. DOI 10.1103/PhysRevLett.34.852
- [KS08a] KONTRYM-SZNAJD, G.: Transform Methods of Computerized Tomography in Studying Electronic Structure and Fermi Surfaces of Solids. *Acta Physica Polonica* 113 (2008), 5
- [KS08b] KUMMAMURU, Ravi K.; SOH, Yeong-Ah: Electrical effects of spin density wave quantization and magnetic domain walls in chromium. *Nature* 452 (2008), 7189, 859–863
- [KSH⁺06] KOTLIAR, G.; SAVRASOV, S. Y.; HAULE, K.; OUDOVENKO, V. S.; PARCOLLET, O. ; MARIANETTI, C. A.: Electronic structure calculations with dynamical mean-field theory. *Review of Modern Physics* 78 (2006), 865–951. DOI 10.1103/RevModPhys.78.865
- [KSS14a] KONTRYM-SZNAJD, Grażyna; SORMANN, Heinrich: Electron–positron momentum densities in crystalline solids. *physica status solidi (b)* 251 (2014), 1, 140–147. DOI 10.1002/pssb.201350116
- [KSS14b] KONTRYM-SZNAJD, Grażyna; SORMANN, Heinrich: The influence of a positron on electron-positron momentum densities in metallic materials. *Physica Scripta* 89 (2014), 1, 015808
- [KSSB12] KONTRYM-SZNAJD, G.; SORMANN, H. ; BOROSKI, E.: General properties of electron-positron momentum densities. *Physical Review B* 85 (2012), 245104. DOI 10.1103/PhysRevB.85.245104
- [KSSCP⁺02] KONTRYM-SZNAJD, G.; SAMSEL-CZEKAŁA, M.; PIETRASZKO, A.; SORMANN, H.; MANNINEN, S.; HUOTARI, S.; HÄMÄLÄINEN, K.; LAUKKANEN, J.; WEST, R. N. ; SCHÜLKE, W.: Electron momentum density in yttrium. *Physical Review B* 66 (2002), 155110. DOI 10.1103/PhysRevB.66.155110
- [KSSW⁺75] KONTRYM-SZNAJD, G.; STACHOWIAK, H.; WIERZCHOWSKI, W.; PETERSEN, K.; THRANE, N. ; TRUMPY, G.: Investigation of the electronic structure of ferro- and paramagnetic nickel by positron annihilation. *Applied Physics* 8 (1975), 2, 151–162. DOI 10.1007/BF00896032
- [KV04] KOTLIAR, G.; VOLLHARDT, D.: *Physics Today* 57 (2004), 3, 53 S
- [KWP⁺04] KETZER, B; WEITZEL, Q; PAUL, S; SAULI, F ; ROPELEWSKI, L: Performance of triple GEM tracking detectors in the COMPASS experiment. *Nuclear Instruments and Methods in Physics Research Section A: Accelerators, Spectrometers, Detectors and Associated Equipment* 535 (2004), 1, 314–318
-

- [Lan87] LANTTO, Lauri J.: Variational theory of multicomponent quantum fluids: An application to positron-electron plasmas at $T=0$. *Physical Review B* 36 (1987), 5160–5170. DOI 10.1103/PhysRevB.36.5160
- [LCW73] LOCK, D G.; CRISP, V H C. ; WEST, R N.: Positron annihilation and Fermi surface studies: a new approach. *Journal of Physics F: Metal Physics* 3 (1973), 3, 561
- [LCW12] LEITNER, Michael; CEEH, Hubert ; WEBER, Josef-Andreas: Eliminating spatial distortions in Anger-type gamma cameras. *New Journal of Physics* 14 (2012), 12, 123014
- [LDM⁺05] LAVEROCK, J.; DUGDALE, S. B.; MAJOR, Zs.; ALAM, M. A.; RU, N.; FISHER, I. R.; SANTI, G. ; BRUNO, E.: Fermi surface nesting and charge-density wave formation in rare-earth tritellurides. *Physical Review B* 71 (2005), 085114. DOI 10.1103/PhysRevB.71.085114
- [LHAD10] LAVEROCK, J.; HAYNES, T. D.; ALAM, M. A. ; DUGDALE, S. B.: Experimental determination of the state-dependent enhancement of the electron-positron momentum density in solids. *Physical Review B* 82 (2010), 125127. DOI 10.1103/PhysRevB.82.125127
- [LKK01] LICHTENSTEIN, A. I.; KATSNELSON, M. I. ; KOTLIAR, G.: Finite-Temperature Magnetism of Transition Metals: An ab initio Dynamical Mean-Field Theory. *Physical Review Letters* 87 (2001), 067205. DOI 10.1103/PhysRevLett.87.067205
- [Lom62] LOMER, W M.: Electronic Structure of Chromium Group Metals. *Proceedings of the Physical Society* 80 (1962), 2, 489
- [LP74] LAM, L.; PLATZMAN, P. M.: Momentum density and Compton profile of the inhomogeneous interacting electronic system. I. Formalism. *Physical Review B* 9 (1974), 5122–5127. DOI 10.1103/PhysRevB.9.5122
- [LWC15] LEITNER, M.; WEBER, J.-A. ; CEEH, H.: Fermi surface determination from momentum density projections. *arXiv:1505.02572* (2015)
- [MAI⁺92] MIZOGAWA, Tatsumi; AWAYA, Yohko; ISOZUMI, Yasuhito; KATANO, Rintaro; ITO, Shin ; MAEDA, Nobuhiro: New readout technique for two-dimensional position-sensitive detectors. *Nuclear Instruments and Methods in Physics Research Section A: Accelerators, Spectrometers, Detectors and Associated Equipment* 312 (1992), 3, 547–552. DOI [http://dx.doi.org/10.1016/0168-9002\(92\)90203-G](http://dx.doi.org/10.1016/0168-9002(92)90203-G)
- [MASAKM88] MANUEL A 4 SINGH A K, Hoffman L. Jarlborg T. Genoud P P. Jarlborg T. Genoud P; M, Peter: *Positron Annihilation edited by L Dorikens-Vanpraet, M Dorikens and D Segen (Singapore: World Scientific) p 109* (1988)
- [MB02] MITROY, J.; BARBIELLINI, B.: Enhancement factors for positron annihilation studies. *Physical Review B* 65 (2002), 235103. DOI 10.1103/PhysRevB.65.235103
-

- [MDE⁺12] MOROZOV, A; DEFENDI, I; ENGELS, R; FRAGA, FAF; GUERARD, B; JURKOVIC, M; KEMMERLING, G; MANZIN, G; MARGATO, LMS; NIKO, H u. a.: A 2D gas scintillation detector for thermal neutrons. In: *Nuclear Science Symposium and Medical Imaging Conference (NSS/MIC), 2012 IEEE IEEE*, 2012, 1572–1576
- [MDW⁺04] MAJOR, Zs.; DUGDALE, S. B.; WATTS, R. J.; SANTI, G.; ALAM, M. A.; HAYDEN, S. M.; DUFFY, J. A.; TAYLOR, J. W.; JARLBORG, T.; BRUNO, E.; BENEÀ, D. ; EBERT, H.: Direct Observation of the Multisheet Fermi Surface in the Strongly Correlated Transition Metal Compound ZrZn₂. *Physical Review Letters* 92 (2004), 107003. DOI 10.1103/PhysRevLett.92.107003
- [MESH14] MAKKONEN, Ilja; ERVASTI, Mikko M.; SIRO, Topi ; HARJU, Ari: Enhancement models of momentum densities of annihilating electron-positron pairs: The many-body picture of natural geminals. *Physical Review B* 89 (2014), 041105. DOI 10.1103/PhysRevB.89.041105
- [MGP⁺13] MERIDA, David; GARCIA, Jose A.; PLAZAOLA, Fernando; SANCHEZ-ALARCOS, Vicente; PÉREZ-LANDEZÁBAL, Jose I. ; RECARTE, Vicente: Defects structure characterization of NiMnGa alloys by PALS. *Journal of Physics: Conference Series* 443 (2013), 1, 012039
- [MHP06] MAKKONEN, I.; HAKALA, M. ; PUSKA, M. J.: Modeling the momentum distributions of annihilating electron-positron pairs in solids. *Physical Review B* 73 (2006), 035103. DOI 10.1103/PhysRevB.73.035103
- [Mil75] MILLS, Allen P.: Effects of collisions on the magnetic quenching of positronium. *The Journal of Chemical Physics* 62 (1975), 7, 2646–2659
- [Mog74] MOGENSEN, O-E_: Spur reaction model of positronium formation. *The Journal of Chemical Physics* 60 (1974), 3, 998–1004
- [MPMH92] MAKINEN, J; PALKO, S; MARTIKAINEN, J ; HAUTOJARVI, P: Positron backscattering probabilities from solid surfaces at 2-30 keV. *Journal of Physics: Condensed Matter* 4 (1992), 36, L503
- [MS79] MIJNARENDS, P. E.; SINGRU, R. M.: Point-geometry angular correlation curves for Cu: A study of enhancement in positron annihilation. *Physical Review B* 19 (1979), 6038–6048. DOI 10.1103/PhysRevB.19.6038
- [MSH⁺95] MANUEL, A.A.; SHUKLA, A.; HOFFMANN, L.; JARLBORG, T.; BARBIELLINI, B.; MASSIDDA, S.; SADOWSKI, W.; WALKER, E.; ERB, A. ; PETER, M.: Fermi surfaces of high-Tc superconductors by positron 2D-ACAR . *Journal of Physics and Chemistry of Solids* 56 (1995), 12, 1951–1954. DOI 10.1016/0022-3697(95)00099-2, – Proceedings of the Conference on Spectroscopies in Novel Superconductors
- [MV89] METZNER, Walter; VOLLHARDT, Dieter: Correlated Lattice Fermions in $d = \infty$ Dimensions. *Physical Review Letters* 62 (1989), 324–327. DOI 10.1103/PhysRevLett.62.324
-

- [NBB⁺11] NEUBAUER, A.; BOEUF, J.; BAUER, A.; RUSS, B.; LOHNEYSEN, H. ; PFLEIDERER, C.: Ultra-high vacuum compatible image furnace. *Review of Scientific Instruments* 82 (2011), 1, 013902–013902. DOI 10.1063/1.3523056
- [NCT⁺01] NAGAI, Y.; CHIBA, T.; TANG, Z.; AKAHANE, T.; KANAI, T.; HASEGAWA, M.; TAKENAKA, M. ; KURAMOTO, E.: Fermi Surface of Nanocrystalline Embedded Particles in Materials: bcc Cu in Fe. *Physical Review Letters* 87 (2001), 176402. DOI 10.1103/PhysRevLett.87.176402
- [Neu11] NEUBAUER, Andreas: *Single crystal growth of intermetallic compounds with unusual low temperature properties*. München, Technische Universität München, Dissertation, 2011
- [NH90] NAGASHIMA, Y.; HYODO, T.: Effects of positron spin polarization on orthopositronium and parapositronium formation in a magnetic field. *Physical Review B* 41 (1990), 3937–3942. DOI 10.1103/PhysRevB.41.3937
- [NNK⁺00] NAGAI, Yasuyoshi; NAGASHIMA, Yasuyuki; KIM, Jaehong; ITOH, Yoshiko ; HYODO, Toshio: Measurement of positron spin polarization by using the Doppler broadening method. *Nuclear Instruments and Methods in Physics Research Section B: Beam Interactions with Materials and Atoms* 171 (2000), 1-2, 199–203. DOI 10.1016/S0168-583X(00)00044-6, – Low Energy Positron and Positronium Physics
- [OK02] OTSUKA, Kazuhiro; KAKESHITA, Tomoyuki: Science and Technology of Shape-Memory Alloys: New Developments. *MRS Bulletin* 27 (2002), 91–100. DOI 10.1557/mrs2002.43
- [OP49] ORE, A.; POWELL, J.: Three-Photon Annihilation of an Electron-Positron Pair. *Physical Review* 75 (1949), 1696–1699. DOI 10.1103/PhysRev.75.1696
- [OP62] OBENSHAIN, Felix E.; PAGE, Lorne A.: Strong Electric Field Experiments on Positronium in Gases. *Physical Review* 125 (1962), 573–581. DOI 10.1103/PhysRev.125.573
- [OSS⁺10] OBERDORFER, Bernd; STEYSKAL, Eva-Maria; SPRENGEL, Wolfgang; PUFF, Werner; PIKART, Philip; HUGENSCHMIDT, Christoph; ZEHETBAUER, Michael; PIPPAN, Reinhard ; WÜRSCHUM, Roland: *In Situ* Probing of Fast Defect Annealing in Cu and Ni with a High-Intensity Positron Beam. *Physical Review Letters* 105 (2010), 146101. DOI 10.1103/PhysRevLett.105.146101
- [PBSM94] PANKALUOTO, R.; BANSIL, A.; SMEDSKJAER, L. C. ; MIJNARENDS, P. E.: *a*-axis-projected electron-positron-momentum density and positron-annihilation spectra in YBa₂Cu₃O_{7-x}. *Physical Review B* 50 (1994), 6408–6415. DOI 10.1103/PhysRevB.50.6408
- [PCG⁺99] PLUZHNIKOV, V. B.; CZOPNIK, A.; GRECHNEV, G. E.; SAVCHENKO, N. V. ; SUSKI, W.: Band structure and Fermi surface of TmGa₃. *Physical Review B* 59 (1999), 7893–7900. DOI 10.1103/PhysRevB.59.7893
-

- [PI97] PACCHIONI, Gianfranco; IERANÒ, Gianluigi: *Ab initio* formation energies of point defects in pure and Ge-doped SiO₂. *Physical Review B* 56 (1997), 7304–7312. DOI 10.1103/PhysRevB.56.7304
- [Pik12] PIKART, Philip: *Advances in Coincident Doppler Broadening Spectroscopy: Element Selective Studies on Metallic Nanolayers with Monoenergetic Positrons*. München, Technische Universität München, Dissertation, 2012
- [PKE⁺08] PIOCHACZ, Christian; KÖGEL, Gottfried; EGGER, Werner; HUGENSCHMIDT, Christoph; MAYER, Jakob; SCHRECKENBACH, Klaus; SPERR, Peter; STADLBAUER, Martin ; DOLLINGER, Günther: A positron remoderator for the high intensity positron source NEPOMUC. *Applied Surface Science* 255 (2008), 1, 98–100
- [PKSD11] PYLAK, M.; KONTRYM-SZNAJD, G. ; DOBRZYŃSKI, L.: Electron–positron momentum density distribution of Gd from 2D ACAR data via Maximum Entropy and Cormacks methods. *Applied Physics A* 104 (2011), 2, 587–592. DOI 10.1007/s00339–011–6350–z
- [PUH⁺01] PFLEIDERER, C.; UHLARZ, M.; HAYDEN, S. M.; VOLLMER, R.; LOHNEYSSEN, H. v.; BERNHOEFT, N. R. ; LONZARICH, G. G.: Coexistence of superconductivity and ferromagnetism in the d-band metal ZrZn₂. *Nature* 412 (2001), 6842, 58–61. ISBN 0028–0836
- [RB07] RUSZ, Ján; BIASINI, Maurizio: Positron wave-function effects in the measurement of the two-dimensional angular correlation of the annihilation radiation of a spin-polarized system. *Physical Review B* 75 (2007), 235115. DOI 10.1103/PhysRevB.75.235115
- [Reh14] <http://positron.physik.uni-halle.de/>
- [RGJ⁺15] REINER, M.; GIGL, T.; JANY, R.; HAMMERL, G. ; HUGENSCHMIDT, C.: Detection and imaging of the oxygen deficiency in single crystalline YBa₂Cu₃O_{7– δ} thin films using a scanning positron beam. *Applied Physics Letters* 106 (2015), 11. DOI 10.1063/1.4916032
- [RM84] RABOU, LPLM; MIJNARENDS, PE: Approximate validity of the Lock-Crisp-West theorem in positron annihilation. *Solid state communications* 52 (1984), 11, 933–936
- [RPH12] REINER, M.; PIKART, P. ; HUGENSCHMIDT, C.: Annealing of Thin Metallic Films Studied by Depth Dependent DB-Spectroscopy and Free Ps Annihilation. *Physics Procedia* 35 (2012), 0, 104–110. DOI 10.1016/j.phpro.2012.06.019, – Positron Studies of Defects 2011
- [RPH13] REINER, Markus; PIKART, Philip ; HUGENSCHMIDT, Christoph: In-situ (C)DBS at high temperatures at the NEPOMUC positron beam line. *Journal of Physics: Conference Series* 443 (2013), 1, 012071
-

- [RPH14] REINER, M.; PIKART, P. ; HUGENSCHMIDT, C.: Thin film annealing and alloying of a Au/Cu two-layer system studied by positron annihilation spectroscopy. *Journal of Alloys and Compounds* 587 (2014), 0, 515–519. DOI 10.1016/j.jallcom.2013.10.094
- [RS88] RUBASZEK, Anna; STACHOWIAK, Henryk: Self-consistent solution of the Kahana equation for a positron in an electron gas. *Physical Review B* 38 (1988), 3846–3855. DOI 10.1103/PhysRevB.38.3846
- [RST02] RUBASZEK, A.; SZOTEK, Z. ; TEMMERMAN, W. M.: Understanding electron-positron momentum densities in paramagnetic chromium. *Physical Review B* 65 (2002), 125104. DOI 10.1103/PhysRevB.65.125104
- [Rut12] RUTZINGER, Martin: *Design und Charakterisierung eines Gas-Electron-Multiplier (GEM) Detektors zum ortsaufgelösten Nachweis von 511 keV Gammastrahlung.* 2012
- [SAA⁺00] SAXENA, S. S.; AGARWAL, P.; AHILAN, K.; GROSCHE, F. M.; HASELWIMMER, R. K. W.; STEINER, M. J.; PUGH, E.; WALKER, I. R.; JULIAN, S. R.; MONTHOUX, P.; LONZARICH, G. G.; HUXLEY, A.; SHEIKIN, I.; BRAITHWAITE, D. ; FLOUQUET, J.: Superconductivity on the border of itinerant-electron ferromagnetism in UGe₂. *Nature* 406 (2000), 6796, 587–592. ISBN 0028–0836
- [SAK03] S. ASAI, O. J.; KOBAYASHI, T.: Solution of Orthopositronium Lifetime Puzzle. *arXiv:hep-ex/0308031* (2003)
- [Sau01] SAULI, Fabio: Gas detectors: achievements and trends. *Nuclear Instruments and Methods in Physics Research Section A: Accelerators, Spectrometers, Detectors and Associated Equipment* 461 (2001), 1, 47–54
- [SBNL03] STEINER, Markus J.; BECKERS, Fabien; NIKLOWITZ, Philipp G. ; LONZARICH, Gilbert G.: Non-Fermi liquid form of the low temperature resistivity in the low moment ferromagnets Ni₃Al and {YNi₃}. *Physica B: Condensed Matter* 329-333, Part 2 (2003), 0, 1079–1080. DOI 10.1016/S0921–4526(02)02341–4
- [Sch87] SCHAEFER, H-E: Investigation of thermal equilibrium vacancies in metals by positron annihilation. *physica status solidi (a)* 102 (1987), 1, 47–65
- [SFB⁺72] STEINITZ, M. O.; FAWCETT, E.; BURLESON, C. E.; SCHAEFER, J. A.; FRISHMAN, L. O. ; MARCUS, J. A.: Orthorhombic Anisotropy of Magnetic Susceptibility in Antiferromagnetic Chromium. *Physical Review B* 5 (1972), 3675–3678. DOI 10.1103/PhysRevB.5.3675
- [SHS08] STADLBAUER, M; HUGENSCHMIDT, C ; SCHRECKENBACH, K: New design of the CDB-spectrometer at NEPOMUC for T-dependent defect spectroscopy in Mg. *Applied Surface Science* 255 (2008), 1, 136–138
- [SJ85] SINGH, A K.; JARLBORG, T: Calculation of Compton profiles and positron annihilation matrix elements using LMTO wavefunctions. *Journal of Physics F: Metal Physics* 15 (1985), 3, 727
-

- [SJ88] SCHRADER, David M.; JEAN, YC: Positron and positronium chemistry. (1988)
- [SKS92] SUNDARARAJAN, V; KANHERE, D. G. ; SINGRU, R. M.: Calculation of momentum distributions in paramagnetic chromium: Compton scattering and positron annihilation. *Journal of Physics: Condensed Matter* 4 (1992), 46, 8975
- [SKS06] SORMANN, H.; KONTRYM-SZNAJD, G.: Many-body effects on the electron-positron momentum density in simple and transition metals: Comparison with positron annihilation spectroscopy data. *Physical Review B* 73 (2006), 075111. DOI 10.1103/PhysRevB.73.075111
- [Sle06] SLEBARSKI, Andrzej: Electron-correlation effects in a disordered Fe₂TiSn Heusler alloy. *Journal of Physics D: Applied Physics* 39 (2006), 5, 856
- [SM74] SINGRU, R. M.; MIJNARENDS, P. E.: Calculation of the momentum density in ferromagnetic nickel. *Physical Review B* 9 (1974), 2372–2380. DOI 10.1103/PhysRevB.9.2372
- [SMB87] SEEGER, A.; MAJOR, J. ; BANHART, F.: The Study of Positron Diffusion in Solids by Positron Spin Relaxation (e+SR) Experiments. *physica status solidi (a)* 102 (1987), 1, 91–106. DOI 10.1002/pssa.2211020107
- [SMW88] SINGH, A. K.; MANUEL, A. A. ; WALKER, E.: Differences in the Fermi Surface Topology of Paramagnetic and Antiferromagnetic Cr Studied by Positron Annihilation. *Europhysics Letters* 6 (1988), 1, 67
- [Sor96] SORMANN, H.: Influence of lattice effects on the electron-positron interaction in metals. *Physical Review B* 54 (1996), 4558–4580. DOI 10.1103/PhysRevB.54.4558
- [SOS⁺77] SHIOTANI, Nobuhiro; OKADA, Takuya; SEKIZAWA, Hisashi; WAKOH, Shinya ; KUBO, Yasunori: Angular Correlation of Positron Annihilation Radiation in Chromium and Molybdenum. *Journal of the Physical Society of Japan* 43 (1977), 4, 1229–1236. DOI 10.1143/JPSJ.43.1229
- [SPK⁺96] SCHNEIDER, C. M.; PRACHT, U.; KUCH, W.; CHASSÉ, A. ; KIRSCHNER, J.: Magnetic dichroism in photoemission as a spin-resolving probe for electronic correlations. *Physical Review B* 54 (1996), R15618–R15621. DOI 10.1103/PhysRevB.54.R15618
- [SS83] SINGH, A. K.; SINGRU, R. M.: Two-dimensional angular correlation of positron annihilation radiation in paramagnetic chromium. *Journal of Physics F: Metal Physics* 13 (1983), 10, 2189
- [SSM⁺69] STEINITZ, M. O.; SCHWARTZ, L. H.; MARCUS, J. A.; FAWCETT, E. ; REED, W. A.: Lattice Anisotropy in Antiferromagnetic Chromium. *Physical Review Letters* 23 (1969), 979–982. DOI 10.1103/PhysRevLett.23.979
- [SSS12] SELVAKUMAR, S.; SIVAJI, K. ; SMITH, S.V.: Electron Momentum Distribution Mapping of Trans-Stilbene Projected to [101] by Positron 2D-ACAR. *Physics Procedia* 35 (2012), 0, 157–161. DOI 10.1016/j.phpro.2012.06.028
-

- [Sta08] STADLBAUER, Martin: *Investigation of the chemical vicinity of defects in Mg and AZ31 with positron coincident Doppler broadening spectroscopy*. München, Technische Universität München, Dissertation, 2008
- [Str74] STROSCIO, Michael A.: Positronium: A Review of the Calculations. / DTIC Document. 1974, – Forschungsbericht
- [Str02] STRASSER, Benno: *Aufbau einer Anlage zur positroneninduzierten Auger-Elektronenspektroskopie*. München, Technische Universität München, Dissertation, 2002
- [Tao72] TAO, S. J.: Positronium Annihilation in Molecular Substances. *The Journal of Chemical Physics* 56 (1972), 11, 5499–5510. DOI 10.1063/1.1677067
- [TFJ⁺87] TOWNSEND, D; FREY, P; JEAUVONS, A; REICH, G; TOCHON-DANGUY, HJ; DONATH, A; CHRISTIN, A; SCHALLER, G u. a.: High density avalanche chamber (HIDAC) positron camera. *Journal of Nuclear Medicine* 28 (1987), 10, 1554–62
- [TKSO05] TOROPOVA, A.; KOTLIAR, G.; SAVRASOV, S. Y. ; OUDOVENKO, V. S.: Electronic structure and magnetic anisotropy of CrO₂. *Physical Review B* 71 (2005), 172403. DOI 10.1103/PhysRevB.71.172403
- [Tsu67] TSUI, D. C.: de Haas—van Alphen Effect and Electronic Band Structure of Nickel. *Physical Review* 164 (1967), 669–683. DOI 10.1103/PhysRev.164.669
- [UHK⁺96] ULLAKKO, K.; HUANG, J. K.; KANTNER, C.; O’HANDLEY, R. C. ; KOKORIN, V. V.: Large magnetic-field-induced strains in Ni₂MnGa single crystals. *Applied Physics Letters* 69 (1996), 13, 1966–1968. DOI 10.1063/1.117637
- [VZG03] VALLERY, R. S.; ZITZEWITZ, P. W. ; GIDLEY, D. W.: Resolution of the Orthopositronium-Lifetime Puzzle. *Physical Review Letters* 90 (2003), 20, 203402
- [WC77] WANG, C. S.; CALLAWAY, J.: Energy bands in ferromagnetic nickel. *Physical Review B* 15 (1977), 298–306. DOI 10.1103/PhysRevB.15.298
- [WCH⁺14] WEBER, J A.; CEEH, H; HUGENSCHMIDT, C; LEITNER, M ; BÖNI, P: The effect of regularization on the reconstruction of ACAR data. *Journal of Physics: Conference Series* 505 (2014), 1, 012047
- [Web15] WEBER, Josef A., Technische Universität München, Diss., 2015
- [WHM⁺01] WILKINSON, I.; HUGHES, R. J.; MAJOR, Zs.; DUGDALE, S. B.; ALAM, M. A.; BRUNO, E.; GINATEMPO, B. ; GIULIANO, E. S.: Fermi Surface Nesting in Disordered Cu_{1-x}Pd_x Alloys. *Physical Review Letters* 87 (2001), 216401. DOI 10.1103/PhysRevLett.87.216401
- [WMK⁺98] WOJCIK, R; MAJEWSKI, S; KROSS, B; STEINBACH, D u. a.: High spatial resolution gamma imaging detector based on a 5" diameter R3292 Hamamatsu PSPMT. *Nuclear Science, IEEE Transactions on* 45 (1998), 3, 487–491
-

-
- [WMW81] WEST, R. N.; MAYERS, J.; WALTERS, P. A.: A high-efficiency two-dimensional angular correlation spectrometer for positron studies. *Journal of Physics E: Scientific Instruments* 14 (1981), 4, 478
- [WN63] WEISSMANN, Sigmund; NAKAJIMA, Koichi: Defect Structure and Density Decrease in Neutron-Irradiated Quartz. *Journal of Applied Physics* 34 (1963), 3, 611–618. DOI 10.1063/1.1729317
- [ZVHRG79] ZITZEWITZ, P. W.; VAN HOUSE, J. C.; RICH, A.; GIDLEY, D. W.: Spin Polarization of Low-Energy Positron Beams. *Physical Review Letters* 43 (1979), 1281–1284. DOI 10.1103/PhysRevLett.43.1281
-

Acknowledgements

Ich möchte allen danken, die zum Gelingen dieser Arbeit beigetragen haben, sei es durch moralische oder finanzielle Unterstützung, durch die zahlreichen Diskussionen oder sei es durch harte körperliche Arbeit.

Zuallererst möchte ich Herrn PD Dr. Christoph Hugenschmidt danken. Und zwar zunächst dafür, dass er mir dieses spannende und herausfordernde Thema für meine Dissertation überlassen hat. Seine Tür stand nicht nur im übertragenen Sinn immer für mich offen, er nahm sich immer die Zeit, Probleme jedweder Art mit mir zu diskutieren. Als Betreuer meiner Doktorarbeit lenkte er meinen Blick über die täglichen messtechnischen Probleme hinaus und ließ mich auch eigene wissenschaftliche Fragestellungen bearbeiten. Ich möchte mich für das entgegengebrachte Vertrauen und den Ansporn zum selbstständigen wissenschaftlichen Arbeiten bedanken. Christoph Hugenschmidt bestärkte mich darin, dass Physiker nicht einfach ein Beruf, sondern vielmehr eine Berufung ist. Die gute Stimmung, die produktive Atmosphäre und die Kollegialität in unserer Gruppe sind maßgeblich sein Verdienst.

Leider habe ich nicht mehr die Gelegenheit, Herrn Prof. Dr. Klaus Schreckenbach persönlich für seine Unterstützung zu danken. Ich möchte hier aber zum Ausdruck bringen, dass seine fundierte, gewissenhafte wissenschaftliche Arbeitsweise und vor allem seine persönliche Integrität für mich immer ein Vorbild waren und sein werden.

Ich möchte Herrn Prof. Dr. Böni für die vielen Diskussionen danken und auch dafür, dass er seine Erfahrungen im Publizieren, sei es beim Anfertigen eines Manuskripts oder eines Strahlzeitproposals immer mit mir geteilt hat. Außerdem möchte ich ihm für seine Unterstützung mit meinem Stipendium danken.

Mein besonderer Dank gilt Herrn Prof. Dr. Liviu Chioncel für die äußerst produktive Zusammenarbeit zwischen Theorie und Experiment, ohne den diese Arbeit in dieser Form nicht möglich gewesen wäre. Ich möchte Herrn Chioncel dafür danken, dass er seine Einblicke in die Tiefen der DMFT mit mir geteilt hat, und für seine Geduld beim Erklären der selbigen. Beim Schreiben des Manuskripts unserer Publikation und der Antwort für die Referees habe ich sehr viel von ihm gelernt.

An dieser Stelle möchte ich mich bei Herrn Prof. Dr. Dieter Vollhardt für seinen Rat und seine unschätzbare Hilfe beim Erstellen des Manuskripts bedanken.

Ganz besonders möchte ich mich bei meinen Büro- und ACAR-Kollegen Josef Weber und Dr. Michael Leitner für die gute Zusammenarbeit und das produktive Umfeld bedanken. Josef möchte ich insbesondere dafür danken, dass er zusammen mit mir die alltäglichen Tücken der experimentellen Arbeit, sei es das Debuggen von 1980er-Elektronik, den Transport der Quelle oder das Messen ganz allgemein, gemeistert hat. Die deutsche Sprache unterscheidet zwar im Prinzip zwischen Kollege und Freund, aber es freut mich, dass in unserem Fall diese Differenzierung aufgehoben ist. Michael möchte ich für seine Unterstützung bei diversen programmiertechnischen Problemen danken. Außerdem für die zahlreichen Diskussionen bei uns im Büro (nicht nur über Physik). Sein tiefes Verständnis der Mathematik und der Physik und seine Bereitschaft es zu teilen waren von unschätzbarem Wert.

Natürlich möchte ich auch allen meinen Kollegen aus der NEPOMUC-Gruppe ganz allgemein danken. Die gute Stimmung und die Kollegialität in unserer Gruppe, auch außerhalb des Labors, hat mich täglich motiviert und mir auch in schwierigen Zeiten, wenn einmal wieder nichts funktioniert hat, Halt gegeben. Dafür möchte ich mich insbesondere bei meinen Doktorandenkollegen Marcel Dickman, Pascal Neibecker, Johannes Mitteneder, Benjamin Rienecker und Samantha Zimmik und auch bei unseren Diplom-/Master-/Bachelor-/Werk-Studenten Florian Lippert, Karin Hain, Lukas Bedrich, Niklas Grill, Josef Schmidbauer und Michaela Schleuder bedanken.

Im Speziellen möchte ich Herrn Dr. Christian Piochacz für seine Hilfe und seine konstruktiven Ratschläge bei der Auslegung des Vakuumsystems danken, sowie Herrn Dr. Philip Pikart für seine Hilfe bei diversen elektronischen Problemen. Außerdem Herrn Dr. Jakob Mayer für seine moralische Unterstützung vor allem gegen Ende der Arbeit. Desweiteren möchte ich Markus Reiner herzlich für seine Unterstützung bei den Dopplermessungen sowie für die zahlreichen Diskussionen und seine stets willkommenen Beiträge zum Lablife danken. Thomas Gigl danke ich für seine Unterstützung bei den Magnetfeldmessungen. Benjamin Löwe möchte ich für seine Hilfe bei diversen programmiertechnischen Problemen, vor allem bei der Datenaufnahme, danken. Herrn Dr. Werner Egger und Herrn Dr. Luca Ravelli möchte ich für die Diskussion und die Hilfe bei den Lebensdauermessungen danken.

Besonders möchte ich mich bei Martin Rutzinger und Christian Herold bedanken, deren Bachelorarbeiten ich betreut habe. Es war mein besonderes Vergnügen, zwei so hoch motivierte und talentierte Studenten zu betreuen und ich hoffe, dass sie ebenso viel dabei gelernt haben wie ich.

Mein Dank gilt auch allen Kollegen von E21, insbesondere Dr. Andreas Bauer, Dr. Michael Wagner, Dr. Andreas Neubauer, Georg Brandl und Alexander Regnat für die Cr-, die Fe₂TiSn- und die CrB₂-Proben, die gute Zusammenarbeit sowie für viele interessante Diskussionen.

Für die Hilfe bei konstruktiven und technischen Problemen danke ich unseren Technikern Reinhard Repper, Florin Repper, Alexander Wolf und Sebastian Vohburger. Ohne ihre tatkräftige Unterstützung wäre diese Projekt in dieser Form sicherlich nur schwer möglich gewesen.

Für die Fertigung der zahlreichen mechanischen Komponenten möchte ich in den Teams der FRMII-Werkstatt um Christian Herzog: Robert Schlecht, Andreas Huber und Thomas Fliegner und der Zentralwerkstatt, insbesondere Herrn Manfred Pfaller, Manfred Reither und Gabriel Reingen, sowie den zahlreichen Lehrlingen danken.

Für die freundliche Aufnahme und das zur Verfügungstellen von Experimentierplatz am Beschleunigerlabor danke ich besonders Herrn Dr. Ludwig Beck, Herrn PD Dr. Andreas Ulrich von E12 und Herrn Dr. Raimund Strauß von E15. Außerdem den Technikern und Operateuren am Beschleuniger für ihre Hilfe und Unterstützung.

Herrn Dr. Engels und Herrn Christian Wesolek danke ich für das zur Verfügungstellen der Multimesh-PMTs und für die Hilfe bei den Messungen.

An dieser Stelle möchte ich mich auch beim Strahlenschutz des Physik Departments, insbesondere bei Frau Sandra Morawitz für die konstruktive Zusammenarbeit bedanken.

Für ihre Hilfe bei der Charakterisierung und Präparation der Proben danke ich den freundlichen Mitarbeitern aus dem Kristalllabor, insbesondere Susanne Mayr, Katarzyna Danielewicz und Michael Stanger.

Für die Finanzierung dieses Promotionsvorhabens und des 2D-ACAR Projekts im Rahmen des TRR 80 danke ich der Deutschen Forschungsgemeinschaft.

Für die Unterstützung durch ein Promotionsstipendium danke ich der Universität Bayern e.V.

I'd also like to thank our colleges from the university of Bristol Prof. Dr. Ashraf Alam, Prof. Dr. Stephen Dugdale, Dr. Thomas Haynes and David Billington for the Anger cameras and their help in dismantling them. I want to express my gratitude towards Stephen Dugdale for his helpful discussions on the chromium data and the introduction into the 2D-ACAR community.

I want to thank Dr. Stefan Eijt and Lily Chai from the university Delft for their help with our first 2D-ACAR measurements in Delft on Fe₂TiSn.

Mein Dank gebührt auch in besonderem Maß all denjenigen, die vielleicht einen weniger fachlichen, aber dennoch entscheidenden Beitrag zu dieser Arbeit geleistet haben.

Besonders möchte ich meiner Mutter Andrea, meinem Bruder Martin und meiner Oma Maria danken, die mich immer unterstützt und gefördert haben und immer für mich da waren. Neben der finanziellen Unterstützung während des Studiums möchte ich mich dabei auch für die vielen Kleinigkeiten wie das Wäschewaschen oder die wöchentlichen Brotzeitpakete bedanken.

Meinen Freunden und Verwandten danke ich für ihre Unterstützung und für das geduldige Ertragen von diversen Laborgeschichten. Meinen ehemaligen Mitbewohnern Raimund und Anni danke ich für die vielen lustigen Abende in unserer kleinen Kommune. Insbesondere danke ich Raimund, dass er mir in allen Lebenslagen, u.A als mein Trauzeuge, zur Seite gestanden ist.

Allen voran danke ich meiner geliebten Frau Doris. Für ihre bedingungslose Liebe, ihre unerschütterliche Unterstützung und für ihre Geduld, die ich zum Teil hart auf die Probe gestellt habe. Doris, du bist die Liebe meines Lebens und die Quelle meiner Inspiration. Danke für elf wunderbare Jahre, denen noch viele folgen werden!
